

**THE  
UNIVERSITY OF WISCONSIN—  
MILWAUKEE**

**COLLEGE OF ENGINEERING  
AND  
APPLIED SCIENCE**



## **DISCLAIMER**

**This report was prepared as an account of work sponsored by an agency of the United States Government. Neither the United States Government nor any agency Thereof, nor any of their employees, makes any warranty, express or implied, or assumes any legal liability or responsibility for the accuracy, completeness, or usefulness of any information, apparatus, product, or process disclosed, or represents that its use would not infringe privately owned rights. Reference herein to any specific commercial product, process, or service by trade name, trademark, manufacturer, or otherwise does not necessarily constitute or imply its endorsement, recommendation, or favoring by the United States Government or any agency thereof. The views and opinions of authors expressed herein do not necessarily state or reflect those of the United States Government or any agency thereof.**

## **DISCLAIMER**

**Portions of this document may be illegible in electronic image products. Images are produced from the best available original document.**

**INTERFACIAL AREA  
AND INTERFACIAL TRANSFER  
IN TWO-PHASE FLOW SYSTEMS**

**Volume IV. Chapters 15 – 19**

**T. Guo, J. Park and G. Kojasoy**

**Department of Mechanical Engineering  
University of Wisconsin-Milwaukee, Milwaukee  
Milwaukee, Wisconsin 53201**

**March 2003**

**Prepared for  
U.S. DEPARTMENT OF ENERGY  
Under Contract No. DE-FG02-87ER13764**



## TABLE OF CONTENTS

EXECUTIVE SUMMARY .....	xv
LIST OF FIGURES .....	xvii
LIST OF TABLES .....	xxx

### VOLUME I

1. INTERNAL FLOW STRUCTURE AND INTERFACIAL AREA IN TWO-PHASE FLOW SYSTEMS .....	1
1.1 Introduction .....	1
1.2 Two-Phase Flow Field Formulations and Importance of Interfacial Area Measurements .....	4
1.3 Interfacial Area Concentration .....	8
1.4 Objectives of the Research Program .....	10
1.5 Highlight of Accomplishments .....	11
1.6 Publications Generated From the Research Program .....	15
Nomenclature .....	18
References .....	19
2. INTERFACIAL AREA MEASUREMENT METHODS .....	21
2.1 Chemical Method .....	21
2.2 Photographic Method .....	24
2.3 Light Attenuation Method .....	26
2.4 Ultrasonic Attenuation Method .....	29
2.5 Summary and Concluding Remarks .....	31
Nomenclature .....	33
References .....	34

3. UNDERLYING THEORETICAL APPROACH FOR INTERFACIAL AREA TRANSPORT AND CLOSURE RELATIONS. . . . .	41
3.1 Introduction . . . . .	41
3.2 Fluid Particle Transport Equation . . . . .	42
3.2.1 Fluid Particle Number Density Transport Equation . . . . .	42
3.2.2 Fluid Particle Interfacial Area Concentration Transport Equation . . . . .	45
3.2.3 Fluid Particle Volume Fraction (Void Fraction) Transport Equation . . . . .	47
3.3 Closure Relation Requirements . . . . .	49
3.4 Break-Up and Coalescence Processes . . . . .	49
3.5 Break-Up Parameters . . . . .	50
3.5.1 Maximum Fluid Particle Size . . . . .	50
3.5.2 Break-Up Frequency . . . . .	54
3.5.3 Number of Daughter Particle Production . . . . .	56
3.5.4 Daughter Particle Distribution . . . . .	56
3.6 Coalescence Parameters . . . . .	57
3.6.1 Description of Coalescence Processes . . . . .	57
3.6.2 Minimum Fluid Particle Size . . . . .	58
3.6.3 Collision Frequency . . . . .	59
3.6.4 Coalescence Efficiency . . . . .	60
3.7 Summary of Modeling Efforts Related to Fluid Particle Interactions . . . . .	61
3.7.1 Droplet Size Modeling Annular flow . . . . .	62
3.7.2 Bubble Size and Interfacial Area Modeling in Horizontal Bubbly Flow . . . . .	64
3.7.3 Fluid Particle Break-up Modeling . . . . .	67
3.7.4 Nonlinear Wave Growth and Break-Up Process of Large Cap Bubbles . . . . .	69
3.8 Formulation of Interfacial Area Transport Equation . . . . .	71
3.8.1 General Functional Dependence of Various Source and Sink Terms. . . . .	71
3.8.2 One-Dimensional Formulation and Relation to Experimental Measurements . . . . .	72

3.8.3 Wall Nucleation Source Term . . . . .	.75
3.9 Conclusions . . . . .	.76
Acknowledgement . . . . .	.77
Nomenclature . . . . .	.77
References. . . . .	.79
4. DESIGN AND DESCRIPTION OF AIR-WATER TWO-PHASE FLOW LOOP AND INSTRUMENTATION . . . . .	.91
4.1 Description of the Flow Loop. . . . .	.91
4.2 Pressure Transducers . . . . .	.94
4.3 Instrumentation . . . . .	.95
5. DEVELOPMENT OF DOUBLE-SENSOR PROBE METHOD FOR BUBBLY TWO-PHASE FLOW MEASUREMENTS . . . . .	100
ABSTRACT . . . . .	100
5.1 Introduction . . . . .	100
5.2 Double-Sensor Resistivity Probe Method . . . . .	102
5.2.1 Measurement Principle . . . . .	102
5.2.2 Double-Sensor Resistivity Probe Design and Signal Processing . . . . .	103
5.2.3 Local Void Fraction . . . . .	106
5.2.4 Local Bubble Interfacial Velocity and Velocity Spectrum . . . . .	106
5.2.5 Local Interfacial Area Concentration . . . . .	107
5.3 Experimental Setup and Procedure . . . . .	109
5.3.1 Description of the Flow Loop. . . . .	109
5.3.2 Experimental Procedure . . . . .	110
5.4 Experimental Results and Discussions . . . . .	111
5.4.1 Local Void Fraction Distribution . . . . .	111
5.4.2 Local Interfacial Area and Bubble Size Distributions . . . . .	112
5.4.3 Local Bubble Interface Velocity . . . . .	114

5.4.4 Bubble Chord-Length and Frequency Distributions . . . . .	116
5.5 Summary and Conclusions . . . . .	117
Acknowledgement . . . . .	118
Nomenclature . . . . .	118
References. . . . .	119

## VOLUME II

6. INTERNAL STRUCTURE AND INTERFACIAL VELOCITY DEVELOPMENT FOR BUBBLY TWO-PHASE FLOW . . . . .	134
ABSTRACT . . . . .	134
6.1 Introduction . . . . .	134
6.2 Experimental Setup and Procedure . . . . .	136
6.2.1 Description of the Flow Loop . . . . .	136
6.2.2 Experimental Procedure . . . . .	138
6.3 Results and Discussions . . . . .	139
6.3.1 Description of Interfacial Parameters . . . . .	139
6.3.2 Axial Flow-Pattern Development . . . . .	144
6.4 Summary and Conclusions . . . . .	146
Acknowledgement . . . . .	147
Nomenclature . . . . .	147
References. . . . .	148
7. USE OF HOT-FILM ANEMOMETRY TECHNIQUE IN HORIZONTAL BUBBLY TWO-PHASE FLOW MEASUREMENTS . . . . .	166
ABSTRACT . . . . .	166
7.1 Introduction . . . . .	167
7.2 Hot-Film Anemometry Technique . . . . .	168
7.2.1 Principle of Measurement . . . . .	168
7.2.2 Signal Processing . . . . .	169
7.2.2.1 Phase Separation . . . . .	169
7.2.2.2 Determination of Proper Data Set for Velocity Analysis . . . . .	172
7.2.3 Statistical Processing of the Data . . . . .	173
7.3 Experimental Set-Up and Procedure . . . . .	174
7.3.1 Experimental Set-Up . . . . .	174

7.3.2	Experimental Procedure	175
7.4	Experimental Results and Discussions	176
7.4.1	Local Void Fraction Description	176
7.4.2	Mean Liquid Velocity Description	177
7.4.3	Turbulence Structure Description	178
7.4.4	Effect of Flow Variables	180
7.5	Summary and Conclusions	182
	Acknowledgement	183
	Nomenclature	183
	References.	184
8.	DEVELOPMENT OF FOUR-SENSOR PROBE METHOD FOR PLUG/SLUG FLOW MEASUREMENTS	189
	ABSTRACT	189
8.1	Introduction	190
8.2	Development of Four-Sensor Resistivity Probe Method	194
8.2.1	Measurement Principle	194
8.2.2	Four-Sensor Probe Design	196
8.2.3	Signal Processing	197
8.2.3.1	Phase Identification	197
8.2.3.2	Separation of Large and Small Bubbles	200
8.2.3.3	Calculation of Time-Averaged Interfacial Area Concentration	200
8.3	Experimental Results and Discussion.	202
8.4	Conclusions	205
	Acknowledgement	206
	Nomenclature	206
	References.	207
9.	USE OF HOT-FILM ANEMOMETRY TECHNIQUE IN PLUG/SLUG FLOW MEASUREMENTS	214

ABSTRACT . . . . .	214
9.1 Introduction . . . . .	215
9.2 Hot-Film Anemometry Technique . . . . .	217
9.2.1 Measurement Principle . . . . .	217
9.2.2 Signal Processing . . . . .	219
9.2.2.1 Phase Identification . . . . .	219
9.2.2.2 Separation of Large and Small Gas Bubbles . . . . .	222
9.2.2.3 Liquid Velocity Field . . . . .	225
9.3 Experimental Setup and Procedure . . . . .	227
9.3.1 Experimental Setup . . . . .	227
9.3.2 Experimental Procedure . . . . .	228
9.4 Experimental Results and Discussion. . . . .	229
(a) Void Fraction . . . . .	230
(b) Mean Velocity Profiles . . . . .	230
(c) Turbulence Structure . . . . .	232
(d) Effect of Flow Variables . . . . .	234
9.5 Summary and Conclusions . . . . .	235
Acknowledgement . . . . .	236
References. . . . .	236
Nomenclature . . . . .	239
 10. SIMULTANEOUS USE OF TWO HOT-FILM PROBES FOR LOCAL STUDIES IN SLUG FLOW . . . . .	 248
ABSTRACT . . . . .	248
10.1 Introduction . . . . .	248
10.2 Hot-Film Anemometry Method . . . . .	251
10.2.1 Measurement Principle . . . . .	251
10.2.2 Signal Processing . . . . .	252
10.3 Experimental Setup and Procedure . . . . .	254

10.3.1 Experimental Setup . . . . .	254
10.3.2 Experimental Procedure . . . . .	255
10.4 Experimental Results and Discussions . . . . .	260
10.4.1 Liquid Ahead of the Gas Slug Nose . . . . .	261
10.4.2 Liquid in the Wake Region . . . . .	263
10.4.3 Liquid Layer Below the Gas Slug . . . . .	265
10.5 Summary and Conclusions . . . . .	268
Nomenclature . . . . .	269
Acknowledgement . . . . .	270
References. . . . .	271



### VOLUME III

## 11. DEVELOPMENT OF DOUBLE-SENSOR, PARALLEL-WIRE CONDUCTIVITY PROBE FOR HORIZONTAL STRATIFIED FLOW PATTERNS . . . . . 274

ABSTRACT . . . . .	274
11.1 Introduction . . . . .	274
11.2 Experimental Set-Up and Procedure . . . . .	276
11.2.1 Description of the Flow Loop . . . . .	276
11.2.2 Test Section . . . . .	277
11.2.3 Experimental Procedure . . . . .	279
11.2.4 Experimental Conditions . . . . .	281
11.3 Results and Discussions . . . . .	282
11.3.1 Interfacial Wave Patterns . . . . .	282
11.3.2 Wave Parameters . . . . .	284
11.3.2.1 Time-Averaged Liquid Thickness . . . . .	284
11.3.2.2 Wave Frequency . . . . .	285
11.3.2.3 Wave Propagation Velocity . . . . .	286
11.3.2.4 Space Separation of Waves . . . . .	287
11.3.2.5 Interfacial Shear . . . . .	287
11.4 Summary and Conclusions. . . . .	289
Acknowledgement . . . . .	290
Nomenclature . . . . .	290
References. . . . .	291

## 12. DEVELOPMENT OF EIGHT-SENSOR CONDUCTIVITY PROBE AND PITOT TUBE SAMPLING PROBE FOR ANNULAR FLOW MEASUREMENTS . . . . . 300

ABSTRACT . . . . .	300
12.1 Introduction . . . . .	300
12.2 Experimental Setup and Procedure . . . . .	301

12.2.1 Experimental System . . . . .	301
12.2.2 Experimental Condition . . . . .	302
12.2.3 Liquid Film thickness Measurement . . . . .	303
12.2.4 Entrainment Measurement . . . . .	303
12.2.5 Average Void Fraction Measurement. . . . .	304
12.3 Analysis and discussion of Results . . . . .	304
12.3.1 Circumferential Liquid Film Thickness Distribution Results . .	305
12.3.2 Entrained Liquid Mass Flux Results . . . . .	306
12.3.3 Void and Liquid Fraction Results . . . . .	309
12.4 Conclusion . . . . .	310
Acknowledgement . . . . .	311
Nomenclature . . . . .	311
References. . . . .	312

### 13. INTERFACIAL STABILITY STUDIES OF STRATIFIED FLOW:

PART 1. PARAMETRIC STUDIES . . . . .	326
ABSTRACT . . . . .	326
13.1 Introduction . . . . .	327
13.2 The Base Flow . . . . .	328
13.3 First-Order Solution . . . . .	333
13.4 Parametric Stability Analysis . . . . .	337
13.4.1 Horizontal Flow . . . . .	337
13.4.2 Inclined and Vertical Flows . . . . .	340
13.4.3 Parametric Interfacial Wave Velocity Studies . . . . .	341
13.5 Summary and Conclusions. . . . .	344
Nomenclature . . . . .	345
References. . . . .	347

14. SIMILARITY REQUIREMENTS FOR TWO-PHASE	
FLOW-PATTERN TRANSITION . . . . .	362
ABSTRACT . . . . .	362
14.1 Introduction . . . . .	363
14.2 Scaling Criteria . . . . .	364
14.2.1 Single-Phase Flow Similarity . . . . .	364
14.2.2 Two-Phase Flow Similarity . . . . .	367
14.2.3 Single-Phase to Two-Phase Transition . . . . .	369
14.3 Flow-Pattern Scaling . . . . .	372
14.3.1 Existing flow-Pattern Transition Criteria . . . . .	372
14.3.2 Flow-Pattern Transition Scaling Studies for Horizontal Pipes . . . . .	373
14.3.2.1 Stratified-Smooth to Stratified-Wavy Transition . . . . .	375
14.3.2.2 Stratified to Intermittent or Annular-Dispersed	
Liquid Transition . . . . .	378
14.3.2.3 Intermittent or Dispersed bubbles and Annular-Dispersed . . . . .	381
14.3.2.4 Intermittent and Dispersed-Bubble Transition . . . . .	382
14.3.2.5 Flow-Pattern Transition Scaling Requirements for	
Horizontal Pipes . . . . .	386
14.3.3 Flow-Pattern Scaling Studies for Vertical Pipes . . . . .	388
14.3.3.1 Bubbly and Slug Flow Transition . . . . .	388
14.3.3.2 Slug and Churn Flow Transition . . . . .	392
14.3.3.3 Slug/Churn and Annular Flow Transition . . . . .	393
14.3.3.4 Flow-Pattern Scaling Requirements for Vertical Pipes . . . . .	397
14.4 Summary and Conclusions . . . . .	397
Acknowledgement . . . . .	400
Nomenclature . . . . .	401
References. . . . .	404

## VOLUME IV

### 15. ON THE SPHERICALLY SYMMETRIC PHASE CHANGE PROBLEM . . . 406

ABSTRACT . . . . .	406
15.1 Introduction . . . . .	406
15.2 Thin Thermal Boundary Layer Approximation . . . . .	408
15.2.1 Temperature Gradient . . . . .	408
15.2.2 Asymptotic Bubble Growth and Scaling Criteria . . . . .	411
15.3 Energy Integral Method . . . . .	412
15.3.1 Procedure . . . . .	412
15.3.2 Temperature Profiles . . . . .	412
15.3.3 Energy Integral . . . . .	414
15.3.4 Time Dependent Interface Temperature . . . . .	415
15.3.5 Time Dependent Heat Flux at the Interface . . . . .	420
15.4 Application to Bubbles and Drops . . . . .	421
15.5 Comparison with Experiments . . . . .	425
15.6 Summary and Conclusions . . . . .	429
Appendix A. General Formulation . . . . .	432
Appendix B. Effect of the Erroneous Temperature Profile . . . . .	438
Acknowledgement . . . . .	439
Nomenclature . . . . .	439
References . . . . .	440

### 16. MECHANISTIC MODELING OF DROPLET SIZE DISTRIBUTION

#### IN ANNULAR TWO-PHASE FLOW . . . . . 442

ABSTRACT . . . . .	442
16.1 Introduction . . . . .	442
16.2 Mechanistic Modeling of Droplet Breakup . . . . .	444
16.3 Maximum Droplet Size Correlation . . . . .	447

16.4	Droplet Size Distribution . . . . .	451
16.4.1	Volume Distribution Function . . . . .	451
16.4.2	Mean Droplet Sizes . . . . .	453
16.5	Summary and Conclusions . . . . .	455
	Acknowledgement . . . . .	456
	Nomenclature . . . . .	456
	References. . . . .	458
17.	BREAK-UP CRITERIA FOR FLUID PARTICLES-BUBBLES AND DROPLETS . . . . .	466
	ABSTRACT . . . . .	466
17.1	Introduction . . . . .	467
17.2	Break-Up Analysis . . . . .	472
17.2.1	Modeling . . . . .	472
17.2.2	Break-Up Mechanisms . . . . .	478
17.2.3	Wake Angle . . . . .	480
17.2.4	Angular Position of Initial Disturbance Generation . . . . .	481
17.2.5	Terminal Velocity . . . . .	482
17.2.6	Wave Number. . . . .	484
17.2.7	Break-Up Correlation . . . . .	485
17.3	Comparison Between Theoretical Predictions and Experimental Break-Up Data . . . . .	498
17.4	Practical Break-Up Correlations . . . . .	500
17.4.1	Freely Falling Drops in Gaseous Media . . . . .	501
17.4.2	Drops in High Gas Velocity Field . . . . .	502
17.4.3	Rising Bubbles in Liquids . . . . .	505
17.4.4	Freely Falling or Rising Drops in Immiscible Liquids . . . . .	506
17.5	Summary and Conclusions . . . . .	508
17.6	Appendix: Kelvin-Helmholtz Instability . . . . .	513
	Acknowledgement . . . . .	516

Nomenclature . . . . .	517
References. . . . .	519
 18. MEASUREMENT AND MODELING OF VOID FRACTION, BUBBLE SIZE AND INTERFACIAL AREA . . . . .	 522
 ABSTRACT . . . . .	 522
18.1 Introduction . . . . .	523
18.2 Experimental Setup . . . . .	524
18.3 Experimental Results and Discussions . . . . .	526
18.3.1 Local distribution of Interfacial Parameters . . . . .	526
18.3.2 Area-Averaged Interfacial Parameters . . . . .	528
18.3.3 Comparison with Interfacial Area Concentrations . . . . .	529
18.4 Modeling of Interfacial Area . . . . .	530
18.4.1 Modeling of Void Fraction . . . . .	531
18.4.2 Modeling of Bubble Size . . . . .	533
18.4.3 Interfacial Area Correlation . . . . .	542
18.5 Summary and Conclusions. . . . .	542
Acknowledgement . . . . .	543
Nomenclature . . . . .	544
References. . . . .	546
 19. SUMMARY AND CONCLUSIONS . . . . .	 562

## EXECUTIVE SUMMARY

Advances in the study of two-phase flow increasingly require detailed internal flow structure information upon which theoretical models can be formulated. The void fraction and interfacial area are two fundamental parameters characterizing the internal flow structure of two-phase flows. However, little information was available on these parameters, and it is mostly limited to vertical flow configuration. Particularly, there was virtually no database for the local interfacial area concentration in spite of its necessity in multidimensional two-fluid model analysis.

In view of the above, a research program, which has been sponsored by the DOE/BES, has been underway at the University of Wisconsin-Milwaukee. The overall objectives of the research program were to develop instrumentation methods, an extensive database and analysis leading to predictive models for describing the internal flow structure and behaviors of two-phase flow in horizontal configurations.

Experimental efforts were directed at developing instrumentation technique for measurements of the local interfacial area concentration and void fraction in the bubbly flow, plug/slug flow, stratified smooth and stratified wavy and annular flow patterns encountered for two-phase flows in horizontal configurations. Chapters 5 through 12 describe several conductivity probe techniques that have been developed under this research program. More specifically:

- Chapters 5 and 6 present the development and utility of the two-sensor conductivity probe for a bubbly flow,
- Chapter 7 describes the utility of hot-film anemometry method for a bubbly flow whereas Chapters 9 and 10 documents the development of hot-film probe method for a plug/slug flow,
- Chapter 8 describes the four-sensor conductivity probe design for measuring the large bubble interfacial area concentration in a plug/slug flow-pattern,
- Chapter 11 summarizes the development and utility of a two-sensor parallel-wire conductivity probe for the stratified, i.e., stratified-smooth,

stratified-wavy and stratified-atomizing, flow patterns encountered in horizontal two-phase flows, finally,

- Chapter 12 involves with the development of eight-sensor parallel-wire probe method designed for a horizontal annular flow-pattern.

Analytical efforts were focused on deriving predictive mechanistic models describing the interfacial structure in various adiabatic two-phase flow patterns as well as predicting fluid particle behavior in boiling channels. Chapters 13 through 18 summarize these efforts. More specifically, they are summarized as follows:

- Chapter 3 deals with the derivation of the interfacial area transport equation and discusses the basic mechanisms affecting the source and sink terms appearing in the interfacial transport equation.
- Chapter 13 is devoted to studies of interfacial instabilities of horizontal stratified flows,
- Chapter 14 describes mechanistic scaling methodologies and derivation of similarity requirements for two-phase flow-regime transitions,
- Chapter 15 presents an analysis of the spherically symmetric phased change (moving boundary) problem to describe the bubble growth and/or collapse in boiling channels,
- Chapter 16 describes several droplet disintegration mechanisms and offers droplet size and size distributions model for an annular flow-pattern, whereas Chapter 17 is devoted to bubble break-up processes and describes a detailed mechanistic model describing the averaged bubble size and size distributions in bubbly flow, finally,
- Chapter 18 deals with modeling of void fraction and interfacial area concentration and concludes that the core break-up is a dominant break-up mechanism, which determines the interfacial area concentration in the core whereas the Taylor break-up mechanism becomes dominant around the pipe perimeter.



## LIST OF FIGURES

### VOLUME I

3.1	Theoretical and Experimental Values of the Maximum Stable Drop Diameter, Lopes and Dukler (1985) . . . . .	83
3.2	Theoretical and Experimental Values of the Maximum Stable Drop Diameter, Cousins and Hewitt (1968) . . . . .	83
3.3	Theoretical and Experimental Values of the Maximum Stable Drop Diameter, Vicks (1967) . . . . .	84
3.4	Example of Upper Limit, Log-Normal Distribution, Lopes and Dukler (1985) . . . . .	84
3.5	Theoretical and Experimental Values of Volume Median Diameter . . . . .	85
3.6	Theoretical and Experimental Values of Sauter Mean Diameter . . . . .	85
3.7	Variation of Average Sauter Mean Diameter of Bubbles with Superficial Gas Velocity . . . . .	86
3.8	Variation of Average Interfacial Area Concentration with Superficial Gas Velocity . . . . .	87
3.9	Comparison of Local Interfacial Area Concentration Predictions with Experimental Data for Two Flow Conditions . . . . .	88
3.10	Schematic Illustration of Flow Around a Rising Cap Bubble . . . . .	89
3.11	Comparison of Predicted Break-up Diameters with Experimental Data . . . . .	89
3.12	Image of a Small Bubble with Liquid Bulb . . . . .	90
3.13	Experimental Curve Fits for Wave Height . . . . .	90
4.1	Schematic of Horizontal Two-Phase Flow Experimental Loop . . . . .	96
4.2	Jet Mixing Chamber of Annular Flow Experiments . . . . .	96
4.3	Porous Media Mixing Chamber for Bubbly and Slug Flow Experiments . . . . .	97
4.4	A Typical Pressure Port Flange . . . . .	97
4.5	Pressure Port Flange Orientation . . . . .	98
4.6	Pressure Transducer Control System . . . . .	98

5.1	Schematic of the Output Signals:	
	(a) Front Sensor	
	(b) Rear Sensor	124
5.2	Double-Sensor Electrical Resistivity Probe Design	124
5.3	Schematic of the Experimental Flow Loop	125
5.4	Schematic of Air-Water Mixing Chamber	125
5.5	Mounting and Traversing Mechanism	126
5.6	Local Void Fraction Distributions Obtained from Front and Rear Sensors	127
5.7	(a) Influence of Gas Flow on the Local void Fraction Distribution	
	at Low Liquid Flow	
	(c) Influence of Gas Flow on the Local Void Fraction Distribution	
	at High Liquid Flow	127
5.8	(a) Influence of Liquid Flow on the Local Void Fraction Distribution	
	at Low Gas Flow	
	(b) Influence of Liquid Flow on the Local Void Fraction Distribution	
	at High Gas Flow	128
5.9	(a) Effects of Gas Flow on the Local Interfacial Area Concentration	
	Profile at Low Liquid Flow	
	(b) Effect of Gas flow on the Local Interfacial Area Concentration	
	Profile at High Liquid Flow	128
5.10	(a) Effect of Liquid flow on the Local Interfacial Area Concentration	
	Profile at Low Gas Flow	
	(b) Effect of Liquid Flow on the Local Interfacial Area Concentration	
	Profile at High Gas Flow	129
5.11	Sauter Mean Diameter Profiles:	
	(a) Effect of Liquid Flow	
	(b) Effect of Gas Flow	129
5.12	Average Interfacial Area Concentration as a Function of Void Fraction	129
5.13	Bubble Interfacial Velocity Distribution:	
	(a) Effect of Liquid Flow	
	(b) Effect of Gas Flow	130

5.14	Typical Bubble Interfacial Velocity Spectra:	
	(a) $\langle j_f \rangle = 3.83$ m/s, $\langle j_g \rangle = 0.72$ m/s; $\langle \epsilon \rangle = 0.152$	
	(b) $\langle j_f \rangle = 4.86$ m/s, $\langle j_g \rangle = 1.34$ m/s; $\langle \epsilon \rangle = 0.204$	131
5.15	$u_g \sim \langle j \rangle$ Presentation	132
5.16	Typical Bubble Chord Length Spectra :	
	$\langle j_f \rangle = 4.96$ m/s, $\langle j_g \rangle = 1.34$ m/s; $\langle \epsilon \rangle = 0.204$ at	
	(a) $r/R = 0.963$ , (b) $r/R = 0.3$	132
5.17	Bubble Frequency Profiles:	
	(a) Effect of Liquid Flow	
	(b) Effect of Gas Flow	133

## VOLUME II

6.1	Schematic of the Experimental Flow Loop	151
6.2	Schematic of the Air-Water Mixing Chamber	151
6.3	Mounting and Traversing Mechanism	151
6.4	Probe Positions Along Vertical Axis of Test Section.	152
6.5	Probe Positions Across Test Section	152
6.6	Void Fraction Distribution Over Pipe Cross-Section at $L/D = 253$ with Increasing Gas Flow	153
6.7	Interfacial Area Concentration Distributions over Pipe Cross-Section at $L/D = 253$ with Increasing Gas Flow	154
6.8	Bubble Frequency Distributions over Pipe Cross-Section at $L/D = 253$ with Increasing Gas Flow	155
6.9	Bubble Interface Velocity Profiles over Pipe Cross-Section at $L/D = 253$ with Increasing Gas Flow	156
6.10	Comparison of Bubble Interface Velocity with Predicted Liquid Velocity	157
6.11	Void Fraction Development in Axial Direction:	
	(a) Low Gas Flow	158
	(b) High Gas Flow	159
6.12	Interfacial Area Concentration Development in Axial Direction:	
	(a) Low Gas Flow	160

	(b) High Gas Flow . . . . .	161
6.13	Bubble Frequency Behavior in Axial Direction:	
	(a) Low Gas Flow . . . . .	161
	(b) High Gas Flow . . . . .	162
6.14	Bubble Interface Velocity in Axial Direction:	
	(a) Low Gas Flow . . . . .	164
	(b) High Gas Flow . . . . .	165
7.1	Two-Phase Flow Data for $\langle j_f \rangle = 5.0$ m/s and $\langle j_g \rangle = 0.25$ m/s . . . . .	186
	(a) Local Mean Velocity	
	(b) Local Turbulence Velocity	
	(c) Local Void Fraction	
	(d) Turbulent Intensity Distribution	
7.2	Two-Phase Flow Data for $\langle j_f \rangle = 5.0$ m/s and $\langle j_g \rangle = 0.5$ m/s . . . . .	186
	(a) Local Mean Velocity	
	(b) Local Turbulence Velocity	
	(c) Local Void Fraction	
	(d) Turbulent Intensity Distribution	
7.3	Two-Phase Flow Data for $\langle j_f \rangle = 5.0$ m/s and $\langle j_g \rangle = 0.8$ m/s . . . . .	186
	(a) Local Mean Velocity	
	(b) Local Turbulence Velocity	
	(c) Local Void Fraction	
	(d) Turbulent Intensity Distribution	
7.4	Influence of Gas Flow on Local Void Fraction . . . . .	187
7.5	Influence of Gas Flow on Local Bubble-Passing Frequency . . . . .	187
7.6	Influence of Gas Flow on Local Mean Liquid Velocity . . . . .	187
7.7	Influence of Gas Flow on Local Turbulent Intensity . . . . .	187
7.8	Influence of Liquid Flow on Local Void Fraction . . . . .	188
7.9	Influence of Liquid Flow on Local Bubble-Passing Frequency . . . . .	188
7.10	Influence of Liquid Flow on Local Mean Liquid Velocity . . . . .	188
7.11	Influence of Liquid Flow on Local Turbulent Intensity . . . . .	188

8.1	Typical Signals of Four-Sensor Probe . . . . .	211
8.2	Phase Identification . . . . .	211
8.3	Total Void Fraction Distribution along Vertical Diameter . . . . .	211
8.4	Slug Void Fraction Distribution along Vertical Diameter . . . . .	211
8.5	Total Void Fraction Distribution over Pipe Cross Section . . . . .	212
8.6	Slug Void Fraction Distribution over Pipe Cross Section . . . . .	212
8.7	Interfacial Area Concentration along Vertical Diameter . . . . .	212
8.8	Slug Bubble Interfacial Area Concentration over Pipe Cross Section . .	213
8.9	Slug Bubble Frequency Dependence on Liquid Superficial Velocity . .	213
8.10	Slug Bubble Frequency Dependence on Gas Superficial Velocity . . . . .	213
9.1	Typical Probe Signals of Two-Phase Measurements for $\langle j_f \rangle = 2.2 \text{ m/s}$ and $\langle j_g \rangle = 1.1 \text{ m/s}$ . . . . .	240
	(a) Probe Pierces Through Elongated Large Bubbles at $r/R = 0.8$	
	(b) Probe Located in Liquid Layer Below Passing Large Bubbles	
9.2	Typical Anemometer Output and Signal Processing . . . . .	241
	(a) Anemometer Output Signals	
	(b) Slope of Voltage Signals	
	(c) Phase Separation Step Signals	
9.3	Bubble Size Spectrum for Varying Gas Velocities at (a) $\langle j_f \rangle = 1.1 \text{ m/s}$ and $\langle u_{LS} \rangle = 2.14 \text{ m/s}$ . (b) $\langle j_f \rangle = 1.65 \text{ m/s}$ and $\langle u_{LS} \rangle = 3.84 \text{ m/s}$ (c) $\langle j_f \rangle = 2.2 \text{ m/s}$ and $\langle u_{LS} \rangle = 4.45 \text{ m/s}$ . . . . .	242
9.4	Axial Velocity Variation in the Liquid Slug and the Liquid Layer under Passing Large Bubbles . . . . .	243
9.5	Schematic of the Experimental Flow Loop . . . . .	244
9.6	Local Void Fraction, Mean Velocity and Turbulence Structure Distributions at (a) $\langle j_f \rangle = 1.65 \text{ m/s}$ and $\langle j_g \rangle = 0.35 \text{ m/s}$	

	(b) $\langle j_f \rangle = 1.65$ m/s and $\langle j_g \rangle = 1.1$ m/s	
	(c) $\langle j_f \rangle = 1.65$ m/s and $\langle j_g \rangle = 2.2$ m/s	245
9.7	Local Variation of Bubble-Induced Axial Turbulence	246
	(a) Effect of Gas Flow at $\langle j_f \rangle = 1.1$ m/s	
	(b) Effect of Liquid Flow at $\langle j_g \rangle = 2.2$ m/s	
9.8	Influence of Gas and Liquid flow on Local Distribution of Void Fraction, Mean Liquid Velocity and Turbulent Intensity	247
	(a) Effect of Gas Flow at $\langle j_f \rangle = 1.65$ m/s and	
	(b) Effect of Liquid Flow at $\langle j_g \rangle = 1.1$ m/s	
10.1	Typical Probe signals of Two-Phase Measurements for $\langle j_f \rangle = 2.2$ m/s and $\langle j_g \rangle = 1.1$ m/s	253
	(a) Probe Pierces through Slug Bubbles at $r/R = 0.8$	
	(b) Probe Located Below Passing Bubbles	
10.2	Schematic of Experimental Flow Loop	254
10.3	Schematic of Air-Water Mixing Chamber	256
10.4	Use of Two Hot-Film Probes	256
10.5	Basic Flow Unit in Slug Flow	261
10.6	A Typical Velocity Profile Development for Liquid Ahead of Gas Slug Nose	262
10.7	A Typical Velocity Profile Development for Liquid in the Wake Region of the Gas Slug	264
10.8	A Typical Velocity Profile Development for Liquid Layer Near Gas Slug Nose	266
10.9	A Typical Velocity Profile Development for Liquid Layer Near Gas Slug Wake	267
10.10	Axial Velocity Variations in Liquid Slug and Liquid Layer Under Gas Slug	268

### VOLUME III

11.1	Schematic of the Experimental Flow Loop . . . . .	294
11.2	Schematic of the Air-Water Mixing Chamber . . . . .	294
11.3	Double-Sensor, Parallel-wire Conductance Probe . . . . .	294
11.4	Typical Output Signals of (From Top to Bottom) Low, Moderate and High Gas Flows . . . . .	295
11.5	Experimental Conditions . . . . .	295
11.6	Recording of Liquid Thickness Signals for a Fixed Liquid Flow Rate . .	296
11.7	Flow-Pattern Transitions . . . . .	295
11.8	Effect of Liquid and Gas Superficial Velocities on Time-averaged Liquid Thickness . . . . .	297
11.9	Comparisons of Time-Averaged Liquid Thickness Measurements with Taitel and Dukler's Predictions . . . . .	297
11.10	Comparisons of Time-Averaged Liquid Thickness Measurements with those predicted by Andritsos and Hanratty's Method . . . . .	297
11.11	Variation in Most Dominant Frequency with Gas and Liquid Superficial Velocities . . . . .	298
11.12	Variation in Mean Wave Propagation Velocity with Gas and Liquid Superficial Velocities . . . . .	298
11.13	Dimensionless Presentation of Mean Propagation Velocity Data . . . . .	298
11.14	Correlation of Mean Propagation Velocity for Air-Water System . . . . .	298
11.15	Variation in Mean Space Separation with Gas and Liquid Superficial Velocities . . . . .	298
11.16	Influence of Gas and Liquid superficial Velocities on Interfacial Friction Factor . . . . .	298
11.17	Presentation of Interfacial Friction Factor Data inn Terms of Cheremisinoff and Davis's Correlation Parameter . . . . .	299
11.18	Comparison of Interfacial Friction Factor Data with Kowalski's Correlation .	299
11.19	Comparison of Interfacial Friction Factor Data with Andritsos and Hanratty's Correlation . . . . .	299

12.1	Schematic of Experimental Flow Loop	316
12.2	Conductance Probe and Probe Manifold	317
12.3	Conductance Probe and Manifold Orientation	318
12.4	Pitot Tube Assembly and Orientation	318
12.5	Droplet Collection System	319
12.6	Pitot tube Sampling Positions	319
12.7	Average Liquid Film Thickness at	
	(a) $\theta = 0^\circ$	
	(b) $\theta = 45^\circ$	
	(c) $\theta = 180^\circ$	320
12.8	Liquid Film Thickness Distribution	321
12.9	Comparison of Predicted Liquid Film Thickness with Experimental Data	321
12.10	Effect of Superficial Velocities on Formation of Liquid Layer Around $\theta = 0^\circ$ ;	
	(a) Effect of Gas Velocity	
	(b) Effect of Liquid Velocity	322
12.11	Distribution of Wave Characteristics	323
12.12	Entrained Liquid Droplet Mass Flux Profiles at	
	(a) Low Gas Flow Rates	
	(b) High Gas Flow Rates	323
12.13	comparison of Predicted Entrainment Fraction with Experimental Data	324
12.14	Variation of Average Void Fraction with Liquid and Gas Reynolds Number	324
12.15	Liquid Fraction Variation	325
12.16	Comparison of Liquid Film Fraction Results of Laurinat and	
	Present Studies with Measured Total Liquid Fraction Data	325
13.1	Base Flow Configuration	348
13.2	Typical Velocity Profile, (a), and shear stress, (b), for horizontal flow	
	when $m \gg 1$ and $n^2 \ll m$ . For This Example $n=4$ , $m=50$ , $\mu_1=1 \cdot 10^{-5} \text{ N}\cdot\text{s/m}$ ,	
	$r=1000$ and $\rho_1=1 \text{ kg/m}^3$ in a 50 mm channel with average velocities	
	$U_1=0.7 \text{ m/s}$ and $U_2=0.475 \text{ m/s}$	349



13.3	Typical Velocity Profile, (a), and shear stress, (b), for horizontal flow when $m=1$ and $n^2 > m$ . For This Example $n=4$ , $m=1$ , $\mu_1=1 \cdot 10^{-5} \text{ N}\cdot\text{s/m}$ , $r=1000$ and $\rho_1=1 \text{ kg/m}^3$ in a 50 mm channel with average velocities $U_1=0.325 \text{ m/s}$ and $U_2=0.7 \text{ m/s}$ . . . . .	350
13.4	Typical Velocity Profile, (a), and shear stress, (b), for horizontal flow when $m \gg 1$ and $n^2 = m$ . For This Example $n=4$ , $m=16$ , $\mu_1=1 \cdot 10^{-5} \text{ N}\cdot\text{s/m}$ , $r=1000$ and $\rho_1=1 \text{ kg/m}^3$ in a 50 mm channel with average velocities $U_1=0.6 \text{ m/s}$ and $U_2=0.6 \text{ m/s}$ . . . . .	351
13.5	The Effect of the Density, viscosity and Depth Ratios on neutral Stability for Horizontal Flow. The Density Ratios 1, 3, 10 and 1000. The Parameters are $G=0.1$ , $R>0$ and $\theta = 0^\circ$ . . . . .	352
13.6	Comparison of the Effect of favorable and Adverse Density Stratifications on Neutral Stability in the $m$ - $n$ plane for Horizontal Flow. The Density Ratios are 1/3, 1 and 3. The Flow Parameters are $G=0.1$ , $R>0$ and $\theta = 0^\circ$ . . . . .	353
13.7	Comparison of the Effect of favorable and Adverse Density Stratifications on Neutral Stability for Horizontal flow in Absence of Gravity in the $m$ - $n$ plane. The Density Ratios are 1/10 and 10. The Flow Parameters are $G=0$ , $R>0$ and $\theta = 0^\circ$ . . . . .	354
13.8	The Effect of $G$ , the Viscosity Ratio and the Depth ratio on Neutral Stability for Horizontal Flow. The Density Ratios are 0.01, 0.1 and 1. The Flow Parameters are $r=10$ , $R>0$ and $\theta = 0^\circ$ . . . . .	355
13.9	The Effect of the Angle on Inclination on Neutral Stability in the $m$ - $n$ Plane for Fluids of Comparable Density. The Angles are $0^\circ$ , $45^\circ$ and $90^\circ$ . The Parameters are $r=1.5$ , $R=3$ and $G=0.1$ . . . . .	356
13.10	The Effect of the Angle on Inclination on Neutral Stability in the $m$ - $n$ Plane. The Angles are $0^\circ$ , $45^\circ$ , $90^\circ$ . The Parameters are $r=10$ , $R=3$ and $G=0.1$ . . . . .	357
13.11	The Effect of the Density, Viscosity and Depth Ratios on Neutral Stability for Vertical Flow. The Density Ratios are 15 and 100. The Parameters are $R=3$ , $\theta = 90^\circ$ and $G=10$ . . . . .	358

13.12	The Effect of G and the viscosity and Depth ratios on Neutral Stability for a Vertical Flow. The Values for G are 0.1 and 1.0. The Parameters are $r=10$ , $R=3$ and $\theta = 90^\circ$ . . . . .	359
13.13	The Effect of R and the viscosity and Depth Ratios on Neutral stability for Vertical Flow. The Values for R are 3 and 10. The Parameters are $r=10$ , $G=0.1$ and $\theta = 90^\circ$ . . . . .	360
13.14	The Effect of the Viscosity and Depth ratios on the dimensionless Interfacial wave Velocity for Horizontal Flow. The Viscosity Ratios are 0.01, 0.1, 1, 10 and 100. The Parameters are $r>0$ , $\theta = 0^\circ$ , $G>0$ and $R>0$ . . . . .	361
14.1	Single-Phase to or From Two-Phase flow Simulation for the Prototypic and Selected Model Fluids . . . . .	371
14.2	Variations of Geometric Variables Used in Taitel and Dukler Horizontal Flow-Pattern Transitions . . . . .	374
14.3	Horizontal flow-Pattern Transitions Between Stratified-Smooth and Stratified-Wavy Flows . . . . .	376
14.4	Horizontal flow-Pattern Transitions Between Stratified, Intermittent and Annular-Dispersed Liquid Flows . . . . .	380
14.5	Horizontal flow-Pattern Transitions Between Intermittent and Dispersed-Bubble Flows . . . . .	384
14.6	Flow-Pattern Scaling Requirements for Horizontal Two-Phase Flow . . .	387
14.7	Vertical Flow-Pattern Transition Between Bubbly and Slug or Churn Flow . . . . .	391
14.8	Vertical Flow-Pattern Transition Between Slug and Churn Flows for Taitel et al. Map . . . . .	394
14.9	Vertical Flow-Pattern Transition Between Slug and Churn Flows for Mishima and Ishii Map . . . . .	395
14.10	Flow-Pattern Scaling Requirements for Vertical Two-Phase Flow . . . . .	395

## VOLUME IV

15.1	Growth and Collapse for Large Jacob Numbers, i.e., for $\epsilon^2/4 < 1.0$	423
15.2	Growth and Collapse for Small Jacob Numbers, i.e., for $\epsilon^2/4 > 1.0$	424
15.3	Comparison Between Present Predictions and Experimental Data of Florschuetz and Chao-Water Vapor bubbles	427
15.4	Comparison Between Present Predictions and Experimental Data of Thorncraft-FC-87 Forced Convection Boiling	431
15.A1	Schematic Description of Spherically Symmetric Phase Change Problem.	433
15.B1	Effects of the Assumed Temperature Profile on the temperature Gradient at the Surface of a Stationary Sphere	438
16.1	Maximum Diameter vs. Dimensionless Fluid Property and Flow Variable Group	461
16.2	Theoretical and Experimental Values of the Maximum Stable Droplet Diameter:	
	(a) Lopes and Dukler [3]	
	(b) Cousin and Hewitt [17]	
	(c) Wicks [14]	462
16.3	Example of Upper Limit, Log-Normal Distribution:	
	(a) Lopes and Dukler [3]	
	(b) Cousin and Hewitt [17]	463
16.4	theoretical and Experimental Values of Sauter mean Diameters:	
	(a) Volume Median Diameter	
	(b) Sauter Mean Diameter	464
16.5	Comparison Between Predicted and Measured Sauter Mean Diameters:	
	(a) Air/ $\text{CH}_3\text{CCl}_3$ Data, Jepsen et al. [5]	
	(b) Air/Water Data, Jepsen et al. [5]	
	(c) He/Water Data, Jepsen et al. [6]	465

17.1	Schematic Illustration of Flow Around A Rising Cap bubble . . . .	476
17.2	Variation of Growth Time, $t_g$ , Propagation Time, $t_p$ , and Time Ratio, $t_g/t_p$ , for a Bubble at $d_c=0.063$ m as Function of Wave Number, $k$ . . . .	487
17.3	Variation of Growth Time, $t_g$ , Propagation Time, $t_p$ , and Time Ratio, $t_g/t_p$ , for a Bubble at $d_c=0.046$ m as Function of Wave Number, $k$ . . . .	488
17.4	Variation of Growth Time, $t_g$ , Propagation Time, $t_p$ , and Time Ratio, $t_g/t_p$ , for a Bubble at $d_c=0.089$ m as Function of Wave Number, $k$ . . . .	489
17.5	Variation of Growth Time, $t_g$ , Propagation Time, $t_p$ , and Time Ratio, $t_g/t_p$ , for a Bubble at $d_c=0.0044$ m as Function of Wave Number, $k$ . . . .	490
17.6	Variation of Growth Time, $t_g$ , Propagation Time, $t_p$ , and Time Ratio, $t_g/t_p$ , for a Bubble at $d_c=0.008$ m as Function of Wave Number, $k$ . . . .	491
17.7	Variation of Growth Time, $t_g$ , Propagation Time, $t_p$ , and Time Ratio, $t_g/t_p$ , for a Bubble at $d_c=0.088$ m as Function of Wave Number, $k$ . . . .	492
17.8	Variation of Growth Time, $t_g$ , Propagation Time, $t_p$ , and Time Ratio, $t_g/t_p$ , for a Bubble at $d_c=0.0104$ m as Function of Wave Number, $k$ . . . .	493
17.9	Variation of Growth Time, $t_g$ , Propagation Time, $t_p$ , and Time Ratio, $t_g/t_p$ , for a Bubble at $d_c=0.0167$ m as Function of Wave Number, $k$ . . . .	494
17.10	Variation of Growth Time, $t_g$ , Propagation Time, $t_p$ , and Time Ratio, $t_g/t_p$ , for a Bubble at $d_c=0.099$ m as Function of Wave Number, $k$ . . . .	495
17.11	Comparison of Predicted Breakup diameters with Experimental Data	498
17.12	Breakup Diameter Correlation for Drops in a High Velocity Gas Stream and Comparison with other Correlations . . . . .	503
17.13	Breakup diameter Correlation for Bubbles and Comparison with Experimental Observations . . . . .	507
17.14	Breakup diameter Correlation for Drops in Liquids and Comparison with Experimental Observations . . . . .	509
17.15	Stability of two Superimposed Fluids flowing concurrently in a Constant Cross Sectional Area Channel . . . . .	515
18.1	Schematic of Experimental Flow Loop . . . . .	550
18.2	Effect of Gas Flow on Local Void Fraction Distribution . . . . .	551

18.3	Effect of Gas Flow on Local Interfacial Area Concentration Profile . . . .	.551
18.4	Effect of Gas Flow on Local Sauter Mean Bubble Diameter Distribution	.552
18.5	Variation of Average Void Fraction with Superficial Gas Velocity . . . .	.553
18.6	Variation of Average Interfacial Concentration with Superficial Gas Velocity . . . . .	.554
18.7	Variation of Average Sauter Mean Diameter of Bubbles with Superficial Gas Velocity . . . . .	.555
18.8	Comparison of Interfacial Area Concentration Data with Energy Dissipation Parameter of Kasturi and Stepanek (1974) . . . . .	.556
18.9	Comparison of Interfacial Area Concentration Data with Energy Dissipation Parameter of Banerjee et al. (1970) . . . . .	.556
18.10	Comparison of Interfacial Area Concentration Data with Energy Dissipation Parameter of Trombouze et al. (1984) . . . . .	.557
18.11	Comparison of Interfacial Area Concentration Data with Energy Dissipation Parameter of Jepsen et al. (1970) . . . . .	.557
18.12	Comparison of Interfacial Area Concentration Data with Energy Dissipation Parameter of Tomida et al. (1978) . . . . .	.558
18.13	Drift-Flux Presentation of Present Data . . . . .	.558
18.15	Comparison Between Predicted and Measured Average Void Fractions	.559
18.16	Comparison Between Predicted Pressure Drop Multiplier by Martinelli-Nelson Correlation and Those Measured Values . . . . .	.559
18.17	Comparison Between Predicted and Measured Average Sauter Mean Diameters . . . . .	.560
18.18	Comparison between Predicted and Delhaye and Brickard's Vertical Flow Data of Photographic and Ultrasound Measurements . . . . .	.560
18.19	Comparison Between Predicted and Measured Average Interfacial Area Concentration . . . . .	.561

## LIST OF TABLES

### VOLUME I

4.1	Summary of Instrumentation Capabilities in Two-Phase Flow Laboratory at UWM . . . . .	99
5.1	Experimental Conditions and Comparisons of Velocities . . . . .	123

### VOLUME III

12.1	Flow Conditions Used in Experiments . . . . .	315
------	---	-----

### VOLUME IV

15.1	Summary of Various Experiments on Droplet Mean Diameters . . . . .	460
17.1	Summary of Various Experiments on Maximum Fluid Particle Size. . . . .	512
18.1	Range of Experimental Data . . . . .	549
18.2	Interfacial Area Concentration for Vertical Flow . . . . .	549

## 15. ON THE SPHERICALLY SYMMETRIC PHASE CHANGE PROBLEM

J. Riznic and G. Kojasoy

Department of Mechanical engineering, University of Wisconsin-Milwaukee  
Milwaukee, WI 53201

N. Zuber

703 New Mark Esplanada  
Rockville, Maryland 20850

### ABSTRACT

Using the energy integral method, an analysis of the spherically symmetric phase change (moving boundary) problems is presented. The expression derived for the temperature gradient shows the effects of both the interfacial area change and the curvature. The results show that the thermal boundary layer from a growing sphere is thinner than that corresponding to a collapsing one.

The solution of the energy equation is then used to analyze the thermal diffusion-controlled bubble (or droplet) growth or collapse problem. The expression derived for the radial velocity takes into account the effects of (a) the Jakob number, (b) the interfacial area change and (c) the curvature. It is shown that (a) for large values of the Jakob number, the radius depends upon the first power of the Jakob number, (b) for small values of the Jakob number it is a function of the square root of this number, and (c) although widely used in the literature, an application of the "thin thermal boundary layer" model to cavitation, i.e., to collapsing bubbles, is incorrect, particularly at low Jakob numbers.

Finally, it is demonstrated that analyses of bubble dynamics based on the energy integral method are in error because the assumed temperature profile was incorrect. It is shown that this erroneous temperature distribution can result in a 100% error when computing the temperature gradient at the interface.

Although the analysis presented in this paper is formulated by considering the thermal diffusion of energy, the same analysis and results with an appropriate redefinition of property terms can be applied to a spherically symmetric mass diffusion problem with a moving boundary.

### 15.1 Introduction

In problems involving both cavitation and boiling heat transfer, the bubble dynamics have been shown to be of fundamental importance. Numerous studies have been undertaken beginning with

the pioneering work of Besant [1] and Rayleigh [2] on cavitation and of Bosnjakovic [3], Jakob [4] and Fritz and Ende [5] on boiling heat transfer. Basically there are three different mechanisms that can control the rate of growth or collapse of a bubble. These mechanisms are referred to as inertia-controlled, thermal diffusion-controlled, and mass diffusion-controlled growth or collapse in the literature. A general review of all aspects of bubble dynamics can be found in review papers by Plesset and Prosperetti [6] and Arndt [7]. In this paper, the discussion will be limited to the thermal diffusion-controlled bubble dynamics, and only relevant work will be cited.

Theoretical studies of the thermal diffusion-controlled growth of a vapor bubble in a uniformly superheated liquid in a constant pressure field have been reported earlier by Plesset and Zwick [8], Forster and Zuber [9], Scriven [10] and Bankoff [11] among others. All the results, which apply to the constant pressure case, agree that during the thermally dominated growth period, after the first few or tens of microseconds, the bubble grows proportional to the square root of time. However, Lipkis et al. [12] and Zwick [13] showed that for the specific case of linear heating the bubble radius growth is dominated by  $(3/2)$  power of time rather than the square root behavior commonly accepted in the constant pressure case.

Jones and Zuber [14] reported the result of vapor bubble growth in variable pressure fields and found that the variable pressure effects can be quite important and dominate the rate of growth. It was shown that for the case where pressure changes cause the vapor temperature to behave as  $t^n$ , ( $t$  being time), the bubble radius will grow as  $t^{n+1/2}$ , significantly faster than the  $t^{1/2}$  behavior. Theofanous et al. [15] reported the numerical solution of bubble growth in time-dependent pressure fields. Their results also include the effects of non-equilibrium at the liquid-vapor interface, inertia of the liquid, and surface tension. Theofanous and Patel [16] refined their previous theoretical analysis to clarify the influence of initial-to-final vapor density ratio on bubble growth. They offered an improved version of universal bubble growth relations, which was originally initiated by Mikic et al. [17]. Inoue and Aoki [18], Cha and Henry [19] and Toda and Kitamura [20] examined the same problem by introducing a coordinate transformation which immobilized the moving boundary. Recently Wang and Bankoff [21] modified the Jones and Zuber's variable pressure solution for the bubble radius by including the contribution of microlayer evaporation from the base of the bubble, as well as from the curved surface. Almost all analyses concerned with the thermal diffusion-controlled bubble dynamics were based on the "thin thermal boundary layer" approximation which is discussed in more detail below.

The theoretical modeling of the collapse of vapor bubbles under conditions in which thermal effects play a significant role is more difficult than the analysis of their growth. The basic difficulty here is due to the fact that the thickness of the liquid layer in which substantial temperature gradients occur cannot be treated to be small compared with the bubble radius for all times. Plesset and Zwick [22] included the effect of heat transfer in a numerical calculation for a particular collapsing bubble. It was found that the effect was insignificant in retarding the collapse rate when compared to the Rayleigh solution which considers only liquid inertia effects. However, the experimental and theoretical analyses of Florschuetz and Chao [23] demonstrated that the thermal diffusion controlled bubble collapse was possible for certain values of dimensionless cavitation numbers obtained from the Rayleigh equation. Depending on the values of this scaling parameter, these authors were able to distinguish three modes of bubble collapse – liquid inertia controlled, thermal diffusion controlled, and the collapse controlled by both effects. Theofanous et al. [24] used the same set of equations that was used in their previous treatment of the non-equilibrium bubble growth [15] to analyze the case of the *collapse* of vapor bubbles. Although their assumption of a thin thermal boundary layer is incorrect for collapsing bubbles (as shown in this paper), they



obtained a good agreement with steam bubble collapse data for certain values of accommodation coefficients used in their calculations.

The recent advances in two-phase flow applications renewed the interest in bubble dynamics. In particular, the formulation of appropriate constitutive equations for evaporation or condensation in flashing flow, as well as the specification of nuclear and chemical reactor safety criteria, called for a re-examination of both assumptions and approximations that have been made previously. Of these assumptions the most restrictive ones were the above mentioned "thin thermal boundary layer" approximation and the assumption of thermodynamic equilibrium for the vapor phase. This paper which is directed at clarifying issues related to growing and collapsing bubbles has four objectives. These are listed as follows:

- To show that the application of the "thin thermal boundary layer" approximation to *collapsing* bubbles is *incorrect* although this approximation has been used by all investigators interested in cavitation.
- To show that the available analyzes based on the heat balance integral method contain a significant error because the assumed temperature profiles are *incorrect* when applied to a spherically symmetric problem.
- To solve the spherically symmetric phase change, i.e., "moving boundary", problem by means of the heat balance integral method using the *appropriate* temperature profile.
- To use the above results in an analysis of thermal diffusion-controlled bubble growth and collapse.

Two solutions of the phase change problem are presented; one corresponding to a time dependent temperature at the vapor-liquid interface, the other to a time dependent heat flux. We note that neither of these two solutions is subject to the "thin thermal boundary layer" approximation.

It is important to note here that the objective of this paper is not directed at solving the complete set of governing equations of bubble growth or collapse by numerical means. It is rather aimed at clarifying issues related to growing and collapsing bubbles as listed above. For this purpose we will concentrate on an analysis of thermal diffusion controlled growth and collapse, which is the case when the effects of inertia and of surface tension can be neglected. For other modes of bubble growth and collapse-liquid inertia-controlled and the process controlled by both effects – a complete formulation of the problem is presented in Appendix A. The simplified procedure outlined here can be easily extended to solve the complete set of governing equations as described in Appendix A by numerical means. It is, however, out of the scope of this paper.

## 15.2 Thin Thermal Boundary Layer Approximation

**15.2.1 The Temperature Gradient** It is customary in analyzes of bubble dynamics to neglect the effects of pressure and of viscous dissipation in the energy equation. For an incompressible fluid and a spherically symmetric problem, the energy equation reduces then to Eq. (A.22):

$$Cp_f \rho_f \left( \frac{\partial T}{\partial t} + \frac{\Delta p}{\rho_f} \frac{R^2 \dot{R}}{r^2} \frac{\partial T}{\partial r} \right) = k_f \left( \frac{\partial^2 T}{\partial r^2} + \frac{2}{r} \frac{\partial T}{\partial r} \right) \quad (1)$$

where Eq. (A.11a) is used for the liquid velocity distribution which assumes the vapor can be treated as incompressible.

The formulation is completed by specifying an initial and two boundary conditions. For the initial condition, i.e., for the initial temperature, we take a prescribed function of position:

$$T(r, 0) = F(r) \quad (2)$$

One boundary condition is given by the temperature at a great distance from the interface. The other is obtained by combining the vapor mass balance and the energy balance at the vapor-liquid interface as expressed by Eq. (A.28):

$$k_f \left( \frac{\partial T}{\partial r} \right)_{r=R(t)} = \rho_g h_{fg} \dot{R} \quad (3)$$

A more general form of this relation can be obtained by eliminating the interfacial mass transfer,  $\dot{m}_{gi}$ , between Eqs. (A.2) and (A.28) when the vapor compressibility effect is significant.

It is this latter boundary condition which puts this problem in the class of "moving boundary" problems that characterize all phase change phenomena. It is also this boundary condition which introduces great difficulties in the analysis because it introduces a nonlinearity in the problem.

In the past, the above problem was solved either by seeking self-similar solutions [10, 25] or by introducing the "thin thermal boundary layer" approximation [9, 26], according to which the thickness of the thermal diffusion layer is much smaller than the radius of the bubble. Using this approximation Plesset and Zwick [26] derived the following expression for the temperature of the vapor-liquid interface:

$$T(R, t) = T_\infty - \left( \frac{\alpha_f}{\pi} \right)^{1/2} \int_0^t \left[ \frac{R^2(x)}{\text{RMS}[R^2]} \right] \left( \frac{\partial T}{\partial r} \right)_{r=R(x)} \frac{dx}{(t-x)^{1/2}} \quad (4)$$

whereas Forster and Zuber [9] derived

$$T(R, t) = T_\infty - \left( \frac{\alpha_f}{\pi} \right)^{1/2} \int_0^t \left[ \frac{R^2(x)}{\text{GM}[R^2]} \right] \left( \frac{\partial T}{\partial r} \right)_{r=R(x)} \frac{dx}{(t-x)^{1/2}} \quad (5)$$

where  $\alpha_f$  is the thermal diffusivity of liquid. In Eq. (4)  $T_\infty$  is the initial liquid temperature assumed to be uniform, and  $\text{RMS}[R^2]$  is the *root mean square value* of  $R^2$  defined by

$$\text{RMS}[R^2] \equiv \left\{ \frac{1}{t-x} \int_x^t R^4(y) dy \right\}^{1/2} \quad (6)$$

whereas in Eq. (5)  $\text{GM}[R^2]$  is the *geometric mean value* of  $R^2$  defined as follows:

$$\text{GM}[R^2] \equiv \left[ \frac{1}{R(t) - R(x)} \int_{R(x)}^{R(t)} \frac{dR}{R^2} \right]^{-1} = R(t)R(x) \quad (7)$$

The significance of these two mean values of  $R^2$  in Eqs. (4) and (5) can be best illustrated by considering a *stationary* interface. For such a case, the ratios of  $R^2$  in Eqs. (4) and (5) become unity and both equations reduce to the well known relation given in Carslaw and Jaeger [27] for the temperature at a *stationary, plane* interface of a semi-infinite solid, when the temperature gradient at

this interface is a prescribed function of time. As observed previously by Forster [28], the two ratios of  $R^2$  in Eqs. (4) and (5) account for the effects of the variable interfacial area on the temperature at the interface.

In order to show the effect of this area change on the temperature gradient at the interface, we shall consider the expressions derived in [8, 9] for the asymptotic bubble growth, which are valid when both the effects of inertia and of surface tension can be neglected. The relation derived by Plesset and Zwick [8] is given by

$$\left( \frac{\partial T}{\partial r} \right)_{r=R(t)} = \sqrt{3} \frac{\Delta T}{(\pi \alpha_f t)^{1/2}} \quad (8)$$

whereas Forster and Zuber [9] derived

$$\left( \frac{\partial T}{\partial r} \right)_{r=R(t)} = \left( \frac{\pi}{2} \right) \frac{\Delta T}{(\pi \alpha_f t)^{1/2}} \quad (9)$$

where  $\Delta T = T_\infty - T_{\text{sat}}$  is the temperature difference of the superheated liquid, and  $T_{\text{sat}}$  is the temperature at saturation.

Equations (8) and (9) should be compared to the temperature gradient at a *stationary, plane interface* of a semi-infinite solid, following a sudden step change of temperature at the interface. The solution is well known [27] and it has been indeed first used by Fritz and Ende [5] in their analysis of bubble dynamics; it is given by

$$\left( \frac{\partial T}{\partial x} \right)_{x=0} = \frac{\Delta T}{(\pi \alpha_f t)^{1/2}} \quad (10)$$

By comparing Eqs. (8) and (9) with Eq. (10), it can be seen that they differ only by a *constant of the order of unity*. The values of the constant, slightly larger than unity are to be attributed to the effects of the *increasing* interface area.

It should be noted that Eqs. (4) and (5) were used in deriving Eqs. (8) and (9). Consequently, both Eqs. (8) and (9) are based on the "thin thermal boundary layer" approximation. Since Eqs. (8) and (9) are in agreement with the solution of a plane stationary problem, i.e., with Eq. (10), it is legitimate to ask "How do they compare to the solution of a *stationary, spherically symmetric problem*?"

For a stationary problem the second term on the left-hand side of Eq. (1) is zero. The solution of this equation for a medium initially at uniform temperature and a step change of temperature at the interface is again well known [27, 29]. The temperature gradient at a *stationary, spherical interface* is given by:

$$\left( \frac{\partial T}{\partial r} \right)_{r=R_s} = \frac{\Delta T}{(\pi \alpha_f t)^{1/2}} \left[ 1 + \frac{(\pi \alpha_f t)^{1/2}}{R_s} \right] \quad (11)$$

where  $R_s$  is the radius of the *stationary* sphere.

By comparing Eqs. (10) and (11), it can be seen that they differ in that Eq. (11) has a term which accounts for the effect of curvature on the temperature gradient. It is obvious that this curva-

ture effect cannot be accounted for by a plane model. It can be seen also that the temperature gradient at a plane interface will be in agreement with that of a spherical one as long as

$$\frac{(\pi\alpha_f t)^{1/2}}{R_s} \ll 1.0 \quad (12)$$

which is indeed the condition that must be satisfied by a model based on the "thin thermal boundary layer" approximation.

Although for fast *growing* bubbles the "thin thermal boundary layer" approximation is satisfied in most cases of practical interest, for *collapsing* bubbles this may not be the case as the above inequality indicates. Clearly, as a bubble collapses or a droplet dissolves there will be a thermal diffusion thickness (which increases) and a radius (which decreases) for which the direction of the inequality will be reversed.

In view of the foregoing it seems that the application of the "thin thermal boundary layer" approximation, i.e., of Eqs. (4) and (5), to *collapsing* bubbles, i.e., to *cavitation* and to *dissolving drops*, although widely used is highly questionable, if not downright incorrect.

**15.2.2 The Asymptotic Bubble Growth and Scaling Criteria** In this section we shall show that the application of the "thin thermal boundary layer" approximation to collapsing bubbles results in an incorrect criterion used to scale cavitation phenomena in various liquids.

The asymptotic bubble growth equation is obtained by eliminating the temperature gradient between Eq. (3) and Eqs. (8), (9) or (10). Thus, upon integration we obtain

$$R(t) \sim 2b \text{Ja} \left( \frac{\alpha_f t}{\pi} \right)^{1/2} \quad (13)$$

where Ja is the Jakob number defined by

$$\text{Ja} \equiv \frac{Cp_f \rho_f \Delta T}{\rho_g h_{fg}} \quad (14)$$

and  $b$  is a numerical constant whose value depends upon which of the three expressions, i.e., Eqs. (8), (9) or (10), is used for the temperature gradient. Thus, according to the Plesset-Zwicky theory  $b = \sqrt{3}$ , according to Forster and Zuber  $b = \pi/2$ , and according to Fritz and Ende  $b = 1$ .

We note that Eq. (13) can be used to express the inequality (12) in terms of the Jakob number. Thus,

$$\frac{(\pi\alpha_f t)^{1/2}}{R(t)} = \frac{\pi}{2b \text{Ja}} \ll 1.0 \quad (15)$$

Consequently, for sufficiently high Jakob numbers, say  $\text{Ja} > 5$ , the "thin thermal boundary layer" approximation can be expected to be valid.

At this point we could consider Eq. (13) as the zeroth-order approximation and substitute it in Eq. (11) in order to obtain the *first correction* for the *effect of curvature*. We would then obtain from Eqs. (3) and (13) upon integration:

$$R(t) \sim 2b Ja \left( \frac{\alpha_f t}{\pi} \right)^{1/2} \left( 1 + \frac{\pi}{2bJa} \right) \quad (16)$$

It is of interest to note here that this expression is almost identical with that suggested by Skinner (see footnote on page 17 of reference [11]) which he obtained from the self-similar solution of Birkhoff et al. [25].

We note, however, that although Eq. (16) may be a satisfactory first correction for growing bubbles and droplets, it is *still inadequate* for applications to collapsing bubbles and dissolving droplets. This statement is based on the fact that for sufficiently small radii, when the inequality given by Eq. (12) is not satisfied, the bubble radius dependence upon the Jakob number has a form which differs entirely from that given by either Eqs. (13) or (16). This can be easily shown by considering only the second term on the right-hand side of Eq. (11), i.e.,

$$\frac{\partial T}{\partial r} = \frac{\Delta T}{R} \quad (17)$$

Eliminating the temperature gradient between Eqs. (17) and (3), we obtain, upon integration,

$$R(t) \sim (2\alpha_f t Ja)^{1/2} \quad (18)$$

By comparing Eqs. (13) and (18) it can be seen that although they exhibit the *same* dependence upon time, they *differ* in their dependence upon the Jakob number. Since the Jakob number is used to scale cavitation phenomena in various liquids, this difference between Eqs. (13) and (18) is not trivial.

It could be argued here that the use of Eq. (17) is not permissible because it was obtained from Eq. (11), which is applicable to media at *rest*. We note, however, that this approach has been widely used in analyses of drop and aerosol dynamics (see for example reference [30]). In the analysis which follows it will be shown, among others, that an equation of the form of Eq. (17) is valid *provided* that the effect of the area change is taken into account.

### 15.3 The Energy Integral Method

**15.3.1 Procedure** The application of integral methods to analyze transient heat transfer problems is well established as a result of studies reported by Goodman [31] and by Veinik [32]. The versatility of this method in solving various nonlinear problems of heat transfer with and without phase change is well illustrated in reference [33].

As in other integral methods, the formulation and solution of the problem consists of three steps. First, a spatial profile of temperature is assumed which must satisfy the boundary conditions of the particular problem. Second, the energy equation is integrated across the thickness,  $\delta$ , of the thermal boundary layer yielding the energy integral equation. Finally, the substitution of the assumed temperature profile in the energy integral equation results in an ordinary differential equation for the thickness of the thermal boundary layer. Its solution yields  $\delta$ , as a function of time and specifies therefore the functional relation between temperature and time. These three steps will be followed in formulating and solving the present problem.

**15.3.2 Temperature Profiles** It has been shown in references [31–33] that for a planar geometry, an assumed parabolic temperature distribution, i.e.,

$$T(r) = A + Br + Cr^2 \quad (19)$$

yields results which are in good agreement with those obtained by exact methods.

This same temperature distribution, i.e., Eq. (19), has been used in references [13, 32, 34] for solving spherically symmetric system and bubble dynamic problems. However, the application of Eq. (19) to geometries other than planar is surprising since it is known that such an application yields erroneous results. Indeed, it was first noted by Sparrow [35] and demonstrated by Lardner and Pohle [36] that an error of 100% and higher results if Eq. (19) is applied to problems of polar symmetry, i.e., to cylindrical geometry.

As discussed in references [33, 35, 36], the erroneous results, which are obtained when Eq. (19) is applied to geometries other than planar, stem from the fact that for these geometries the volume into which heat diffuses does not remain the same for equal increments of  $r$ , as in the planar case. Consequently, a modification of the assumed parabolic profile is necessary. It was suggested therefore in these references that for spherical geometry, the appropriate spatial temperature distribution should be of the form:

$$T(r) = \frac{A + Br + Cr^2}{r} \quad (20)$$

In the present analysis we shall assume that the profile is given by Eq. (20). The results obtained by using Eqs. (19) and (20) are compared in the Appendix B with those derived by exact methods. It can be seen there that, whereas Eq. (20) yields excellent results, very poor agreement is obtained by using Eq. (19).

The coefficients  $A$ ,  $B$  and  $C$  in Eq. (20) are to be determined from the boundary conditions for the particular problem under consideration. In the present one we shall distinguish two types of boundary conditions at the vapor-liquid interface: one a time dependent temperature, the other a time dependent radial heat flux.

We denote by  $R(t)$ , the radius of the bubble or of the drop, by  $\delta(t)$  the thickness of the thermal boundary layer, and by  $T_\infty(t)$  the temperature of the liquid at a great distance from the interface. We can express then the boundary conditions for the case of *time dependent interface temperature* by

$$\begin{aligned} \text{at } r = R(t) \quad T &= T_i(t) \equiv T_i \\ \text{at } r = R(t) + \delta(t) \quad T &= T_\infty(t) \equiv T_\infty \quad \text{and} \quad \frac{\partial T}{\partial r} = 0 \end{aligned} \quad (21)$$

whereas for the case of *time dependent heat flux* at the interface, we have

$$\begin{aligned} \text{at } r = R(t) \quad \frac{\partial T}{\partial r} &= \frac{\dot{q}_i(t)}{k_f} \equiv \frac{\dot{q}_i}{k_f} \\ \text{at } r = R(t) + \delta(t) \quad T &= T_\infty(t) \equiv T_\infty \quad \text{and} \quad \frac{\partial T}{\partial r} = 0 \end{aligned} \quad (22)$$

In Eqs. (21) and (22) the two conditions at  $r = R(t) + \delta(t)$  define the thickness of the thermal boundary layer  $\delta(t)$ .

We define now the dimensionless length,  $\xi$ , by

$$\xi \equiv \frac{R + \delta}{R} \quad (23)$$

where for simplicity we have written  $R$  and  $\delta$  instead of  $R(t)$  and  $\delta(t)$ .

Evaluating the constants in Eq. (20) by means of Eqs. (21) and (22), we obtain for the case of *variable interface temperature* the following temperature distribution:

$$T(r, t) = \frac{T_{\infty} - T_i}{(\xi - 1)^2} \left[ \xi^2 \left( 1 - \frac{R}{r} \right) + 1 - \frac{r}{R} \right] + T_i \quad (24)$$

whereas the temperature gradient at the interface is given by:

$$\left( \frac{\partial T}{\partial r} \right)_{r=R(t)} = \left( \frac{T_{\infty} - T_i}{\delta} \right) (\xi + 1) = \left( \frac{T_{\infty} - T_i}{R} \right) \left( \frac{\xi + 1}{\xi - 1} \right) \quad (25)$$

Similarly, for the case of variable heat flux at the interface, we obtain from Eqs. (20) and (22) the following expressions for the temperature distribution:

$$T(r, t) = T_{\infty} - \left( \frac{\dot{q}_i}{k_f} \right) \left( \frac{r}{\xi^2 - 1} \right) \left[ \frac{R}{r} \xi - 1 \right]^2 \quad (26)$$

whence the temperature of the interface becomes

$$T(R, t) = T_{\infty} - \left( \frac{\dot{q}_i}{k_f} \right) \left( \frac{\xi - 1}{\xi + 1} \right) R \quad (27)$$

**15.3.3 The energy Integral** We turn our attention now to the energy integral equation which is obtained by integrating Eq. (1) between the limits  $R$  and  $R + \delta$ . It is given by Eq. (A.23). For the purpose of convenience it is re-written here

$$\begin{aligned} \frac{d}{dt} \int_R^{R+\delta} T(r, t) r^2 dr &= \alpha_f \left[ (R+\delta)^2 \frac{\partial T}{\partial r} \Big|_{r=R+\delta} - R^2 \frac{\partial T}{\partial r} \Big|_{r=R} \right] \\ &+ (R + \delta)^2 T(R + \delta, t) \frac{d(R + \delta)}{dt} - R^2 T(R, t) \frac{dR}{dt} - R^2 V_f [T(R + \delta, t) - T(R, t)] \quad (28) \end{aligned}$$

where  $V_f$  is the liquid velocity at the vapor-liquid interface. Various forms of  $V_f$  are given in Appendix A. For general purposes it is specified by Eq. (A.9) or by Eq. (A.11) for simplified cases.

Inserting in Eq. (28) the boundary conditions given by Eq. (21), and the temperature gradient give by Eq. (25), we obtain the energy integral for the case of *variable interface temperature*, i.e.,

$$\begin{aligned} \frac{d}{dt} \left[ \int_R^{R+\delta} T(r, t) r^2 dr \right] &= \left( \frac{T_{\infty}}{3} \right) \frac{d}{dt} [R^3 (\xi^3 - 1)] \\ &- R \alpha_f (T_{\infty} - T_i) \left( \frac{\xi + 1}{\xi - 1} \right) - R^2 (T_{\infty} - T_i) (V_f - \dot{R}) \quad (29) \end{aligned}$$

Similarly, by substituting Eq. (22) and the interface temperature given by Eq. (27) into Eq. (28), we obtain the energy integral for the case of *variable heat flux at the interface*. Thus,

$$\frac{d}{dt} \left[ \int_R^{R+\delta} T(r, t) r^2 dr \right] = \left( \frac{T_\infty}{3} \right) \frac{d}{dt} [R^3 (\xi^3 - 1)] - R \alpha_f \left( \frac{\dot{q}_i}{k_f} \right) - R^3 \left( \frac{\dot{q}_i}{k_f} \right) (V_{\beta} - \dot{R}) \quad (30)$$

Equations (29) and (30) represent the energy integral for the case of variable interfacial temperature and variable interface heat flux, respectively. For an incompressible vapor with  $\rho_g \ll \rho_f$ , the last term appearing in Eqs. (29) and (30) becomes zero. For the reasons of simplicity, these are the assumptions made in the remaining part of this paper. The neglect of compressibility effect may break down during the process as soon as the bubble interface velocities become comparable with the speed of sound in the vapor. The assumption of  $\rho_g \ll \rho_f$  is normally satisfied by substances at pressures sufficiently below the critical point. However, its applicability in some special situations (such as cryogenics) may be questionable. Nevertheless, these two assumptions furnish an order-of-magnitude estimate of the several quantities involved, and it gives a qualitative and even quantitative picture of the vapor bubble growth and collapse processes. In their general review Plesset and Prosperetti [6] analyzed the effects of vapor compressibility on bubble dynamics.

In what follows we shall consider variable interface temperature and interface heat flux cases separately.

**15.3.4 Time Dependent Interface temperature** The differential equation for the thickness of the thermal boundary layer is obtained by substituting the appropriate temperature distribution in the energy integral.

For the boundary condition given by Eq. (21), the corresponding temperature distribution and gradient are given by Eqs. (24) and (25), whereas the energy integral is given by Eq. (29). Consequently, by substituting Eqs. (24) and (25) into Eq. (29), we obtain upon integration and some rearrangement the following expression:

$$\begin{aligned} \frac{d}{dt} \left\{ \frac{(T_\infty - T_i)}{(\xi - 1)^2} \frac{R^3}{12} [4(\xi^2 + 1)(\xi^3 - 1) - 6\xi^2(\xi^2 - 1) - 3(\xi^4 - 1)] + T_i \frac{R^3}{3} (\xi^3 - 1) \right\} \\ = \frac{T_\infty}{3} \frac{d}{dt} [R^3 (\xi^3 - 1)] - \alpha_f (T_\infty - T_i) (R) \frac{\xi + 1}{\xi - 1} \end{aligned} \quad (31)$$

In general, both the temperature of the bulk liquid  $T_\infty$  and of the interface  $T_i$ , as well as  $R$  and  $\delta$ , or  $\xi$ , are functions of time. Consequently, additional relations are required if Eq. (31) is to be used to determine the thickness of the thermal boundary layer  $\delta$ . For example, by specifying the rate of heating (or of cooling) of the bulk liquid, we obtain one of these relations, i.e., we obtain  $T_\infty$  as a function of time. A second relation is provided by the momentum and Clausius-Clapeyron's equations which can be used to express  $T_i$  as a function of time.

For reasons of simplicity, let us first assume that the temperature of the bulk liquid is constant. Equation (31) then becomes:

$$\frac{d}{dt} \left\{ (T_\infty - T_i) R^2 [(\xi + 1)^2 - 4] \right\} = 12 \alpha_f \frac{(\xi + 1)}{(\xi - 1)} (T_\infty - T_i) \quad (32)$$



Let us consider next three problems: in the first one both  $T_i$  and  $R$  will be assumed constant, whereas in the second one  $T_i$  will again be assumed constant but  $R$  will be a function of time. Finally, in the third one both  $T_i$  and  $R$  will be assumed variable. We note here that the solution of the first problem will provide a check on the accuracy of the integral method. Since the exact solution to this problem is known, it is given by Eq. (11), whereas the second one corresponds to the asymptotic bubble growth problem in which the effects of inertia and of surface tension are negligibly small.

**Constant Temperature, Stationary Radius** For a constant temperature ( $T_\infty - T_i$ ) and a stationary radius  $R_s$ , Eq. (32) reduces to

$$\frac{d}{dt} (\xi + 1)^2 = \frac{12\alpha_f}{\delta R_s} (\xi + 1) \quad (33)$$

whence, in view of Eq. (23), we obtain

$$\frac{d\delta^2}{dt} = 12\alpha_f \quad (34)$$

which upon integration yields the following expression for the thickness of the thermal boundary layer  $\delta_s$ , adjacent to a sphere with a *stationary* radius:

$$\delta_s = 2(3\alpha_f t)^{1/2} \quad (35)$$

By substituting this relation in Eq. (25), we obtain the following expression for the temperature gradient at the surface of a *stationary* sphere

$$\left( \frac{\partial T}{\partial r} \right)_{r=R_s} = \frac{\Delta T}{(3\alpha_f t)^{1/2}} \left[ 1 + \frac{(3\alpha_f t)^{1/2}}{R_s} \right] \quad (36)$$

This gradient, obtained by means of the integral method and the assumed temperature distribution, i.e., Eq. (20), should be compared to the exact solution given by Eq. (11). It can be seen that the agreement is rather good, which confirms the usefulness and versatility of the integral method as well as the validity of the assumed spatial temperature distribution, i.e., of Eq. (20). The erroneous results which are obtained when Eq. (19) is applied to a spherical geometry are demonstrated in Appendix B.

**Constant Temperature, Time Dependent Radius** Assuming again that the temperature ( $T_\infty - T_i$ ) is constant but that the bubble radius is a function of time, Eq. (32) reduces to:

$$\frac{d}{dt} \left[ R^2 \delta \left( 4 + \frac{\delta}{R} \right) \right] = 12\alpha_f \left( \frac{R^2}{\delta} \right) \left( 2 + \frac{\delta}{R} \right) \quad (37)$$

where we have taken into account Eq. (23).

Let us consider now two cases: for the first  $\frac{\delta}{R} \ll 2$ , whereas for the second:  $\frac{\delta}{R} \gg 8$

For the first case, i.e., when

$$\frac{\delta}{R} \ll 2 \quad (38)$$

then Eq. (37) becomes

$$R^2 \delta \frac{d}{dt} (R^2 \delta) = 6 \alpha_f R^4 \quad (39)$$

whence upon integration

$$R^4 \delta^2 = 12 \alpha_f \int_0^t R^4(x) dx \quad (40)$$

Using the definition of the root mean square of  $R^2(t)$ , i.e.,  $\text{RMS} [R^2]$  given by Eq. (6), we obtain from Eq. (40) the following expression for the thickness of the thermal boundary layer for a *growing* or *collapsing* bubble (or droplet):

$$\delta = 2(3\alpha_f t)^{1/2} \frac{\text{RMS} [R^2(t)]}{R^2(t)} \quad (41)$$

Defining by  $b$  the "area change" parameter:

$$b = \frac{R^2(t)}{\text{RMS} [R^2(t)]} \quad (42)$$

and, using the expression for the thickness of the thermal boundary layer for a stationary sphere given by Eq. (35), we can express Eq. (41) as

$$\delta = \frac{\delta_s}{b} \quad (43)$$

We can distinguish now three cases according to whether the bubble or droplet is growing, collapsing, or remaining stationary.

For *growing* bubbles or droplets, we have:  $\dot{R}(t) > 0$ ; consequently,

$$R^2(t) > \text{RMS} [R^2(t)] \quad (44)$$

Therefore,

$$b > 1 \quad \text{and} \quad \delta < \delta_s \quad (45)$$

For *stationary spheres*  $\dot{R}(t) = 0$ ; consequently,

$$R^2(t) = \text{RMS} [R^2(t)] \quad (46)$$

Therefore,

$$b = 1 \quad \text{and} \quad \delta = \delta_s \quad (47)$$

For *collapsing* bubbles or droplets,  $\dot{R}(t) < 0$ ; consequently,

$$R^2(t) < \text{RMS}[R^2(t)] \quad (48)$$

Therefore,

$$b < 1 \quad \text{and} \quad \delta > \delta_s \quad (49)$$

These relations clearly indicate that the thermal boundary layer for a growing sphere differs from that corresponding to a collapsing one, i.e., it is much thinner. This difference is due to the effect of area changes during the process of growth or collapse and is accounted for by the coefficient  $b$  given by Eq. (42).

Since the thickness of the thermal boundary for a growing sphere differs from that corresponding to a collapsing one, it can be expected that the temperature gradient will also differ. This is indeed the case which can be verified by substituting Eq. (41) in Eq. (25). Thus we obtain for the temperature gradient at the surface of a growing or collapsing sphere the following relation:

$$\left( \frac{\partial T}{\partial r} \right)_{r=R(t)} = \Delta T \left\{ \frac{b}{(3\alpha_f t)^{1/2}} + \frac{1}{R(t)} \right\} \quad (50)$$

Since for a growing sphere  $b > 1$  whereas for a collapsing one  $b < 1$ , it can be seen that the temperature gradient is larger for growing than for collapsing bubbles or droplets. Note also that for a stationary sphere  $R(t) = R_s$ ,  $b = 1$ , and Eq. (50) reduces to Eq. (36).

It should be noted here that the coefficient  $b$ , given by Eq. (42), is a numerical coefficient. For example, if we assume that the radius can be expressed by a power law, i.e., by

$$R = (\text{const})t^n \quad \text{with} \quad n > 0 \quad (51)$$

then Eq. (42) yields for the coefficient,  $b$ , the value of

$$b = (4n + 1)^{1/2} \quad (52)$$

Thus, if we assume that the radius grows as a square root of time, i.e., that  $n = 1/2$ , then Eq. (52) yields

$$b = \sqrt{3} \quad (53)$$

which is identical with the value given by Eq. (8), derived previously in references [8, 10, 20] using similarity transformation.

Indeed, if, following the "thin thermal boundary" approximation of Eq. (12), we neglect the second term in the bracket of Eq. (50), then this equation reduces to the form of Eqs. (8, 9 or 10). We have noted in connection with these equations that the coefficients  $\sqrt{3}$  or  $\pi/2$  which appear on Eqs. (8) and (9), respectively, account for the effect of area change on the temperature gradient.

This effect is clearly demonstrated by the coefficient  $b$ , given by Eq. (42). However, whereas Eq. (50) accounts also for the effect of curvature (see the second term in the bracket), neither Eq. (8) nor (9) takes this effect into consideration. It is for this reason that the "thin thermal boundary layer" approximation is *incorrect* when applied to collapsing bubbles.

Let us consider now the second case, i.e., of a thick thermal boundary layer,

$$\frac{\delta}{R} \gg 8 \quad (54)$$

Then Eq. (37) becomes

$$\frac{d}{dt}(R\delta^2) = 12\alpha_f R \quad (55)$$

and the thermal boundary layer can be expressed as

$$\delta = \delta_f \frac{\text{RMS}[R(t)^{1/2}]}{[R(t)]^{1/2}} \quad (56)$$

In view of Eq. (54) the temperature gradient given by Eq. (25) becomes

$$\left(\frac{\partial T}{\partial r}\right)_{r=R(t)} = \frac{\Delta T}{R(t)} \quad (57)$$

It is noteworthy that the same expression can be obtained as a limiting case from Eq. (50). Consequently, the latter equation can be considered valid for both thin and thick thermal boundary layers.

*Variable Temperature, Time Dependent Radius.* It is interesting to note that the above arguments can be easily extended to the case of variable  $(T_\infty - T_i)$  and time dependent radius. In this case Eq. (32) reduced to:

$$\frac{d}{dt}\left[R^2\delta\left(4 + \frac{\delta}{R}\right)(T_\infty - T_i)\right] = 12\alpha_f\left(\frac{R^2}{\delta}\right)\left(2 + \frac{\delta}{R}\right)(T_\infty - T_i) \quad (58)$$

For the case  $\delta/R \ll 2$ , Eq. (58) becomes

$$\frac{d}{dt}\left[R^4\delta^2(T_\infty - T_i)^2\right] = 12\alpha_f R^4(T_\infty - T_i)^2 \quad (59)$$

which can be integrated to obtain the thermal boundary layer thickness as follows:

$$\delta = 2(3\alpha_f t)^{1/2} \frac{\text{RMS}[R^2(T_\infty - T_i)]}{R^2 |T_\infty - T_i|} \quad (60)$$

Similarly, for the case of  $\delta/R \gg 8$ , Eq. (58) yields

$$\delta = \delta_s \frac{\text{RMS}[R^{1/2}|T_\infty - T_i|^{1/2}]}{R^{1/2}|T_\infty - T_i|^{1/2}} \quad (61)$$

Arguments made in Sections 3.4.1 and 3.4.2, respectively, can be easily extended with respect to Equations (60) and (61) provided that modifications in the argument of RMS taken into account properly as suggested here.

**15.3.5 Time Dependent Heat Flux at the Interface** We shall consider now the case of a time dependent heat flux at the interface. For the boundary condition given by Eq. (22), the corresponding temperature distribution is given by Eq. (26), whereas the energy integral is given by Eq. (30).

Substituting, therefore, Eq. (26) in Eq. (30), we obtain upon integration and some rearrangement

$$\frac{d}{dt} \left[ \frac{\dot{q}_i''}{k_f} R^2 \delta^2 \left( \frac{4 + \delta/R}{2 + \delta/R} \right) \right] = 12 \alpha_f R^2 \frac{\dot{q}_i''}{k_f} \quad (62)$$

We note that the value of the parenthesis within the square bracket can vary from 2 to 1, depending on whether the thermal boundary layer is thin or thick. Using the value of 2 for this approximation, Eq. (62) becomes upon integration

$$\frac{\dot{q}_i''}{k_f} R^2 \delta^2 = 6 \alpha_f \int_0^t R^2(x) \frac{\dot{q}_i''(x)}{k} dx \quad (63)$$

or

$$\delta = (6 \alpha_f t)^{1/2} \frac{\text{RMS}[R \dot{q}_i''^{1/2}]}{R \dot{q}_i''^{1/2}} \quad (64)$$

The temperature at the interface is obtained by substituting Eq. (64) into Eq. (27); thus,

$$T(R) = T_\infty - \frac{\dot{q}_i''}{k_f} \left( \frac{3 \alpha_f t}{2} \right)^{1/2} \frac{\text{RMS}[R \dot{q}_i''^{1/2}]}{R \dot{q}_i''^{1/2}} \quad (65)$$

when  $\dot{q}_i$  and  $R$  are constant. Then Eq. (65) reduces to:

$$T(R) = T_\infty - \frac{\dot{q}_i''}{k_f} \left( \frac{3 \alpha_f t}{2} \right)^{1/2} \quad (66)$$

which is in fair agreement with the exact solution given by Carslaw and Jaeger [27].

$$T(R) = T_\infty - \frac{\dot{q}_i''}{k_f} \left( \frac{4 \alpha_f t}{\pi} \right)^{1/2} \quad (67)$$

As to the effect of growth, or of collapse on the thickness of the thermal boundary layer, we note that arguments similar to those presented in the proceeding section could be made with regard to Eq. (64). Consequently, they will not be repeated here.

However, we note in closing that for a thick thermal boundary layer, instead of Eq. (66) we obtain the following relation:

$$T(R) = T_{\infty} - \frac{\dot{q}_i''}{k_f} R(t) \quad (68)$$

#### 15.4 Application to Bubbles or Drops

When the effects of inertia and of surface tension can be neglected, the bubble (or droplet) growth (or collapse) is governed by thermal diffusion. Such a thermal diffusion-controlled bubble growth is expressed by Eq. (13) which is subject to the "thin thermal boundary layer" approximation since it was derived by using Eqs. (8), (9) or (10). Instead of using one of these three equations for the temperature gradient, some investigators in the past have also used Eq. (11) (see for example references [30, 37], among others). However, although this latter equation is not subject to the "thin thermal boundary layer" approximation, its application to phase change problems, i.e., to *moving* boundary problem, was rather questionable in view of the fact that Eq. (11) was derived for a *stationary* spherical boundary.

We have shown in the analysis presented in the preceding section that for a moving interface, the form of Eq. (11) is still valid provided that the effect of area change is taken into account. We have shown also (cf. Eq. (50)), that this effect can be taken easily into account by means of the coefficient  $b$  given by Eq. (42). In what follows we shall use Eqs. (50) and (3) to analyze the thermal diffusion-controlled bubble (or droplet) growth (or collapse) problem.

By eliminating the temperature gradient between Eqs. (3) and (50), we obtain the following relation for the radial velocity of a bubble:

$$\frac{dR}{dt} = \pm \alpha_f \text{Ja} \left\{ \frac{b}{(3\alpha_f t)^{1/2}} + \frac{1}{R(t)} \right\} \quad (69)$$

where the plus sign stands for growth and the negative for collapse. Equation (69) can be expressed in a dimensionless form by means of the following dimensionless parameters

$$r^* \equiv \frac{R}{R_0} \quad (70)$$

$$\tau \equiv \left( \text{Ja} \frac{2\alpha_f t}{R_0^2} \right)^{1/2} \quad (71)$$

$$\epsilon \equiv \left( \text{Ja} \frac{2b^2}{3} \right)^{1/2} \quad (72)$$

Thus,

$$\frac{dr^*}{d\tau} = \pm \left( \frac{\tau}{r^*} + \varepsilon \right) \quad (73)$$

For the initial condition given by

$$\text{at } \tau = 0 \quad r^* = 1 \quad (74)$$

the solution of Eq. (73) is

$$r^* = \tau u(\tau, \varepsilon) \quad (75)$$

where the variables  $u(\tau, \varepsilon)$  are given by:

$$\frac{(u - u_1)^{u_1}}{(u - u_2)^{u_2}} = \tau^{u_2 - u_1} \quad (76)$$

For a *growing* sphere, the coefficients  $u_1$  and  $u_2$  are:

$$u_1 = \frac{\varepsilon}{2} + \left( \frac{\varepsilon^2}{4} + 1 \right)^{1/2} \quad \text{and} \quad u_2 = \frac{\varepsilon}{2} - \left( \frac{\varepsilon^2}{4} + 1 \right)^{1/2} \quad (77)$$

whereas for a *collapsing* one they are:

$$u_1 = -\frac{\varepsilon}{2} + \left( \frac{\varepsilon^2}{4} + 1 \right)^{1/2} \quad \text{and} \quad u_2 = -\frac{\varepsilon}{2} - \left( \frac{\varepsilon^2}{4} + 1 \right)^{1/2} \quad (78)$$

In order to examine the important features of this solution, let us consider the effect of the Jakob number.

For large Jakob numbers we have

$$\frac{\varepsilon^2}{4} \gg 1 \quad (79)$$

Therefore, for a *growing* sphere, Eqs. (77) and (76) become

$$u_1 = \varepsilon \quad \text{and} \quad u_2 = 0$$

$$u = \frac{1}{\tau} + \varepsilon \quad (80)$$

whereas for a *collapsing* sphere, Eqs. (78) and (76) reduce to

$$u_1 = 0 \quad \text{and} \quad u_2 = -\varepsilon$$

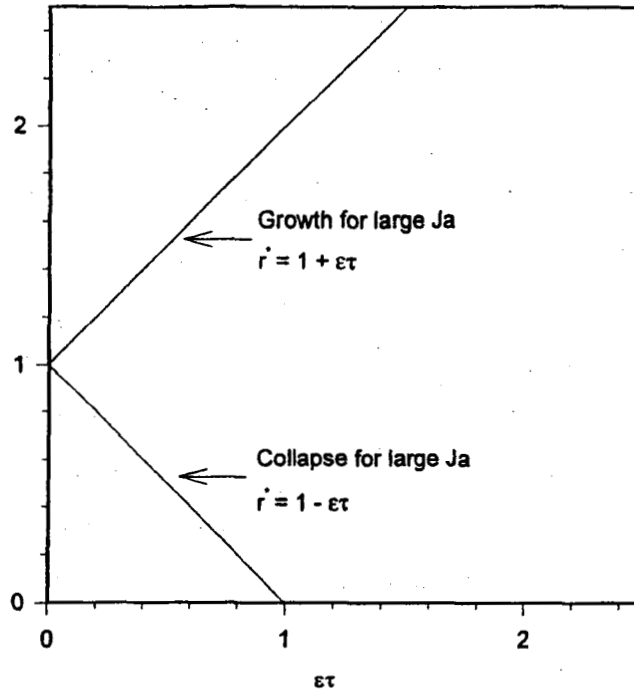


Fig. 1. Growth and collapse for large Jakob numbers, i.e., for  $\frac{\epsilon^2}{4} > 1.0$ .

$$u = \frac{1}{\tau} - \epsilon \quad (81)$$

Substituting these relations in Eq. (75), we obtain

$$r^* = 1 \pm \epsilon\tau \quad (82)$$

which is plotted in Figure 1. From this equation and from the definitions of  $\epsilon$  and  $\tau$ , we see that at large Jakob numbers (corresponding to thin thermal boundary layers) the radius varies as

$$R \sim 2bJa \left( \frac{t\alpha_f}{3} \right)^{1/2} \quad (83)$$

which should be compared to Eq. (13).

For small Jakob numbers (corresponding to thick thermal boundary layers), we have

$$\frac{\epsilon^2}{4} \ll 1 \quad (84)$$

whence Eqs. (77) and (76) yield for a growing sphere

$$u_1 = 1 \quad \text{and} \quad u_2 = -1$$

$$u = \frac{(1 + \tau^2)^{1/2}}{\tau} \quad (85)$$

whereas for a *collapsing* sphere, we have from Eqs. (78) and (76)



$$u_1 = i \quad \text{and} \quad u_2 = -i$$

$$u = \frac{(1 - \tau^2)^{1/2}}{\tau} \quad (86)$$

Substituting these expressions in Eq. (75), we obtain

$$r^* = (1 \pm \tau^2)^{1/2} \quad (87)$$

which is shown in Figure 2. Consequently, for small Jakob numbers the radius varies as:

$$R \sim (Ja^2 \alpha_f t)^{1/2} \quad (88)$$

which should be compared to Eq. (18).

An approximate solution which has the same limiting values as large and small Jakob numbers can be obtained by substituting  $u_1$  from Eq. (77) into Eq. (75). Thus,

$$r^* \sim \left( \frac{\epsilon \tau}{2} \right) \left[ 1 + \left( 1 + \frac{4}{\epsilon^2} \right)^{1/2} \right] \quad (89)$$

It is important to note here that since according to either Eq. (83) or (88) the radius changes as the square root of time, the *area change parameter*  $b$  given by Eq. (42) has a value equal to  $\sqrt{3}$  given by Eq. (53). Consequently, the inequalities  $\epsilon^2/4 \gtrless 1$  which define the domains of large and of small Jakob numbers respectively can be expressed also by

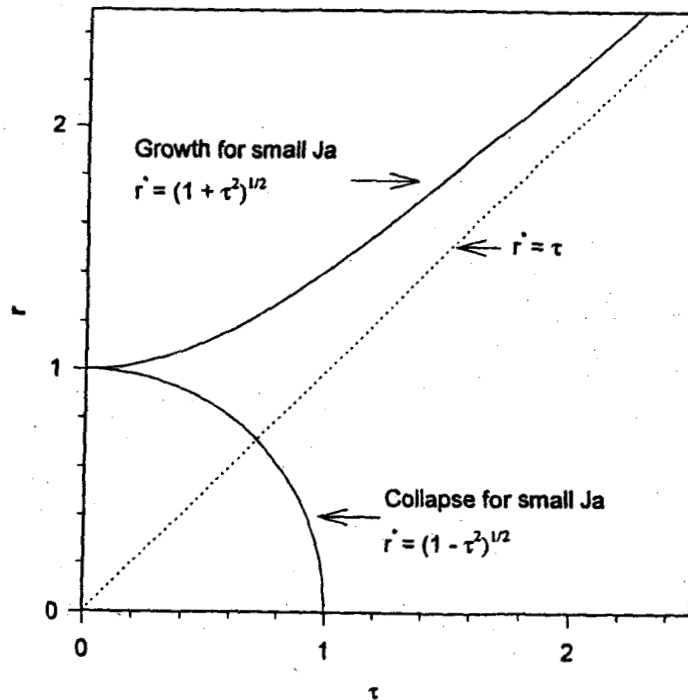


Fig. 2. Growth and collapse for small Jakob numbers, i.e., for  $\frac{\epsilon^2}{4} > 1.0$ .

$$Ja \gtrsim 2 \quad (90)$$

Equation (69) clearly shows how the Jakob number, the curvature and the area change affect the rate of bubble (or droplet) growth (or collapse). Thus, at large Jakob numbers, Eq. (82) indicates that the radius depends on the area change parameter  $b$ , and on the Jakob number at the first power, whereas for small Jakob numbers Eq. (88) shows that the radius is a function of the square root of  $Ja$  and is independent of  $b$ .

Consequently, when the Jakob number is used to scale boiling or cavitation processes or drop-let phenomena, one should differentiate the domains of large and small Jakob numbers. Thus when  $Ja \gg 2$ , the process should be scaled according to

$$\pi_1 \equiv Ja \quad (91)$$

whereas when  $Ja \ll 2$ , it should be scaled according to

$$\pi_2 \equiv (Ja)^{1/2} \quad (92)$$

## 15.5 Comparison with Experiments

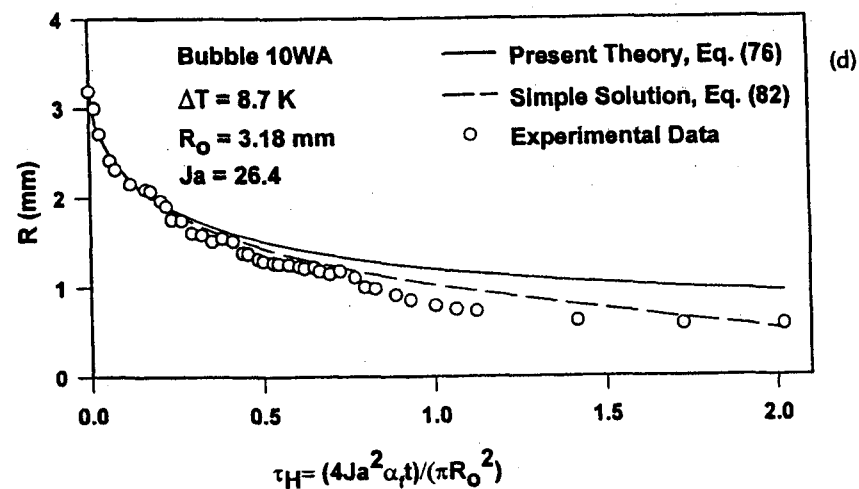
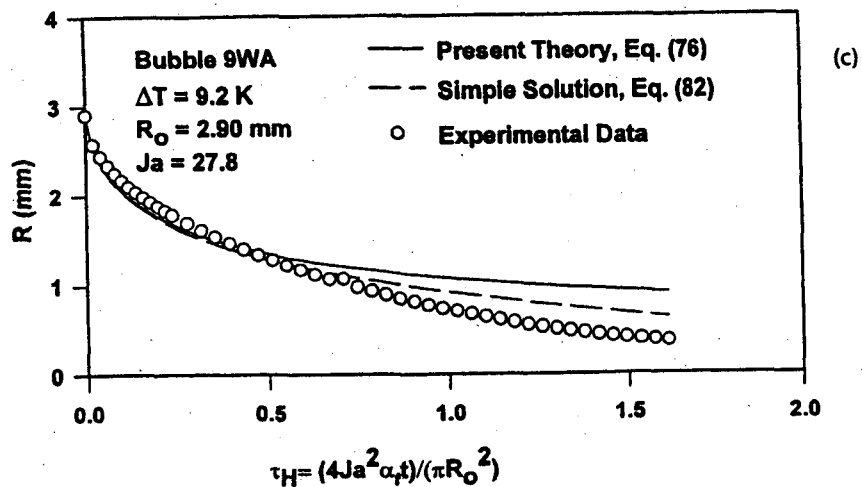
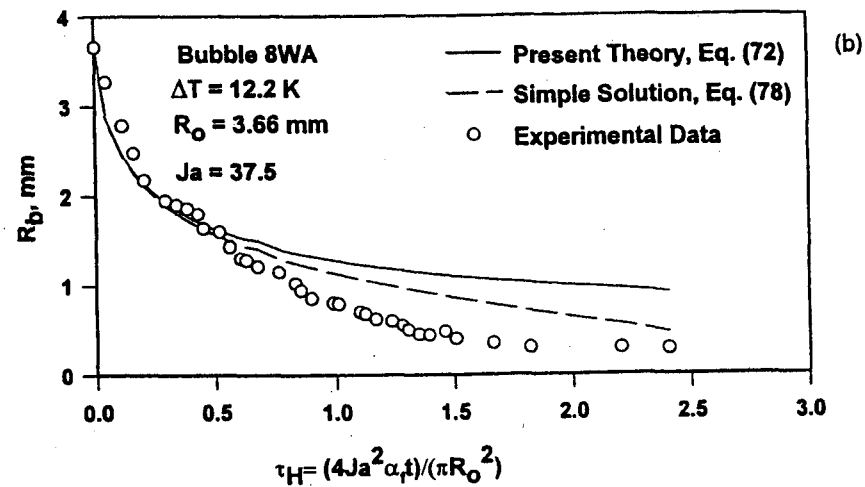
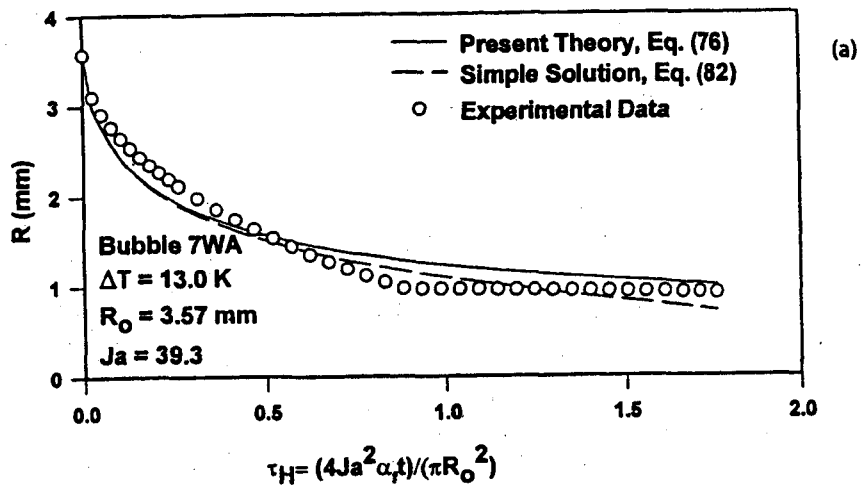
For the purpose of verification of the validity of the theoretical model developed here, Florschuetz and Chao's [23] collapsing bubble experiments were chosen among the available experimental data [23, 38–41]. The major reason for such a choice is that Florschuetz and Chao's experiments were performed with the aid of a free-fall tower to minimize the effects of translational motion and initial-buoyancy induced deformation. In a normal gravitational field, bubbles in a liquid experience the strong effect of a buoyant force which gives rise to appreciable translational velocities. Furthermore, they depart from a spherical shape and may assume various configurations depending on their size.

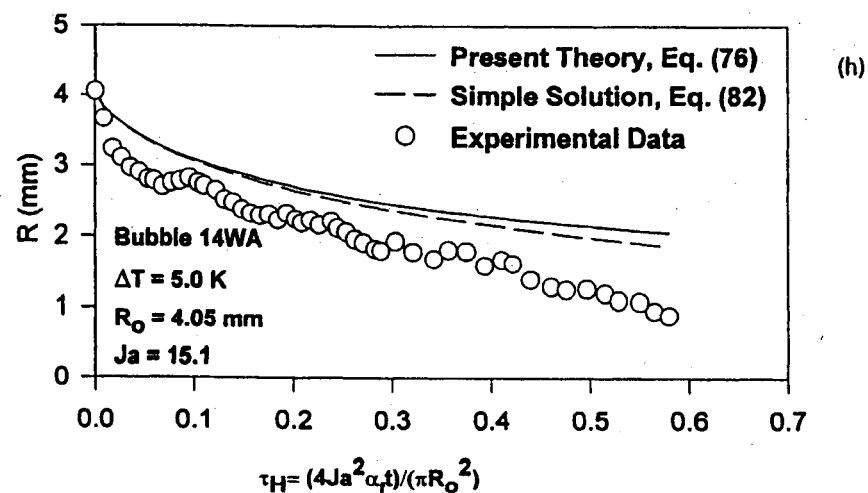
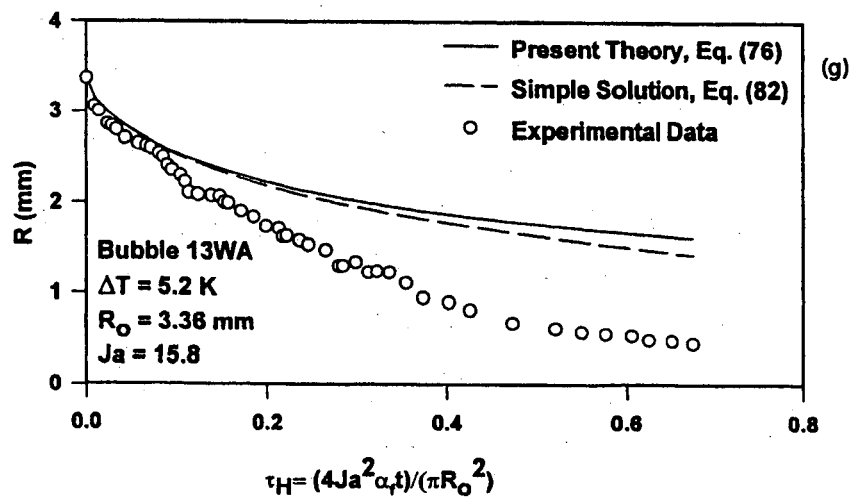
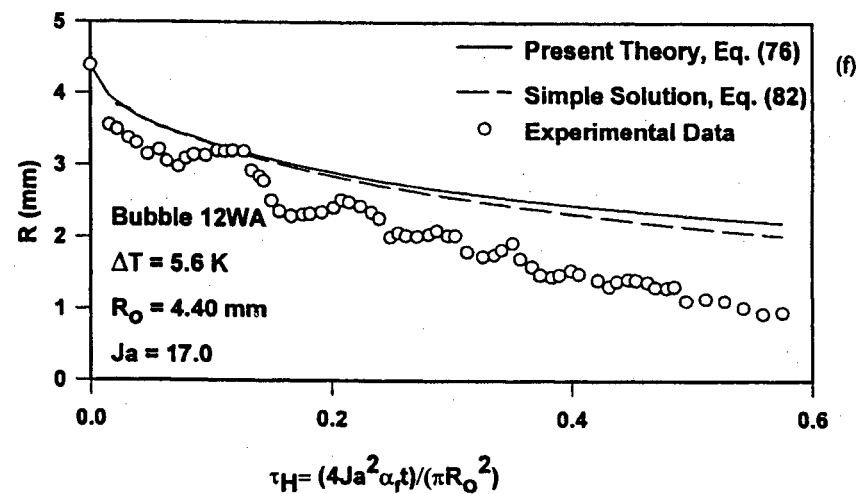
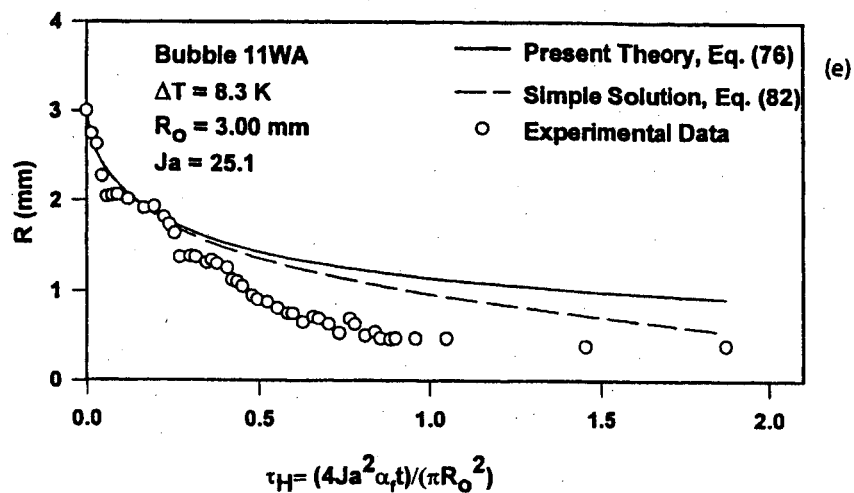
The inducement of translational velocities not only augments the heat transfer but also causes errors in the precise determination of the equivalent bubble radius during the collapse process. With the drop-tower experiments translational motions were prevented at least up to 0.1 seconds. In addition to minimizing the influence of translational motion of bubbles, the initial conditions of the bubbles are well specified, and the non-condensables were controlled in the experiments reported in reference [23]. Although the data for bubbles containing non-condensables were also reported by Florschuetz and Chao, these data are not considered here.

Since the plotted data points showed an oscillatory behavior, the authors of reference [23] smoothed the data and presented it in bubble radius,  $R$ , against dimensionless time,  $\tau_H \equiv 4Ja^2\alpha_f t / \pi R_0^2$ . Figure 9 of reference [23] describes 8 water bubbles. The dimensionless smoothed water data are compared to the theoretical predictions obtained from the complete solution, Eq. (76), in Figures 3a through 3h. Included in these figures are the predictions from the approximate solution for  $\varepsilon^2/4 > 1.0$  as given by Eq. (82).

Referring to Figure 3, it can be seen that both predictions from the complete equation and approximate equation generally follow the trend of experimental curves. It is to be noted that the collapse of bubbles 7, 8, 9, and 10 as demonstrated by Figures 3a through 3d exhibit good agreement and 11, 12, 13, and 14 as shown on Figures 3e through 3h show large deviations. The collapse rate for these bubbles appears to be drastically higher than the other cases.

The increased collapse rate for bubbles 11, 12, 13, and 14 over what would be expected for a purely radial collapse can be attributed to increased translation velocities of these bubbles in the liquid, improving the heat transfer, and to increasing the rate of collapse [41]. While such translational





velocities are much smaller than those under normal gravitational conditions, these velocities for bubbles 11, 12, 13, and 14 are appreciable when compared to the radial velocities of the bubble interface. The ratio of the bubble translational velocity to its radial velocity at  $r^* = 0.8$  and 0.5 is tabulated in Table 3 of reference [23]. This table clearly shows that the velocity ratios for the collapsing bubbles 11, 12, 13, and 14 is at least 3 to 10 times greater than those listed for bubbles 7, 8, 9, and 10. Whenever the ratio is small, reasonable agreement between theory and experiment is obtained.

In addition to the effect of convective motion on the collapse rate, other reasons for the obvious disagreement between the predictions and the experimental data toward the final stage of the collapse process may be the neglect of the surface tension and of the vapor and liquid incompressibilities. These effects are discussed below:

The effect of surface tension can be demonstrated by including the surface tension on the dynamics of the interfacial motion. Such an equation is derived in Appendix A expressed by Eq. (A.17). When this equation is integrated from an initial bubble radius of  $R_i$  to any radius  $R$  one obtains

$$\dot{R}^2 = \left(\frac{R_i}{R}\right)^3 \dot{R}_i^2 + \frac{2}{3} \left(\frac{P_{f\infty} - P_g}{\rho_f}\right) \left[ \left(\frac{R_i}{R}\right)^3 - 1 \right] + \frac{2\sigma}{\rho_f R} \left[ \left(\frac{R_i}{R}\right)^2 - 1 \right] \quad (93)$$

where it was assumed that  $P_g$  is constant. This assumption is not rigorously correct. Nevertheless, this assumption furnishes an-order of magnitude estimate of direct effect of surface tension on the bubble collapse rate. For the later stages of the collapse process,  $R_i/R \gg 1$ , the collapse rate equation can be approximated as follows:

$$\dot{R}^2 \sim \left(\frac{R_i}{R}\right)^3 \left[ \dot{R}_i^2 + \frac{2}{3} \left(\frac{P_{f\infty} - P_g}{\rho_f}\right) + \frac{2\sigma}{\rho_f R_i} \right] \quad (94)$$

It is evident from this equation that the surface tension accelerates the collapse rate. However, its relative effect remains the same as that of initiation of the collapse process. For the bubble collapse process  $P_{f\infty} - P_g > 0$ , and Eq. (94) yields

$$\dot{R} \sim R^{-3/2} \quad (95)$$

which predicts that the bubble interface velocity approaches infinity as  $R^{-3/2}$  as  $R \rightarrow 0$ . As it is discussed in great detail by Plesset and Prosperetti [6] this is not an acceptable solution. They demonstrated that at the final stages of the collapse the compressibility effects of both the gas and liquid becomes significant to yield  $\dot{R} \sim R^{-1/2}$  as  $R \rightarrow 0$ , in contrast to the incompressible approximation that was shown to give  $\dot{R} \sim R^{-3/2}$ .

Effects of vapor compressibility can be demonstrated by using the complete form of vapor mass balance equation expressed by Eq. (A.2) as follows:

$$\dot{R} = - \left( \frac{1}{\rho_g} \right) \left( \dot{m}_{gi} + \frac{1}{3} R \frac{d\rho_g}{dt} \right) \quad (96)$$

where  $\dot{m}_{gi} > 0$  for the condensation process. By using the Clausius-Clapeyron relation to relate the vapor temperature to its pressure and assuming that the vapor behaves as an ideal gas it can be shown that

$$\frac{d\rho_g}{dt} = \left(\frac{\rho_g}{T_g}\right) \left(\frac{h_{fg}}{\bar{R}T_g} - 1\right) \frac{dT_g}{dt} \quad (97)$$

where  $\bar{R}$  is the ideal gas constant for the vapor.  $\frac{h_{fg}}{\bar{R}T_g} > 1$  except around the critical point where the

ideal gas approximation breaks down. It is evident from Eq. (97) that the vapor density rate proportional to the vapor temperature rate. Considering the fact that the pressure drop across the liquid/vapor interface due to surface tension may be significant enough to cause the interfacial temperature to be higher than assuming that  $T_g$  corresponds to the saturation temperature at  $P_{f\infty}$ . This argument leads to  $dT_g/dt > 0$ , and in turn Eq. (96) yields  $d\rho_g/dt > 0$ . Therefore, from Eq. (95) it becomes clear that the vapor compressibility accelerates the collapse process. Furthermore, a higher vapor temperature would result in greater heat transfer, which will also accelerate the collapse.

In view of the above discussion it can be concluded that the vapor compressibility effect in addition to the convective effects may be responsible for the over predicting the radius when compared with the experiments of Florschuetz and Chao. Both the compressibility and surface tension effects can be easily taken into account by the general formulation given in Appendix A and by the methodology presented in the text. However, as it is specified at the beginning of this paper such a numerical solution is out of the scope of this paper.

For the case of bubble growth, prediction of the present model are compared with the most recent convective boiling experiments of Thorncraft [44] on Figure 4. The data are for FC-87 for superheats ranging from 0.55°C to 6.34°C. The initial bubble radius was not clear from this reference. It is assumed that the bubble starts from its unstable equilibrium radius, and the initial bubble radius is calculated accordingly. The original data was smoothed out by Thorncraft and presented as a curve-fit. Due to difficulties associated with the bubble growth experiments, Thorncraft used a set of 5 growth curves at various points in the film set, and the constants in his curve-fit model were averaged to obtain the mean growth curves at each condition. For the purpose of comparison the original mean curve-fit bubble growth data were re-produced here. Since the majority of experimental conditions falls into the transition values of Jacob number for simple approximate solutions, the complete solution given by Eq. (76) is used for the predictions.

Although the experiments were taken under the convective boiling conditions, the agreement between the present model predictions and experimental data is satisfactory. In most of the comparisons the predictions of the bubble radius are lower than the experimental data. This can be attributed to the facts that the inertia-controlled stage of bubble growth where  $R \sim t$  was neglected in the present analysis and that the present analysis is limited by the diffusive rate at which heat is transported to the liquid-vapor interface. Again the convective effects which greatly enhances the heat transfer and the bubble growth rate has not been included in the present analysis. However, the limiting factor of neglecting inertia effects can be easily removed by using the general formulation presented in Appendix A.

## 15.6 Summary and Conclusions

1. An analysis of the spherically symmetrical phase change (moving boundary) problem has been presented. Neither the formulation based on the energy integral method nor the results are subject to the "thin thermal boundary layer" approximation used heretofore to solve this problem. In the formulation two boundary conditions at the spherical interface have been considered; one a time dependent temperature, the other a time dependent heat flux.

2. The effects of the area change as well as of the curvature are accounted for in the expression derived for the temperature gradient at the spherical interface. The results show that the thermal boundary layer for a growing sphere is thinner than that corresponding to a collapsing one.

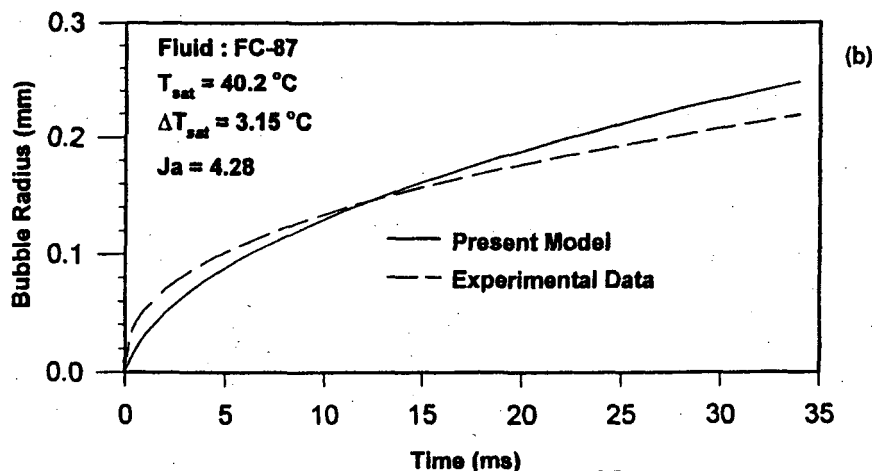
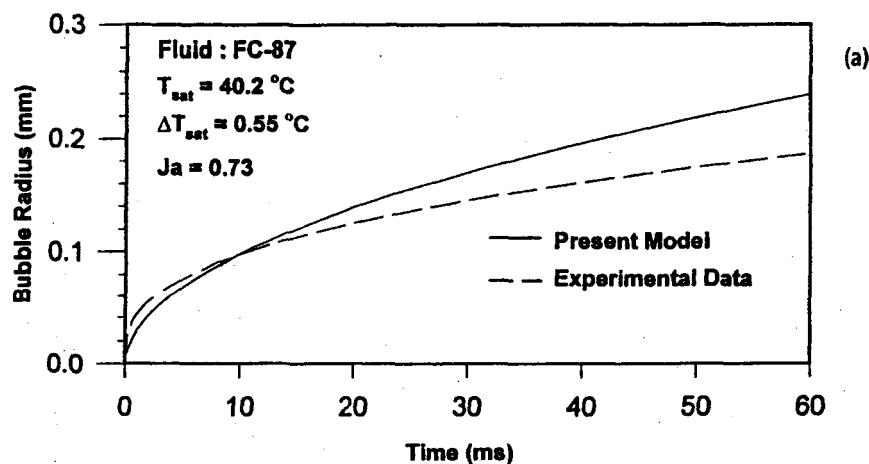
3. The solution of the energy equation has been used to analyze the diffusion controlled bubble (or droplet) growth (or collapse) problem. The effects of the Jakob number, of the area change and of the curvature are accounted for in the expression derived for the radial velocity. It is shown that for large Jakob numbers the radius depends upon the first power of the Jakob number, whereas for small Jakob numbers it is a fraction of the square root of this number.

4. It is shown that although widely used in the literature, an application of the "thin thermal boundary layer" model to cavitation, i.e., to collapsing bubbles or to dissolving or evaporating droplets, is *incorrect*, particularly so at low Jakob numbers.

5. It is shown also that recent analyzes of bubble dynamics based on the energy integral method are in error because the assumed temperature profile was incorrect. It is shown, in particular, that this erroneous temperature distribution can result in a 100% error when computing the temperature gradient of the spherical interface.

6. Although the analysis presented in this paper was formulated by considering the diffusion of energy, the same analysis and results, with an appropriate redefinition of property terms, can be applied to a spherically symmetrical mass diffusion problem with a moving boundary.

7. Comparison of a representative set of experimental bubble collapse data in a near-zero gravity environment with a negligible translational velocity of bubbles and of convective boiling bubble growth data indicates the general validity of the theoretical analysis.



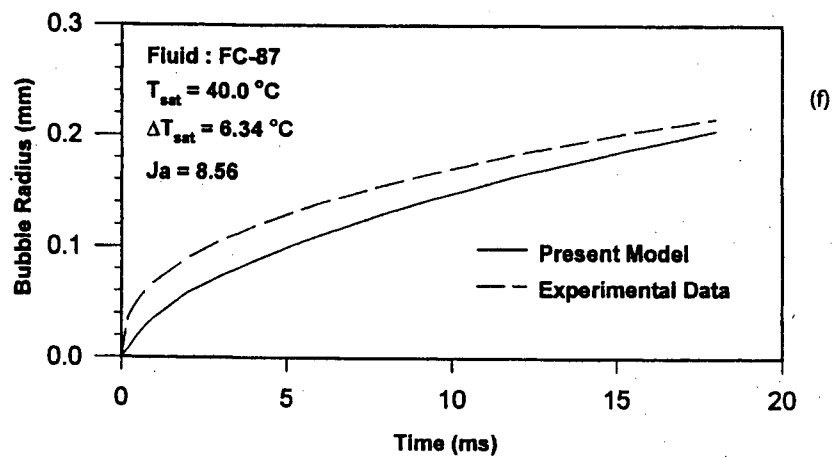
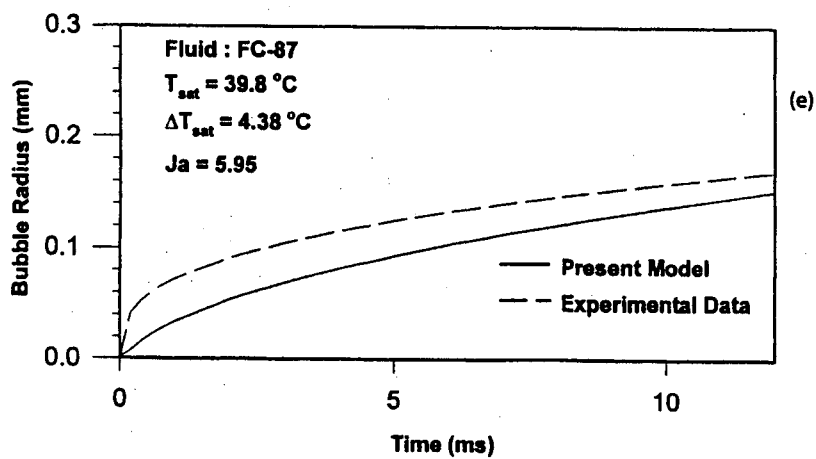
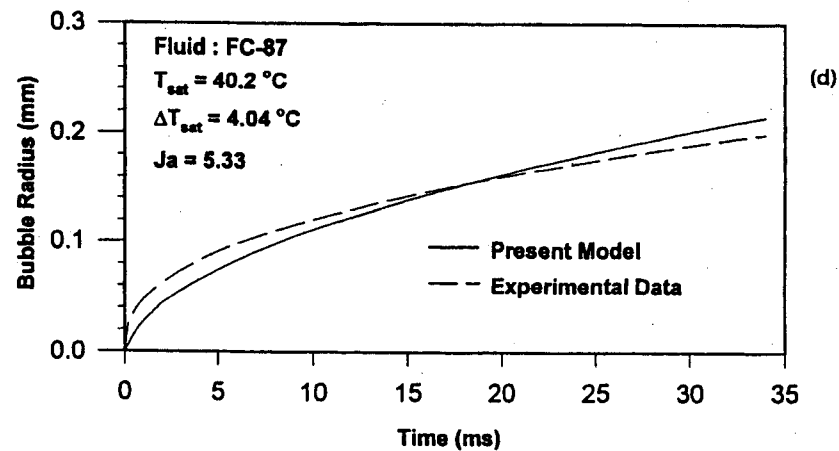
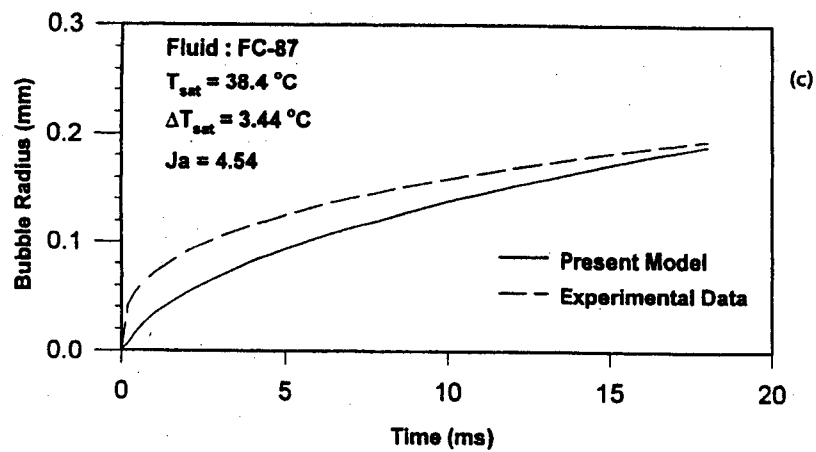


Fig. 4. Comparison between present predictions and experimental data of Thorncraft – FC-87 Forced convection boiling.



## Appendix A

### General Formulation

The objective of this appendix is to show that the methodology described in the main text can be easily extended to the most general treatment of a bubble growth or collapse problem. A complete set of governing equations consistent with the general interfacial conditions for mass, momentum and energy transports will be derived here. For this purpose consider the spherically symmetric growth or collapse of a single-component, single bubble originally at equilibrium with the surrounding liquid. Referring to Figure A.1, the origin of the coordinate system is the bubble center, which is at rest. The vapor bubble is assumed to be at uniform temperature, pressure and density. The gravitational effects on the bubble motion will be neglected. The liquid is assumed to be incompressible with constant thermophysical properties.

For an incompressible liquid and spherical symmetry, the differential form of the continuity equation is integrated from the bubble surface,  $r = R(t)$ , to  $r$  to yield:

$$V_f(r, t) = \left( \frac{R}{r} \right)^2 V_f(R, t) \quad \text{for} \quad r \geq R \quad (\text{A.1})$$

where  $V_f(R, t)$  is the liquid velocity at the bubble surface which will be identified as  $V_{fl}$ .

The volume integral of the continuity equation for the vapor from  $r = 0$  to  $r = R(t)$  results in

$$\frac{d}{dt} \left( \frac{\rho_g R^3}{3} \right) = -R^2 \dot{m}_{gi} \quad (\text{A.2})$$

where  $\dot{m}_{gi}$  is the mass flux of vapor at the interface. It is defined by

$$\dot{m}_{gi} = \rho_g (\vec{V}_{gi} - \vec{V}_i) \cdot \hat{n}_{gi} \quad (\text{A.3})$$

where  $\hat{n}_{gi}$  is the interfacial normal unit vector directed outward from the vapor phase.  $\vec{V}_{gi}$  and  $\vec{V}_i$ , respectively, are the vapor particle velocity at the interface and the interfacial velocity with  $\vec{V}_i \cdot \hat{n}_{gi}$  is begin the speed of displacement of the interfacial surface. For a spherically symmetric growth or collapse

$$\vec{V}_i \cdot \hat{n}_{gi} = \frac{dR}{dt} \equiv \dot{R} \quad (\text{A.4})$$

From Figure A.1 it is evident that  $\dot{m}_{gi} > 0$  for condensation, and  $\dot{m}_{gi} < 0$  for evaporation.

Equation (A.1) and (A.2) are matched at the interface by the interfacial mass balance equation. It is given by

$$\dot{m}_{fl} + \dot{m}_{gi} = 0 \quad (\text{A.5})$$

where  $\dot{m}_{fl}$  is the liquid mass flux at the interface and defined by

$$\dot{m}_{fi}'' \equiv \rho_f (\vec{V}_{fi} - \vec{V}_i) \cdot \hat{n}_{fi} \quad (\text{A.6})$$

where  $\vec{V}_{fi}$  is the liquid particle velocity at the surface whereas  $\hat{n}_{fi}$  is the interfacial normal unit vector outward from the liquid phase. From Figure A.1 it is evident that

$$\hat{n}_{fi} = -\hat{n}_{gi} \quad (\text{A.7})$$

In view of Eqs. (A.4) and (A.7), the liquid and vapor velocities at the interface can be obtained from Eqs. (A.6) and (A.3), respectively, as follows:

$$V_{fi} \equiv V_f(R, t) = \dot{R} + \frac{\dot{m}_{gi}''}{\rho_f} \quad (\text{A.8a})$$

and

$$V_{gi} \equiv V_g(R, t) = \dot{R} + \frac{\dot{m}_{gi}''}{\rho_g} \quad (\text{A.8b})$$

When the interfacial phase change is neglected then the interfacial phasic velocities become equal to the surface displacement velocity,  $\dot{R}$ . Other forms of interfacial phasic velocities can be formulated. For example from Eq. (A.2) and (A.8) it can be shown that the liquid velocity can be expressed as

$$V_{fi} = \left( \frac{1}{\rho_f} \right) \left[ \Delta \rho \dot{R} - \left( \frac{R}{3} \right) \frac{d\rho_g}{dt} \right] \quad (\text{A.9})$$

Finally, the liquid velocity distribution for  $r \geq R$  can be expressed from Eqs. (A.1) and (A.8) or (A.9) as follows:

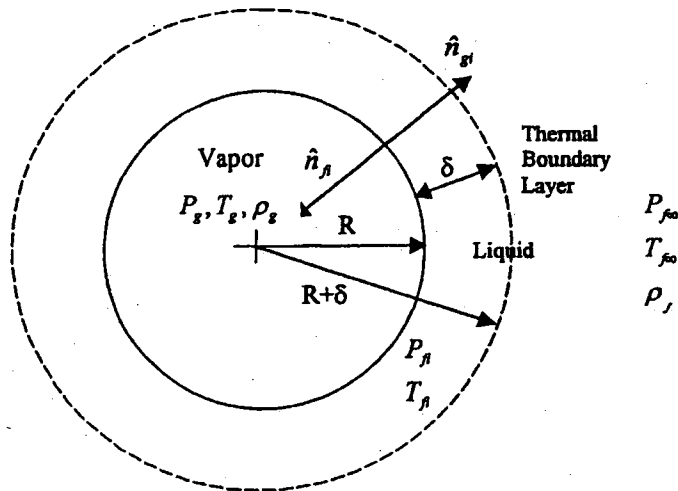


**Fig. A1.** Schematic description of spherically symmetric phase change problem.

$$V_f(r, t) = \left( \dot{R} + \frac{\dot{m}_{gi}}{\rho_f} \right) (R/r)^2 = \left( \frac{1}{\rho_f} \right) \left[ \Delta \rho \dot{R} - \left( \frac{R}{3} \right) \frac{d\rho_g}{dt} \right] \left( \frac{R}{r} \right)^2 \quad (\text{A.10})$$

It is interesting to note that when the vapor phase can be treated as an incompressible substance then the interfacial liquid velocity becomes

$$V_{fi} = \left( \frac{\Delta \rho}{\rho_f} \right) \dot{R} \quad (\text{A.11a})$$

Furthermore, for  $\Delta \rho / \rho_f = 1$ , the liquid velocity at the interface can be approximated by

$$V_{fi} \approx \dot{R} \quad (\text{A.11b})$$

The motion of the liquid is governed by the liquid phase momentum equation:

$$\frac{\partial \rho_f \vec{V}_f}{\partial t} + \nabla \cdot (\rho_f \vec{V}_f \vec{V}_f) = -\nabla P_f + \nabla \cdot \bar{\bar{\tau}}_f + \rho_f g \quad (\text{A.12})$$

where  $\bar{\bar{\tau}}_f$  is the viscous stress tensor. For spherical symmetry, incompressible Newtonian fluid with no external body forces, integrating the radial component of the liquid momentum equation from  $r = R(t)$  to  $r \rightarrow \infty$  one obtains

$$2 \dot{R} V_{fi} + R \left( \frac{dV_{fi}}{dt} \right) - \frac{V_{fi}^2}{2} = (P_{fi} - P_{f\infty}) / \rho_f \quad (\text{A.13})$$

where  $P_{fi}$  and  $P_{f\infty}$ , respectively, are the liquid pressure at the bubble surface and at a far distance from the bubble surface.

The dynamic field of the liquid motion is complemented by the interfacial momentum balance. In the absence of interfacial variation of the surface tensions, the interfacial momentum balance can be written as [42, 43]

$$\dot{m}_{gi} \vec{V}_{gi} + \dot{m}_{fi} \vec{V}_{fi} + P_{gi} \cdot \hat{n}_{gi} + P_{fi} \cdot \hat{n}_{fi} - \hat{n}_{gi} \cdot \bar{\bar{\tau}}_{gi} - \hat{n}_{fi} \cdot \bar{\bar{\tau}}_{fi} = (2\sigma/R) \hat{n}_{gi} \quad (\text{A.14})$$

Neglecting the vapor motion within the bubble and in view of the interfacial mass balance relation, Eq. (A.5), and Eqs. (A.7) and (A.8), the radial component of the interfacial momentum balance can be expressed by

$$P_{gi} - P_{fi} = \frac{2\sigma}{R} + \frac{4\mu_f}{R} V_{fi} - \left( \frac{\Delta \rho}{\rho_g} \right) \dot{m}_{gi} (V_{fi} - \dot{R}) \quad (\text{A.15})$$

Substituting  $P_{fi}$  from Eq. (A.15) into the integrated liquid momentum equation yields an equation governing the interfacial motion.

Thus,

$$\begin{aligned} \left( 2\dot{R} - \frac{1}{2}V_{fi} \right) V_{fi} + R \left( \frac{dV_{fi}}{dt} \right) - \left( \frac{\Delta\rho}{\rho_f \rho_g} \right) \dot{m}_{gi} (V_{fi} - \dot{R}) \\ + \left( \frac{4\mu_f}{R\rho_f} \right) V_{fi} + \frac{2\sigma}{R\rho_f} + \frac{P_{f\infty} - P_g}{\rho_f} = 0 \end{aligned} \quad (\text{A.16})$$

where an expression for the interfacial liquid velocity,  $V_{fi}$ , is provided by Eq. (A.8a).

In the studies of vapor bubble dynamics a special form of the liquid momentum equation is often used. With neglecting liquid viscosity and the interfacial mass flux and with the assumption of vapor incompressibility and  $\Delta\rho/\rho_f = 1$ , Eq. (A.16) reduces to

$$R\ddot{R} + \frac{3}{2}\dot{R}^2 = \frac{P_g - P_\infty}{\rho_f} - \frac{2\sigma}{R\rho_f} \quad (\text{A.17})$$

where Eq. (A.11b) is used for  $V_{fi}$ . Furthermore, by neglecting the effect of surface tension, then one obtains the well-known Rayleigh equation [2].

The differential form of the vapor enthalpy energy equation

$$\frac{\partial}{\partial t} (\rho_g h_g) + \nabla \cdot (\rho_g h_g \vec{V}_g) = \nabla \cdot \vec{q}_g + \frac{\partial P_g}{\partial t} + \vec{V}_g \cdot \nabla P_g + \overline{\vec{\tau}_g} : \nabla \vec{V}_g \quad (\text{A.18})$$

is integrated from  $r = 0$  to  $r = R$  to obtain the volume integral of the enthalpy equation. Thus,

$$\begin{aligned} \frac{d}{dt} \int_{V_g} \rho_g h_g dV = \frac{d}{dt} \int_{V_g} P_g dV \\ - 4\pi R^2 \left[ \dot{m}_{gi} h_{gi} + \vec{q}_{gi} \cdot \hat{n}_{gi} + P_{gi} (\vec{V}_i \cdot \hat{n}_{gi}) \right] + \int_{V_g} (\overline{\vec{\tau}_g} : \nabla \vec{V}_g) dV \end{aligned} \quad (\text{A.19})$$

where  $V$  is the volume of vapor bubble. Neglecting the vapor motion within the bubble and assuming uniform distribution of vapor properties, the volume integral of the vapor enthalpy balance becomes

$$\frac{d}{dt} \left( \frac{4}{3} \pi R^3 \rho_g h_g \right) = \frac{d}{dt} \left( \frac{4}{3} \pi R^3 P_g \right) - 4\pi R^2 \left[ \dot{m}_{gi} h_g + P_g (\vec{V}_i \cdot \hat{n}_{gi}) \right] \quad (\text{A.20})$$

The vapor enthalpy balance equation can be further simplified by using the vapor mass balance equation given by Eq. (A.12) and by expanding the enthalpy in terms of temperature and pressure. Thus,

$$\rho_g C p_g \frac{dT_g}{dt} = T_g \alpha_{gp} \frac{dp_g}{dt} \quad (\text{A.21})$$

where  $\alpha_{gp}$  is the coefficient of thermal expansion.

We turn our attention now to the energy equation in the liquid phase. For a spherical symmetry the equation for the temperature field in the liquid is

$$\frac{\partial T_f}{\partial t} + V_f \frac{\partial T_f}{\partial r} = \alpha_f \left[ \frac{1}{r^2} \frac{\partial}{\partial r} \left( r^2 \frac{\partial T_f}{\partial r} \right) \right] \quad (\text{A.22})$$

where  $\alpha_f$  is the thermal diffusivity of liquid. In writing this equation the viscous dissipation is neglected and material properties are assumed constant.

The energy integral equation is obtained by integrating Eq. (A.21) through the finite thermal boundary layer thickness of  $\delta(t)$  from  $r = R(t)$  to  $r = R(t) + \delta(t)$ ; thus,

$$\begin{aligned} \frac{d}{dt} \int_R^{R+\delta} T_f(r, t) r^2 dr &= \alpha_f \left[ (R + \delta)^2 \frac{\partial T_f}{\partial r} \Big|_{r=R+\delta} - R^2 \frac{\partial T_f}{\partial r} \Big|_{r=R} \right] \\ &+ (R + \delta)^2 T_f(R + \delta, t) \frac{d(R + \delta)}{dt} - R^2 T_f(R, t) \frac{dR}{dt} \\ &- R^2 V_{fi} [T_f(R + \delta, t) - T_f(R, t)] \end{aligned} \quad (\text{A.23})$$

where  $V_{fi}$  is specified by Eq. (A.10).

The liquid energy integral equation, Eq. (A.23), is dealt with in great detail in the text with a proper temperature profile and the time dependent interface temperature as well as the time dependent heat flux at the interface.

The vapor and liquid energetic field equations are complemented by the proper interfacial energy balance equation. The interfacial energy balance can be written as [42, 43].

$$\begin{aligned} \dot{m}_{gi} \left( u_{gi} + \frac{V_{gi}^2}{2} \right) + \dot{m}_{fi} \left( u_{fi} + \frac{V_{fi}^2}{2} \right) + \bar{q}_{gi} \cdot \hat{n}_{gi} + \bar{q}_{fi} \cdot \hat{n}_{fi} + P_{gi} \bar{V}_{gi} \cdot \hat{n}_{gi} \\ + P_{fi} \bar{V}_{fi} \cdot \hat{n}_{fi} - \left( \bar{\tau}_{gi} \cdot \bar{V}_{gi} \right) \cdot \hat{n}_{gi} - \left( \bar{\tau}_{fi} \cdot \bar{V}_{fi} \right) \cdot \hat{n}_{fi} = \left( \frac{2\sigma}{R} \right) \bar{V}_i \cdot \hat{n}_{gi} \end{aligned} \quad (\text{A.24})$$

where  $u$  is the specific internal energy. The enthalpy balance equation can be obtained from Eq. (A.24) by subtracting the interfacial mechanical energy balance equation from Eq. (A.20), where the mechanical energy balance equation can be obtained from the interfacial momentum balance equation given by Eq. (14). The enthalpy balance at the interface becomes

$$\begin{aligned} \dot{m}_{gi} \left[ h_{gi} + \frac{1}{2} (V_{gi} - V_i)^2 \right] + \dot{m}_{fi} \left[ h_{fi} + \frac{1}{2} (V_{fi} - V_i)^2 \right] + \bar{q}_{gi} \cdot \hat{n}_{gi} + \bar{q}_{fi} \cdot \hat{n}_{fi} \\ - \left[ \bar{\tau}_{gi} \cdot (\bar{V}_{gi} - \bar{V}_i) \right] \cdot \hat{n}_{gi} - \left[ \bar{\tau}_{fi} \cdot (\bar{V}_{fi} - \bar{V}_i) \right] \cdot \hat{n}_{fi} = 0 \end{aligned} \quad (\text{A.25})$$

Equation (A.25) is the interfacial enthalpy balance equation in its most general form. However, this expression can be simplified further by using the no-slip condition at the interface. With this no-slip condition imposed on the tangential component of interfacial velocities, it can be shown that Eq. (A.25) reduces to

$$\begin{aligned} \dot{m}_{gi} \left[ h_{gi} + \frac{1}{2} (\vec{V}_{gi} - \vec{V}_i)^2 - \frac{1}{\rho_g} (\vec{\tau}_{gi} \cdot \hat{n}_{gi}) \cdot \hat{n}_{gi} \right] + \dot{m}_{fi} \left[ h_{fi} + \frac{1}{2} (V_{fi} - V_i)^2 \right. \\ \left. - \frac{1}{\rho_f} (\vec{\tau}_{fi} \cdot \hat{n}_{fi}) \cdot \hat{n}_{fi} \right] + \vec{q}_{gi} \cdot \hat{n}_{gi} + \vec{q}_{fi} \cdot \hat{n}_{fi} = 0 \end{aligned} \quad (A.26)$$

The assumptions that the vapor motion and property variations within the bubble can be neglected and that the kinetic energy and viscous effects within the liquid phase are negligibly small when compared with the thermal energy result in a considerable simplification of the general interfacial enthalpy balance equation. With these simplification now we have:

$$\dot{m}_{gi} h_{gi} + \dot{m}_{fi} h_{fi} + k_f \left( \frac{\partial T_f}{\partial r} \right)_{r=R} = 0 \quad (A.27)$$

Finally, in view of Eq. (A.5) the thermal equilibrium condition at the interface yields

$$\dot{m}_{gi} h_{fg} + k_f \left( \frac{\partial T_f}{\partial r} \right)_{r=R} = 0 \quad (A.28)$$

where  $h_{fg}$  is the heat of evaporation. This is the form of the energy balance equation that has been used in the literature for the thermal equilibrium vapor bubble growth or collapse analysis.

The above set of equations consisting of Eqs. (A.1, A.2, A.5, A.8a, A.16, A.20, A.23, A.27) involves ten dependent variables,  $R(t)$ ,  $\delta(t)$ ,  $V_f(r, t)$ ,  $V_f(R, t)$ ,  $\dot{m}_{fi}$ ,  $\dot{m}_{gi}$ ,  $T_f(r, t)$ ,  $T_g(t)$ ,  $\rho_g(t)$  and  $P_g(t)$ . In order to complete the system of equations consistent with the number of dependent variables two more constitutive relations are needed. An equation of state for the vapor in the form of  $(\rho_g, P_g, T_g)$  should be specified. The other constitutive relation would be the specification of thermal nonequilibrium between liquid and vapor when  $T_{fi} \neq T_{gi}$ . In this case the net rate of mass transfer at the interface can be simplified on the basis of the elementary kinetic theory of gases. Nonequilibrium analyses of vapor bubble-growth and vapor bubble collapse have been treated, respectively, by Theofanous et al. [15] and [24], although their assumption of a thin thermal boundary layer is incorrect for the reasons stated in the text. In the case of thermal equilibrium at the interface the interfacial energy balance, Eq. (A.28) is used to determine the rate of interfacial phase change, the rate of evaporation or condensation.

In view of the proper formulation of a spherically symmetric phase change problem presented here, the methodology described in the text can be easily extended to the most general treatment of the growth or collapse of vapor bubbles. This methodology gives an insight in the physics, that is the importance of various parameters and processes which can be lost through the use of numerical solutions.

## Appendix B

### The Effect of the Erroneous Temperature Profile

It was noted in Section 3.2 that the energy integral method was used in references [15, 32, 34] to analyze bubble dynamics. The temperature profile assumed by these authors was given by Eq. (19). However, for reasons discussed in Section 3.2, this profile predicts *incorrect* results when applied to *spherical* geometry.

It is the purpose of this Appendix to compare the temperature gradients obtained from the two temperature profiles, i.e., from Eqs. (19) and (20), to those computed using the exact solution given by Eq. (11).

The temperature gradient of the spherical interface predicted by Eq. (19) is (see Eq. (38) in reference [34]):

$$\frac{R_s}{\Delta T} \left( \frac{\partial T}{\partial r} \right)_{r=R_s} = \frac{R_s}{\delta(t)} \quad (\text{B.1})$$

For a constant superheat temperature  $\Delta T$ , and for a stationary radius  $R_s$ , Eq. (19) yields, when inserted in the energy integral equation, the following differential equation for the thickness of the thermal boundary layer (see Eq. (33) in reference [34]):

$$\frac{1}{\delta} \frac{d\delta}{dt} \left[ \frac{1}{3} + \frac{1}{3} \left( \frac{\delta}{R_s} \right) + \frac{1}{10} \left( \frac{\delta}{R_s} \right)^2 \right] = \frac{2\alpha}{\delta^2} \quad (\text{B.2})$$

whence upon integration, we obtain an algebraic equation for the thickness of the thermal boundary layer  $\delta(t)$ , as a function of time:

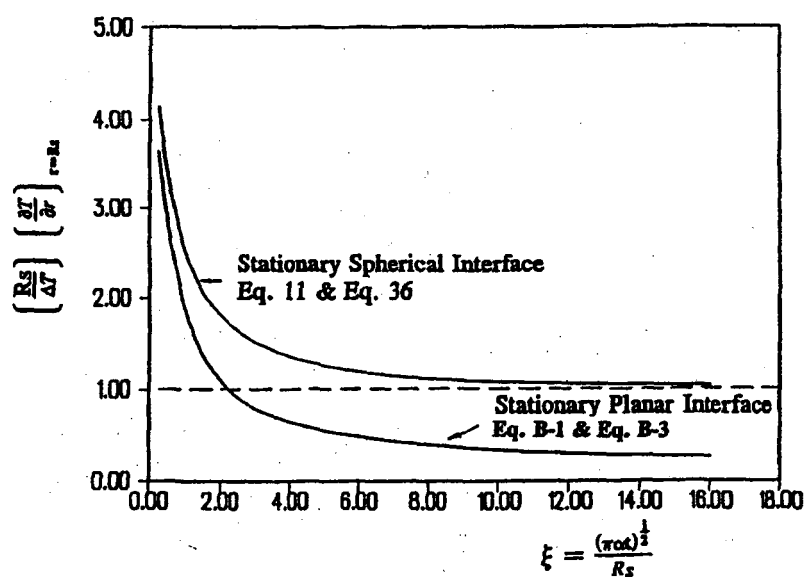


Fig. B1. Effect of the assumed temperature profile on the temperature gradient at the surface of a stationary sphere.

$$9 \left( \frac{\delta}{R_s} \right)^4 + 40 \left( \frac{\delta}{R_s} \right)^3 + 60 \left( \frac{\delta}{R_s} \right)^2 = \frac{720}{\pi} \left( \frac{\pi \alpha t}{R_s^2} \right) \quad (\text{B.3})$$

The numerical solution of this equation was inserted into Eq. (B.1) to obtain the relation between the temperature gradient and time which is plotted on Figure B1. The temperature gradients computed from Eq. (11) (obtained by exact methods) and from Eq. (36) (obtained by using the assumed profile, i.e., Eq. (20)) are also shown on Figure B1.

It can be seen that whereas the application of Eq. (20) yields excellent results, very poor agreement is obtained by using the temperature profile given by Eq. 19.

## Acknowledgment

This work was partially supported by the U.S. Department of Energy, Office of Basic Energy Science under Grant R.E. FG02-87 ER13764. The authors would like to express their sincere appreciation for the support.

## Nomenclature

- $b$  "area change" parameter defined by Eq. (42)
- $C_{p_f}$  specific heat of the liquid
- GM [ $R^2$ ] geometric mean value of  $R^2$ , defined by Eq. (7)
- $h_{fg}$  heat of evaporation
- Ja Jakob number, defined by Eq. (14)
- $k_f$  thermal conductivity of the liquid
- $R$  instantaneous radius of the bubble or of the drop
- $R_s$  radius of the stationary sphere
- $\bar{R}$  ideal gas constant for vapor
- RMS [ $R^2$ ] root mean square value of  $R^2$ , defined by Eq. (6)
- $r$  radial coordinate
- $r^*$  dimensionless radius, defined by Eq. (70)
- $\dot{q}_i$  radial heat flux at the interface
- $T$  liquid temperature
- $T_\infty$  liquid temperature at a great distance from the interface
- $T_i$  temperature at the interface
- $T_{\text{sat}}$  temperature at the saturation
- $t$  time
- $u$  function defined by Eq. (77) and (78)

## Greek Symbols

- $\alpha_f$  thermal diffusivity of the liquid
- $\epsilon$  dimensionless parameter, defined by Eq. (72)
- $\Delta$  differences of
- $\delta$  thickness of the thermal boundary layer
- $\delta_s$  thickness of the thermal boundary layer adjacent to stationary sphere
- $\rho_f$  density of the liquid



- $\rho_g$  density of the vapor  
 $\xi$  dimensionless length, defined by Eq. (23)  
 $\tau$  dimensionless parameter, defined by Eq. (71)  
 $\pi_1, \pi_2$  dimensionless parameters, defined by Eqs. (91) and (92), respectively.

## References

1. Besant, W. H., *Hydrostatics and Hydrodynamics*, Art. 158, Cambridge University Press, London, 1859.
2. Rayleigh, Lord, On the Pressure Developed in a Liquid during the Collapse of a Spherical Cavity, *Philosophical Magazine*, 1917, 34, 94–98.
3. Bosnjakovic, F., Verdampfung und Flussigkeitsuberhitzung, *Tech. Mech. Thermo-Dynamics*, 1930, 1, 358–362.
4. Jakob, M., *Zhurn. D. Ver. Deutch. Inq.*, 1932, 76, 1161 (*Heat Transfer*, John Wiley & Sons, New York, p. 267, 1949).
5. Fritz, W. and Ende, W., "Über den Verdampfungsvorgang nach kinematographischen" Aufnahmen an Dampfblasen, *Phys. Zeitsh.*, 1936, 37, 391–401.
6. Plesset, M. S. and Prosperetti, A., Bubble Dynamics and Cavitation, *Ann. Review Fluid Mechanics*, 1977, 9, 145–185.
7. Arndt, R. E. A., Recent Advances in Cavitation Research, *Advances in Hydrosience*, Academic Press, New York, 1981, 12, 1–78.
8. Plesset, M. S. and Zwick, S. A., The Growth of Vapor Bubbles in Superheated Liquids, *J. of Applied Physics*, 1954, 25, 493–500.
9. Forster, H. K. and Zuber, N., Growth of a Vapor Bubble in a Superheated Liquid, *J. of Applied Physics*, 1954, 25, 474–478.
10. Scriven, L. E., On the Dynamics of Phase Growth, *Chem. Engngr. Sci.*, 1959, 10, 1–13.
11. Bankoff, S. G., Diffusion-Controlled Bubble Growth, *Advances in Chemical Engineering*, 1966, 6, 1–60.
12. Lipkis, R. P., Liu, C., and Zuber, N., Measurement and Prediction of Density Transients in a Volume Heated Boiling System, *AIChE Chem. Engr. Prog. Symp. Ser.*, 1956, 52, No. 18, 105–113.
13. Zwick, S. A., Growth of Vapor Bubbles in a Rapidly Heated Liquid, *Phys. Fluids*, 1960, 3, 685–692.
14. Jones, O. C. Jr. and Zuber, N., Bubble Growth in Variable Pressure Field, *J. Heat Transfer*, 1978, 100, 453–459.
15. Theofanous, T., Biasi, L., Isbin, H. S., and Fauske, H., A Theoretical Study of Bubble Growth in Constant and Time-Dependent Pressure Fields, *Chem. Engngr. Sci.*, 1969, 24, 885–897.
16. Theofanous, T. G., and Patel, P. D., Universal Relations for Bubble Growth, *Int. J. Heat Mass Transfer*, 1975, 19, 425–429.
17. Mikic, B. B., Rosenhow, W. M., and Griffith, P., On Bubble Growth Rates, *Int. J. Heat Mass Transfer*, 1970, 13, 657–662.
18. Inoue, A. and Aoki, S., On the Dynamics of Bubble Growth under Time Dependent Pressure Field, *Bull. Tokyo Inst. Technol.*, 1975, 127, 25–43.
19. Cha, Y. S. and Henry, R. E., Bubble Growth During Decompression of a Liquid, *J. Heat Transfer*, 1981, 103, 56–60.
20. Toda, S. and Kitamura, M., Bubble Growth in Decompression Fields, *Proc. ASME – JSME Thermal Engineering Joint Conference*, ASME, New York, 1983, 3, 395–402.

21. Wang, Z. and Bankoff, S. G., Bubble Growth on a Solid Wall in a Rapidly – Depressurizing Liquid Pool, *Int J. Multiphase Flow*, 1991, 17, 425-437.
22. Plesset, M. S. and Zwick, S. A., On the Dynamics of Small Vapor Bubbles in Liquid, *J. Mathematics and Physics*, 1955, 32, 309-314.
23. Florschuetz, L. W., and Chao, B. T., On the Mechanics of Vapor Bubble Collapse, *J. Heat Transfer*, 1965, 87, 209-220.
24. Theofanous, T. B., Biasi, L., Isbin, H. S., and Fauske, H. K., A Non-Equilibrium Bubble Collapse: A Theoretical Study, *Chem. Engr. Symp. Series*, 1970, 66, 102, 37-47.
25. Birkhoff, G., Margulies, R. S., and Horning, W. A., Spherical Bubble Growth, *Physics of Fluids*, 1958, 1, 201-204.
26. Plesset, M. S. and Zwick, S. A., On the Dynamics of Small Vapor Bubbles in Liquid, *J. of Applied Physics*, 1955, 23, 95-98.
27. Carslaw, H. S. and Jaeger, Y. C., *Conduction of Heat in Solids, Second Edition*, Oxford University Press, London, 1959, p. 338.
28. Forster, H. K., 1957, Diffusion in a Moving Medium with Time-Dependent Boundaries, *AIChE Journal*, 3, 535-538.
29. Arpaci, V. S., *Conduction Heat Transfer*, Addison-Wesley Pub. Co., 1966.
30. Fuks, N. A., *Evaporation and Droplet Growth in Gaseous Media*, Pergamon Press, New York, 1959.
31. Goodman, T. R., The Heat Balance Integral and its Application to Problems Involving a Change of Phase, *ASME Transactions*, 1959, 80, 335-342.
32. Veinik, A. I., *Approximate Calculation of Heat Conduction Processes*, Gosud. Energet. Izdat., Moscow, 1959.
33. Goodman, T. R., Application of Integral Methods to Transient Nonlinear Heat Transfer, *Advances in Heat Transfer*, T. F. Irvine and J. P. Hartnett, Eds., Academic Press, New York, 1964, 1, 51.
34. Bornhorst, W. J., and Hatsopoulos, G. N., Analysis of a Liquid Vapor Phase Change by the Methods of Irreversible Thermodynamics, *J. of Applied Mechanics, ASME Transactions-Series E*, 1967, 34, 840-846.
35. Sparrow, E. M., Discussion of "The Melting of Finite Slabs", by T. R. Goodman and J. J. Shea, *J. of Applied Mechanics, ASME Transactions-Series E* 82, 1960, 27, 598.
36. Lardner, T. J., and Pohle, F. V., Application of the Heat Balance Integral to Problems of Cylindrical Geometry, *Journal of Applied Mechanics, ASME Transactions*, 1961, 28, 310-312.
37. Epstein, P. S. and Plesset, M. S., On the Stability of Gas Bubbles in Liquid-Gas Solutions, *J. Chem. Phys.*, 1950, 18, 1505-509.
38. Plesset, M. S., The Dynamics of Cavitation Bubbles, *J. of Applied Mechanics*, 1949, 16, 277-282.
39. Levenspiel, Collapse of Steam Bubbles in Water, *Ind. Eng. Chem.*, 1959, 51, 787-790.
40. Hewitt, H. G., and Parker, J. D., Bubble Growth and Collapse in Liquid Nitrogen, *J. Heat Transfer*, 1968, 90, 22-26.
41. Wittke, D. D. and Chao, B. T., Collapse of Vapor Bubbles with Translatory Motion, *J. Heat Transfer*, 1967, 89, 17-24.
42. Kocamustafaogullari, G., *Thermo-Fluid Dynamics of Separated Two-Phase Flow*, Ph. D. Thesis, School of Mechanical Engineering, Georgia Institute of Technology, 1971.
43. Delhay, J. M., Jump Conditions and Entropy Sources in Two-Phase Systems, Local Instant Formulation, *Int. J. Multiphase Flow*, 1974, 1, 395-409.
44. Thorncroft, G. E., *Heat Transfer and Vapor Bubble Dynamics in Forced Convection Boiling*, Ph. D. Dissertation, University of Florida, Gainesville, Florida, 1997.

## 16. MECHANISTIC MODELING OF DROPLET SIZE DISTRIBUTION IN ANNULAR TWO-PHASE FLOW

G. Kojasoy, S. R. Smits and J. Razi

Department of Mechanical Engineering

University of Wisconsin-Milwaukee, Milwaukee, WI 53201, U.S.A.

### Abstract

The initial drop size in an annular flow which is determined in terms of the mechanism of droplet generation by shearing off of roll-wave crests by gas flow can be larger than the maximum stable droplet size in forced convection pipe flow. In this case the droplet size is further determined by droplet disintegration mechanism. Disintegration of droplets in a gas stream has been studied by a number of researchers. Several disruptive mechanisms of droplet break-up have been suggested. Each of these controlling mechanisms was evaluated as applied to the annular flow. It was concluded that in a case of partial entrainment the maximum size of a fluid particle was mainly controlled by the action of the dynamic force a fluid particle experiences in a relative motion. Based on this dynamic force and the stabilizing effect of surface tension, a detailed method for predicting the maximum droplet size in annular flow was presented. The correlations for the representative droplet mean diameters as well as the size distribution were then developed. A comparison with experimental data covering a wide range of fluid and flow variables indicated that indeed the postulated droplet disintegration mechanism was the dominant factor in determining the drop size.

### 16.1. Introduction

The initial droplet size in an annular flow is determined in terms of the mechanism of droplet generation such as shearing off of roll-wave crests forming on a thin liquid film by a streaming gas flow, Kataoka *et al.* [1]. From annular flow visualization studies of Whalley *et al.* [2], it was observed that the droplets emerge from a roll-wave. However, the largest droplets with a diameter larger than the maximum stable size start oscillating for a while, and suddenly, irrespective of their position in the tube cross-section, a higher frequency oscillation starts that results in the break-up of the droplet in a short period of time. Lopes and Dukler's [3] local

droplet size measurements confirmed qualitative observations of Whalley *et al.* that the average drop size decreases towards the center of the annular two-phase flow column. These experimental findings are a clear indication that the droplet size in an annular flow is not determined at the time of entrainment. It is mainly controlled by the mechanics of the gas-droplet interaction in the turbulent gas stream.

For the purpose of providing basic information on the maximum size a droplet can reach, a number of processes which may cause break-up of droplets in a gas flow have been studied by several investigators, and a number of disruptive force mechanisms of the droplet break-up have been identified in the literature. Each of these controlling mechanisms was tested by Lopes and Dukler [3] against their experimental air/ water data. It was concluded that the maximum droplet size in an annular flow is mainly controlled by the action of forces resulting from the pressure fluctuations of the turbulent flow of the gas around a droplet. Based on the theory presented by Kolmogorov [4], Lopes and Dukler suggested a simple predictive method for the droplet size. The method incorporated a critical Weber number of 0.194 determined from their air/water data at about atmospheric conditions. In the present study, the Sauter mean droplet sizes predicted by the Lopes and Dukler method were compared using the recent data of Jepson *et al.* [5, 6], where the property effects such as the surface tension and the fluid density ratios were investigated systematically. The method gave a reasonably good estimate of droplet sizes for those data where the density ratios are comparable to the atmospheric air/water system. However, differences between predictions and the experimental data became larger and larger as the density ratio moves away from the air/water density ratio of atmospheric conditions.

In view of the above comparison, an investigation has been undertaken to clarify the property effects on the droplet disintegration in an annular flow. This paper which summarizes our findings has three objectives. Based on the competing forces between stabilizing surface stresses and the disruptive dynamic force exerted on a particle partially entrained by the surrounding fluids, the first objective is to develop a method to describe the break-up of entrained droplets in the gas core of an annular flow. The second objective is to develop an experimentally based simple correlation for the maximum stable size a droplet can reach in a turbulent flow field. Finally, the third objective is to extend the maximum droplet size predictions to obtain the droplet size distribution as well as mean droplet sizes.

## 16.2. Mechanistic Modeling of Droplet Break-Up

A generalized break-up mechanism can be expressed as a balance between external stresses,  $\tau$ , and the surface stress,  $\sigma/(d/2)$ , where ( $J$  is the surface tension and  $d$  is the droplet diameter). These stresses influence both the size of droplets which are torn away from their point of formation and also the maximum droplet size which is stable in the flow field. Therefore, the stability condition can be characterized by the ratio of the external stresses and surface stress by a suitably chosen Weber number. The critical Weber number above which the droplet is no longer stable is defined as

$$We_c \equiv \frac{\tau d_{\max}}{2\sigma} \quad (1)$$

where  $d_{\max}$  is the maximum stable droplet size.

Basically there are two external disruptive stresses that are involved in the breaking up of particles, namely, viscous and dynamic stresses. The relative order of magnitude of these stresses is determined by the ratio of length scales,  $d_{\max}/\lambda$ , where  $\lambda$  is the internal length scale of local turbulence for the equilibrium range (usually called the Kolmogorov microscale). When  $d_{\max} \leq \lambda$  viscous forces play a dominant role. In this case, the phenomena associated with the break-up of a drop or a bubble are similar to those investigated by Taylor [7]. In most applications, the particle Reynolds numbers which are characteristic of the internal flow field are much greater than unity so viscous effects are negligible. In this case, the disruptive dynamic forces and stabilizing surface tension are dominant in the process of fluid particle break-up.

The disruptive forces may develop either through the local relative motion around the droplet, or through the changes in eddy velocities over the length of a droplet. For both cases, however, the external stress appearing in equation (1) can be expressed in terms of the kinetic energy differences around the droplet. From equation (1), the former yields

$$We_{cr)1} = \rho_c u_{r) \max}^2 d_{\max} / 2\sigma \quad (2)$$

whereas the latter gives

$$We_{cr)2} = \rho_c \overline{u_c^2} d_{\max} / 2\sigma \quad (3)$$

The mean-square spatial fluctuating velocity term,  $\overline{u_c^2}$ , describes the turbulent pressure forces of eddies of size  $d_{max}$  and is defined as the average of the square of the differences in velocity over a distance equal to the fluid particle diameter.  $u_{r)max}$  is that limiting local relative velocity at which a fluid will flow around a particle suspended in it. The subscript c identifies the continuous phase.

Considering the simplest case of turbulence, namely, an isotropic homogeneous turbulence, the main contribution to the kinetic energy,  $\overline{u_c^2}$ , is made by the fluctuations in the region of wavelength where the Kolmogorov energy distribution is valid. In this region the local turbulence pattern is solely determined by the energy dissipation rate per unit mass,  $\varepsilon$ . The mean square velocity difference,  $\overline{u_c^2}$ , between two points,  $d_{max}$ , is given by Batchelor [8] as follows:

$$\overline{u_c^2} \sim (\varepsilon d_{max})^{2/3} \quad (4)$$

whereas  $u_{r)max}$  is given by Levich [9] as

$$u_{r)max} \sim [\varepsilon d_{max} (\rho_d / \rho_c)]^{1/3} (|\Delta\rho| / \rho_a)^{1/2} \quad (5)$$

where the subscript  $d$  identifies the dispersed phase.

When equations (4) and (5) are inserted into their respective places in equations (2) and (3), the following critical Weber numbers can be obtained:

$$We_{cr)2} = k_2 \rho_c \varepsilon^{2/3} d_{max}^{5/3} / \sigma \quad (6)$$

and

$$We_{cr)1} = k_1 \rho_c \varepsilon^{2/3} d_{max}^{5/3} (\rho_d / \rho_c)^{2/3} (|\Delta\rho| / \rho_a) / \sigma \quad (7)$$

where  $k_1$  and  $k_2$  are proportionality coefficients. The numerical coefficients probably have no great significance. They are set forth here only in order to stress the absence in these formulas of large numerical coefficients. Both  $k_1$  and  $k_2$  are the same order of one.

Equations (6) and (7) can be used to determine the maximum fluid particle size as follows:

$$d_{max} = (\sigma We_{cr)2} / k_2 \rho_c)^{3/5} \varepsilon^{-2/5} \quad (8)$$

and

$$d_{max} = (\sigma We_{cr)1} / k_1 \rho_c)^{3/5} \varepsilon^{-2/5} (\rho_d / \rho_c)^{2/5} (|\Delta\rho| / \rho_a)^{-3/5} \quad (9)$$

Both equations relate the maximum stable bubble or drop diameter to the energy dissipation rate of  $\varepsilon$  and the surface tensions but differ in their functional dependence on the fluid densities. These equations have previously been used to describe liquid-liquid and gas-liquid dispersions in horizontal pipelines, but their application to liquid-gas droplet systems has not been evaluated for a wide range of fluid properties. Sevik and Park [10] were able to predict, theoretically, the value of  $We_{cr2} = 1.24$  for the air bubbles in a water jet and  $We_{cr2} = 0.52$  for the case of liquid droplets in turbulent liquid of equal density. These numerical values of the critical Weber number are remarkably good for the air/water bubbly flow experimental observations of Sevik and Park and for the liquid-liquid dispersions experiments of Hinze [11]. As mentioned above, however,  $We_{cr2} = 0.194$  obtained for water droplets in turbulent air stream by Lopes and Dukler [3] does not give good results in the whole experimental range of Jepson *et al.* [5, 6], where the density ratio ranged from  $\rho_d/\rho_c = 550$  to 3700. The discrepancy can be explained by comparing the expression for fluid velocity relative to the particle,  $u_{r,max}$ , with the change in velocity of turbulence eddies over a distance equal to the dimension  $d_{max}$  of the particle,  $(\overline{u_c^2})^{1/2}$ .

A comparison of equations (4) and (5) shows, that, when  $\rho_d \leq \rho_c$  (gas bubbles or lighter liquid droplets in a surrounding liquid),  $u_{r,max} \ll (\overline{u_c^2})^{1/2}$ . In this case, large-scale eddies of continuous phase completely entrain the fluid particle together with portions of fluid adhering to it, and transfer both as a single unit. The entrainment of particles by turbulent eddies is complete. Therefore, the second Weber number criterion,  $We_{cr2}$ , which is based on  $\overline{u_c^2}$ , mechanistically describes the fragmentation of drops and bubbles in a turbulent liquid flow for  $\rho_d \leq \rho_c$ .

However, the disintegration of a drop in a turbulent gas stream, i.e. where the density of the medium is low as compared to that of the liquid within the drop, occurs in a somewhat different way. In this case, the entrainment of particles by turbulence eddies cannot be complete. The smaller-scale fluid motions are unable to entrain the particle, and in relation to them, the particle acts as a motionless solid body. The fluid participating in these small-scale motions flows over the surface of the particle. In this case, the local relative velocity given by equation (5) plays an important role in the mechanism of the drop's disintegration. In the case of  $\rho_d \gg \rho_c$ , from equations (4) and (5) it is evident that

$$u_{r,max} / (\overline{u_c^2})^{1/2} \approx (\rho_d / \rho_c)^{1/3} \quad (10)$$

which indicates that  $u_{r)max}^2 \gg \overline{u_c^2}$ . Therefore, the disruptive forces based on  $u_{r)max}$  become much larger than the disruptive forces generated by changes in eddies. In this case, the first critical Weber number criterion  $We_{cr)1}$ , describes the disintegration of drops in a turbulent gas stream. This is the mechanistic approach that will be taken in the remaining part of this paper.

### 16.3. Maximum Droplet Size Correlation

In view of the above discussion, equation (9) describes the maximum droplet size in an annular flow as a function of the local energy dissipated by the turbulence and the physical properties of the fluids. Considering the fact that  $\rho_d \gg \rho_c$ , equation (9) can be simplified as follows:

$$d_{max} = (\sigma We_{cr)1} / k_1 \rho_g)^{3/5} (\rho_g / \rho_f)^{2/5} \epsilon^{-2/5} \quad (11)$$

where the subscripts c and d identifying the continuous and dispersed phase, respectively, are replaced by the subscripts f and g for the liquid and gaseous phases.

In a pipeline the local energy dissipation rate,  $\langle \epsilon \rangle$ , is equal to the average energy dissipation rate,  $(e)$ , and approximated by Lopes and Duckier [3] as follows:

$$\langle \epsilon \rangle \approx (\langle j_g \rangle / \rho_g) (-dP/dz)_f = (\langle j_g \rangle / \rho_g) (4\tau_i / d_h) \quad (12)$$

where  $\langle j_g \rangle$ ,  $(-dP/dz)_f$ ,  $\tau_i$  and  $d_h$ , respectively, are the average superficial gas velocity, frictional component of the axial pressure gradient, interfacial shear and, the hydraulic diameter of flow channel. With equation (12) for  $\epsilon$ , the maximum stable droplet size can be calculated from equation (11) as follows:

$$d_{max} = We_{cr)1}^{3/5} (\sigma / k_1 \rho_g)^{3/5} (\rho_g / \rho_f)^{2/5} [(\langle j_g \rangle / \rho_g) (4\tau_i / d_h)]^{-2/5} \quad (13)$$

Ishii and Grolmas [12] slightly modified Wallis' [13] interfacial shear correlation, and derived the following expression for the annular flow.

$$\tau_i = 0.0428 (C_g C_w)^{2/3} Re_f^{1/6} Re_g^{-2/3} (\rho_g / \rho_f)^{1/3} (\mu_f / \mu_g)^{2/3} (\rho_g \langle j_g \rangle^{2/3}) \quad (14)$$

where  $C_g$  is a constant coefficient, and  $C_w$  is given in terms of the viscosity number as follows:

$$C_w = 1/35.34 N\mu^{4/5} \quad \text{for} \quad N\mu \leq 1/15 \quad (15a)$$

and



$$C_w = 0.25 \quad \text{for} \quad N\mu > 1/15 \quad (15b)$$

where the viscosity number,  $N\mu$ , is defined by

$$N\mu \equiv \mu / [\rho_f \sigma (\sigma / g \Delta \rho)^{1/2}]^{1/2} \quad (16)$$

Finally, substituting equation (14) into equation (13) for  $\tau_i$  and rearranging the resulting equation, an expression for the maximum drop diameter can be obtained.

$$d_{\max} = 2.673 [We_{cr1}^{3/5} / C_g^{4/5} k_1^{3/5}] (\sigma / \rho_g < j_g >^2)^{3/5} \times (Re_g^4 / Re_f)^{1/15} [(\rho_g / \rho_f)(\mu_g / \mu_f)]^{4/15} d_h^{2/5} \quad (17)$$

In terms of dimensionless groups, equation (17) can be expressed as follows:

$$d_{\max}^* = 2.673 [We_{cr1}^{3/5} / C_g^{4/5} k_1^{3/5}] We_m^{-3/5} (Re_g^4 / Re_f)^{1/15} [(\rho_g / \rho_f)(\mu_g / \mu_f)]^{4/15} \quad (18a)$$

or

$$d_{\max}^* = 2.673 [We_{cr1}^{3/5} / C_g^{4/5} k_1^{3/5}] K \quad (18b)$$

where  $K$  is defined by

$$K = C_w^{-4/15} We_m^{-3/5} (Re_g^4 / Re_f)^{1/15} [(\rho_g / \rho_f)(\mu_g / \mu_f)]^{4/15} \quad (19)$$

In the above equations,  $d_{\max}^*$  is the dimensionless drop diameter, and  $We_m$  is a modified Weber number based on macroscopic variables. They are defined by:

$$d_{\max}^* \equiv d_{\max} / d_h \quad \text{and} \quad We_m \equiv \rho_g d_h < j_g >^2 / \sigma \quad (20)$$

The foregoing expressions describe the maximum droplet size as a function of the liquid and gas phase Reynolds numbers, modified Weber number and the dimensionless physical property groups. For practical applications, the proportionality constant in the above equation should be correlated in collaboration with experimental data.

Several experiments have been carried out to study droplet size distributions in annular two-phase flow [14-17]. Among these available data, only the Lopes and Dukler [3] data were used for the correlation purpose. There are several reasons for this preference, (1) In their study the actual measured maximum drop diameters were listed together with the statistically determined diameter, (2) They carefully distinguished the maximum diameter measurements in the core from those measured close to the interface. (3) Finally, there was no way of assessing the statistical reliability of the values of  $d_{\max}$  measured experimentally. However, Lopes and Dukler's measured  $d_{\max}$  values were close to the statistically expected  $d_{\max}$  values, It is then expected that

the values of measured  $d_{\max}$ , represent well the maximum probable diameter within a reasonable accuracy. Figure 1 shows the dimensionless experimental maximum diameter vs a new dimensionless variable,  $K$ .

Most of the data in Fig. 1 fall within  $\pm 15\%$  of the following correlation

$$d_{\max}^* = 2.609 C_w^{-4/15} We_m^{-3/5} (Re_g^4 / Re_f)^{1/15} [(\rho_g / \rho_f)(\mu_g / \mu_f)]^{4/15} \equiv 2.609 K \quad (21)$$

Several observations can be made with respect to equation (21).

(1) The drop size decreases with increasing superficial gas velocity,  $d_{\max} \sim \langle j_g \rangle^{-14/15}$ . Given that the critical Weber number identifies the maximum stable drop size permissible by balancing the disruptive local inertial and stabilizing surface tension forces, increasing the gas velocity will cause a decrease in drop size. The power of  $\langle j_g \rangle$  is in line with the previous experimental results of the volume median diameter,  $d_{vm} \sim \langle j_g \rangle^{-n}$  where the power  $n$  is between 0.8 (Linstead *et al.* [18] and Tatterson [16]), and 1.2 (Wicks and Dukler [14, 15] and Cousins and Hewitt [17]), This tendency is also similar to the experimental results of Jepson *et al.* [5, 6] where the Sauter mean diameter of droplets decreases approximately to the 1.2 power of the gas flux. The above correlation yields a power of  $n = 14/15$  which is within the range of previously reported experimental observations.

(2) The drop size slightly decreases with increasing superficial liquid velocity,  $d_{\max} \sim \langle j_g \rangle^{-1/15}$ . Experimental observations of Cousins and Hewitt [17], Wicks and Dukler [14, 15], Pogson *et al.* [19], Tatterson [16], Azzopardi *et al.* [20-22] and Lopes and Dukler [3] indicate that the average droplet size is almost independent of the liquid flow rate. These experimental observations are consistent with the present correlation where a very weak dependence with a power of  $-1/15$  can be found. However, recent experimental observations of Jepson *et al.* [5, 6] indicate that for increasing liquid mass flux, the Sauter mean diameter shows a minimum for the air/water system, continuously decreases with the He/water and increases for the air/ $CH_3CCl_3$  system. Azzopardi *et al.* [22] and Jepson *et al.* related this mean droplet size dependence on the liquid flow rate to the interfacial shear and droplet concentration in the gas core, and, hence, the droplet coalescence resulting in increased droplet size. In the above derivations, none of these effects were considered. Recent experimental observations of Kocamustafaogullari *et al.* [23] for air/ water bubbly flow in horizontal pipelines showed a very strong dependence of the mean bubble size with void fraction. These observations are consistent

with the hypothesis of refs. [5,6,22]. The above derivations leading to the maximum stable size correlation considered a single liquid particle in a gas stream. Presently an analytical study has been initiated to relate the turbulence level to the volumetric concentration of the dispersed phase. Hopefully this study will clarify the above disagreements of the mean droplet size dependence on the liquid flow rate.

(3) Equation (21) indicates that the maximum stable diameter increases with increasing pipe size,  $d_{max} \sim d_h^{3/5}$ . This is consistent with the experimental observations of Veda [24] with 10 and 30 mm pipe sizes. However, it contradicts experimental results of Azzopardi *et al.* [20-22], who performed experiments in two different pipe diameters, 22 mm and 125 mm. It is to be noted that at the lower end the pipe sizes of both investigators are comparable. On the other hand, the pipe size used by the latter was much higher than the former although the gas superficial velocities used by both investigators were comparable ( $\langle j_g \rangle = 20 - 85$  m/s used by Ueda and  $\langle j_g \rangle \approx 24 \sim 64$  m/s used by Azzopardi *et al.*). By the time the tube diameter reaches 125 mm many phenomena in gas-liquid flow are altered. For example, the wave structure is changed. It is not surprising, therefore, that results in this large tube diameter show different effects. Drop size measurements with a more systematic pipe size change would be desirable in order to resolve the controversy and to test further the proposed mechanism and the method outlined here to predict droplet size.

(4) Irrespective of whether equation (15a) or (15b) is used for  $C_w$ , the maximum stable droplet size from equation (21) varies slightly with the liquid viscosity, and does not depend on the gas viscosity. The viscous forces within the droplet increases its stability, and become important when they are the same order of magnitude as the surface tension forces. By comparing the number mean diameters measured for annular flows by Pogson *et al.* [19] and by Namie and Veda [25] for liquid viscosities of 0.28 and 1.0 mN s m<sup>-2</sup>, Tatterson *et al.* [26] found no appreciable influence of liquid viscosity. The agreement with respect to the liquid viscosity dependence is particularly encouraging since the experiments cover a wide range of liquid viscosities.

(5) Finally, comparing equations (18) and (21), one obtains

$$2.673 We_{cr)1}^{3/5} / C_g^{4/5} k_1^{3/5} = 2.609 \quad (22)$$

The order of magnitude of the critical Weber number can be estimated as follows. According to Kataoka *et al.* [1], the value of  $C_g$  is approximately 300 or less. From Levich [9],  $k \leq 1.0$ . Using these values, the critical Weber number can be calculated from equation (22) as

$$We_{cr1} \leq 12.2 \quad (23)$$

Comparing equations (8) and (9) yields

$$We_{cr2} \approx k_2 (\rho_c / \rho_d)^{2/3} (\Delta \rho / \rho_d) We_{cr1} \quad (24)$$

For air/water annular flow at about 1.2 atm pressure with  $k_2 \approx 1.0$ , which is the value used by Lopes and Dukler [3], equation (24) yields

$$We_{cr2} \approx 0.17 \quad (25)$$

which is very close to the value of 0.194 correlated by Lopes and Dukler. Thus, the critical Weber number value based on the Kolmogorov [4] theory is recovered. This suggests that the interfacial shear used in the above derivations was correct for the air/water annular flow although its utility, as discussed in the second section may cause some problems for a wide range of fluid properties.

The maximum stable droplet sizes predicted by equation (21) are compared in Figs. 2(a)-(c), where the liquid Reynolds number is treated as a parameter. Considering the origin of the above correlation coming from the Lopes and Dukler data, a good agreement between the predictions and experimental data of Lopes and Dukler is not surprising. The Cousins and Hewitt data are overpredicted by the present correlation whereas the Wicks data are under-predicted. It is to be noted here that the highest drop sizes appearing in the list of ref. [17] were considered to be the maximum drop sizes in this comparison. As noted above, however, there was no way of assessing the statistical reliability of the values of  $d_{max}$  measured experimentally. The data presented in Figs. 2(a)-(c) show no systematic dependence of  $d_{max}$  on the liquid flow rate, although the newly developed correlation indicates a weak dependence. Considering the range of data fluctuations in Figs. 2(b)-(c), the agreement between the predictions and experimental measurements is fairly good.

## 16.4. Droplet Size Distribution

### 16.4.1. Volume Distribution Function

Mugelc and Evans [27] analyzed several size distribution formulas for dispersed materials, and their application to spray data. A modification of the log- probability equation, called the upper-limit log- normal distribution equation, was developed and proposed as a standard for describing droplet size distributions in sprays. It introduced a new and physically significant parameter,  $d_{max}$ , the maximum stable droplet diameter, for which an expression was developed above.

The upper-limit log-normal distribution advanced by Mugele and Evans for atomizing jets has been used with relative success by several investigators [1, 3, 14- 16, 18,26,28] in annular dispersed flow. It is given in the following form:

$$\frac{dv}{d\xi} = (\mu / \sqrt{\pi}) \exp(-\eta^2 \xi^2) \quad (26)$$

where  $v$  is the volume fraction of droplets having diameter less than the droplet diameter,  $d$ ,  $\eta$  is the size distribution parameter, and  $\xi$  is the dimensionless function of  $d$  defined as

$$\xi = \ln(ad / (d_{max} - d)) \quad (27)$$

The drop size measurements of refs. [3, 14--18] which had a large enough sample size were used to determine  $a$  and  $\xi$ . The data were fitted to an upper limit, log-normal distribution. Two typical examples of such a fit are illustrated in Figs. 3(a) and (b) for several runs of Lopes and Dukler [3], and Cousins and Hewitt [17]. In these plots,  $d_{max}$  represents the maximum expected diameter. The parameters  $a$  and  $\eta$  were determined as follows:

$$a = (d_{max} - d_{50}) / d_{50} \quad (28)$$

and

$$\eta = \frac{0.394}{\log \left\{ \frac{d_{90} / (d_{max} - d_{90})}{d_{50} / (d_{max} - d_{50})} \right\}} \quad (29)$$

where  $d_{50}$  and  $d_{90}$  are 50th and 90th percentiles which were read from Fig. 3(a).

It is important to notice from Fig. 3(a) that the values of  $a$  and  $\eta$  are not completely independent of flow variables. There is a systematic shift on the data points as  $\langle j_g \rangle$  varies. Similar shifts can also be observed from Fig. 3(b) as  $\langle j_g \rangle$  varies, although the shift is not as consistent as that seen in Fig. 3(a).  $\eta$  and  $a$  would be only weakly dependent on flow variables. For practical purposes, they are treated constant in the present study.

The experimental data collected from various sources were analyzed in the same way as shown in Figs. 3(a) and (b) to determine  $\alpha$  and  $\eta$  values for each set. Then the results were averaged to obtain  $\alpha = 1.93$  and  $\eta = 0.75$ . Therefore, one obtains a correlation for droplet distribution as

$$\frac{dv}{d\xi} = (0.75 / \sqrt{\pi}) \exp(-0.563\xi^2) \quad (30)$$

with

$$\xi = \frac{1.93d}{d_{\max} - d} \quad (31)$$

The above correlation for the droplet size distribution implies that the distribution can be uniquely determined by the maximum stable diameter which is a function of the gas and liquid properties and their respective flow rates as indicated by the correlation for  $d_{\max}$  given by equation (21).

#### 16.4.2. Mean Droplet Sizes

By knowing the droplet size distribution, one may calculate expressions for the mean diameters according to the upper-limit log-normal distribution. The Sauter mean diameter,  $d_{32}$  and the volume median diameter,  $d_{vm}$ , can be easily derived in terms of the maximum stable droplet diameter. They are given by

$$d_{\max} / d_{vm} = 2.93 \quad \text{and} \quad d_{\max} / d_{32} = 4.01 \quad (32)$$

These equations can be used together with  $d_{\max}$  correlation given by equation (21) to derive expressions for  $d_{vm}$  and  $d_{32}$ . They are given in dimensionless form as follows:

$$d_{vm} / d_h = 0.90 C_w^{-4/15} We_m^{-3/5} (Re_g^4 / Re_f)^{1/15} [(\rho_g / \rho_f)(\mu_g / \mu_f)]^{4/15} \equiv 0.90K \quad (33)$$

and

$$d_{32} / d_h = 0.64 C_w^{-4/15} We_m^{-3/5} (Re_g^4 / Re_f)^{1/15} [(\rho_g / \rho_f)(\mu_g / \mu_f)]^{4/15} \equiv 0.64K \quad (34)$$

The above equations are compared with experimentally measured mean diameters of several investigators [5, 6, 12-14] in Figs. 4(a)-5(c). The conditions of these experiments are described in Table 1. Figure 4(a) illustrates such a comparison in terms of the volume median diameters whereas Fig. 4(b) shows a comparison in terms of the Sauter mean diameter. Figures 5(a)-(c)

illustrate more detailed comparison with Jepson *et al.* data covering a wide range of physical properties of fluids.

The Cousins and Hewitt data compare fairly well with predictions. Wicks' data are consistently under-estimated by the present correlation in the range of lower values of  $K$  in Fig. 4(a). However, a systematic similarity in tendency between predictions and measurements of  $d_{vm}$  is a strong indication that the mechanistic model used here to derive the maximum stable droplet size properly accounts for the essentials of the droplet break-up process. Tatterson's data show much higher spread with the measurement of  $d_{vm}$ . There may be several reasons for the apparent but consistent discrepancies.

(1) Still photography was used by Cousins and Hewitt for upward flow of air and water in a circular channel of 9.5 mm. Wicks [14] and Wicks and Dukler [15] used an electrical conduction probe technique for the downward flow of air and water in a rectangular channel, 150 mm wide and 19 mm deep. The probe consists of two needles pointing at each other in the air stream containing droplets. By varying the spacing between the needle tips, the functionality between the counting rate and distance of separation was determined, and the drop size distribution was extracted from these results by numerical methods. Tatterson applied an electrical probe technique to measure drop sizes for air/water flow in a horizontal rectangular channel 25 mm deep and 305 mm wide. The signal from the probe was analyzed electrically to get the drop size distribution. From these experimental techniques, those based on photographic data are certainly the most reliable. The probe techniques used by Wicks and Tatterson consistently yield higher droplet sizes as compared to the predictions.

(2) Both Wicks' and Tatterson's experimental test section consisted of rectangular channels. One possibility of the apparent but consistent disagreement on the  $d_{vm}$  is that the interfacial shear used for the present correlation might not have been proper for the rectangular flow channels. However, as the mechanistic model implies, the similarity in tendency would indicate that the drop size is not very sensitive to the flow orientation.

(3) As demonstrated by Lopes and Dukler [3], the place where the droplet size sampling is made in the annular core is very important in the droplet size measurements since the average drop size decreases towards the center of the annular two-phase column. It is evident, therefore, that any droplet size measurement close to the interface will yield higher average droplet sizes.

This may also be an important factor for the obvious but consistent disagreement shown in Fig. 4(a).

The overall agreement in Fig. 4(b) is particularly encouraging since the experiments cover a large range of physical property group from 540 to 3700 for  $(\rho_f/\rho_g)$  and the modified Weber number group from 125 to 3285. Considering the experimental uncertainties involved in the droplet size measurements, the predicted mean droplet sizes agree reasonably well with those measured sizes. This indicates that the principle mechanisms involved in the droplet break-up process were properly accounted for in the development of the theoretical model.

Figures 5(a)-(c) compare the predicted dependence of the Sauter mean drop diameter on liquid and gas Reynolds number with the drop size data for the fluid systems air/ $\text{CH}_3\text{CCl}_3$ , air/water and He/water. All systems show the drop size decreasing with increasing gas Reynolds number as predicted. However, there is a general disagreement in terms of the liquid Reynolds number dependence. The experimental observations of Jepson *et al.* indicate that for increasing  $Re_f$ , the Sauter mean diameter shows a minimum for air/water system, a continuous decrease with He/water and an increase for air/ $\text{CH}_3\text{CCl}_3$  system, whereas the predictions show a slight decrease with  $Re_f$ . As discussed in the Mechanistic Modeling of Droplet Break-up section, this apparent disagreement may be attributed to the insensitivity of the interfacial shear stress,  $\tau_i$ , to the different entrainment mechanisms and of the droplet volumetric concentration. It is believed that both of these factors play important roles in determining the mean droplet size in an annular flow. More specifically, mechanistic interfacial shear expressions which can be used for a wide range of flow variables are needed. Presently an analytical study is underway to clarify the above disagreements.

## 16.5. Summary and Conclusions

Two Weber number criteria, one based on the classical Kolmogorov theory and the other on Levich's theory, were discussed and compared to each other. It was concluded that when  $\rho_d \ll \rho_c$ , the entrainment of fluid particles by turbulence may be complete, and that Weber number criterion based on Kolmogorov's theory mechanistically describes the fragmentation of drops and bubbles in a turbulent liquid flow. However, in the case of droplets in a gas stream with  $\rho_d \gg \rho_c$ ,



the entrainment of droplets by turbulent eddies cannot be complete, and relative motions play a major role instead of eddies in the mechanism of droplet disintegration.

Based on the competing stresses between stabilizing surface forces and disruptive dynamic forces, a theoretical model was developed to describe the break-up of entrained droplets in the gas core of an annular flow. The experimental data of the maximum droplet size were correlated in terms of  $Re_g$ ,  $Re_f$ ,  $We_m$  and the physical property groups of  $(\rho_f/\rho_g)$ ,  $(\mu_f/\mu_g)$  and  $N\mu$ . Effects of each group in determining the maximum stable droplet size were discussed in the context of available experimental data. It was concluded that the functional dependence of  $d_{max}$  on these groups could be experimentally verified. Contradictory experimental data on pipe size and liquid flow dependency indicate that drop size measurements with a larger range of flow channel sizes and of liquid flow rates would, however, be desirable in order to test further the proposed mechanism and the method outlined to predict droplet size. In particular, it is essential to obtain more and more detailed data on droplet size at various portions after droplet entrainment.

An upper limit log-normal volume distribution function was fitted to the experimental data with distribution parameters  $a = 1.93$  and  $\eta = 0.75$ . Based on these parameters, predictive equations were developed for the most representative mean droplet sizes, the volume median diameter and Sauter mean diameter. The predicted mean droplet sizes were found to agree reasonably well with those measured mean sizes. This indicates that the principal mechanisms involved in the droplet break-up process in a turbulent gas stream were properly accounted for in the development of the theoretical model.

### Acknowledgements

This work was supported by the U.S. Department of Energy, Office of Basic Energy Science under Grant D, E, FG02-87ER 13764. The authors would like to express their sincere appreciation for the encouragement, support and technical comments on this program from Dr O.P. Maley of U.S. DOE/BES.

### Nomenclature

- $a_w$  roll wave amplitude
- $C_g$  coefficient in equation (16)

$C_w$	coefficient defined by equation (15)
$d$	spherical droplet diameter
$d_h$	hydraulic diameter of flow channel
$d_{max}$	maximum spherical bubble diameter
$d_{sm}$	Sauter mean diameter of droplets ( $= d_{32}$ )
$d_{vm}$	volume median diameter of droplets
$j$	superficial velocity
$K$	dimensionless quantity defined by equation (19)
$p$	pressure
$Re_f$	liquid Reynolds number ( $\equiv \rho_f d_h \langle j_f \rangle / \mu_f$ )
$Re_g$	gas Reynolds number ( $\equiv \rho_g d_h \langle j_g \rangle / \mu_g$ )
$u$	velocity
$\overline{u_c^2}$	mean square fluctuation velocity difference between two points at a distance $d_{max}$
$u_{r,max}$	maximum value of local relative velocity
$We_{cr}$	critical Weber number
$We_m$	modified Weber number
$z$	axial coordinate

#### Greek Symbols

$\delta$	average liquid film thickness
$\Delta\rho$	density difference
$\varepsilon$	energy dissipation rate per unit mass
$\eta$	distribution parameter in upper limit, log-normal distribution
$\lambda$	scale of local turbulence
$\mu$	dynamic viscosity
$\xi$	parameter defined by equation (31)
$\rho$	density
$\sigma$	surface tension
$\tau$	external stresses

- $\tau_i$      interfacial shear stress
- $v$        normalized volume of droplet in distribution.

#### Subscripts

- c       continuous phase
- d       dispersed phase
- f       liquid phase
- g       gas phase.

#### Symbols

- <>     area-averaged value.

#### References

1. I, Kataoka, M, Ishii and K. Mishima, Generation and size distribution of droplet in annular two-phase flow, *J. Fluid Engng* 105,230-238 (1983).
2. P. B. Whalley, G, F, Hewitt and J. W. Terry, Photo-graphic studies of two-phase flow using a parallel light technique, UKAEA Report, AERE-R9389 (1979).
3. J. C, B, Lopes and A, E, Dukler, Droplet sizes, dynamics and deposition in vertical annular flow, University of Houston Report, NUREG/CR-4424 (1985).
4. A, N, Kolmogorov, On the disintegration of drops in a turbulent flow, *Doklady Akad. Nauk.*, SSSR 66, 825- 833 (1949).
5. D, M, Jepson, B, J. Azzopardi and p, B, Whalley, The effect of gas properties on drops in annular flow, *Intl. J. Multiphase Flow*, 15, 327-339 (1989).
6. D. M. Jepson, B. J. Azzopardi and p, B, Whalley, The effect of physical properties on drop size in annular flow, *Proc. Ninth Int. Heat Transfer Conf*, Vol, 6, pp, 95-100 (1990).
7. G. I. Taylor, The formation of emulsion in definable field of flow, *Proc. Royal Soc, (Lon.)* A164, 501-507 (1934).
8. G. K, Batchelor, Pressure fluctuations in isotropic turbulence, *Proc, Cambridge Phil. Sac.* 47, 359-374 (1951)
9. V. G, Levich, *Physicochemical Hydrodynamics*, Prentice Hall, Englewood Cliffs, New Jersey (1962).
10. M, Sevik and S, H, Park, The splitting of drops and bubbles by turbulent fluid flow, *J. Fluids Engng* 95, 53- 59 (1973).
11. J. O. Hinze, Fundamentals of the hydrodynamic mechanism of splitting dispersion processes, *A.I.Ch.E. Jl* 1, 289-295 (1955).
12. M. Ishii and M. A. Grolmes, Inception criteria for drop- let entrainment in two-phase concurrent film flow, *A.I.Ch.E. Jl* 21,308-316 (1975).
13. G. B. Wallis, *One Dimensional Two-Phase Flows*, McGraw-Hill, New York (1969).
14. M. Wicks, Liquid film structure and drop size distribution in two-phase flow, Ph.D. Dissertation, University of Houston, Houston. Texas (1967).

15. M. Wicks and A. E. Dukler. In situ measurements of drop size distribution in two-phase flow. a new method for electrically conducting liquids, *Int. Heat Transfer Conf.*, Chicago, Illinois (1966).
16. D. F. Tatterson, Rates of atomization and drop size in annular two-phase flow, Ph.D. Dissertation. University of Illinois, Illinois (1975).
17. L. B. Cousins and G. F. Hewitt, Liquid phase mass transfer in annular two-phase flow: droplet deposition and liquid entrainment, UKAEA Report, AERE-R5657 (1968).
18. R. D. Linstead, D. L. Evans. I. Gass and R. V. Smith. Droplet and flow pattern data. vertical two-phase (air- water) flow using axial photography, Wichita State University, Department of -Mechanical Engineering (1978).
19. J. T. Pogson, I. H. Roberts and P. I. Whibler. An investigation of the liquid distribution in annular-mist flow, *J. Heat Transfer* 92, 651-658 (1970).
20. B. J. Azzopardi, G. Freeman and D. I. King, Drop sizes and deposition in annular two-phase flow, UKAEA Report, AERE-R9634 (1980).
21. B. J. Azzopardi, G. Freeman and P. R. Whalley, Drop sizes in annular two-phase flow, UKAEA Report. AERE-R9074 (1978).
22. B. J. Azzopardi, S. Taylor and D. B. Gibbons, Annular two-phase flow in a large diameter tube, *Proc. Int. Conf. on the Physical Modeling of Multiphase Flow*, BHRA Fluid Engineering, Coventry, England (1983).
23. G. Kocamustafaogullari, W. D. Huang and I. Razi. Measurement and modeling of average void fraction bubble size and interfacial area. *J. Nucl. Engng Design* (in press).
24. T. Ueda, Entrainment rate and size of entrained droplets in annular two-phase flow, *Bull. JSME* 22, 1258-1265 (1979).
25. S. Namie and T. Ueda, Droplet transfer in two-phase annular mist flow, *Bull. JSME* 15, 1568~1565 (1972).
26. D. F. Tatterson, J. C. Dallman and T. J. Hanratty. Drop sizes in annular gas-liquid flows. *A.I.Ch.E. J* 23, 68-76 (1977).
27. R. A. Mugele and H. D. Evans. Droplet size distribution in sprays, *Ind. Engng Chern.* 43, 1317-1324 (1951).
28. P. Andreussi, G. Romero and S. Zanelli, Drop size distribution in annular-mist flows. *First Int. Conf. on Liquid Atomization and Spray Systems*, Tokyo, Japan (1978).

Table 1. Summary of various experiments on droplet mean diameters

Source	Fluids	Flow channel	Flow direction	Experimental technique	$Re_g \times 10^{-3}$	$Re_f \times 10^{-3}$	$We_m$	$\rho_l/\rho_g$	$\mu_l/\mu_g$	$N\mu \times 10^3$
Wicks and Dukler [15], Wicks [14]	Air/Water	19 x 150 mm channel ( $d_h = 33.7$ mm)	Vertical down	Electrical conductance	66-170	0.75-3.9	320-4100	750	54	2.24
Cousins and Hewitt [17]	Air/Water	9.5 mm ID tube	Vertical up	Photographic	36-62	0.60-4.0	276-850	420	54	2.24
Tatterson [16]	Air/Water	25 x 30.5 mm channel ( $d_h = 46.2$ mm)	Horizontal	Electrical conductance	101-182	0.85-3.9	880-2900	725	54	2.24
Lopes and Dukler [3]	Air/Water	50.74 mm ID tube	Vertical up	Laser optical	52-96	1.7-7.0	180-560	760	54	2.26
Jepson <i>et al.</i> [5]	Air/Water	10.26 mm ID tube	Vertical up	Laser diffraction	22-67	0.41-1.5	125 ~ 1130	555	54	2.24
Jepson <i>et al.</i> [6]	He/Water	10.26 mm ID tube	Vertical up	Laser diffraction	63-108	0.41-1.5	75-218	3700	52	2.24
Jepson <i>et al.</i> [5]	Air/CH <sub>2</sub> Cl <sub>2</sub>	10.26 mm ID tube	Vertical up	Laser diffraction	26-78	0.92-1.8	365-3285	540	50	4.17

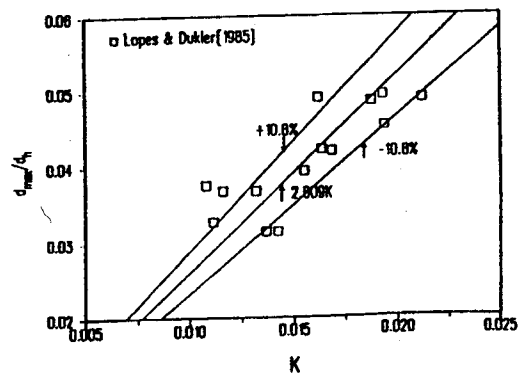


Fig. 1 Maximum diameter vs dimensionless fluid property and flow variable groups

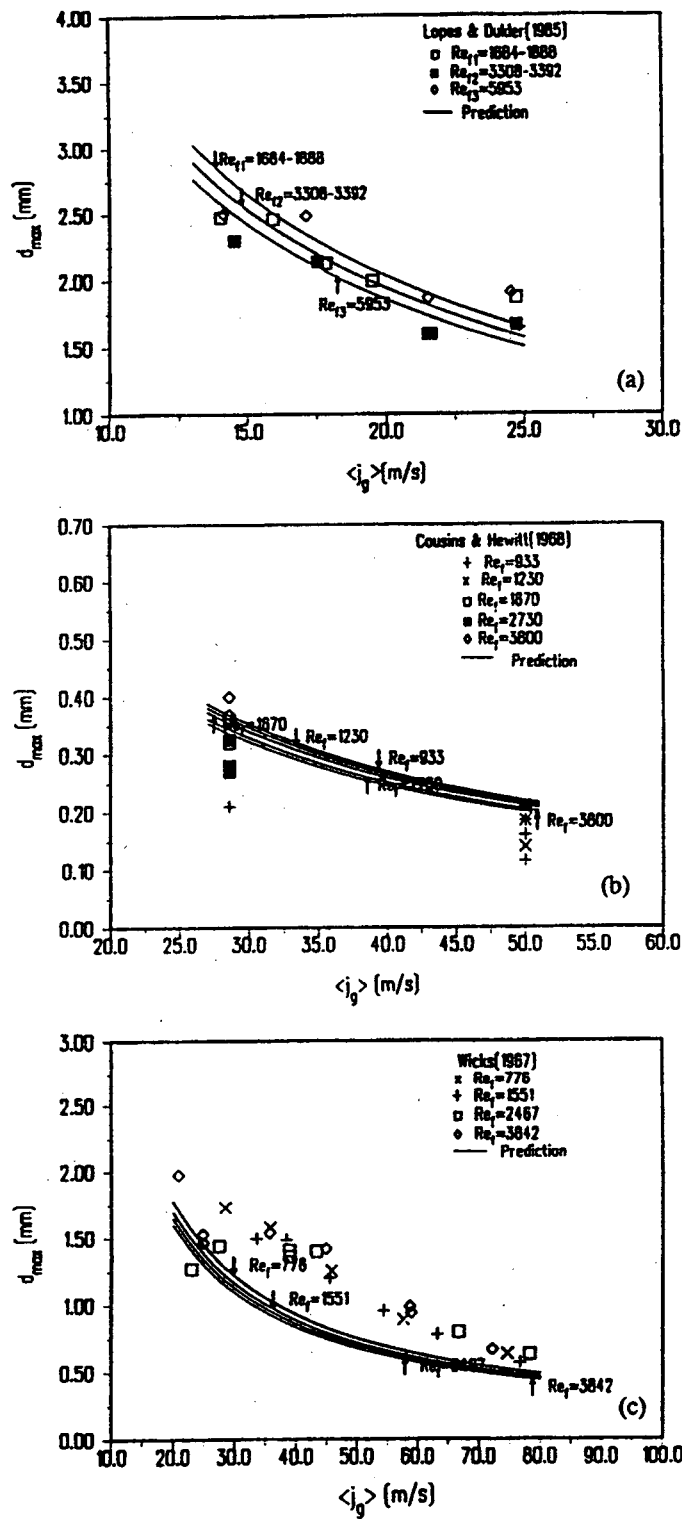


Fig. 2 Theoretical and experimental values of the maximum stable droplet diameter:  
(a) Lopes and Dukler[3]; (b) Cousins and Hewitt[17]; (c) WICKS[14]

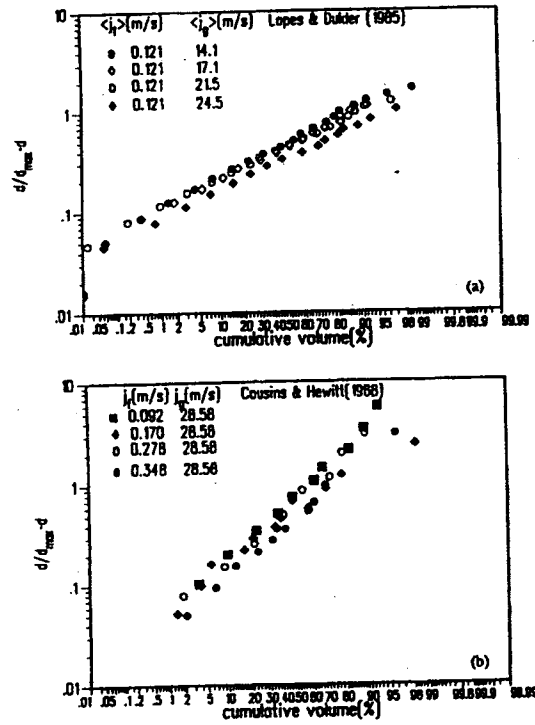


Fig. 3 Example of upper limit, log-normal distribution:  
(a) Lopes and Dukler [3]; (b) Cousin and Hewitt [17]



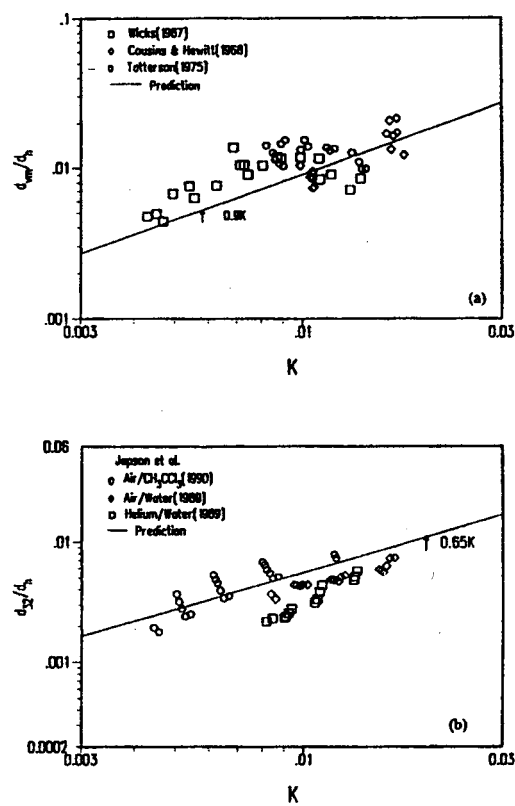


Fig. 4. Theoretical and experimental values of Sauter mean diameters:  
(a) volume median diameter; (b) Sauter mean diameter.

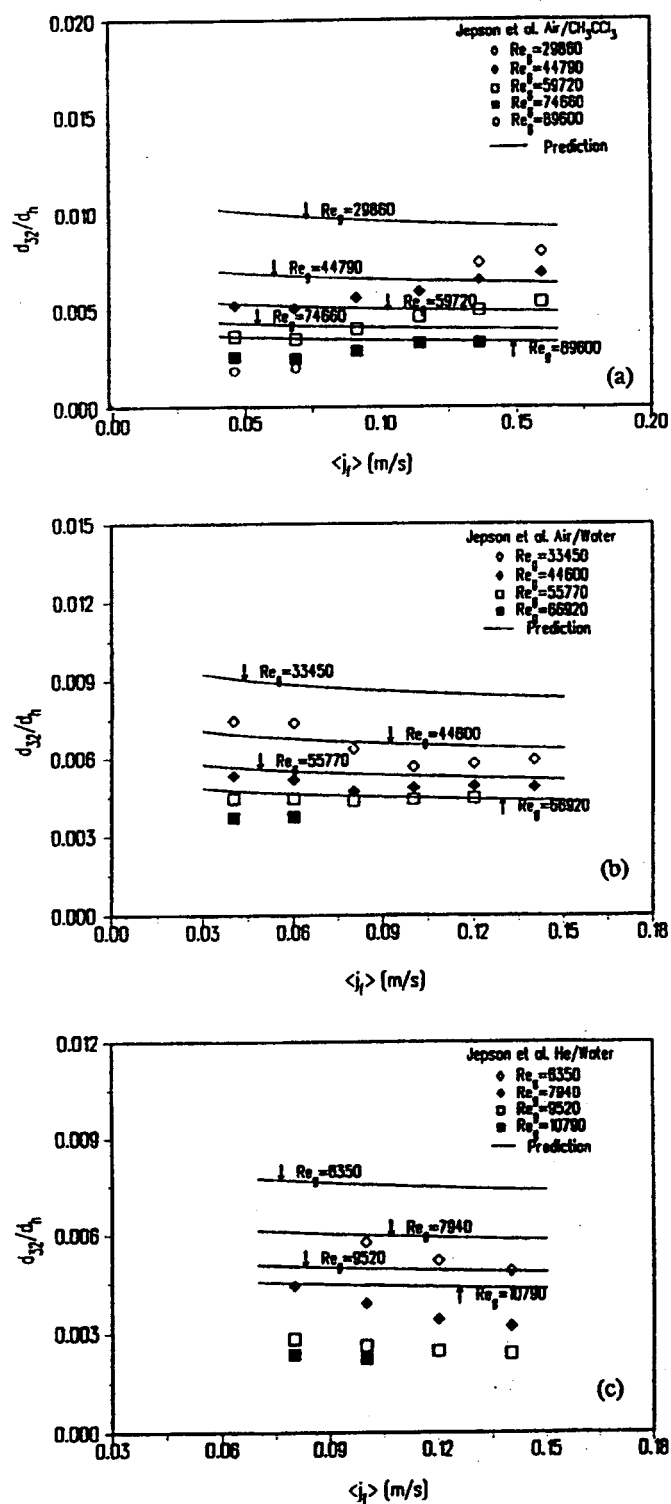


Fig. 5 Comparison between predicted and measured Sauter mean diameters:  
 (a) air/ $\text{CH}_3\text{CCl}_3$  data, Jepson et al. [5]; (b) air/water data, Jepson et al. [5];  
 (b) (c) He/water data, Jepson et al. [6]

## 17. BREAK-UP CRITERIA FOR FLUID PARTICLES

### BUBBLES AND DROPLETS

J. Kitscha, S. Burli and G. Kojasoy

Department of Mechanical Engineering

University of Wisconsin-Milwaukee

Milwaukee, WI 53201, U.S.A.

#### ABSTRACT

A simple mechanistic model is developed based on the combination of Kelvin-Helmholtz and Rayleigh-Taylor instability theory to describe the breakup of freely rising or falling fluid particles, i.e., bubbles and drops. The breakup is predicted to occur if the growth rate of interfacial waves on the leading front is faster than the rate at which waves propagate around the interface to the side of the particle. Based on this theoretical model and available experimental data, simple correlations are developed to predict the maximum size a fluid particle can reach. Predicted values of the breakup diameter are compared with experimental data for cases of freely rising bubbles, falling drops in gas, and freely falling or rising drops in immiscible liquids. The results are extended to predict the maximum droplet size in a high velocity gas field which is the most interesting case in terms of practical applications. Good agreement between predicted values and experimental data indicates that the principal mechanisms involved in the fluid particle breakup process are properly accounted for by the proposed model.

## 17.1. Introduction

Breakup size of fluid particles, bubbles and drops, in dispersed two-phase flow systems including the liquid-liquid particulate systems is an important factor in determining the fluid particle size distribution and, hence, the effectiveness of the interfacial transport of mass, momentum and energy. A knowledge of disintegration of bubbles and drops is essential to the eventual understanding of the interfacial transfer mechanisms and two-phase flow-pattern transitions in a large number of engineering applications. These include gas-liquid droplet systems, such as atomizers, dryers, absorbers, wet steam separators and cryogenic heat exchangers, liquid-liquid droplet systems, such as liquid-liquid extractors, separators used with distillation columns, and packed towers when the packing is not wetted by the dispersed phase, and finally liquid-gas (or vapor bubbly systems), such as boiling water and pressurized boiling water reactors, boilers, flash distillation and aeration units etc. Although drops and bubbles seldom occur in isolation in such systems, it is essential to understand the behavior of a single fluid particle before a full knowledge of interacting bubbles and drops can be achieved.

For the purpose of providing basic information on the maximum size a fluid particle can reach, a number of processes which may cause breakup of fluid particles have been identified in the literature. The most important breakup mechanisms are classified as rapid accelerations, high shear stresses, and turbulent fluctuations in the surrounding continuous fluid.

The breakup mechanism in a rapidly accelerating gas applies to drops suddenly exposed to a high velocity gas stream. According to this mechanism, gas flowing over the surface of a liquid droplet causes the dynamic pressure

normal to the surface of the droplet to be nonuniform, resulting in a deformation of the liquid droplet. If the pressure forces cause a distortion severe enough to overcome the surface tension force, the liquid drop will eventually split. Large free-falling drops in still air, or somewhat smaller drops in a steady stream of air, were first considered by Lenard [1]. Since then this breakup process has been studied both experimentally and theoretically. Results of various experimental investigations can be expressed by a simple Weber number criterion, indicating that drops will break when

$$We_{cr} \equiv \frac{\rho_c (d_e)_{\max} (u_c - u_d)^2}{\sigma} = \text{constant} \quad (1)$$

where  $(u_c - u_d)$  is the relative velocity between continuous and the particulate phase,  $(d_e)_{\max}$  is the maximum volume-equivalent drop diameter,  $\sigma$  is the surface tension, and  $\rho_c$  is the mass density of the continuous phase.

From the data of Merrington and Richardson [2], Hinze [3] has estimated the constant appearing in Eq. (1) to be 13.0 for low-viscosity liquids. This may be compared with the value of 10.6 from the data of Lane [4], 10.3 for mercury drops in air, obtained by Haas [5], and 7.2 to 16.8 (with an average of 13.0) for water, methyl alcohol, and a low-viscosity silicone obtained by Hanson et al. [6]. Subsequently Hinze [7] and Brodkey [8] considered the effect of viscosity and suggested that the critical Weber number should be function of dispersed phase viscosity instead of a constant. They proposed an empirical relation expressed by

$$We_{cr} = We_{cr} |_{\mu=0} [1 + f(N'_{\mu d})] \quad (2)$$

where  $N_{ud} \equiv \nu_d / [\rho_d (d_e)_{\max} \sigma]^{1/2}$  is the dispersed phase modified viscosity number, and  $We_{cr} |_{\nu=0}$  is the value of the critical Weber number for vanishing viscosity effect of the drop, which is equal to the constant appearing in (1). The data of Hanson et al. [6] give only a qualitative support to the effect, but do not agree in detail.

The second breakup mechanism, the breakup in high shear stresses, applies to fluid particles surrounded by viscous fluid where there exists strong velocity gradient in the vicinity of the particle. In this case the continuous fluid Reynolds number is so small that the dynamic forces are no longer important, and the breakup is controlled by the viscous shear and surface tension forces. If the viscous shear force is large enough, the interfacial forces are no longer able to maintain the fluid particle intact, and it ruptures into two or more smaller particles.

The first fundamental work on splitting of drops and bubbles under the action by surface tension and viscous forces were performed by Taylor [9]. Taylor made numerous experimental observations, many of which subsequently explained by Tomotika [10]. According to the Taylor's findings, the breakup of the fluid particle occurs at a critical value of the Weber number based on the velocity gradient defined as

$$We_v \equiv \frac{\nu_c S (d_e)_{\max}}{\sigma} \quad (3)$$

Where  $S$  is the maximum velocity gradient in the continuous flow field. Taylor has studied the deformation of a single drop as a function of  $S$ ; he determined the value of  $S$  at which the breakup of the drop occurs.

Taylor's theory has been modified over the years by Rumscheidt and Mason [11], Karam and Bellinger [12], Buckmaster [13]. For example, Rumscheidt and

Mason proposed that breakup occurs if  $We_v$  exceeds a critical value given by

$$We_v = \frac{1 + (\mu_d/\mu_c)}{1 + (19/16)(\mu_d/\mu_c)} \quad (4)$$

which varies only between 1.0 and 0.82 as  $(\mu_d/\mu_c)$  varies from zero to infinity.

Finally, according to the third breakup mechanism, disintegration due to external flow turbulent fluctuations, it is assumed that the dynamic pressure forces of the turbulent motions are the factor determining the size of the largest fluid particle. These dynamic pressure forces are caused by changes in velocity over distances within the diameter of a particle. Kolmogorov [14], Hinze [7] Sleicher [15] and Sevik and Park [16] took this view, and expressed their breakup criteria in terms of a Weber number based on the local turbulent fluctuations by

$$We_{tr} \equiv \frac{\rho_c (\Delta u)^2 (d_e)_{\max}}{\sigma} = 2\rho_c \epsilon^{2/3} (d_e)_{\max}^{5/3} = \text{constant} \quad (5)$$

where  $(\Delta u)^2$  is the spatial average value of the square of velocity difference over a distance equal to the particle diameter, and  $\epsilon$  is the energy dissipation per unit mass and time.

Based on tests involving the dispersion of various immiscible liquids, Hinze calculated a value of 1.18 for the constant in Eq. (5) whereas Sevik and Park suggested 1.04 for droplets and 2.6 for bubbles. This indicates that the critical Weber number for bubble breakup in turbulent flow fields is greater than that for drop breakup by about a ratio of 2.5.

In the foregoing breakup mechanisms, disturbances which cause fluid particle splitting are due to rapid acceleration, high shear stresses, and turbulent fluctuations in the continuous surrounding fluids. It has been observed that even when none of such external disturbances are present, there is a limit to the size to which bubbles and drops can reach. The maximum size attained by a single bubble or drop rising or falling freely through stagnant media in the absence of such disturbances has been attributed to Rayleigh-Taylor instability. This type of breakup mechanism was first considered by Komaboyashi et al. [17] to determine the maximum size of falling drops in air. This theory has been extended over the years by Blanchard [18], Cotton and Gokhale [19], Klett [20], Hendricksen and Ostergaard [21], Clift et al. [22-24], and Grace et al. [25]. For example Grace et al. [25] developed a semi-empirical relation to predict the maximum particle diameter in which a constant was correlated using existing experimental data. It was found that the data for bubbles requires a different constant, 3.8, than the data for liquid drops. For the latter case, the optimum value of the constant was found to be 1.40.

It is important to note that in this type of analysis the breakup criteria were based on the growth of the standing waves, i.e., Rayleigh-Taylor instability, where there is no relative velocity permitted between the particulate and continuous phases. However, in reality, even for the breakup of the stagnant media there exists a relative motion between particulate and continuous fluids, and the growth of disturbances generated at the interface depends on the magnitude of the relative velocity. Therefore, the use of the Rayleigh-Taylor instability analysis seems inconsistent in this case. This is particularly true for falling drops in a gaseous media where the relative



velocity can be very high. It is natural to expect an effect of the relative velocity on the wave propagation and breakup processes.

Kelvin-Helmholtz theory allows a relative motion between two superposed fluid layers. Disturbances generated by this instability propagate at the interface with a certain speed while they grow or decay. Furthermore, since the breakup of fluid particles proceeds from the advancing interfacial surface, i.e., from the upper surface for rising bubbles and drops and from the lower surface for falling drops, it is natural to expect both the Kelvin-Helmholtz and Rayleigh-Taylor instabilities become effective in the breakup process.

In view of the above discussion, this study has three objectives. Based on the combination of Kelvin-Helmholtz and Rayleigh-Taylor instability theories, the first objective is to develop a unique method to describe the breakup of fluid particles. The method thus developed is unique in the sense that it can be used for predicting breakup diameter of rising bubbles as well as falling or rising drops in a gas or in an immiscible different liquid. The second objective is to develop a series of simple correlations to determine the maximum size fluid particle can reach. Finally, the third objective is to extend the theory to predict the maximum droplet size in a high velocity gas stream which is the most interesting case in terms of practical applications. This extension is possible since the mechanistic model developed here partly depends on the Kelvin-Helmholtz instability theory.

## **17.2. Break-Up Analysis**

### **17.2.1. Modeling**

As noted above, even for the case of freely rising bubbles and drops, and falling drops in a stagnant media there exists a relative motion between fluid

particles and its surrounding fluid. Hence, interfacial stability analysis used for a breakup mechanism should take into account the effect of the relative motion. Taking this view a breakup mechanism based on Kelvin-Helmholtz instability of interfacial progressive waves rather than the instability of standing waves will be developed here.

For the purpose of using the plane flow Kelvin-Helmholtz theory to describe the breakup of fluid particles, a series of approximations will be introduced as follows:

- a. The compressibility of dispersed and continuous fluids is neglected. Since the mechanistic modeling is based on the propagation of interfacial waves, this assumption does not exclude the breakup in single component fluids.
- b. The effects of viscosity in both dispersed and continuous fluids are neglected. Hence, the breakup criteria will not be expected to hold for extremely high viscous fluids.
- c. The circulation within the fluid particle is neglected.

The surface contamination theory implies that all bubbles and drops, no matter how small, will show internal circulation if the system is sufficiently free of surface-active contaminants. However, traces of surface-active contaminants may have profound effect on the behavior of drops and bubbles, Clift et al. [24]. Even though the amount of impurity may be so small that there is no measurable change in the bulk fluid properties, a contaminant can eliminate internal circulation. Systems which exhibit high interfacial tension, including common fluid pairs like air-water, liquid metals-air, and aqueous liquid-nonpolar liquids, are subject to this effect, Davies [25] and Linton and Sutherland [27]. The measures required to purify such systems and the precautions needed to ensure no further contamination

are so stringent that one must accept the presence of surface-active contaminants in most systems of practical importance. Finally, it is to be noted that when a drop or bubble moves through a continuous medium, absorbed surface active materials at the interface between the two fluids are swept to the rear. The concentration gradient results in a tangential gradient of surface tension which, in turn, causes tangential stress tending to retard surface motion and internal circulation.

The above discussion is not a full justification for ignoring the internal circulation. However, the reduction of internal circulation due to the presence of surface-active contaminant and surface-active contaminant concentration gradient may justify, to a certain degree, the approach taken in this work.

- d. The effects of fluid particle advancing from curvature are neglected except insofar as it determines the value of tangential velocity component. It can be argued that these effects are of minor consequences for drops and bubbles which are sufficiently large for breakup to be a factor.
- e. The breakup of fluid particles in a stagnant fluid proceeds from the advancing interfacial surface, i.e., from the upper surface for rising bubbles and drops and from the lower surface for falling drops, which is in agreement with most experimental observations. Hence it is assumed here that it will always be the advancing interface of a freely moving particle that is prone to instability.

Under these conditions the two-dimensional plane flow Kelvin-Helmholtz instability results which are summarized in Appendix A can be applied. Identifying the continuous and dispersed fluids by subscript c and d,

respectively, the results given in Appendix A for the speed of propagation,  $c_r$ , and the growth factor  $kc_i$ , can be expressed as follows.

$$c_r = \frac{\rho_c \coth(kh_c) u_c + \rho_d \coth(kh_d) u_d}{\rho_c \coth(kh_c) + \rho_d \coth(kh_d)} \quad (6)$$

$$kc_i = \left\{ \frac{\rho_c \rho_d \coth(kh_c) \coth(kh_d) k^2 (u_{c\theta} - u_{d\theta})^2}{[\rho_c \coth(kh_c) + \rho_d \coth(kh_d)]^2} - \frac{\sigma k^2 - g|\Delta\rho|k}{\rho_c \coth(kh_c) + \rho_d \coth(kh_d)} \right\}^{1/2} \quad (7)$$

where  $(u_{c\theta} - u_{d\theta})$  is interpreted as the tangential velocity difference at the interface.

Now consider a cap bubble rising in stagnant liquid as illustrated in Figure 1. Here a cap bubble is chosen for the purpose of reference. The present theory will be equally applicable to rising or falling drops with spherical or ellipsoidal shapes. In Figure 1,  $\theta_w$  represents the wake angle of a cap bubble and  $R_p$  denotes the particle radius.

Using the potential flow theory for flow around a spherical particle, it can be shown that the tangential velocity components at an angular position of  $\theta$  can be given by

$$u_{c\theta} = \frac{3}{2} u_c \sin\theta \quad (8)$$

Furthermore, in view of the assumption c, the circulation within the fluid particle is negligible, one can write the tangential velocity component within the fluid particle as follows:

$$u_{d\theta} \approx 0. \quad (9)$$

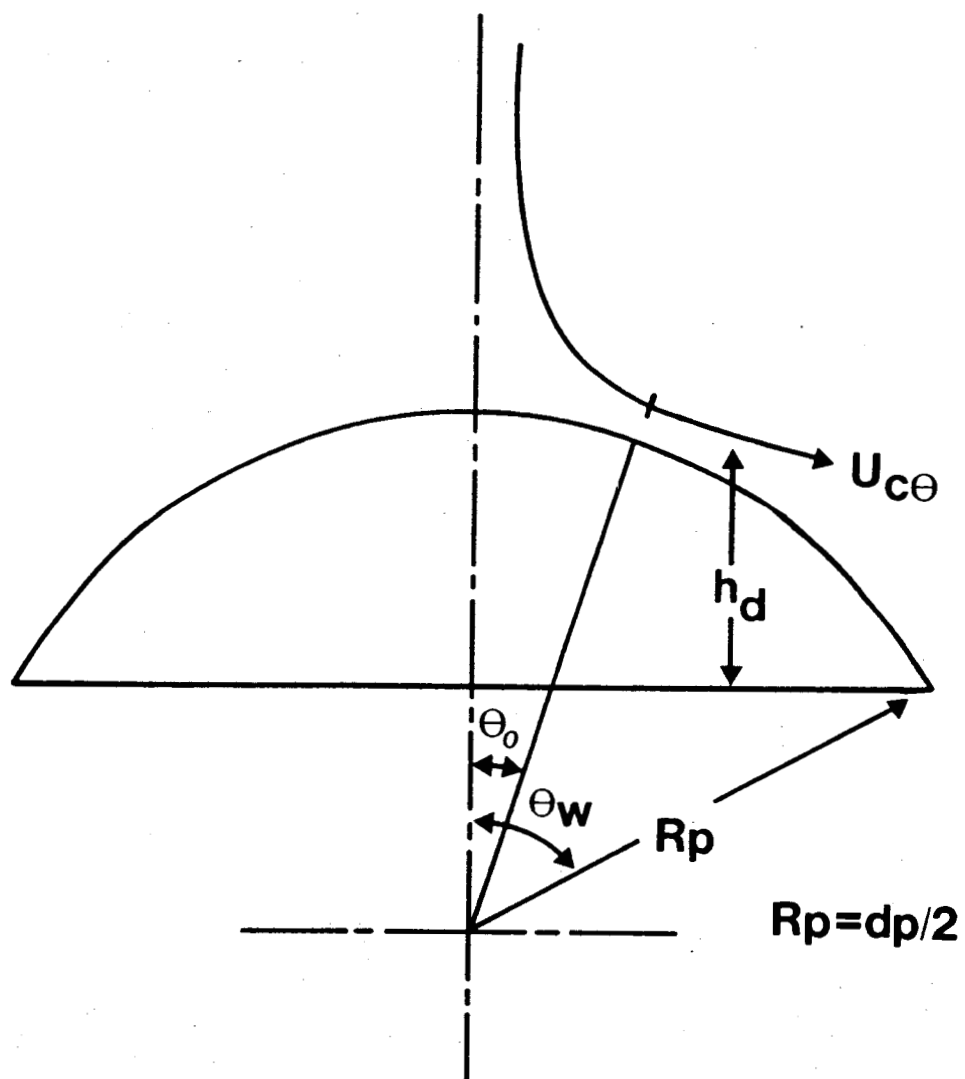


Figure 1. Schematic illustration of flow around a rising cap bubble.

It is noted here that the surrounding fluid dimension is much larger than the particle size. Thus,  $h_c \rightarrow \infty$  and for large arguments  $\coth(kh_c)$  can be approximated by

$$\coth(kh_c) \approx 1.0. \quad (10)$$

In view of equations (8) through (10), equations (6) and (7) can be approximated by

$$c_r = \frac{3}{2} \frac{\rho_c u_c \sin \theta}{\rho_c + \rho_d \coth(kh_d)} \quad (11)$$

$$kc_i = \left\{ \frac{\rho_c \rho_d \coth(kh_d) k^2 (1.5 u_c \sin \theta)^2}{[\rho_c + \rho_d \coth(kh_d)]^2} - \frac{\sigma k^3 - g |\Delta \rho| k}{\rho_c + \rho_d \coth(kh_d)} \right\}^{1/2} \quad (12)$$

It is evident from Eqs. (11) and (12) that the speed of propagation as well as the growth factor depend upon the local angular position, original disturbance location, and the dispersed phase fluid thickness at the origination of disturbances. Referring to Figure 1, it can be shown that  $h_d$  is given by the following equation

$$h_d = \frac{d_p}{2} (\cos \theta_0 - \cos \theta_\omega) \quad (13)$$

here  $d_p$  is given in terms of the mean radius of curvature,  $d_p = 2R_p$ ; and  $\theta_0$  describes angular position at which disturbances originate.

Equation (12) represents the growth factor of Kelvin-Helmholtz instability as applied to a rising cap bubble. Thus when  $(kc_i) > 0$ , the flow configuration is unstable. It should be emphasized here that the above stability criteria represents only the first step in developing a correlation for the breakup of a fluid particle interface. This information simply

indicates when these interfacial waves occur and what their growth rates are. However, the appearance of the wave on the interface does not necessarily imply that it leads to drastic changes at the interface such as the breakup of particles. To answer this question, whether the waves can lead to a breakup or not, it is necessary to know the time required for these waves to grow to a certain amplitude so that splitting eventually can occur.

### 17.2.2. Break-Up Mechanisms

A mathematical model is proposed here to predict the point at which breakup will be attained under given conditions. If  $t_g$  denotes the growth time at which the instability at the interface lead to a breakup,  $t_g$  can be calculated from the assumed wave form given by Eq. (A2). Thus

$$t_g \sim \frac{1}{kc_i} \quad (14)$$

For the purpose of convenience a proportionality factor,  $C_g$ , may be introduced as follows

$$t_g = \frac{C_g}{kc_i} \quad (15)$$

and

$$t_g = C_g t_g' \quad (16)$$

where  $t_g' \equiv 1/kc_i$ . In view of Eq. (7),  $t_g'$  can be expressed as

$$t_g' = \left[ \frac{\rho_c \rho_d \coth(kh_d) (1.5 u_c k \sin \theta_o)^2}{[\rho_c + \rho_d \coth(kh_d)]^2} - \frac{\sigma k^3 - g |\Delta \rho| k}{\rho_c + \rho_d \coth(kh_d)} \right]^{-1/2} \quad (17)$$

Disturbances originate near the top of the roof of a bubble and propagate down to the periphery with the local speed of propagation,  $c_r$ . In practice a bubble does not split unless the disturbance has grown sufficiently before the tip of the growing spike reaches the side of the bubble. If the wave travels to the end of a cap bubble or to the equator of a spherical particle without causing a breakup, it will be swept away at the edge into the continuous fluid. An estimate of the likelihood of splitting may be obtained by comparing the time required for a disturbance to grow with the time available for the growth. If  $t_p$  represents the propagation time, that is the time required for a disturbance to travel from its origination to the side of the bubble,  $t_p$  can be calculated by

$$t_p = \int_{\theta_0}^{\theta_\omega} \left( \frac{d_p}{2 c_r} \right) d\theta \quad (18)$$

where  $\theta_0$  is the angular position where disturbances initiate. In view of Eq. (11), the propagation time can be calculated from Eq. (15). Thus

$$t_p = \left[ \frac{\rho_c + \rho_d \coth(kh_d)}{3 \rho_c u_c} \right] d_p \ln \left( \frac{|\tan(\theta_\omega/2)|}{|\tan(\theta_0/2)|} \right) \quad (19)$$

The likelihood of a breakup may now be assessed by comparing the values of  $t_g$  and  $t_p$ . The model proposed here postulates that fluid particles are likely to split if the time available for disturbances to grow that is the propagation time,  $t_p$ , is sufficiently large relative to the growth time,  $t_g$ . Accordingly a fluid particle tends to breakup by a disturbance if

$$t_p \geq t_g \text{ or } \frac{t_p}{t_g} \geq c_g \quad (20)$$



Combining equations (17) and (19) with (20), breakup criterion may be expressed

$$\left[ \frac{\rho_c + \rho_d \coth(kh_d)}{3 \rho_c u_c} \right] d_p \ln \left[ \frac{|\tan(\theta_\omega/2)|}{|\tan(\theta_0/2)|} \right]$$

$$\left\{ \frac{\rho_c \rho_d \coth(kh_d) (1.5 u_c k \sin \theta_0)^2}{[\rho_c + \rho_d \coth(kh_d)]^2} - \frac{\sigma k^3 - g |\Delta \rho| k}{\rho_c + \rho_d \coth(kh_d)} \right\}^{1/2} \geq C_g \quad (21)$$

The breakup criterion developed here is similar to that used previously by Grace et al. [25]. However, the approach moves away from previous analyses, which were largely based on Rayleigh-Taylor instability. Here disturbances generated at the interface grow much more rapidly due to the relative velocity, and the degree of instability is affected by the relative motion between two phases.

Assuming that the wave angle,  $\theta_\omega$ , angular position of initial disturbance,  $\theta_0$ , the terminal velocity  $u_c$ , and the amplitude ratio,  $C_g$ , are expressible in terms of the particle diameter and the wave number, basically there will be only two variables in Eq. (21), namely the wave number and the particle diameter. Then once  $k$  is specified  $d_p$  can be calculated from (21). Evaluation of these parameters are discussed below.

### 17.2.3. Wake Angle

Large fluid particles which are prone to splitting have been studied in some detail previously, and several transition criteria for fluid particle shape regimes have been proposed by Clift et al. [24]. When these studies are compared with available experimental data it is seen that drops falling in gases and drops falling or rising in another liquid never reach the spherical-cap particle regime. However, very large bubbles in the order of

centimeters and most bubbles at the breakup point attain the spherical-cap shape.

Attempts to predict wake angles theoretically for spherical-caps have met with only limited success, Moore [28], Collins [29] and Rippin and Davidson [30]. Based on experimental observations Clift et al. [24] recommended the following empirical equation

$$\theta_{\omega} = 50 + 190 \exp[-0.62 \text{Re}_c^{0.4}] \quad (22)$$

where  $\theta_{\omega}$  is expressed in degrees, and  $\text{Re}_c \equiv \rho_c u_c d_e / \mu_c$  is continuous phase Reynolds number. In the present analysis Eq. (22) is used for bubbles, and  $\theta_{\omega} \approx 90^\circ$  is used for liquid droplets falling or rising in another fluid.

#### 17.2.4. Angular Position of Initial Disturbance Generation

From Eq. (19) it is evident that disturbances which originated at the axis of symmetry, i.e., at  $\theta_0 = 0$ , would never reach the side of the cap bubble or the equator of spherical particles. They are purely standing waves in nature. Observations of splitting bubble experiments performed by Clift et al. [24] indicated that disturbances usually develop in a regular pattern to either side of the leading nose. According to Clift et al. there are two fundamental patterns which may be possible.

Pattern A. The bubble is a node when the initial disturbance originates, then

$$\theta_0 = \frac{\lambda}{2d_p} = \frac{\pi}{kd_p} \quad (23)$$

Pattern B. A node is located at  $\lambda/4$  distance from the bubble nose so that the nose is an antinode in the initial disturbance form, then

$$\theta_o = \frac{\lambda}{d_p} = \frac{2\pi}{kd_p} \quad (24)$$

By comparing the values of  $\theta_o$  in both cases, it can be concluded that the disturbance originated in the pattern A is closer to the bubble nose than the one calculated by the pattern B. Therefore, the pattern A yields larger propagation time, and, in view of the breakup criterion expressed by Eq. (20) this pattern becomes more critical. The pattern A will be used throughout analysis.

#### 17.2.5. Terminal Velocity

There is a substantial body of data in the literature on the terminal velocity of a single bubble or drop. From these data many correlations for calculating the velocity,  $u_c$ , are developed by Hu and Kintner [31], Klee and Treyball [32], Mendelson [33], Marruici et al. [34], Wallis [35], Grace et al. [25]. Similar studies have also been carried out for multiparticle systems by Ishii and Zuber [36]. The terminal velocity correlations were reviewed in detail by Grace et al. [37]. Here, the correlations recommended by Grace et al. are used. These are summarized below.

1. For large bubbles rising through liquid

$$u_c = \left(\frac{2}{3}\right) \left[\frac{g|\Delta\rho|d_p}{2\rho_c}\right]^{1/2} \quad (25)$$

2. For drops falling through gas

$$u_c = 2.0 \left[\frac{g|\Delta\rho|\sigma}{2\rho_c}\right]^{1/4} \quad (26)$$

3. For drops rising or falling through liquid

$$u_c = 0.5 \left[ \frac{\nu_c}{\rho_c d_e} \right] [(F^2 + 2Ar)^{1/2} - F] \quad (27)$$

where Ar is Archimedes number. It is defined as

$$Ar \equiv \frac{g|\Delta\rho|\rho_c d_e^3}{\mu_c^2} \quad (28)$$

and parameter F is defined as  $F \equiv 3[2 + 3(\nu_d/\nu_c)]/(1 + \nu_d/\nu_c)$ .

In the above expressions  $d_e$  is the volume equivalent diameter. As in the case of the empirical correlations documented above, in most drop or bubble experiments, data are tabulated in terms of the volume equivalent diameter,  $d_e$ , rather than the mean curvature diameter or the particle diameter,  $d_p$ . Therefore, it is desirable to express the equations in terms of  $d_e$ . A relation may be given in the form

$$d_p = C_e d_e \quad (29)$$

where  $C_e$  is a constant that can be determined through the use of  $\theta_\omega$ .

Referring to Figure 1, it may be shown that

$$C_e = \left[ \frac{4}{(1 - \cos\theta_\omega)^2 (2 + \cos\theta_\omega)} \right]^{1/3} \quad (30)$$

Once  $\theta_\omega$ ,  $\theta_o$  and  $u_c$  are determined in terms of  $k$  and  $d_p$  (or  $d_e$ ) it is evident from Eq. (21) that in order to arrive at a predictive criterion for  $d_p$ , one still needs to know  $k$  and  $C_g$ .

### 17.2.6. Wave Number

The interface between the dispersed and continuous phases is unstable only for  $kc_i \geq 0$ . In view of Eq. (12) the instability condition can be expressed as

$$\frac{\rho_d \coth(kh_d)(1.5 u_c \sin \theta_0)^2 k}{\rho_c + \rho_d \coth(kh_d)} - \frac{\sigma k^2 - g|\Delta \rho|}{\rho_c} \geq 0 \quad (31)$$

The wave number determined from this condition sets an upper limit on wave number which need to be considered. The leading surface of a bubble or drop may therefore become unstable if the wave number of a disturbance at the interface is less than a critical value,  $k < k_{cr}$ , where  $k_{cr}$  is determined from Eq. (31). Thus,

$$k_{\max} = k_{cr} \quad (32)$$

There is also an upper limit on the wave length,  $\lambda$ , or a lower limit on the wave number, imposed by the fact that a disturbance, if  $\lambda$  were too large, represent a gross deformation of the bubble or drop and not a perturbation of the leading interface, Grace et al. [25]. A reasonable upper limit corresponds to half the circumference of the fluid particle. Hence, for a cap bubble of wake angle  $\theta_\omega$ , the maximum wavelength becomes

$$\lambda_{\max} = \theta_\omega d_p \quad (33)$$

or in terms of the wave number, ( $k \equiv 2\pi/\lambda$ ),

$$k_{\min} = \frac{2\pi}{\theta_\omega d_p} \quad (34)$$

Equations (31) and (34), respectively, put a higher and a lower limit on the acceptable values of wave numbers. Hence instability occurs for some  $k$  such that

$$\frac{2\pi}{\theta_{\omega} d_p} \leq k \leq k_{cr} \quad (35)$$

#### 17.2.7. Break-Up Correlation

Variations of  $t_g$  and  $t_p$  as calculated from Eqs. (17) and (19), respectively, are illustrated in Figures 2 to 10 for some of the fluid pairs. It is to be noted that the experimental values of breakup diameter are used to construct these figures. These nine sample figures represent basic characteristics of the other data listed in references [2, 25, 29, 38-40]. For example, Figures 2 to 4 represent bubbles [25] whereas the rest represent drop in gases [2,39,40] and liquids [25, 29, 38]. For the purpose of convenience  $(t_p/t_g')$  ratio is also given in these figures.

It is interesting to note that  $t_p$  is always greater than  $t_g'$  in the acceptable range of wave numbers as given by Eq. (35) except a very narrow range close to  $k_{max} = k_{cr}$ , where the growth factor,  $k_{ci} \rightarrow 0$ , and, hence  $t_g' \rightarrow \infty$ , which makes the ratio  $(t_p/t_g')$  approach to zero. It is noted, however, that this range corresponds to very small wavelengths for which the linearized stability analysis is not expected to hold. Furthermore, it is to be noted that the minimum values of  $(t_p/t_g')$  which is required by Eq. (20) can only be achieved at the minimum value of wave number. Although it is usual practice in linearized stability analysis to consider the wave number which causes the most unstable wave growth determined by the root of  $d(kc_i/dk) = 0$ , the most unstable wave for liquid drops as illustrated by Figure 5 to 10 falls into unacceptable wave number range.

Another words the most unstable wave number is so small that the corresponding wavelength,  $\lambda = 2\pi/k$ , becomes longer than a half of the circumference.

This implies a gross deformation of the bubble or drop and not a perturbation of the leading interface. Such a disturbance is considered not to cause a particle disintegration. Therefore, instead of the most unstable wave, we propose here to consider the wave which yields the minimum value of  $(t_p/t_g)$  as required by Eq. (20).

Using  $k = k_{\min}$  value obtained from Eq. (34) and  $\theta_0$  value calculated from Eq. (23), the breakup criterion may be expressed from Eq. (21) in dimensionless form as follows:

$$\begin{aligned} (1+\rho^*)^{1/2} \ln \left[ \frac{|\tan(\theta_\omega/2)|}{|\tan(\theta_\omega/4)|} \right] \{ 2.25 \left( \frac{2\pi}{\theta_\omega} \right)^2 \left( \frac{\rho^*}{1+\rho^*} \right) \sin^2 \left( \frac{\theta_\omega}{2} \right) \\ + \frac{1}{We} \left[ \left( \frac{2\pi}{\theta_\omega} \right) C_e d_e^{*2} - \left( \frac{1}{C_e} \right) \left( \frac{2\pi}{\theta_\omega} \right)^3 \right]^{1/2} \geq 3 C_g \end{aligned} \quad (36)$$

where  $d_e^*$ ,  $We$  and  $\rho^*$  are dimensionless volume equivalent diameter, Weber number and density ratio, respectively. They are defined as

$$\begin{aligned} d_e^* &\equiv \left( \frac{g |\Delta \rho| d_e^2}{\sigma} \right)^{1/2}; \\ We &\equiv \frac{\rho_c d_e u_c^2}{\sigma}; \\ \rho^* &\equiv \frac{\rho_d \coth(k_{\min} h_d)}{\rho_c} \end{aligned} \quad (37)$$

The term  $(k_{\min} h_d)$  appearing in Eq. (37) can be expressed from Eqs. (13) and (24) in terms of  $\theta_\omega$ . Thus,

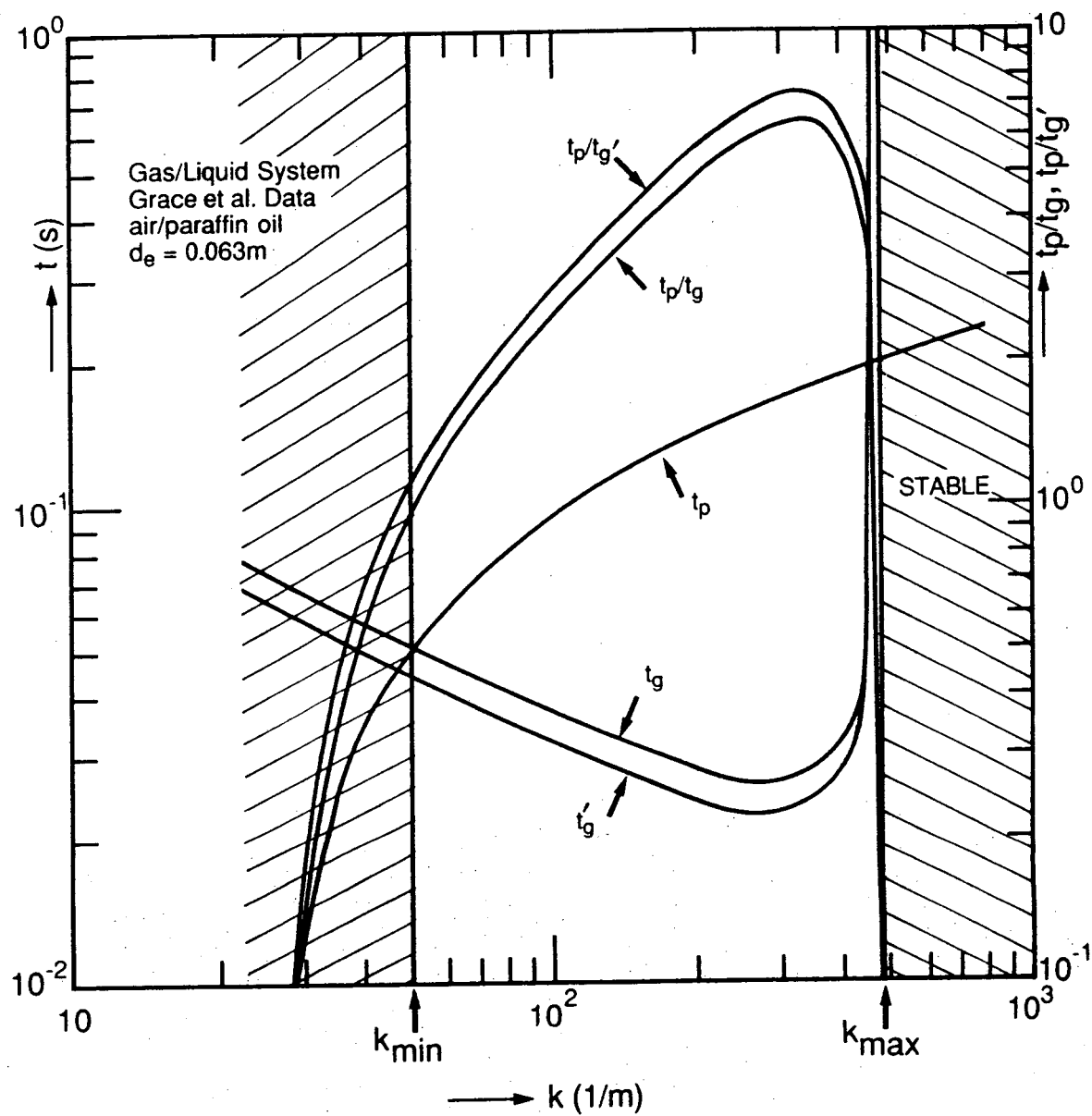


Figure 2. Variation of growth time,  $t_g$ , propagation times,  $t_p$ , and time ratio,  $t_p/t_g$ , for a bubble at  $d_e = 0.063 \text{ m}$  as a function of wave number,  $k$ .



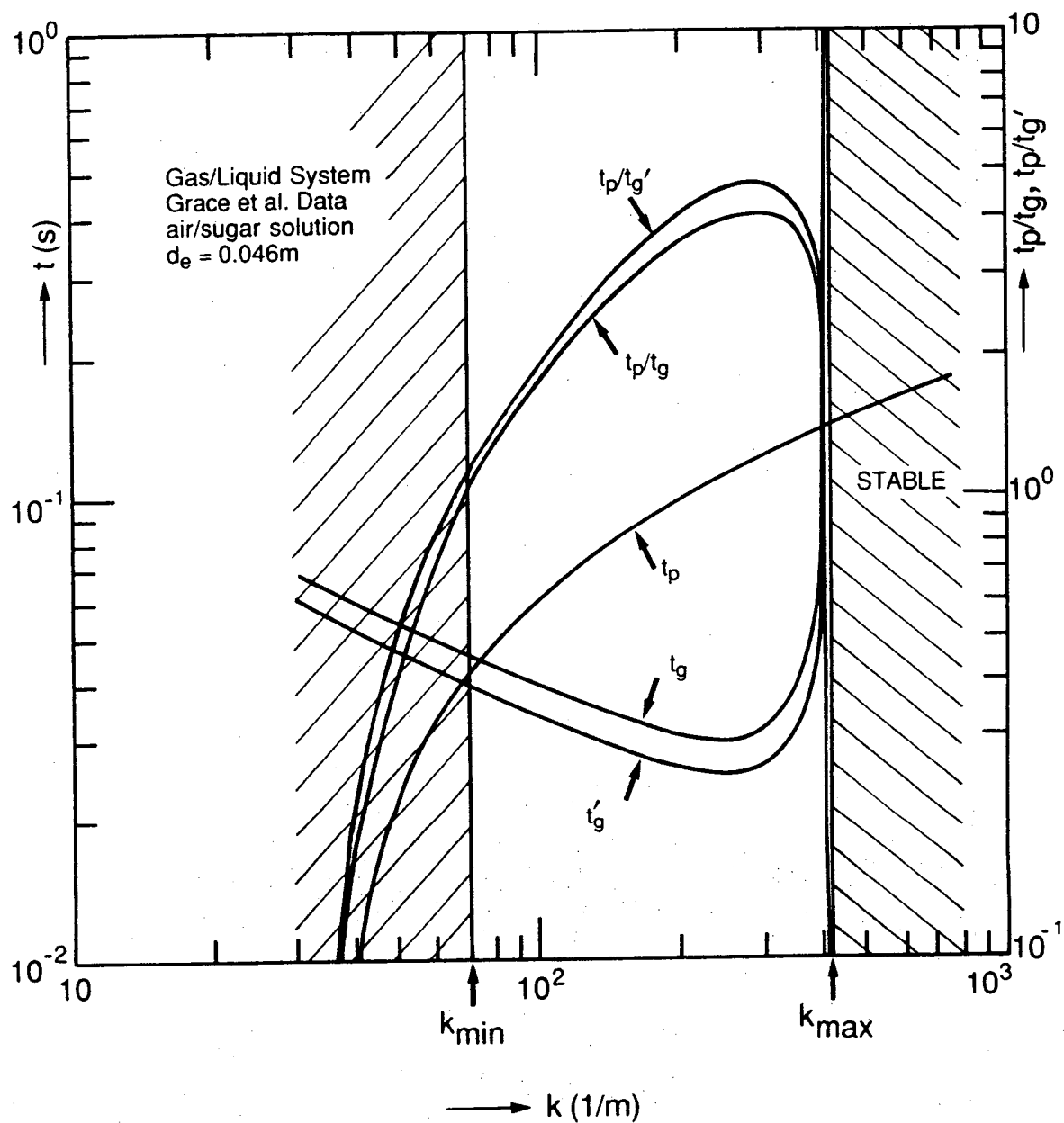


Figure 3. Variation of growth time,  $t_g$ , propagation time,  $t_p$ , and time ratio,  $t_p/t_g$ , for a bubble at  $d_e = 0.046 \text{ m}$  as a function of wave number,  $k$ .

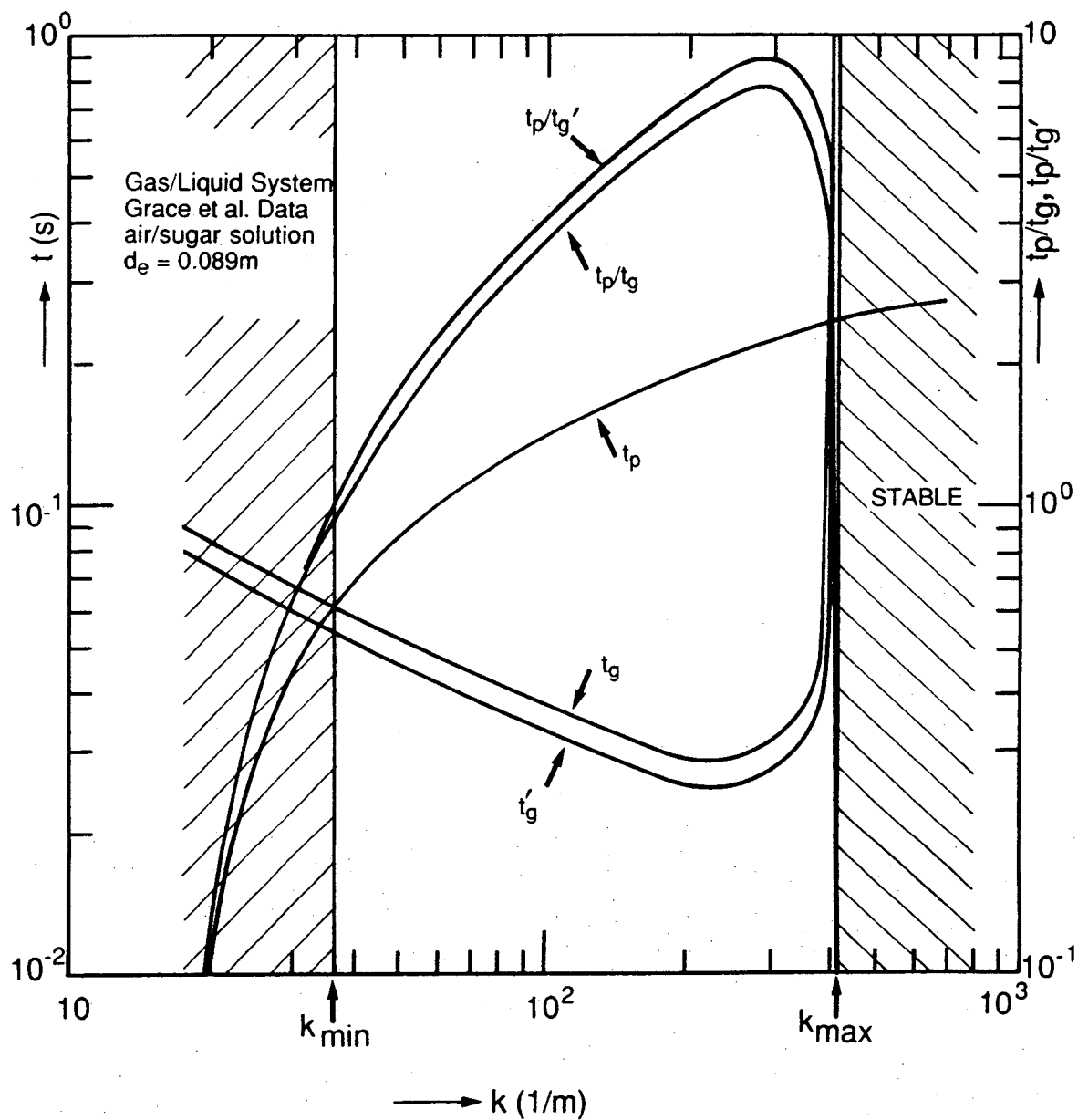


Figure 4. Variation of growth time,  $t_g$ , propagation time,  $t_p$ , and time ratio,  $t_p/t_g$ , for a bubble at  $d_e = 0.089\text{ m}$  as a function of wave number,  $k$ .

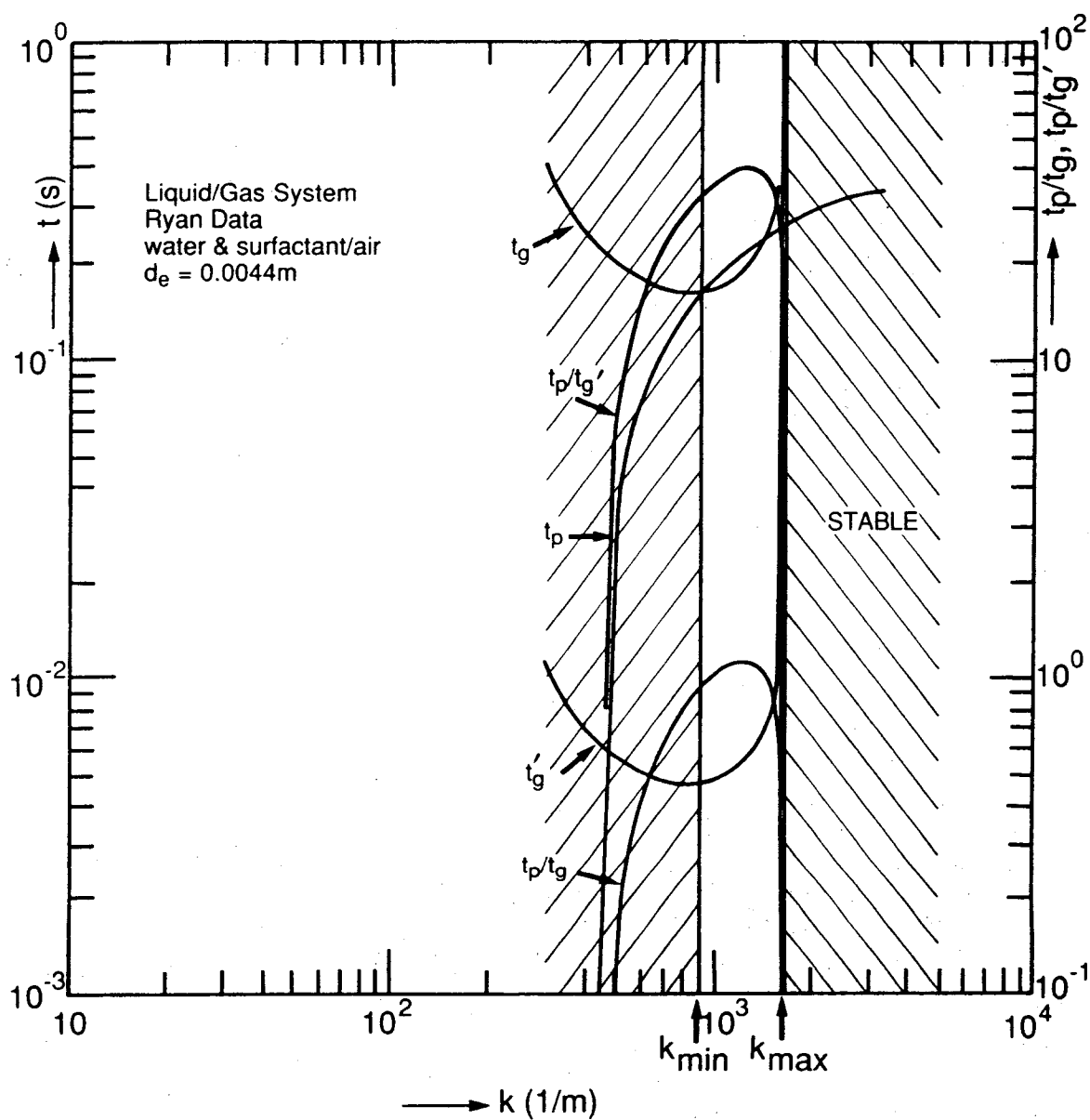


Figure 5. Variation of growth time,  $t_g$ , propagation time,  $t_p$ , and time ratio,  $t_p/t_g$ , for a drop in air at  $d_e = 0.0044 \text{ m}$  as a function of wave number,  $k$ .

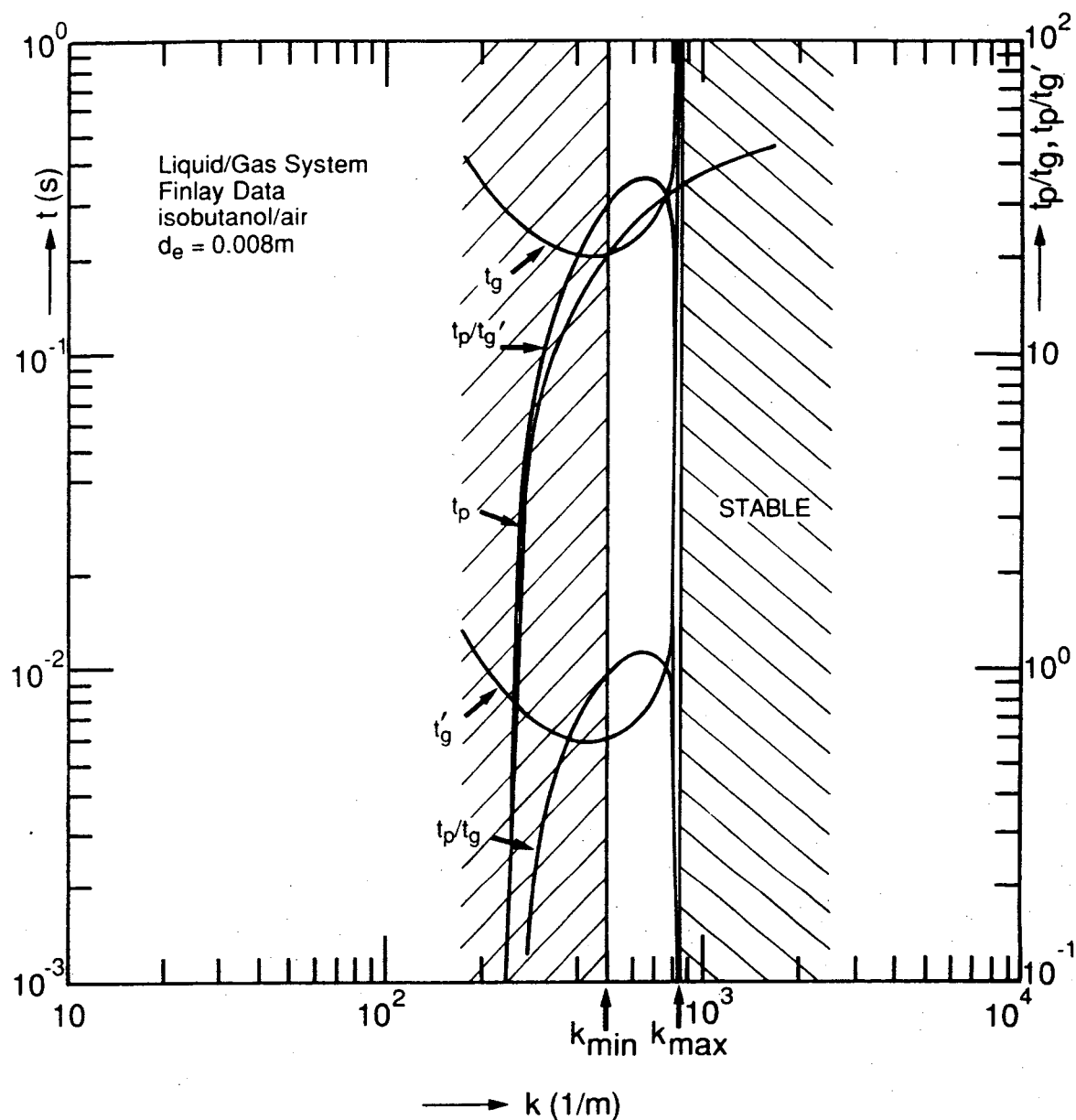


Figure 6. Variation of growth time,  $t_g$ , propagation time,  $t_p$ , and time ratio,  $t_p/t_g$ , for a drop in air at  $d_e = 0.008$  m as a function of wave number,  $k$ .

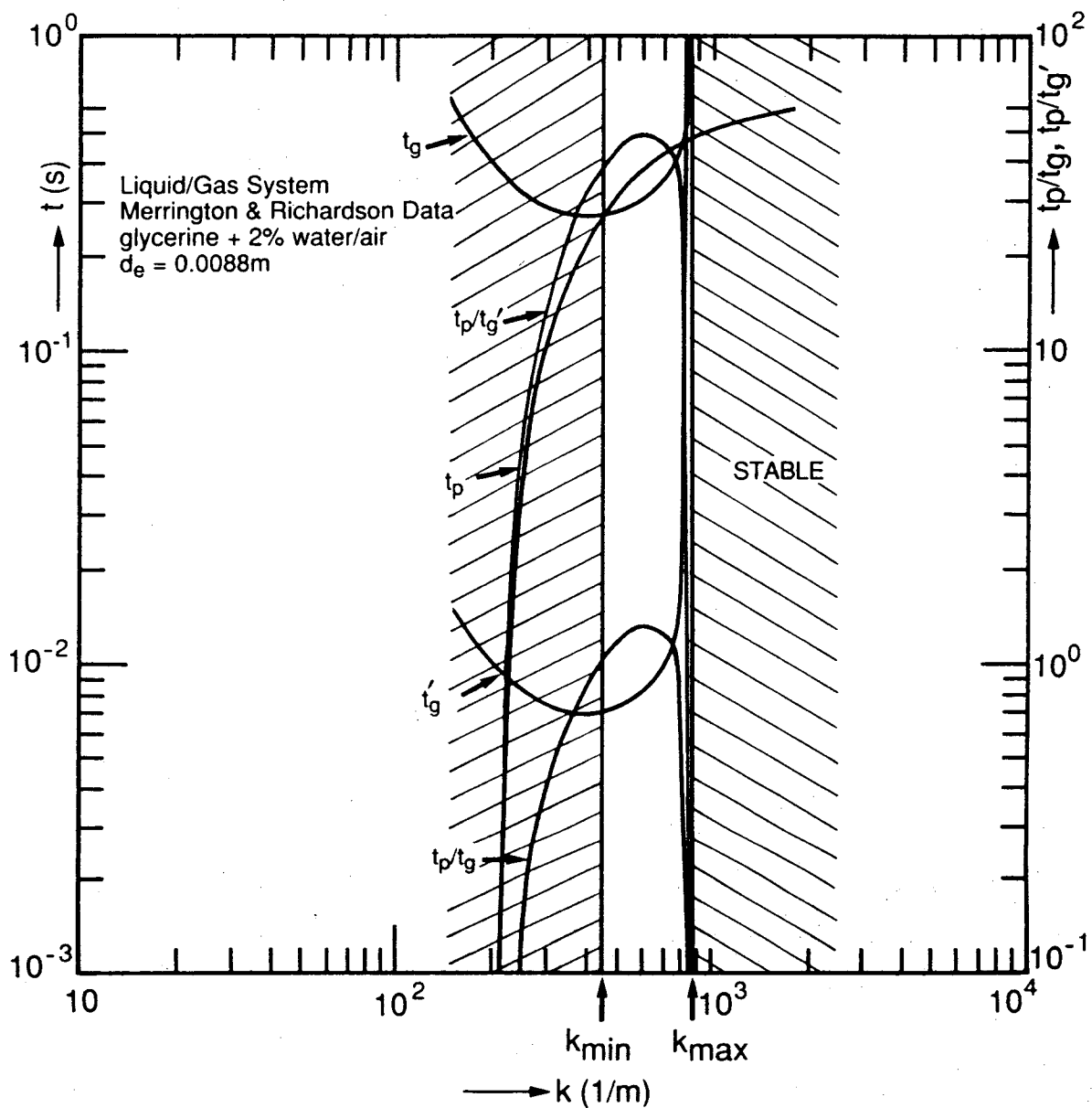


Figure 7. Variation of growth time,  $t_g$ , propagation time,  $t_p$ , and time ratio,  $t_p/t_g$ , for a drop in air at  $d_e = 0.0088\text{ m}$  as a function of wave number,  $k$ .

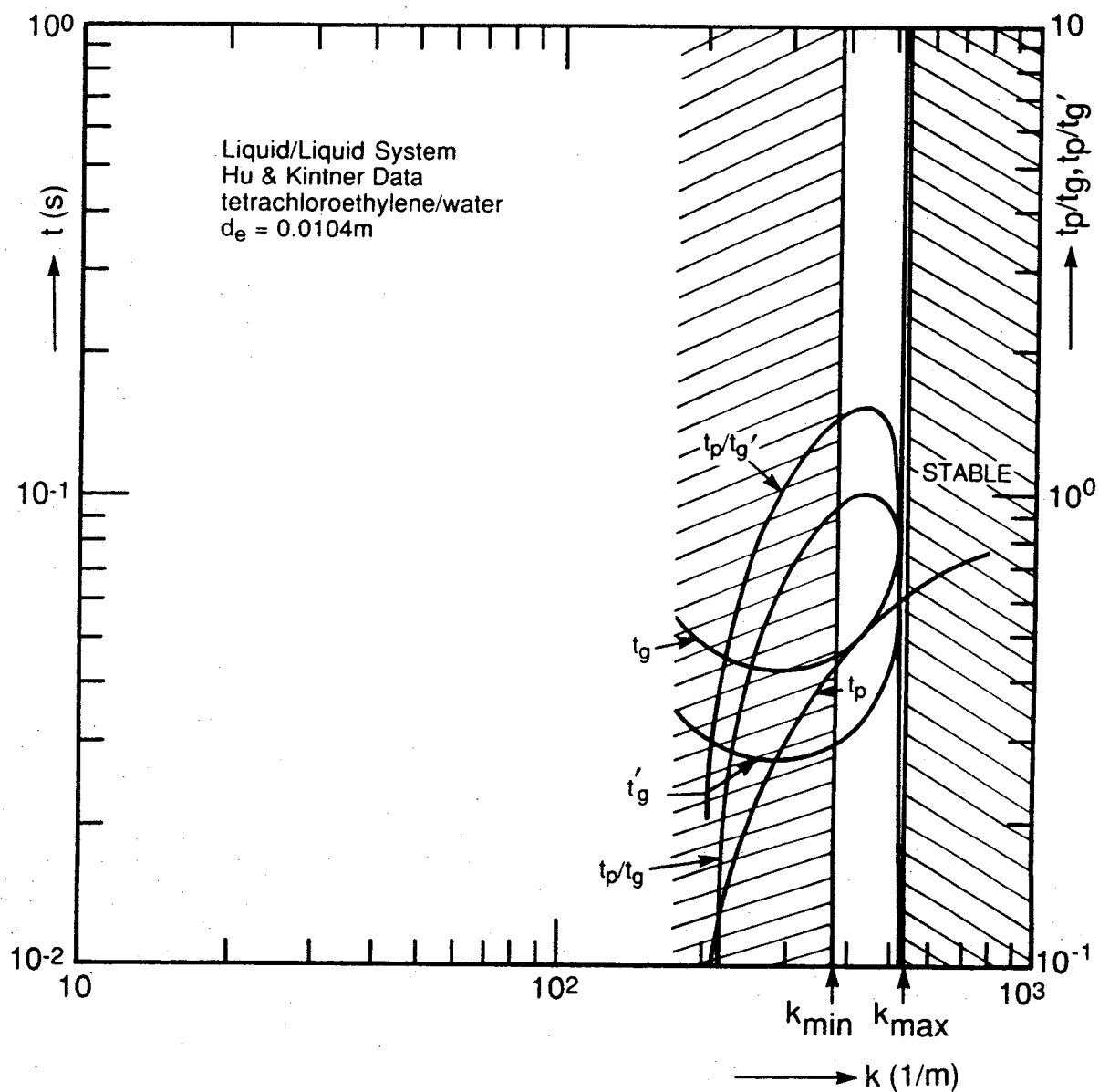


Figure 8. Variation of growth time,  $t_g$ , propagation time,  $t_p$ , and time ratio,  $t_p/t_g$ , for a drop in a liquid at  $d_e = 0.0104 \text{ m}$  as a function of wave number,  $k$ .

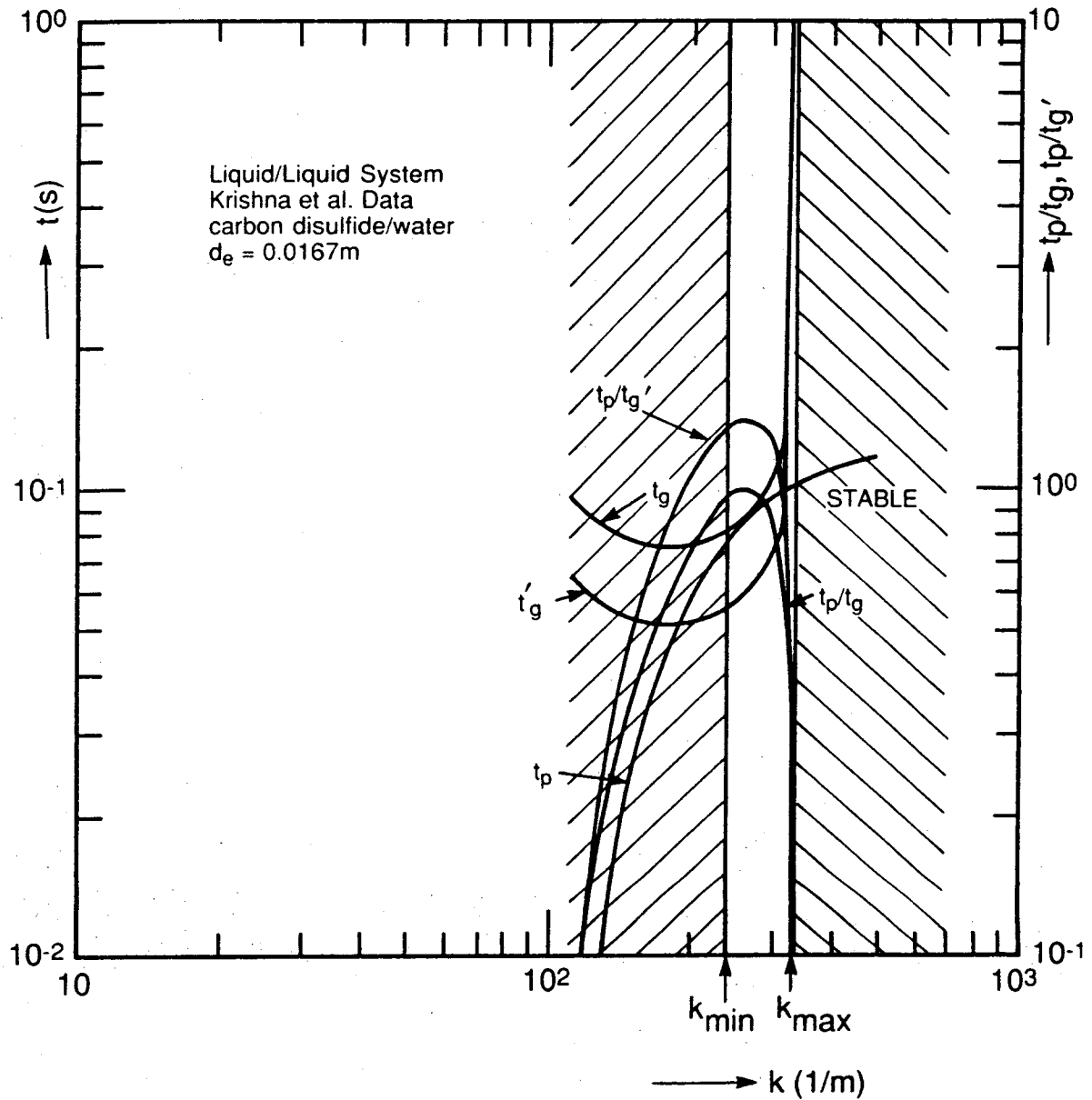


Figure 9. Variation of growth time,  $t_g$ , propagation time,  $t_p$ , and time ratio,  $t_p/t_g$ , for a drop in a liquid at  $d_e = 0.0164 \text{ m}$  as a function of wave number,  $k$ .

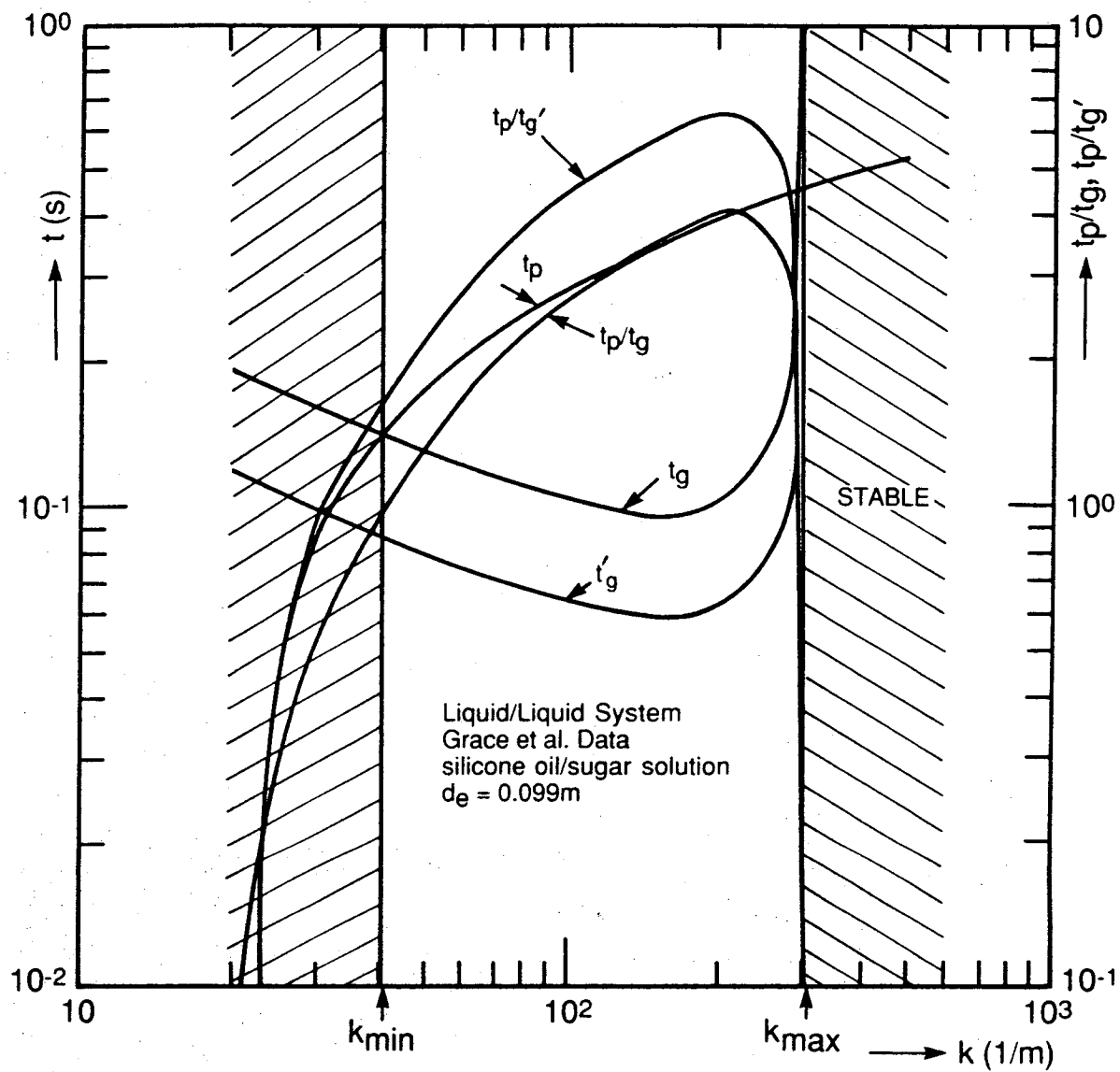


Figure 10. Variation of growth time,  $t_g$ , propagation time,  $t_p$ , and time ratio,  $t_p/t_g$ , for a drop in a liquid at  $d_e = 0.099$  m as a function of wave number,  $k$ .



$$k_{\min} h_d = (2\pi/\theta_\omega) \sin(3\theta_\omega/4) \sin(\theta_\omega/4) \quad (38)$$

It is evident from Eq. (36) that in order to arrive at a predictive criterion, one needs to know  $C_g$ . In a linearized stability analysis as it is the case here, there exists no analytical way to predict the value of  $C_g$  on purely theoretical basis. It is necessary to resort to experiments. A reasonable approach is to correlate this term in terms of basic variables affecting the breakup process.

Observations on a large number of figures such as Figures 2 and 10 regarding the numerical value of  $(t_p/t_g')$  at  $k = k_{\min}$  lead to the following conclusions:

1. For bubbles  $(t_p/t_g')$  is order of unity,
2. For drops  $(t_p/t_g') \sim (1 + \rho^*)^m$  with  $m$  being order of 0.5 at  $k = k_{\min}$ .

Since for bubbles  $1 + \rho^* \approx 1$ , these observations lead to a conclusion that at  $k = k_{\min}$ ,

$$C_g \approx C(1 + \rho^*)^{1/2} \quad (39)$$

where  $C$  is a constant to be determined.

Considering the magnitude of variations in the dimensionless density ratio group from bubbles to drops falling in gases, emergency of such a dimensionless group as a correlation parameter is not surprising. Furthermore, noting that the viscous effects were completely neglected in the present analysis, it is reasonable to use another correlation parameter representative of the viscous effects. Equation (39) is modified, and a correlation in the following form is sought

$$\frac{C_g}{(1+\rho^*)^{1/2}} = f(\rho^*, N_{\mu_c}) \quad (40)$$

where  $N_{\mu_c}$  is the viscosity number of the continuous phase. It is defined as

$$N_{\mu_c} \equiv \left[ \frac{\mu_c^2}{\rho_c (\sigma^3 / g \Delta \rho)} \right]^{1/2} \quad (41)$$

Using the substantial amount of data covering a wide range of fluid properties as listed in Table I, the functional dependence of  $C_g$  on  $\rho^*$  and  $N_{\mu_c}$  is determined by linear regression analysis. It is given by

$$\frac{C_g}{(1+\rho^*)^{1/2}} = 0.348 \left( \frac{2+3\rho^*}{1+\rho^*} \right)^{1.135} (1 + N_{\mu_c})^{0.18} \quad (42)$$

In view of Eq. (16), Eq. (42) yields the growth time as

$$t_g = 0.348 (1+\rho^*)^{1/2} \left( \frac{2+3\rho^*}{1+\rho^*} \right)^{1.135} (1 + N_{\mu_c})^{0.18} t_g' \quad (43)$$

The growth time predicted from Eq. (43) is also illustrated in Figures 2 to 10. It can be observed from these figures that at  $k = k_{\min}$ ,  $t_p \approx t_g$ . Furthermore, using Eq. (42) in (36) the general breakup criterion becomes

$$2.25 \left( \frac{2\pi}{\theta_\omega} \right)^2 \left( \frac{\rho^*}{1+\rho^*} \right) \sin^2 \left( \frac{\theta_\omega}{2} \right) + \frac{1}{We} \left[ \left( \frac{2\pi}{\theta_\omega} \right) C_e d_e^{*2} - \left( \frac{1}{C_e} \right) \left( \frac{2\pi}{\theta_\omega} \right)^3 \right] \geq$$

$$1.09 \left( \frac{2+3\rho^*}{1+\rho^*} \right)^{2.27} (1+N_{\mu_c})^{0.36} \left[ \ln \left( \frac{|\tan(\theta_\omega/2)|}{|\tan(\theta_\omega/4)|} \right) \right]^{-2} \quad (44)$$

Equation (44) can be used to predict the maximum fluid particle diameter at breakup. The breakup diameter suggested here is general in the sense that it is applicable for gas-liquid bubbly systems as well as liquid-liquid and liquid-gas droplet systems for relatively low viscosity fluids. It is important to note that the basic parameters affecting the breakup are  $Nu_c$ ,  $We$ ,  $\rho^*$  and  $\theta_\omega$ . Since  $\theta_\omega$  depends on  $Re_c$  by Eq. (22) it can be replaced by  $Re_c$ . Effects of these groups on  $d_e^*$  will be explored in detail in forthcoming sections.

### 17.3. Comparison Between Theoretical Predictions and Experimental Break-Up Data

Predicted values of  $(d_e)_{\max}$  obtained from Eq. (42) are compared against experimental values in Figure 11. It is evident from Table I that the experimental data covers broad range of liquid-liquid, liquid-gas and gas-liquid systems. The results include the data by Hu and Kintner [29], Krishna et al. [38] and Grace et al. [25] for liquid-liquid systems, by Merrington and Richardson [2], Finlay [39] and Ryan [40] for liquid drops falling through gas, and finally by Grace et al. [25] and Sundell [41] for rising bubbles through stagnant liquid. The mean deviation between the predicted and experimental values of  $(d_e)_{\max}$  for each group is also listed in Table I.

The average deviation between predicted and experimental value of  $(d_e)_{\max}$  varies from about + 5.80 for Ryan's data to + 29.55 for Grace et al. data with an overall mean deviation of + 13.94. Four of the systems studied by Hu and Kintner are in common with systems investigated by Krishna et al., while two of the Finlay systems are essentially identical with Merrington and Richardson systems. However, the mean deviation changes

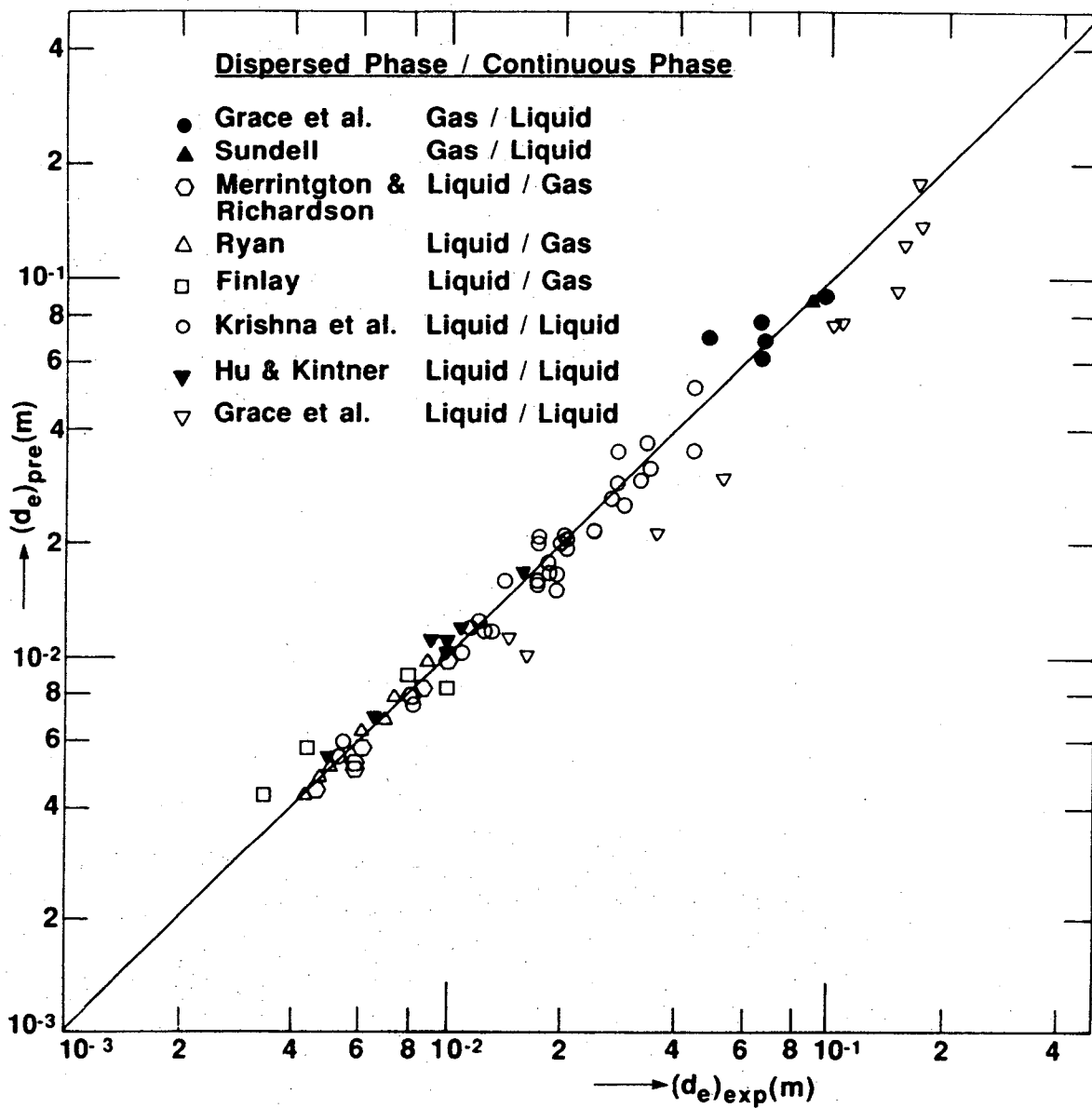


Figure 11. Comparison of predicted breakup diameters with experimental data.

drastically between Hu and Kintner and Kirshna et al. data and between Merrington and Richardson and Finlay data. Although there are some differences in reported values of fluid properties, a significant part of the discrepancy between predictions and theory arises from experimental scatter or bias.

Relatively high disagreements between the predicted and the Grace et al. data for liquid-liquid systems can be attributed to the viscosity effects of the continuous fluid. Although a viscosity correction has been made in the final correlation it is not expected that the correlation would be good for very viscous fluids. Grace et al. experiments cover a dynamic viscosity range of 0.0124 to 3.08 Ns/m. If this set of data,  $\nabla$  in Figure 11, is excluded from the comparison overall mean deviation decreases drastically.

Taking the experimental scatter and the very viscous fluids used for some experiments into consideration, and furthermore recalling the approximate nature of the theory developed here, the agreement between the theoretical predictions and the experimental results is favorably well. The overall mean deviation between the predicted and experimental values of  $(d_e)_{\max}$  is  $\pm 13.94$ . Agreements with experimental results indicate that the principle physical mechanisms involved are properly accounted for.

#### 17.4. Practical Break-Up Correlations

It is to be noted that the general breakup correlation developed above is not closed in the sense that it requires iteration process to obtain the maximum fluid particle size. This may hinder its practical utilization. For the purpose of practical applications the general criterion may be simplified for falling drops in gas, drops in high relative velocity field rising bubbles and falling or rising drops in liquids.

#### 17.4.1. Freely Falling Drops in Gaseous Media

As discussed above  $\theta_\omega = \pi/2$  for drops, and  $C_e = 1$ . Noting that  $\rho^* \gg 1.0$  and  $Nu_c \ll 1.0$  for this case, the breakup criterion can be simplified for practical purposes. It may be shown that the criterion becomes

$$d_e^* + 0.26 We - 16 = 0 \quad (45)$$

With the terminal velocity given by Eq. (19), the  $We$  can be expressed in terms of  $d_e^*$ . Thus,

$$We = 4 d_e^* \quad (46)$$

In view of Eq. (46), Eq. (45) yields a very simple expression for  $d_e^*$  as follows.

$$d_e^* \approx 3.52 \quad (47)$$

It is interesting to note that when the slight effects of  $\rho^*$  and  $Nu_c$  are neglected the newly found breakup criterion reduces to the classical Weber number criterion as

$$We = 4 d_e^* = 14.08 \quad (48)$$

In the case of a falling drop, the classical Weber number criterion as suggested by Hinze [7], Sevik and Park [16] and Haas [5] is given by  $We = 22$ . This yields somewhat larger  $d_e^*$  values than those predicted from Eqs. (47) or (48). However, as can be observed from Figure 11, a comparison of the present predictions with available experimental data indicate a very good agreement with Merrington and Richardson [2] and Ryan [40] data with a mean deviation of + 8.2%. Somewhat poor predictions may be seen with Finlay's [39] four data points. Including the Finlay's data the mean deviation is + 12.08.

Before closing this section it is interesting to compare the Grace et al. [25] method, which was based on the Rayleigh-Taylor instability analysis, with the same experimental data set used here. Based on the numerical predictions presented in Grace et al. [25], the mean deviation from the experimental data of Merrington and Richardson [2], Ryan [40] and Finlay [39] is in the order of + 31.85%. When this figure is compared with the present model mean deviation of + 12.08% from the same data set indicates the effects of relative velocity on the interfacial stability. Although the breakup models used here and by Grace et al. are similar in nature inclusion of the relative velocity effects considerably improves the predictions.

#### 17.4.2. Drops in High Gas Velocity Field

In this case, again,  $\theta_w = \pi/2$ ,  $\rho^* \gg 1.0$  and  $Nu_c \ll 1/0$ ; however,  $u_c$  is not uniquely expressed in terms of  $d_e$ . In order to de-couple  $We$  and  $d_e^*$ , a modified Weber number,  $We_m$ , is defined as

$$We_m \equiv \frac{\rho_c u_c^2}{(\sigma g |\Delta \rho|)^{1/2}} = \frac{We}{d_e^*} \quad (49)$$

It may be shown from Eq. [45] that the criterion becomes

$$d_e^{*2} + 0.26 We_m d_e^* - 4 = 0 \quad (50)$$

The breakup diameter for droplets in a high velocity gas stream as predicted by Eq. (50) is illustrated in Figure 12. The predictions are also compared in the figure with those determined by classical Weber number criterion,  $We \approx 12-16$ , and by Kataoka et al. [42] correlation. The latter which was obtained in collaboration with a large number of experimental air-water data of Wicks and Dukler [43], Cousins and Hewitt [44] and Linsted et al. [45], is given in its original form as

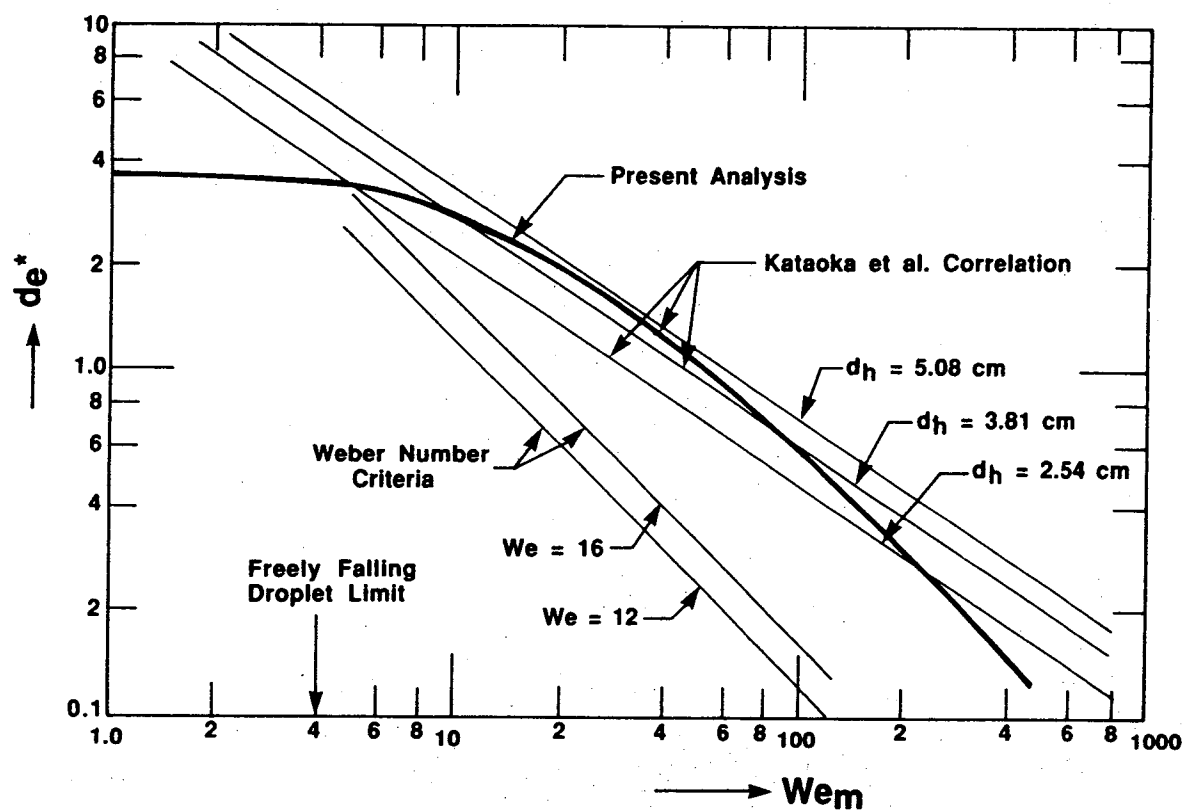


Figure 12. Breakup diameter correlation for drops in a high velocity gas stream and comparison with other correlations.



$$We = 0.031 Re_{cd}^{2/3} (\rho_c/\rho_d)^{-1/3} (\nu_c/\nu_d)^{2/3} \quad (51)$$

where  $Re_{cd}$  is the continuous phase Reynolds number based on the hydraulic equivalent diameter of flow passage. For the purpose of convenience Kataoka et al.'s correlation may be recast into the following form

$$d_e^* = 0.031 \left( \frac{d_h^*}{Nu_d We_m} \right)^{2/3} \quad (52)$$

where  $d_h^*$  and  $Nu_d$ , respectively, are the dimensionless hydraulic equivalent diameter of flow passage,  $d_h^* \equiv d_h (g|\Delta\rho|/\sigma)^{1/2}$ , and dispersed phase viscosity number,  $Nu_d \equiv \nu_d/(\rho_c^2 \sigma^3/g|\Delta\rho|)^{1/4}$ . For the purpose of comparisons, air-water properties at atmospheric conditions are used for evaluating  $Nu_d$ , and the hydraulic diameter is treated as a parameter in Figure 12.

It is important to note from Figure 12 that as the hydraulic diameter increases Kataoka et al.'s data based predictions approaches to the present model predictions in the general trend as well as numerical values. The agreement is remarkably good in relatively large flow channels. This is an expected result since the present model is based on the stability of a single particle in an infinite medium neglecting the effects of surrounding particles and the wall effects. On the other hand, the classical Weber number criterion with constant being 12 and 16 as shown in the figure consistently underestimates the breakup diameter. Although general trends are similar to the present model, predictions of the Weber number criterion are quite different from those obtained from the present model and the Kataoka et al.'s correlation. The classical Weber number criterion and its predictions are discussed in more detail in Kataoka et al. [42].

In conclusion, the comparison with experimentally data based correlation of Kataoka et al. [42] indicates that indeed the proposed breakup mechanism

has been the dominant factor in determining the maximum fluid particle size. Presently, an investigation has been underway to improve the present model to take into account the effects of surrounding particles and wall effects.

#### 17.4.3. Rising Bubbles in Liquids

In view of (25), the Weber number can be expressed as

$$We = \left(\frac{2C_e}{9}\right) d_e^{*2} \quad (53)$$

Noting that  $\rho^* \ll 1.0$  for rising bubbles, and using Eq. (53) in Eq. (44), the breakup criterion becomes

$$d_e^{*2} = \left[ 4 \left(\frac{2\pi}{\theta_\omega}\right)^4 \left(\frac{1}{C_e}\right)^2 \right] / \left\{ 2.25 \left(\frac{2\pi}{\theta_\omega}\right)^2 \sin^2 \left(\frac{\theta_\omega}{2}\right) \rho^* + 0.5 \left(\frac{2\pi}{\theta_\omega}\right) - [0.584 (1+N\mu_c)^{0.35} \left[ \ln \left( \frac{|\tan(\theta_\omega/2)|}{|\tan(\theta_\omega/4)|} \right) \right]^{-2} \right\} \quad (54)$$

where  $\theta_\omega$  is given as a function of  $Re_c$  by Eq. (22).

Basically it seems there are three independent variables, namely  $\theta_\omega$ ,  $\rho^*$  and  $N\mu_c$ , affecting  $d_e^*$ . However, with the terminal velocity for large bubbles given by Eq. (25), the  $Re_c$  can be expressed as

$$Re_c = \left(\frac{2}{3}\right) \left(\frac{C_e}{2}\right)^{1/2} \left(\frac{d_e^*}{N\mu_c}\right)^{3/2} \quad (55)$$

This indicates that there are two independent variables rather than three. Furthermore, noting that the term containing  $\rho^*$  is much smaller than the other two terms in Eq. (54), and in view of Eq. (53) it may be observed that  $d_e^* = f(N\mu_c)$  only. Hence a simpler correlation yet can be developed in this functional form. It may be shown that

$$d_e^* = 27.07 (1 + N_{\mu_c}')^{0.83} \quad (56)$$

is a very good representation of Eq. (54) for bubble breakup diameter.

Modified viscosity number  $N_{\mu_c}'$  is defined as

$$N_{\mu_c}' \equiv N_{\mu_c} d_e^* \quad (57)$$

Equation (56) is very simple to use when compared to Eq. (54). It is presented in Figure 13 along with the Grace et al. data. The breakup diameter slightly increases as the modified continuous phase viscosity number increases. As demonstrated by Kocamustafaogullari [46], this may be attributed to the smoothing effect of the interfacial shear on the growth of interfacial waves. Unfortunately number of experimental data available in the literature is very limited for this case to check the validity of Eq. (56) in more detail.

#### 17.4.4. Freely Falling or Rising Drops in Immiscible Liquids

Recalling that  $\theta_\omega = \pi/2$  for drops, the breakup criterion can be simplified to obtain

$$d_e^{*2} + [4.5 \left( \frac{\rho^*}{1+\rho} \right) - 0.35 \left( \frac{2+3\rho^*}{1+\rho} \right)^{2.27} (1 + N_{\mu_c}')^{0.36} We - 16 = 0 \quad (58)$$

With the terminal velocity given by Eq. (27) and the Archimedes number defined by Eq. (28), We number can be expressed as

$$We = 0.25 \frac{N_{\mu_c}^2}{d_e^*} \left\{ \left[ F^2 + 2 \left( \frac{d_e^{*3}}{N_{\mu_c}^2} \right)^{1/2} - F \right]^2 \right\} \quad (59)$$

where  $F$  is defined as

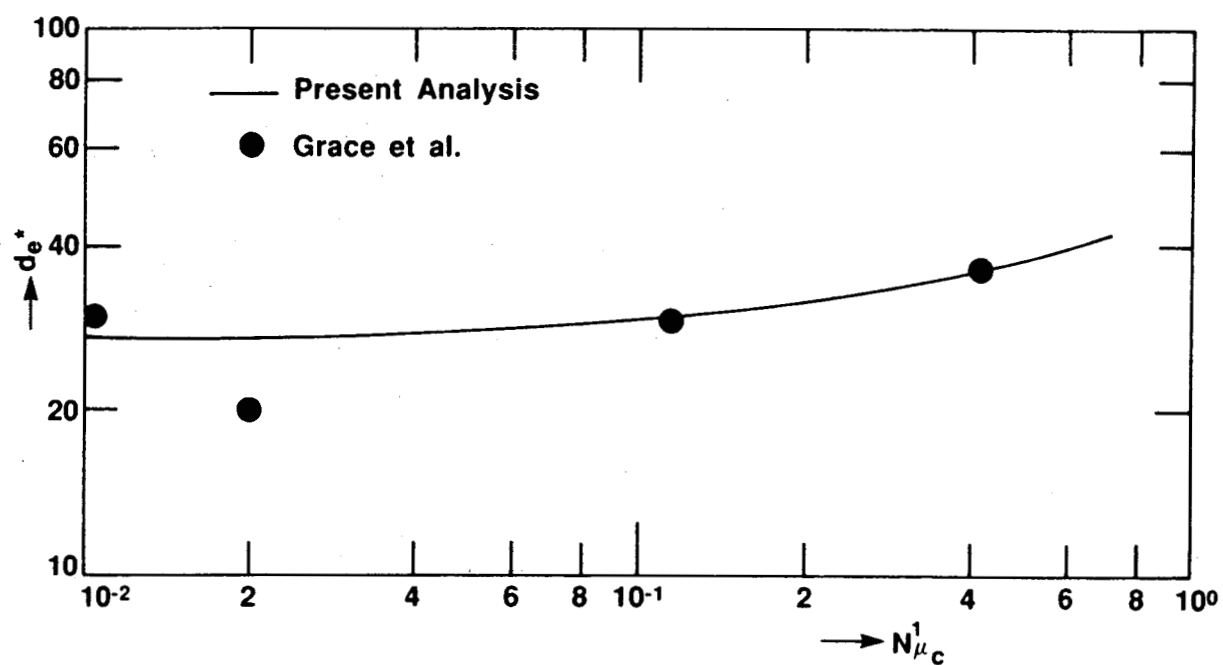


Figure 13. Breakup diameter correlation for bubbles and comparison with experimental observations.

$$F \equiv \frac{3[2+3(\nu_d/\nu_c)]}{1 + (\nu_d/\nu_c)} \quad (60)$$

It is important to note that as  $(\nu_d/\nu_c)$  increases from 0 to  $\infty$ ,  $F$  varies only from 6 to 9, indicating the insignificant effect of  $(\nu_d/\nu_c)$  ratio on the Weber number. Therefore,  $We$  can be approximated from Eq. (59) as follows:

$$We \approx 0.5 d_e^{*2} \quad (61)$$

In view of Eq. (61) the breakup criterion for drops in liquids can be further simplified resulting in the following expression:

$$d_e^{*2} = \frac{16}{1 + 0.5 \left[ 4.5 \left( \frac{\rho^*}{1+\rho} \right) - 0.35 \left( \frac{2+3\rho^*}{1+\rho} \right)^{2.27} (1+N_{\mu_c})^{0.36} \right]} \quad (62)$$

This equation can be safely used for  $N_{\mu_c} \leq 4$  to predict the breakup diameter of freely falling or rising liquid droplets in stagnant liquids. The influence of  $N_{\mu_c}$  is illustrated in Figure 14. The dimensionless breakup diameter slightly increases as the continuous phase viscosity number increases. This behavior is similar to the bubble breakup behavior as illustrated in Figure 13. Comparison between predicted and experimental observations are good for low values of  $N_{\mu_c}$  which is the case for most practical applications. However, when  $N_{\mu_c} > 4$  Eq. (58) is recommended with  $We$  expressed by Eq. (59).

## 17.5. Summary and Conclusions

Based on the combination of Kelvin-Helmholtz and Rayleigh-Taylor stability theory, a simple mechanistic model is developed to describe the breakup of

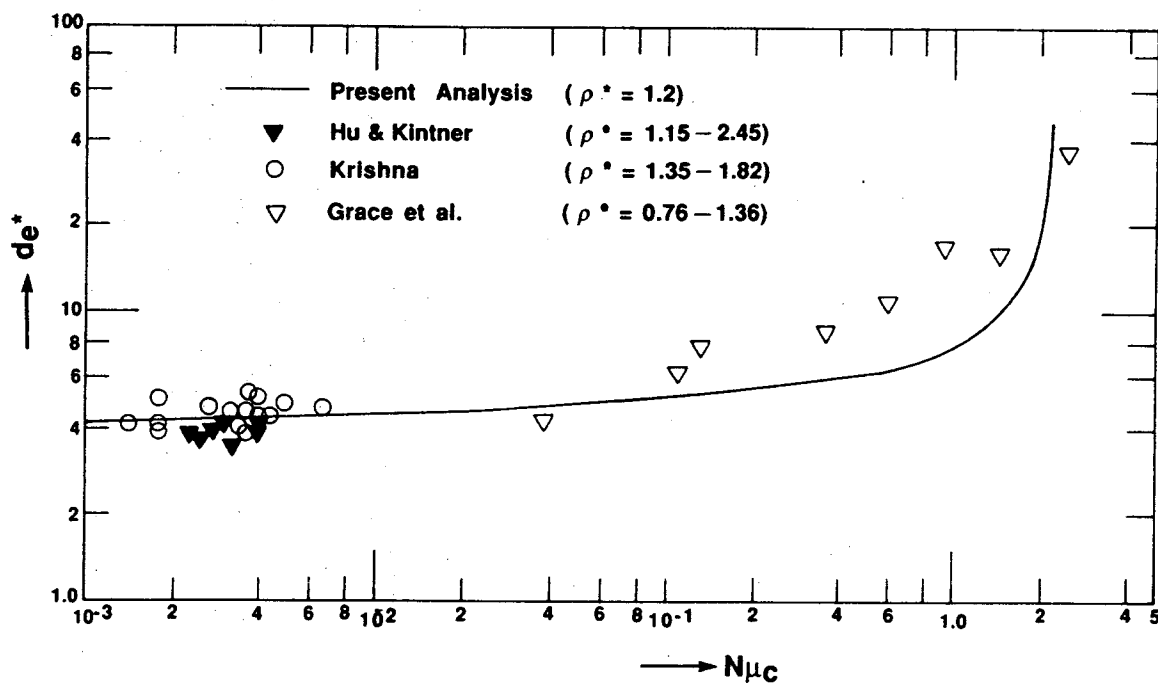


Figure 14. Breakup diameter correlation for drops in liquids and comparison with experimental observations.

drops and bubbles falling or rising freely in a stagnant media. Breakup is predicted to occur if the growth of disturbances on the leading front is rapid enough relative to the rate at which the disturbance is propagated around the interface. In collaboration with a large number of experimental data for liquid-gas, liquid-liquid and gas-liquid systems, a general correlation is developed to predict the maximum stable particle size in a stagnant fluid. The results are extended to predict the maximum droplet size in a high velocity gas field. Important dimensionless parameters affecting the breakup process are properly identified. They are Weber number, continuous phase viscosity number, density and viscosity ratio groups. For each case importance of these groups are assessed.

Predicted values of the maximum particle size are compared with experimental data. An average deviation of  $\pm 13.94\%$  between predicted and experimental value is observed. Considering the various simplifications made in the analysis the agreement is favorably good, and much better than those obtained from the Rayleigh-Taylor instability.

For the purpose of practical applications, the general breakup criterion is simplified for four separate cases, i.e., for freely falling drops in a gas, droplets in a high velocity gas stream, freely rising bubbles and finally for freely falling or rising drops in liquids. Simple correlations are developed for each case. With the proper form of the terminal velocity it is demonstrated that the dimensionless break-up diameter can be expressed in terms of  $\rho^*$ ,  $Nu_c$  and  $(\mu_d/\mu_c)$ . Depending on the bubbles or drops effective dimensionless groups can be further reduced as given by Eqs. (47), (50), (56) and (61).

The theoretical model developed in this study is clearly approximate in nature, including such simplifications as treatment of growth of three-

dimensional disturbances on curved interfaces by means of two-dimensional, small-amplitude waves on a flat interface. Despite these approximations agreement with experimental results indicate that the principal physical mechanisms involved are properly accounted for.



TABLE I Summary of Various Experiments on Maximum  
Fluid Particle Size

Reference	Dispersed/Continuous Fluids	$\rho^*$	$N_{\mu C}$	$d_e^*$	Mean Deviation (%)
Merrington & Richardson	Liquid/Gas	884 - 1442	$1.1 \times 10^{-3} - 2.7 \times 10^{-3}$	3.73 - 4.63	+10.36
Ryan	Liquid/Gas	953	$1.6 \times 10^{-3} - 3.5 \times 10^{-3}$	3.25 - 3.42	+5.80
Finlay	Liquid/Gas	767 - 2834	$1.2 \times 10^{-3} - 2.6 \times 10^{-3}$	2.67 - 4.32	+25.85
Krishna et al.	Liquid/Liquid	1.15 - 3.32	$1.4 \times 10^{-3} - 6.7 \times 10^{-3}$	3.74 - 5.65	+9.80
Hu & Kintner	Liquid/Liquid	1.64 - 3.33	$2.4 \times 10^{-3} - 4.0 \times 10^{-3}$	3.50 - 4.38	+10.39
Grace et al.	Liquid/Liquid	0.75 - 1.36	$3.8 \times 10^{-2} - 6.9$	4.06 - 37.06	+29.55
Grace et al.	Gas/Liquid	$10^{-3} - 1.6 \times 10^{-3}$	$4.5 \times 10^{-2} - 2.6$	19.27 - 36.95	+14.66
Sundell	Gas/Liquid	$1.41 \times 10^{-3}$	$2.3 \times 10^{-3}$	30.98	+6.79

## 17.6. Appendix

### Kelvin-Helmholtz Instability

The stability of two superposed incompressible, inviscid fluids to be considered here is illustrated in Figure 15. The lower fluid is identified by subscript 1 and the upper fluid by 2. The fluids are flowing concurrently in a horizontal, constant area channel. The velocities of the two fluids are assumed to be horizontal in direction, and denoted by  $u_1$  and  $u_2$ , respectively. Assuming the fluids are inviscid and the perturbed flow is irrotational, the complex wave celerity,  $c$ , has been obtained as follows:

$$c = \frac{\rho_1 \coth(kh_1) u_1 + \rho_2 \coth(kh_2) u_2}{\rho_1 \coth(kh_1) + \rho_2 \coth(kh_2)} \pm \left\{ \frac{\sigma k^2 + g(\rho_1 - \rho_2)}{[\rho_1 \coth(kh_1) + \rho_2 \coth(kh_2)]k} - \frac{\rho_1 \rho_2 \coth(kh_1) \coth(kh_2) (u_1 - u_2)^2}{[\rho_1 \coth(kh_1) + \rho_2 \coth(kh_2)]^2} \right\}^{1/2} \quad (A1)$$

where, as illustrated in Figure 15,  $h_1$  and  $h_2$  represent the fluid thickness of the lower and upper fluids, respectively, and  $k$  is the wave number,  $k = 2\pi/\lambda$ . In deriving this equation, it was assumed that the interfacial perturbation is periodic in  $x$ . Thus,

$$\eta = \eta_i \exp[ik(x-ct)] \quad (A2)$$

where  $\eta_i$  is the perturbation amplitude at the interface.

Details of derivations leading to [A1] were not given here because the derivations here closely followed Chendresekher [47], Lamb [48] and Yih [49], where the stability of the two superposed fluids with semi-infinite depth was studied. Separating the complex wave celerity into real and imaginary parts by

$$c = c_r + i c_i \quad (A3)$$

the components can be expressed as follows:

$$c_r = \frac{\rho_1 \coth(kh_1) u_1 + \rho_2 \coth(kh_2) u_2}{\rho_1 \coth(kh_1) + \rho_2 \coth(kh_2)} \quad (A4)$$

and

$$kc_i = \left\{ \frac{\rho_1 \rho_2 \coth(kh_1) \coth(kh_2) (u_1 - u_2)^2 k^2}{[\rho_1 \coth(kh_1) + \rho_2 \coth(kh_2)]^2} - \frac{\sigma k^3 - g (\rho_1 - \rho_2) k}{[\rho_1 \coth(kh_1) + \rho_2 \coth(kh_2)]} \right\}^{1/2} \quad (A5)$$

where  $c_r$  denotes the velocity of propagation of the wave in the x-direction whereas  $kc_i$  is the growth factor which determines the degree of amplification or damping. The disturbances are damped if  $kc_i < 0$  and the mean flow configuration is stable, the disturbances are amplified if  $kc_i > 0$ , and the mean flow is unstable. Finally the mean flow is said to be neutrally stable if  $kc_i = 0$ .

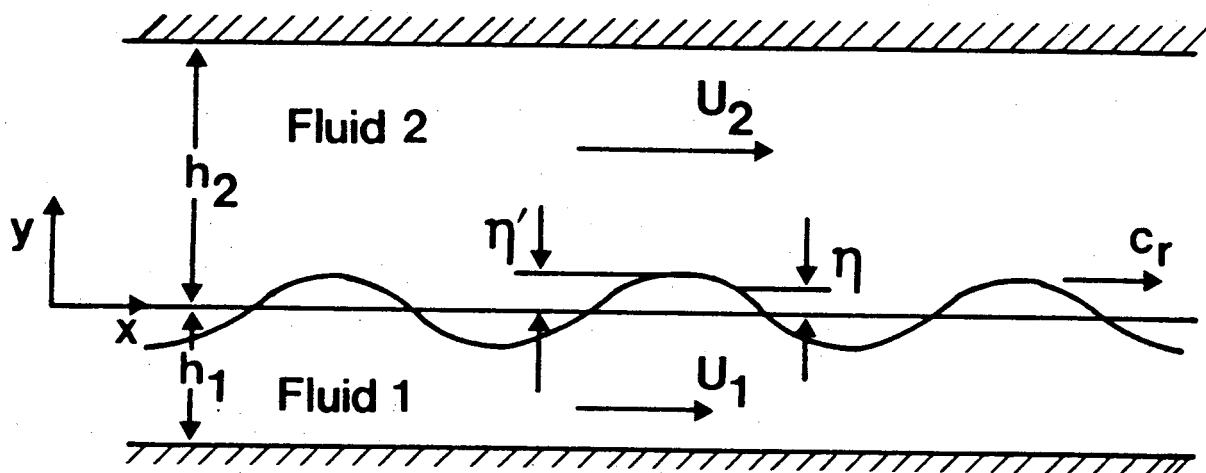


Figure 15. Stability of two superimposed fluids flowing concurrently in a constant cross sectional area channel.

## **Acknowledgement**

The work reported in this report was supported by a grant from the U.S. Department of Energy (DE-FG02-87ER13764).

## Nomenclature

$Ar$	Archimedes number
$c$	Complex wave celerity
$c_i$	Imaginary part of wave celerity
$c_r$	Speed of propagation
$d$	Diameter
$d_e$	Volume-equivalent sphere diameter
$(d_e)_{\max}$	Maximum value of $d_e$ at breakup
$d_p$	Twice the mean radius of curvature
$F$	Dimensionless group defined by Eq. (60)
$h$	Fluid thickness
$g$	Gravitational acceleration
$k$	Wave number, $2\pi/\lambda$
$k_m$	Wave number at particle breakup
$M$	Morton number
$N_\mu$	Viscosity number
$N'_\mu$	Modified viscosity number
$P$	Pressure
$R_p$	Mean radius of curvature
$S$	Maximum velocity gradient in the continuous fluid
$t$	Time
$t_g$	Growth time
$t_p$	Propagation time
$u$	Velocity
$u_c$	Rise or fall velocity
$u_{c\theta}$	Tangential component of $u_c$ at the interface
$We$	Weber number

$x$	Horizontal coordinate axis
$y$	Vertical coordinate axis
$\epsilon$	Energy dissipation per unit mass per unit time
$ \Delta\rho $	Absolute value of density difference, $ \rho_c - \rho_d $
$\eta$	Local wave height
$\eta_i$	Wave amplitude
$\theta$	Angular position
$\theta_0$	Angular position of initial disturbances
$\theta_w$	Wake angle
$\lambda$	Wave length
$\rho$	Mass density
$\sigma$	Surface tension

#### Subscripts

1	Lower fluid in Kelvin-Helmholtz instability
2	Upper fluid in Kelvin-Helmholtz instability
c	Continuous fluid
$c_r$	Critical value
d	Dispersed fluid
max	Maximum value
tr	Turbulent

#### Superscript

'	Disturbances
*	Dimensionless variables

## References

1. LENARD, P., Ueber Regen. Meteor. Zeit., Vol. 21, pp. 248-262 (1904).
2. MERRINGTON, A. C. and RICHARDSON, E. G., "The Break-up of Liquid Jets," Proc. Phys. Soc. (London), Vol. 59, pp. 1-13 (1947).
3. HINZE, J. O., "Critical Speeds and Sizes of Liquid Globules," Appl. Sci. Res., A. 1, pp. 273-281 (1948).
4. LANE, W. R., "Shatter of Drops in Streams of Air," Ind. Eng. Chem., Vol. 43, pp. 1312-1317 (1951).
5. HAAS, F. C., "Stability of Droplets Suddenly Exposed to a High Velocity Gas Stream," AIChE J., Vol. 10, pp. 920-924 (1964).
6. HANSON, A. R., DOMICH, E.G., and ADAMS, H. S., "Shock Tube Investigation of the Breakup of Drops by Air Blasts," Phys. Fluids, Vol. 6, pp. 1070-1080 (1963).
7. HINZE, J. O., "Fundamentals of the Hydrodynamic Mechanism of Splitting Dispersion Processes," AIChE J., Vol. 1, pp. 289-295 (1955).
8. BRODKEY, R. S., The Phenomena of Fluid Motions, Addison-Wesley Pub. Co. (1967).
9. TAYLOR, G. E., "The Function of Emulsion in Definable Field Flow," Proc. Roy. Soc. (London), Series A, Vol. 146, pp. 501-523 (1934).
10. TOMOTIKA, S., "Breaking Up of a Drop of Viscous Liquid Immersed in Another Viscous Fluid Which is Extending at a Uniform Rate," Proc. Roy. Soc. (London), Series A, Vol. 153, pp. 302-320 (1936).
11. RUMSCHEIDT, F. F. and MASON, S. G., "Particle Motion in Sheared Suspensions, XII. Deformation and Burst of Fluid Drops in Shear and Hyperbolic Flows," J. Colloid Sci., Vol. 16, pp. 238-261 (1967).
12. KARAM, H. J. and BELLINGER, J. C., "Deformation and Breakup of Liquid Droplets in a Simple Shear Field," Ind. Eng. Chem. Fundam., Vol. 7, pp. 576-581 (1968).
13. BUCKMASTER, J. D., "The Bursting of Pointed Drops in Slow Viscous Flow," J. Appl. Mech., Vol. 40, pp. 18-24 (1973).
14. KOLMOGOROV, A. M., "On the Disintegration of Drops in a Turbulent Flow," Doklady Akad. Nauk, SSR, Vol. 66, pp. 825-832 (1949).
15. SLEICHER, C. A., "Maximum Drop Size in Turbulent Flow," AIChE J., Vol. 8, pp. 471-477 (1962).
16. SEVIK, M. and PARK, S. H., "The Splitting of Drops and Bubbles by Turbulent Fluid Flow," J. Fluids Eng., Vol. 95, pp. 53-60 (1973).



17. KOMABOYASHI, M., GONDA, T., and ISONO, K., "Lifetime of Water Drops Before Breaking and Size Distribution of Fragment Drops," J. Meteor. Soc. Japan, Ser. 2, Vol. 42, pp. 330-340 (1964).
18. BLANCHARD, D. C., "Comments on the Breakup of Raindrops," J. Atmos. Sci., Vol. 19, pp. 119-120 (1962).
19. COTTON, W. R. and GOKHALE, N. R., "Collision Coalescence and Breakup of Large Water Drops in a Vertical Wind Tunnel," J. Geophys. Res., Vol. 72, pp. 4041-4049 (1962).
20. KLETT, J. D., "On the Breakup of Water Drops in Air," J. Atmos. Sci., Vol. 28, pp. 646-647 (1971).
21. HENDRICKSEN, H. K. and OSTERGAARD, K., "On the Mechanism of Breakup of Large Bubbles in Liquids in Three-Phase Fluidized Beds," Chem. Eng. Sci., Vol. 29, pp. 626-629 (1974).
22. CLIFT R., GRACE, J. R., "The Mechanisms of Bubble Breakup in Fluidized Beds," Ind. Eng. Chem. Fundam., Vol. 27, pp. 2309-2310 (1973).
23. CLIFT R., GRACE, J. R., and WEBER, M. E., "Stability of Bubbles in Fluidized Beds," Ind. Eng. Chem. Fundam., Vol. 13, pp. 45-51 (1974).
24. CLIFT R., GRACE, J. R., and WEBER, M. E., Bubbles, Drops and Particles, Academic Press, New York (1978).
25. GRACE, J. R., WAIREGI, T. and BROPHY, J., Break-up of Drops and Bubbles in Stagnant Media, Can. J. Chem. Eng., Vol. 56, pp. 3-8 (1978).
26. MOORE, D. W., J. Fluid Mech. Vol. 6, pp. 113-130 (1959).
27. LINTON, M., and SUTHERLAND, K. L., Proc. Int. Congr. Surface Act., London, Vol. 1, pp. 494-502 (1957).
28. MOORE, D. W., J. Fluid Mech. Vol. 6, pp. 113-130 (1959).
29. COLLINS, R., J. Fluid Mech., Vol. 25, pp. 469-480 (1976).
30. RIPPIN, D. W. T., and DAVIDSON, J. F., Chem. Eng. Sci., Vol. 22, pp. 217-228 (1967).
31. HU, S. and KINTNER, R. G., "The Fall of Single Liquid Drops Through Water," AIChE J., Vol. 1, pp. 43-49 (1955).
32. KLEE, A. J. and TREYBALL, R. E., "Rate of Rise or Fall of Liquid Drops," AIChE J., Vol. 2, pp. 444-447 (1956).
33. MENDELSON, H. D., "Prediction of Bubble Terminal Velocities from Wave Theory," AIChE J., Vol. 13, pp. 250-252 (1967).
34. MARRUICI, G., APUZZO, G. and ASTARITA, G., "Motion of Liquid Drops in Non-Newtonian Systems," AIChE J., Vol. 16, pp. 538-541 (1970).

35. WALLIS, G. B., "The Terminal Speed of Single Drops or Bubbles in an Infinite Medium," *Int. J. Multiphase Flow*, Vol. 1, pp. 491-511 (1974).
36. ISHII, M., and ZUBER, N., "Drag Coefficient and Relative Velocity in Bubbly, Droplet or Particulate Flows," *AIChE Journal*, Vol. 25, pp. 843-855 (1979).
37. GRACE, J. R., WAIREGI, T., and NGUYEN, T. H., "Shapes and Velocities of Single Drops and Bubbles Moving Freely Through Immiscible Fluids," *Trans. Inst. Chem. Eng.*, Vol. 54, pp. 167-173 (1976).
38. KRISHNA, P.M., VENKATESWARLU, D. and NARASIMHAMURTY, G. S. R., "Fall of Liquid Drops in Water, Drag Coefficients, Peak Velocities and Maximum Drop Sizes," *J. Chem. Eng. Data*, Vol. 4, pp. 340-343 (1959).
39. FINLAY, B. A., "A Study of Liquid Drops in Air," Ph.D. Thesis, Univ. Birmingham (1957).
40. RYAN, R. T., "The Possible Modification of Convective Systems by the Use of Surfactants," *J. Appl. Meteor.*, Vol. 15, pp. 3-8 (1978).
41. SUNDELL, R. D., Ph.D. Thesis, Yale Univ. (1978).
42. KATAOKA, I., ISHII, M., and MISHIMA, K., "Generation and Size Distribution of Droplets in Annular Two-Phase Flow," *J. Fluids Engr.*, Vol. 105, pp. 230-238 (1983).
43. WICKS, M. and DUKLER, A. E., "In Situ Measurements of Drop Size Distribution in Two-Phase Flow," *Int. Heat Trans. Conf.*, Chicago (1966).
44. COUSINS, L. B. and HEWITT, G. F., "Liquid Phase Mass Transfer in Annular Two-Phase Flow: Droplet Deposition and Liquid Entrainment," AERE-R5657 (1968).
45. LINSTED, R. D., EVANS, D. L., GASS, J. and SMITH, R.V., "Droplet and Flow-Pattern Data, Vertical Two-Phase (Air-Water) Flow Using Axial Photography," Wichita State University, Department of Mechanical Engineering (1978).
46. KOCAMUSTAFAOGULLARI, G., "Two-Fluid Modeling in Analyzing the Interfacial Stability of Liquid Film Flows," *Int. J. Multiphase Flow*, Vol. 11, pp. 63-89 (1985).
47. CHANDRESEKHER, S., Hydrodynamic and Hydromagnetic Stability, Oxford Univ. Press (1968).
48. LAMB, H., Hydrodynamics, (Sixth Ed.), Dover Publications (1945).
49. YIH, C. H., Stratified Flows, (Second Ed.), Academic Press (1980).

## **18. MEASUREMENT AND MODELING OF VOID FRACTION, BUBBLE SIZE AND INTERFACIAL AREA**

G. Kojasoy, W.D. Huang and J. Razi  
Department of Mechanical Engineering  
University of Wisconsin-Milwaukee  
Milwaukee, WI 53201, U.S.A.

### **ABSTRACT**

Local void fraction, bubble size and interfacial area concentration for cocurrent air-water bubbly flow through a horizontal pipe of 50.3 mm ID have been experimentally investigated by using double-sensor resistivity probe method. The local and area-averaged void fractions and interfacial area concentrations were analyzed as a function of liquid and gas flow rates. These parameters were found to increase systematically with decreasing liquid flow and increasing gas flow. However, variations with the liquid flow were not as significant as with the gas flow. A consistent variation of the gas phase drift velocity and distribution parameter with the liquid flow rate was observed. It was demonstrated that presentation of average void fraction in terms of flowing volumetric concentration was more appropriate for horizontal bubbly flow.

Several bubble breakup mechanisms are discussed. It is concluded that average pressure fluctuations generated by the turbulent liquid fluctuations acting across a bubble diameter is the only mechanism which causes distortion of a bubble. Based on this force and the competing surface tension force a theoretical model is developed for mean bubble size and interfacial area concentration. The theoretically predicted mean bubble size and interfacial area concentration are found to agree reasonably well with those measured by the double-sensor resistivity method.

## 18.1. Introduction

The bubbly two-phase flow-pattern is characterized by the presence of bubbles, with maximum size much smaller than the diameter of the containing vessel or pipe, dispersed in a continuous liquid phase. This flow-pattern is of great importance in the process industry, where a number of gas-liquid contractors operate under bubbly flow conditions in order to increase interfacial areas for mass and/or heat transfer between phases.

The void fraction, interfacial area and the Sauter mean diameter of bubbles are three fundamental geometric parameters characterizing the internal structure of bubbly two-phase flow-pattern. The void fraction represents the phase distribution and is a required parameter for hydrodynamic and thermal design in various industrial processes. The interfacial area describes the available interfacial area for the interfacial transport of mass, momentum and energy in steady and transient two-phase flows and is a required parameter for a two-fluid model formulation. Finally, the third parameter, the Sauter mean diameter, serves as a link between the void fraction and interfacial area. It is an essential parameter for interfacial area modeling. However, experimental data on the local values of these parameters are very scarce. Most of the available experimental data are limited to the volume averaged interfacial area concentration over a section of a flow channel. There are very few data available on the local measurements of interfacial area concentration. Furthermore, there are very few established theoretical foundations for relating the interfacial area to some easily measureable quantities. According to the authors' knowledge there has been no experimental data or fundamental studies available on the local distribution of interfacial area concentration in horizontal bubbly two-phase flow.

Several methods are available at present to measure interfacial area concentration in gas-liquid and liquid-liquid flows. These are photographic, light attenuation, ultrasonic attenuation, chemical absorption and double-sensor probe methods [1-10]. Due to relatively developed state and ability to give reliable results in studies of two-phase flow structure, particularly in high speed two-phase flow with local void fractions possibly ranging from zero to 60 ~ 65% which would be expected in horizontal bubbly two-phase flow, the electrical resistivity probe technique was used to experimentally study the local interfacial parameters in a horizontal bubbly two-phase flow. Local and average void fraction, interfacial area concentration, interfacial velocity and bubble size were measured. This paper which summarizes the experimental set-up and experimental data on local interfacial parameters has two objectives. The first is to interpret experimental data on averaged value of interfacial parameters in terms of flow variables. The second objective is to mechanistically model the interfacial area concentration to obtain experimentally supported predictive methods.

## **18.2. Experimental Setup**

The overall flow schematic is illustrated in Figure 1. The loop basically consists of 50.3 mm ID circular Pyrex glass tubings with pressure tabs installed between them. The entire test section is about 15.4 m in length, and it is all transparent. It is designed such that various local instrumentations for two-phase flow measurements and different mixing chambers can be easily accommodated.

The air and water are used as coupling fluids. The air to the test section is supplied from the central air system available in the institution. It is, however, regulated through a 250 gallon-capacity high-pressure storage tank, and

metered by a series of turbine flow meters. The water is recirculated. It is pumped from a 500 gallon-capacity storage tank by a stainless-steel centrifugal pump and regulated by a transistor inverter. The water flow rate is measured by a series of paddle wheel flow meters assembled in a parallel configuration.

As shown above in Figure 1 the air enters the mixing chamber from a 90° vertical leg and is injected into the water flow through a cylindrical porous media of 100  $\mu\text{m}$  porosity to achieve a uniform mixing and a quick development of a bubbly two-phase flow-pattern. The cylindrical porous media is centered in the glass test section, and directs the air flow from 90° angle to an axially symmetric aligned downstream direction. The water enters the mixing chamber from axially aligned upstream section of the mixing chamber. The two-phase mixture from the test section is discharged to an air-water separator. The air is vented to the atmosphere, and the water is returned to the water storage tank.

The experiments were carried out under fully developed bubbly flow conditions by using a double-sensor resistivity probe. Liquid and gas volumetric superficial velocities ranged from 3.74 to 6.59 m/s and 0.21 to 1.34 m/s, respectively, and averaged void fractions ranged from 3.73 to 21.5%. Details of the experimental conditions are summarized in Table I. The local values of void fraction, interfacial area concentration, bubble interface velocity, Sauter mean bubble diameter and bubble frequency distributions were measured at  $L/D = 253$  downstream of the air-water mixing chamber. Twenty-three probe locations were selected through the vertical pipe diameter. For more information concerning the flow loop, air-water mixing and experimental procedure, see Kocamustafaogullari et al. [1,2].

## 18.3. Experimental Results and Discussions

### 18.3.1. Local Distribution of Interfacial Parameters

Details of experimental procedure and signal processing are given elsewhere by Kocamustafaogullari et al. [1,2]. A sample of local measurements using the double-sensor probe in the air-water loop is shown in Figures 2-4. Here  $r/R$  is the ratio between the probe location along the vertical axis from pipe center,  $r$ , and the pipe radius,  $R$ . The area-averaged superficial liquid velocity,  $\langle j_f \rangle$ , is kept constant whereas the superficial gas velocity,  $\langle j_g \rangle$ , is treated as a parameter. The data set presented in these figures are typical distributions of various interfacial parameters for the horizontal bubbly two-phase flow investigated in this study.

It can be seen from Figure 2 that, in horizontal pipes, buoyancy provokes the migration of gas bubbles toward the top of the pipe and the flow becomes highly non-symmetric in the pipe cross-section. The profiles of the void fraction for a given liquid flow rate show that with an increase in gas flow the local void fraction increases. Although it cannot be observed from these figures, the local void fraction slightly decreases with an increase in the liquid flow rate for a given gas flow rate. The void fraction under all test conditions generally exhibits a distinct peak near the top wall at about  $r/R \approx 0.8 \sim 0.9$ , and that the profiles tend to be uniform with increasing gas flow or average void fraction,  $\langle \alpha \rangle$ . This range corresponds to 2.5 ~ 5 mm distance from the wall. When these values are compared with observed mean bubble diameter, the geometry seems to explain the steep decrease in the local void fraction toward the wall. In other words, the bubble size determines the location of maximum in the void fraction.

The interfacial area concentration profiles show similar behavior as the void fraction profiles with changes in the gas and liquid flow rates, Figure 3.

For the horizontal flow, the observed local void fraction can reach 0.65, the peak interfacial area concentration can go up to  $900 \sim 1000 \text{ m}^2/\text{m}^3$ . Since the local transport of mass, momentum and energy are directly proportional to the interfacial area concentration the figures point to the fact of a highly non-symmetric interfacial transport in a horizontal two-phase flow configurations. The wall peaking in void fraction has been observed in vertical flow configurations by several investigators [3-11]. However, the numerical values of local peaks of void fraction and interfacial area reported here are much larger than those observed in vertical flow configurations.

Using the relation between the local interfacial area concentration, void fraction and the Sauter mean diameter of bubbles, the mean bubble size is calculated. The local Sauter mean diameter profiles are illustrated in Figure 4. The mean bubble size ranges from 2.5 to 5 mm depending on the location and flow conditions. The bubble diameter generally increases with the gas flow at a given liquid flow rate, although the effect is not as significant as those observed for the local void fraction and interfacial area concentration.

It is interesting to note that the bubble size distribution is almost uniform in the core and exhibits a decrease toward the wall. This observation led us to believe that the bubble size in the core is significantly affected by the core turbulence, which can be approximated homogeneous isotropic. For such conditions it is expected a uniform bubble size in the core. However, the flow conditions in the vicinity of the wall are farthest from these conditions. Near the wall there exists very strong velocity gradient which causes further breakup according to Taylor's breakup mechanism into smaller bubble sizes resulting in smaller void fractions toward the wall. From this argument it can be concluded that the maximum void fraction can only occur within a distance of a core bubble size from the wall, which justifies experimental observations for the location



of maximum void fraction at about  $r/R \approx 0.8 \sim 0.9$  corresponding to the core bubble size observations.

### 18.3.2. Area-Averaged Interfacial Parameters

The area-averaged values of the void fraction and the interfacial area concentration are defined by

$$\langle \alpha \rangle \equiv \frac{1}{A} \int_A \alpha(r) dA \quad (1)$$

$$\langle a_i \rangle \equiv \frac{1}{A} \int_A a_i(r) dA \quad (2)$$

The averaged value of Sauter mean diameter, then, is given by

$$\langle d_{sm} \rangle \equiv \frac{6 \langle \alpha \rangle}{\langle a_i \rangle} \quad (3)$$

The effects of the liquid and gas flow on the void fraction, interfacial area concentration and Sauter mean diameter are illustrated in Figures 5, 6 and 7 for ten different cases of the liquid superficial velocities. All the data lie on different lines, each corresponding to a particular value of the liquid superficial velocity. Exactly similar observations were made recently by Delhayé and Brickard [10] for vertical pipe flow.

From these figures one can observe that the influence of  $\langle j_f \rangle$  on these parameters is generally very small. This is particularly true for the case of interfacial area concentration. However, these average parameters are significantly affected by the superficial gas velocity regardless of the superficial liquid velocity. The interfacial parameters increase sharply with increasing  $\langle j_g \rangle$  at low values of superficial gas velocity, and the rate of increase decreases as the superficial gas velocity increases. Similar behavior

of void fraction with gas flow rate has been reported by Shilimkan [12], Watson et al. [13] and DeJesus and Kawaji [14] for the vertical flow configuration.

### 18.3.3. Comparison with Interfacial Area Correlations

There are several correlations for interfacial areas [15-20]. They all were established from experimental observations on vertical two-phase flow systems. Kasturi and Stepanek [15], Banerjee et al. [16], Tomida et al. [17], Trombouze et al. [18] and Jepsen [19] considered that the interfacial mass transfer or interfacial area is dependent on the dissipation in the fluid. This led them to correlate interfacial area in terms of frictional pressure drop and some kind of superficial velocity scale. Thus

$$\langle a_i \rangle = f \left[ \left( \frac{dP}{dz} \right)_{fr}, \langle j \rangle \right] \quad (4)$$

Then a power law relation between  $\langle a_i \rangle$  and  $(dP/dz)_{fr}$  and  $\langle j \rangle$  or a relevant superficial velocity was assumed. By plotting data against these parameters in log-log scale, power and proportionality constants were obtained. These correlations are summarized in Table II.

From Table II it is evident that both the power and proportionality constants change considerably with system geometries, bubble generation mechanism and possibly with the void fraction. There are no models available to calculate these constants without experimental data for that particular system. In other words, these existing correlations may be useful to rearrange data into a practical correlation. However, recent comparative studies of Delhaye and Brickard [5] show that the use of these correlations cannot be easily extended to other systems.

Although the existing correlations listed in Table II are all based on the vertical flow configurations, predictions based on some of these correlations are compared with the horizontal bubbly flow data of the present measurements. The

comparisons are illustrated in Figures 8-12 with various dissipation parameters of Refs. [15-19]. Considerable scatter can be observed from these figures. The Tomida et al.'s [17] energy dissipation parameter was found to best correlate the present data compared to other previously proposed parameters. However, the scatter was still considerable and better correlating approaches should be developed. Similar scatter was also observed by Delhaye and Brickard [10] and DeJesus and Kawaji [14] for their vertical bubbly flow data.

From physical point of view, there is no doubt that there exists some relation between the frictional pressure drop and the interfacial area. Furthermore, there is a practical advantage for a chemical engineer to use the above correlation methods, since, in most cases, a simple prototypic experiment can be carried out to establish the needed data base. However, for general two-phase flow systems, the correlation model expressed by Eq. (4) may not be suitable. Since the interfacial area concentration is a parameter which characterizes the internal structure of a two-phase flow-pattern, its mechanistic modeling should be based on the geometric factors, void fraction and flow. A mechanistic modeling of interfacial area based on bubble size and the void fraction is described below.

#### **18.4. Modeling of Interfacial Area**

The interfacial area is very strongly affected by the bubble size and void fraction since the surface to volume ratio of a small bubble is larger than that of a larger bubble. Furthermore, when the bubbles are not spherical, the volume to surface area also depends on the shape of the bubble at the same void fraction. Assuming that the bubbles are spherical, the area-averaged void fraction and Sauter mean diameter can be used to calculate the interfacial area concentration from Eq. (3) as follows:

$$\langle a_i \rangle = \frac{6 \langle \alpha \rangle}{\langle d_{sm} \rangle} \quad (5)$$

It is apparent from this equation that correct modeling of  $\langle a_i \rangle$  requires simultaneous modeling of void fraction and the Sauter mean diameter provided that the bubbles are spherical.

#### 18.4.1. Modeling of Void Fraction

Based on the gas velocity and void fraction measurements, the drift-flux model presentation as suggested by Zuber and Findlay [21] is conveniently performed. According to this model, the weighted mean gas velocity,  $\bar{u}_g$ , can be represented by

$$\bar{u}_g = \bar{u}_{gj} + c_o \langle j \rangle \quad (6)$$

where  $\bar{u}_{gj}$  is the weighted mean gas phase drift velocity, whereas  $c_o$  is the velocity distribution parameter, and  $\langle j \rangle$  is the area-averaged value of the superficial volumetric velocity of the mixture. These quantities are defined as follows:

$$\langle j \rangle \equiv \frac{1}{A} \int_A [j_f(r) + j_g(r)] dA \quad (7)$$

$$\bar{u}_g \equiv \frac{\int_A \alpha(r) u_g(r) dA}{\int_A \alpha(r) dA} = \frac{\langle j_g \rangle}{\langle \alpha \rangle} \quad (8)$$

$$\bar{u}_{gj} \equiv \frac{\int_A \alpha(r) u_{gj}(r) dA}{\int_A \alpha(r) dA} = \frac{\langle \alpha u_{gj} \rangle}{\langle \alpha \rangle} \quad (9)$$

and

$$c_o \equiv \frac{\int_A \alpha(r) j(r) dA}{\int_A \alpha(r) dA \cdot \int_A j(r) dA} = \frac{\langle \alpha j \rangle}{\langle \alpha \rangle \langle j \rangle} \quad (10)$$

The drift-flux model presentation is illustrated in Figure 13 where  $\langle j_f \rangle$  is treated as a parameter. From this figure it is evident that a linear relationship between  $\bar{u}_g$  and  $\langle j \rangle$  exists for a given value of  $\langle j_f \rangle$ . However, a systematic effect of the liquid flow can be noticed. For relatively low values of  $\langle j_f \rangle$  and  $\langle j \rangle$ ,  $\bar{u}_{gj} < 0$  and  $c_o > 1.0$ . However, as  $\langle j_f \rangle$  or  $\langle j \rangle$  increases,  $\bar{u}_{gj}$  gradually increases and becomes positive whereas  $c_o$  decreases and can be as low as 0.82. Therefore, the data can be represented by a family of curves with the liquid flow rate as a parameter. In a recent experimentation of Andreussi et al. [22], the drift-flux presentation resulted in  $\bar{u}_{gj} < 0$  and  $c_o < 1.0$ , which seems to agree with the present observations.

The reverse behavior of  $\bar{u}_{gj}$  and  $c_o$  suggests another plane, i.e., the  $\langle \alpha \rangle$  -  $\langle \beta \rangle$  plane, to correlate and analyze the data. From Eq. (6) it can be shown that

$$\langle \alpha \rangle = \frac{\langle \beta \rangle}{c_o + \bar{u}_{gj} / \langle j \rangle} \equiv K \langle \beta \rangle \quad (11)$$

where  $\langle \beta \rangle$  is the flowing volume concentration,

$$\langle \beta \rangle \equiv \frac{\langle j_g \rangle}{\langle j_f \rangle + \langle j_g \rangle} \quad (12)$$

The data represented by  $\langle \alpha \rangle$  -  $\langle \beta \rangle$  plane is shown in Figure 14. By examining and comparing the  $\bar{u}_g$  -  $\langle j \rangle$  and  $\langle \alpha \rangle$  -  $\langle \beta \rangle$  planes,  $\langle \alpha \rangle$  -  $\langle \beta \rangle$  is clearly superior because it correlates the data very well for the entire data range. This is not the case for the  $\bar{u}_g$  -  $\langle j \rangle$  plane. Figure 14 indicates a constant K value of 1.03 independent of the flow rates. This apparent success of Eq. (11) can be explained by the fact that the horizontal bubbly flow occurs at relatively high mass flow rates. For such conditions, the local relative velocity is very small, which justifies the omission of the relative velocity effect accounted for by the first term on the right-hand side of Eq. (6). Hence, a constant value of K results from Eq. (11).

The average void-fraction predicted by Eq. (11) is illustrated in Figure 14 by solid lines for each value of superficial liquid velocity. An overall comparison with the present experimental data is given in Figure 15. Equation (11) predicts the data very well within a mean deviation of  $\pm 2.58\%$ , and can be used to evaluate the average void-fraction for horizontal bubbly two-phase flow-pattern. Although it has the limitations of the present data range, the present form justifies nearly homogenous flow, which has been an adopted procedure in a horizontal bubbly flow modeling.

#### 18.4.2. Modeling of Bubble Size

The initial bubble or drop size is determined in terms of the mechanism of fluid particle generation such as formation of bubbles at an orifice and generation of droplets by shearing off of roll-waves in an annular flow. However, in forced convection pipe flow or mechanically agitated systems the initial fluid particle size may be too large to be stable. In this case the particle size is further determined by a break-up mechanism. A generalized break-up mechanism can be expressed as a balance between external stresses,  $\tau$ , and the surface stress,  $\sigma/(d/2)$ , where  $\sigma$  is the surface tension and  $d$  is the fluid particle diameter. These stresses influence both the size of fluid particles which are torn away from their point of formation and also the maximum particle size which is stable in the flow field. Therefore, the stability condition can be characterized by the ratio of the external stress and surface stress, i.e., by a suitably chosen Weber number. The critical Weber number above which the fluid particle is no longer stable is defined as

$$We_c \equiv \tau d_{\max}/2\sigma \quad (13)$$

where  $d_{\max}$  is the maximum stable fluid particle size.

Basically there are two external forces that are involved in the breaking up of liquid drops or gas bubbles, namely, viscous and inertial forces. In most applications, the Reynolds numbers that are characteristic of the flow field are so large that viscous effects are negligible. In other cases, however, inertial effects play a minor role and may be neglected. Existing experimental and theoretical information can, therefore, be classified into two categories, namely, in which surface tension and viscous forces interact, and another in which capillary and inertial forces are dominant.

The first fundamental experiments on the breakup of drops and bubbles under the action of external viscous stresses and surface stress were made by Taylor [23]. Taylor made numerous observations, many of which were subsequently explained by Tomotika [24]. The breakup criterion is expressed in terms of external viscous stress in Eq. (13). It is given by

$$We_c = \mu_c S d_{\max}/2\sigma \quad (14)$$

where  $\mu_c$  is the absolute viscosity of the continuous phase, and  $S$  is the maximum velocity gradient in the external flow field.

The Taylor mechanism of bubble or drop deformations applies if both the undeformed and the elongated particles are small compared with the local regions of viscous flow. When the Reynolds number of the external flow field is large, as it is in most practical applications, the spatial dimensions of such local regions are very small compared with the drop size.

Fundamental studies on the breaking up of drops and bubbles by surface forces and dynamic pressures were made by several investigators [25-29]. Kolmogorov [25] concluded that the splitting of a drop or bubble of size  $d$  must depend on three dimensionless ratios, namely

$$\text{the Weber number: } We = \rho_c \bar{u}_c^2 d/2\sigma \quad (15)$$

ratio of length scales:  $d_d/\eta$  (16)

and ratio of kinematic viscosities:  $\nu_d/\nu_c$  (17)

where  $u_c^2$  is the spatial average value of the square of velocity differences over a distance equal to  $d$ , and  $\eta$  is the internal scale of local turbulence for the equilibrium range (usually called the Kolmogorov scale). Kolmogorov's conclusions are summarized in Table III.

In cases A1 and B1, the bubble or drop size is much smaller than the Kolmogorov microscale which is a length scale of the flow where viscous forces play a dominant role. In these cases, the phenomena associated with the breakup of a drop or bubble are similar to those investigated by Taylor [23]. In contrast, cases A3 and B4 apply whenever viscous forces are negligible but the dynamic forces and the capillary forces are dominant in the process of fluid particle breakup. More specifically B4 is the case studied in the present investigation.

The force due to the dynamic pressure may develop either through the relative velocity of liquid flowing around the bubble or through the turbulent liquid fluctuations acting over the bubble causing average pressure fluctuations. As indicated in the preceding sections the relative velocity in a horizontal bubbly two-phase flow is negligibly small. Therefore, the average pressure fluctuations generated by the turbulent liquid fluctuations acting across a bubble diameter is the only means which causes distortion of the bubble. Furthermore, a uniform bubble size distribution that was observed in the core, Figure 4, except very near the wall, indicates the bubble size is primarily determined by the local turbulence. However, in the vicinity of the pipe wall where steep velocity gradient exists, it is expected that bubble breakup must be governed by Taylor breakup mechanism which, as shown by Levich [30], usually



yields smaller bubbles. Experimental data illustrated in Figure 4 justifies this conclusion. Since the number of bubbles generated by the Taylor breakup mechanism would be confined to the very vicinity of pipe wall and be much less than the global core breakup, the core breakup mechanism will be adopted here to model the average mean bubble size.

In view of the above discussion the external stresses can be expressed in terms of velocity fluctuations, and Eq. (13) yields:

$$We_c = \rho_c \bar{u}_c^2 d_{\max} / 2\sigma \quad (18)$$

where  $\bar{u}_c^2$  is the spatial average value of the square of velocity differences over a distance equal to  $d_{\max}$ , and  $\rho_c$  is the continuous phase density.

Considering the simplest case of turbulence, namely an isotropic homogeneous turbulence, the main contribution to the kinetic energy,  $\bar{u}_c^2$ , is made by the fluctuations in the region of wave lengths where the Kolmogorov energy distribution law is valid. In this region the turbulence pattern is solely determined by the energy dissipation rate per unit mass,  $\epsilon$ . The mean square fluctuation velocity difference,  $\bar{u}_c^2$ , between two points,  $d_{\max}$ , is given by Kolmogorov [25] as follows:

$$\bar{u}_c^2 = 2 (\epsilon d_{\max})^{2/3} \quad (19)$$

Replacing this value for  $\bar{u}_c^2$  in Eq. (18) yields:

$$We_c = \rho_c \epsilon^{2/3} d_{\max} / 2\sigma \quad (20)$$

It is to be noted that in experimental verification of this model of bubble breakup a string of bubbles were used. In this case there exists only one bubble in a length of single bubble diameter. However, in multi-bubble systems as in

the case of a pipe flow, the energy must be shared by the total number of bubbles present within one bubble diameter length of  $d_{\max}$ .

Taking this view the number of bubbles present in a distance  $d_{\max}$  is calculated as  $(3/2) \langle \alpha \rangle (d_h/d_{\max})^2$ , and the energy dissipation rate is divided by this number resulting in the following equation:

$$We_c = \rho_c \epsilon^{2/3} d_{\max}^{5/3} / [(3/2) \langle \alpha \rangle (d_h/d_{\max})^2]^{2/3} \quad (21)$$

This equation can be used to determine the maximum bubble size as follows:

$$d_{\max} = (\sigma We_c / \rho_c)^{1/3} (1.5 \langle \alpha \rangle d_h^2 / \epsilon)^{2/9} \quad (22)$$

The value of  $\epsilon$  is obtained from the mechanical energy equation

$$\epsilon = (\langle j \rangle / \rho_m) (-dP/dz) \quad (23)$$

where  $\langle j \rangle$ ,  $\rho_m$ ,  $(d_h)$  and  $(dP/dz)$ , respectively, are the mixture volumetric flux, mixture density, hydraulic diameter of channel and the pressure gradient. With Eq. (23) for  $\epsilon$ , the maximum stable bubble size can be calculated from Eq. (22) as follows:

$$d_{\max} = (\sigma We_c / \rho_f^{1/3})^{1/3} [1.5 \langle \alpha \rangle (1 - \langle \alpha \rangle) d_h^2]^{2/9} / [\langle j \rangle (-dP/dz)]^{2/9} \quad (24)$$

The critical value of the Weber number appearing in Eq. (24) can be calculated by considering the natural frequency and mode oscillation of a spherical bubble or drop. The zeroth order mode is a simple volume pulsation while the first mode corresponds to a translational oscillation. The second and higher modes involve oscillations of shape with fixed volume. According to Lamb [31], the natural frequency,  $f_n$ , of the  $n_{th}$  order mode of a spherical drop or bubble performing small amplitude oscillation is given by

$$(2\pi f_n)^2 = \frac{8 n [(n+1)(n-1)(n+2)] \sigma}{[(n+1) \rho_d + n \rho_c] d^3} \quad (25)$$

Due to small amount of damping, the amplitude of response of a bubble to a steady-state sinusoidal external pressure increases enormously as one of the natural frequencies is reached. Now, a characteristic frequency of the turbulent flow is given by

$$f = (\bar{u}_c^2)^{1/2} / \ell \quad (26)$$

To obtain the lowest Weber number at which bubble breakup will occur, we set  $f$  equal to the natural frequency of the lowest fixed volume oscillation of the bubble and  $\ell$  equal to the bubble diameter. This is equivalent to saying that

$$\bar{u}_c^2 = (f_2 d_{\max})^2 \quad (27)$$

For the case of gas bubbles in water,  $\rho_d \ll \rho_c$ , Eq. (25) can be used to calculate  $f_2$ , and Eq. (27) yields

$$\bar{u}_c^2 = 24 \sigma / \pi^2 \rho_c d_{\max} \quad (28)$$

Finally, replacing  $\bar{u}_c^2$  in Eq. (18) by Eq. (20)

$$We_c \equiv \rho_c \bar{u}_c^2 d_{\max} / 2\sigma = 12/\pi^2 = 1.24 \quad (29)$$

For air bubbles in water jet Sevik and Park [28] experimentally determined the critical Weber number and found to be 1.3. Using the value of the critical Weber number given by Eq. (29), the maximum bubble size in a multi-bubble system is obtained from Eq. (24) as follows:

$$d_{\max} = 1.176 (\sigma/\rho_f^{1/3})^{1/3} [\langle \alpha \rangle (1-\langle \alpha \rangle) d_h^2]^{2/9} / [\langle j \rangle (-dP/dz)]^{2/9} \quad (30)$$

Predictions from Eq. (29) were compared with the measured values of Sauter mean diameters,  $d_{sm}$ . A certain consistency in the ratio between  $d_{max}$  and  $d_{sm}$  was observed. Once this ratio which is about 1.11, is replaced in Eq. (30), the resulting equation can be used to determine  $d_{sm}$ .

$$d_{sm} = 1.06 (\sigma/\rho_f)^{1/3} [\langle\alpha\rangle (1-\langle\alpha\rangle) d_h^2]^{2/9} / [\langle j \rangle (-dP/dz)]^{2/9} \quad (31)$$

In order to be able to compare the Sauter mean diameters predicted by the newly developed expression, Eq. (31), with the present experimental data a relation for pressure gradient appearing in Eq. (31) is needed. In Figure 16 the present experimental pressure drop data is presented in terms of pressure-drop multiplier,  $\phi_f^2$ , as suggested by Martinelli and Nelson [32]. In view of a good presentation of the pressure-drop multiplier, the Martinelli-Nelson pressure-drop correlation is used for  $d_{sm}$  predictions from Eq. (31), and the  $d_{sm}$  predictions from Eq. (31) are illustrated in Figure 7 by solid lines for each value of the superficial liquid velocity. An overall comparison with the present experimental measurements is given in Figure 17.

From Figures 7 and 17 a good agreement between the predicted and experimental values can be observed. In fact, a mean deviation of  $\pm 4.62\%$  between predicted and experimental values can be seen from Figure 17. The good agreement with experimental results indicates that the principal physical mechanisms involved in a bubble breakup are properly accounted for in the development of theoretical model. Irrespective of good comparisons, limitations of the experimental work and theoretical modeling have to be taken into account when applying Eq. (31):

- a) The pipe diameter dependence of the mean bubble size seems relatively large. Presently an investigation has been underway to carry out experimentation in a 25.4 mm-ID pipe with the same bubble generation

mechanism. Based on a very few data the bubble size is somewhat smaller in the present set-up. However, the number of data does not warrant a conclusion yet.

- b) The only one bubble size generation mechanism was used during the course of experimentations. Therefore, effects of initial bubble size were not systematically investigated in the present work. However, it is proper to mention that fundamental studies regarding the initial bubble size were undertaken in horizontal bubbly two-phase flow configurations by Sevik and Park [28] and Sleicher [27]. Both indicated that irrespective of initial bubble size the maximum fluid particle size was uniquely defined as long as the pipe was long enough. The residence time of a bubble size was in all cases very much longer than the following characteristic times: natural period of bubble vibration, mean time of diffusion of bubble from core toward the top of tube wall and Lagrangian time scale. Then intuition based on the above reasoning suggested that a pipe length of 13 meters was sufficient for bubble interactions resulting in a relatively uniform bubble size distribution due to coalescence and breakup processes. Recently, the importance of the effects of initial bubble size on flow modeling has been stressed by Zun [33], Sarizawa and Kataoka [34,35], Lahey [36] and Liu [11]. However, all these investigations were concerned with vertical flow configurations, where the bubbly flow-pattern is limited to relatively lower velocities than those experienced in horizontal flow situations.
- c) The simplest case, namely, an isotropic homogeneous turbulence was considered in developing the bubble breakup model. For this case,

Kolmogorov's Universal Equilibrium theory implies that energy transfer through the spectrum is independent of viscosity resulting in Eq. (19). This case can be justified if the Reynolds number of the flow is sufficiently high. However, derivation leading to bubble size can not be applicable for highly viscous liquids. In this case other breakup mechanisms should be used.

- d) Finally, it is important to recognize that there are two basic dissimilarities between vertical upflow and horizontal bubbly flow patterns. In the vertical flow there exists a significant positive relative velocity between bubbles and continuous liquid phase, whereas a small but negative average relative velocity was observed in the horizontal flow. The gravitational pressure gradient in the vertical flow is so large that the pressure difference along one single bubble may be solely determined by a macroscopic pressure gradient leading to a global bubble deformation and an eventual bubble breakup. In spite of these two basic differences between two bubbly flow configurations, a comparison is made between average Sauter mean diameter predicted by Eq. (31) and those vertical flow experimental observations reported by Delhay and Brickard [10]. The result is illustrated in Figure 18. This figure shows a rather good agreement in behavior and general tendency for photographic measurements. However, there exists a large data scatter for ultrasonic measurements. In spite of basic differences between vertical upflow and horizontal flow configurations, the comparison in Figure 18 is encouraging for extending the theoretical model developed here to the vertical upflow configuration.

### 18.4.3. Interfacial Area Concentration

Now Eq. (11) for void fraction and Eq. (31) for the maximum bubble size can be used in Eq. (5) to determine the averaged interfacial area concentration as follows:

$$\langle a_i \rangle = \frac{6 \langle \alpha \rangle [(\langle j_f \rangle + \langle j_g \rangle) (-dP/dz)]^{2/9}}{1.06 (\sigma/\rho_f^{1/3})^{1/3} [\langle \alpha \rangle (1-\langle \alpha \rangle) d_h^2]^{2/9}} \quad (32)$$

Predictions for the average interfacial area concentration are compared with the experimental data in Figure 6 for each value of the superficial liquid velocity. Solid lines in Figure 6 represent the predictions from Eq. (32) where  $(-dP/dz)$  is calculated from the Martinelli-Nelson correlation. An overall comparison is given in Figure 19. From Figure 19 it is evident that the newly developed interfacial area concentration expression predicts the experimentally measured values within a mean deviation of  $\pm 5.13\%$ . Surprisingly good estimate of bubble sizes based on competing surface forces and dynamic pressure fluctuations is a good indication of the mean bubble size and interfacial area occurring in practice.

### 18.5. Summary and Conclusions

The internal phase distribution of air-water bubbly two-phase flow in a 50.3 mm ID transparent horizontal pipeline has been experimentally investigated. The local values of the interfacial geometric parameters, i.e., void fraction, interfacial area concentration and Sauter mean bubble size were measured.

The local and area-averaged interfacial parameters were analyzed as a function of superficial volumetric flux of liquid and gas phases. It was found that either decreasing the liquid flow rate or increasing the gas flow would increase the local and area-averaged interfacial parameters, although the effect

of liquid flow is found to be not as significant as the gas flow. The experimental observations reported in the present paper indicated that the gas phase drift velocity,  $\bar{u}_{gj}$ , and gas phase distribution parameter,  $c_o$ , were systematically affected by the liquid flow. Therefore, a drift-flux model correlation was not appropriate for horizontal bubbly flow. It was demonstrated that  $\langle \alpha \rangle - \langle \beta \rangle$  plane representation of average void fraction was more appropriate for horizontal bubbly flow correlation.

Finally, based on the mechanistic modeling of bubble breakup process, the Sauter mean diameter and interfacial area concentration were theoretically modeled. The theoretically predicted bubble size and interfacial area concentration were found to agree reasonably well with those measured by using double-sensor resistivity probe. This indicates that the principal mechanisms involved in the bubble breakup process are properly accounted for in the development of the theoretical model.

### Acknowledgement

The work reported in this paper was performed under the auspices of U.S. Department of Energy, Office of Basic Energy Science (D.E. FG02-87ER13764). The authors would like to express their sincere appreciation for the encouragement, support and technical comments on this program from Drs. O. P. Manley and D. Frederic of U.S. DOE/BES.



## Nomenclature

$A$	pipe cross sectional area
$a_i$	interfacial area concentration
$c_o$	distribution parameter
$d$	spherical bubble diameter
$d_{\max}$	maximum spherical bubble diameter
$d_h$	hydraulic diameter of flow channel
$d_{sm}$	Sauter mean diameter of bubbles
$j$	superficial velocity
$P$	pressure
$R$	pipe radius
$r$	radial coordinate
$u$	velocity
$u_{gj}$	gas phase drift velocity
$We_c$	critical Weber number
$z$	axial coordinate

## Greek Symbols

$\alpha$	void fraction of gas phase
$\beta$	flowing volume concentration
$\epsilon$	energy dissipation rate per unit mass
$\phi_f^2$	pressure-drop multiplier
$\mu$	dynamic viscosity
$\rho$	density
$\sigma$	surface tension
$\tau$	external stresses
$X_{tt}$	Martinelli-Nelson parameter

### Subscripts

c continuous phase  
d dispersed phase  
f liquid phase  
g gas phase  
m mixture

### Symbols

< > area-averaged value  
— void fraction weighted mean value

## References

1. G. Kocamustafaogullari, Z. Wang, "An Experimental Study on Local Interfacial Parameters in a Horizontal Bubbly Two-Phase Flow," *Int. J. Multiphase Flow*, IN PRINT (1991).
2. G. Kocamustafaogullari, Z. Wang and W. D. Huang, "Interfacial Characteristic Measurements in Horizontal Bubbly Two-Phase Flow," Univ. of Wisconsin--Milwaukee Report, DOE/NE/13764-4 (1990).
3. H. B. Bensler, "Ultrasonic Determination of Interfacial Area, Void Fraction and Sauter Mean Diameter in Bubbly Two-Phase Flow," Ph.D. Dissertation, de l'institut National Polytechnique de Grenoble (1989).
5. C. Lackmé, "Structure et Cinématiques des écoulements diphasiques a Bulles," Centre d'Etudes Nuclearies de Grenoble, Report No. CEA, 1967.
6. K. Kobayasi, Y. Iida and N. Kanegae, "Distribution of Local Void Fraction of Air-Water Two-Phase Flow in a Vertical Channel," *Bull. JSME*, Vol. 13, pp. 1005-1012 (1970).
7. V. I. Subbotin, M. K. Ibraginov, V. P. Bobkov and N. A. Tychinski, "Turbulent Channel-Flow Characteristics of Gas-Water Mixtures," *Soviet Physics-Doklady*, Vol. 16, pp. 192-194 (1971).
8. A. Serizawa, I. Kataoka and I. Michiyoshi, "Turbulence Structure of Air-Water Bubbly Flow-I. Measuring Techniques," *Int. J. Multiphase Flow*, Vol. 2, pp. 221-233 (1975).
9. M. Ishii, S. T. Revankar, W. H. Leung, K. Price and J. Miller, "Multi-Sensor Probe Method for Local Measurements in Two-Phase Flow," *Proc. Ninth Symposium on Energy Engineering Sciences*, Argonne National Laboratory, May 13-15 (1991).
10. J. M. Delhaye and P. Brickard, "Interfacial Area in Bubbly Two-Phase Flow Experimental Data and Correlations," *ANS Thermal Hydraulics Proceedings*, Vol. 5, pp. 3-13, 1991, National Heat Transfer Conference, Minneapolis, MN, July 28-31, 1991.
11. T. J. Liu, "The Effect of Bubble Size on Void Fraction Distribution in a Vertical Channel," *Proc. Int. Conf. on Multiphase Flow*, Tsukuba, Japan, Vol. 1, p. 453-457 (1991).
12. R. V. Shilimkan, "Mass Transfer in Co-Current Gas-Liquid Vertical Flows," Ph.D Thesis, University of Salford (1975).
13. A. P. Watson, D. E. Cormak and M. E. Charles, "A Preliminary Study of Interfacial Areas in Vertical Cocurrent Two-Phase Flow," *Can. J. Chem. Eng.*, Vol. 57, pp. 16-23 (1979).
14. J. M. DeJesus and M. Kawaji, "Measurement of Interfacial Area and Void Fraction in Upward, Cocurrent Gas-Liquid Flow," *ANS Proceedings, Nat. Heat Transfer Conference*, Vol. 4, pp. 137-146 (1989).

15. G. Kasturi and J. B. Stepanek, "Two-Phase Flow-III. Interfacial Area in Cocurrent Gas Liquid Flow," *Chem. Eng. Sci.*, Vol. 29, pp. 713-719 (1974).
16. S. Banerjee, D. S. Scott and E. Rhodes, "Studies on Cocurrent Gas-Liquid Flow in Helically Coiled Tubes-II," *Can. J. Chem. Eng.*, Vol. 48, pp. 542-551 (1970).
17. T. Tomida, F. Yusa and T. Okazaki, "Effective Interfacial Area and Liquid-Side Mass Transfer Coefficient in the Upward Two-Phase Flow of Gas-Liquid Mixtures," *Chem. Eng. J.*, Vol. 16, pp. 81-88 (1978).
18. P. Trombouze, H. Van Landeghem and J. P. Wanquier, "Les Réacteurs Chimiques-Conception, Calcul, Mise en Oeuvre," Publication de l'Institut Français du Pétrole, *Science et Technique du Pétrole*, No. 26, Chapitre 8, Editions Technip, Paris (1984).
19. J. C. Jepsen, "Mass Transfer in Two-Phase Horizontal Pipelines," *AIChE J.*, Vol. 16, pp. 705-711 (1970).
20. P. H. Calderbank, "Physical Rate Processes in Industrial Fermentation, Part II-Mass Transfer Coefficients in Gas-Liquid Contacting With and Without Mechanical Agitation," *Trans. Inst. of Chem. Eng.*, Vol. 37, pp. 173-185 (1959).
21. N. Zuber and J. A. Findlay, "Average Volumetric Concentration in Two-Phase Flow Systems," *J. Heat Transfer*, pp. 453-468 (1965).
22. P. Andreussi, S. Pintus, O. J. Nydal and F. S. Silva, "Measurement of the Mean Gas Velocity in Horizontal Bubbly Flow," *Transient Phenomena in Multiphase Flow, ICHMT Int. Seminar, Dubrovnik*, pp. 225-231 (1988).
23. G. E. Taylor, "The Formation of Emulsion in Definable Field of Flow," *Proc. Roy. Soc. (London)*, Ser. Vol. A164, p. 501 (1934).
24. S. Tomotika, "Breaking Up of a Drop of Viscous Liquid Immersed in Another Viscous Fluid Which is Extending at a Uniform Rate," *Proc. Roy. Soc. (London)*, Ser. Vol. A153, p. 302 (1936).
25. A. N. Kolmogorov, "On the Disintegration of Drops in a Turbulent Flow," *Doklady Akad. Nauk., SSSR*, Vol. 66, p. 825 (1949).
26. J. O. Hinze, "Fundamentals of the Hydrodynamic Mechanism of Splitting Dispersion Processes," *AIChE J.*, Vol. 1, p. 289 (1955).
27. C. A. Sleicher, "Maximum Drop Size in Turbulent Flow," *AIChE J.*, Vol. 8, p. 471 (1962).
28. M. Sevik and S. H. PARK, "The Splitting of Drops and Bubbles by Turbulent Fluid Flow," *J. Fluids Engng.*, Vol. 95, p. 53 (1973).
29. W. R. Lane, "Shatter of Drops in Streams of Air," *Ind. Engng. Chem.*, Vol. 43, p. 1312 (1951).
30. V. G. Levich, *Physicochemical Hydrodynamics*, Prentice-Hall, 1962.

31. H. Lamb, *Hydrodynamics*, Dover Press, New York 1932.
32. R. C. Martinelli and D. B. Nelson, "Prediction of Pressure Drop During Forced Circulation Boiling of Water," *Trans. ASME*, Vol. 70 (6), pp. 695-702 (1948).
33. I. Zun, "Transition from Wall Void Peaking to Core Void Peaking in Turbulent Bubbly Flow," *Transient Phenomena in Multiphase Flow, ICHMT Int. Seminar, Dubrovnik*, pp. 225-245 (1988).
34. A. Serizawa and I. Kataoka, "Phase Distribution in Two-Phase Flow," *Transient Phenomena in Multiphase Flow, ICHMT Int. Seminar, Dubrovnik*, pp. 179-224 (1988).
35. I. Kataoka and A. Serizawa, "Interfacial Area Concentration in Bubbly Flow," *Nucl. Engng. & Des.*, Vol. 120, pp. 163-180 (1990).
36. R. T. Lahey, Jr., "The Analysis of Phase Separation and Phase Distribution Phenomena Using Two-Fluid Models," *Nucl. Engng. & Des.*, Vol. 122, pp. 17-40 (1989).

Table I. Range of Experimental Data

Geometry	50.3 mm ID
Gas	Air
Liquid	Water
Gas Superficial Velocity	0.21-1.34 m/s
Liquid Superficial Velocity	3.74-6.59 m/s
Average Void Fraction	0.037-0.214
Average Interfacial Area	82.6-337.3 m <sup>2</sup> /m <sup>3</sup>
Average Sauter-Mean Diameter	2.35-4.37 mm

Table II. Interfacial Area Correlations for Vertical Flow

Author	Form of Correlation
Banerjee et al. (1970)	$\langle a_i \rangle = a [Q_f (-dP/dz)_t]^b$
Jepsen (1970)	$\langle a_i \rangle = a [(\langle j_f \rangle + j_g) (-dP/dz)_f]^b$
Kasturi & Stepanek (1974)	$\langle a_i \rangle = a [1 - \langle \alpha \rangle / Q_f] (-dP/dz)_f^b$
Tomida et al. (1978)	$\langle a_i \rangle = 0.22 \langle \alpha \rangle (-dP/dz)_t$ for $\langle j_g \rangle < 8$ m/s $\langle a_i \rangle = 0.62 \langle \alpha \rangle \langle j_g \rangle^{-1/2} (-dP/dz)_t$ for $\langle j_g \rangle > 8$ m/s
Trombuza et al. (1984)	$\langle a_i \rangle = a [\langle j_g \rangle (-dP/dz)_t]^b$

Table III.

Length Scales	Case A $v_d \ll v_c$ or $v_d = v_c$	Case B $v_d \gg v_c$
1. $d \ll \eta$	$We \in v_d/v_c$	$We$ and $v_d/v_c$
2. $d \cong \eta$	$We, d/\eta, v_d/v_c$	$We, d/\eta, v_d$
3. $d \gg \eta$	$We$	$We \in Re_d$
4. $d \gg v_d/v_c$	$We$	$We$

where  $Re_d = d(\bar{u}^2)^{1/2}/2v_d$  is the Reynolds number of the dispersed phase.

# HORIZONTAL TWO-PHASE FLOW LOOP

- |   |  |
|---|--|
| A - Interchangeable Air-Water mixing chambers | K - Pneumatic operated Ball valves             |
| B - Water flow meters of appropriate size     | L - Motor control                              |
| C - Water flow meter control valves           | M - Computer and data acquisition system       |
| D - Air flow meters of appropriate size       | N - 250 gal. Air tank                          |
| E - Air flow meter control valves             | P - 500 gal. Water tank                        |
| F - Air flow regulating valves                | Q - Air-Water separator, with internal baffles |
| G - Air pressure regulator                    | R - Water shut-off valve                       |
| H - Air filter                                | S - 20 hp. 750 gpm Water pump                  |
| I - Water pressure relief valves              | T - Glass pipe couplings with pressure taps    |
| J - Water flow regulating valves              |  |

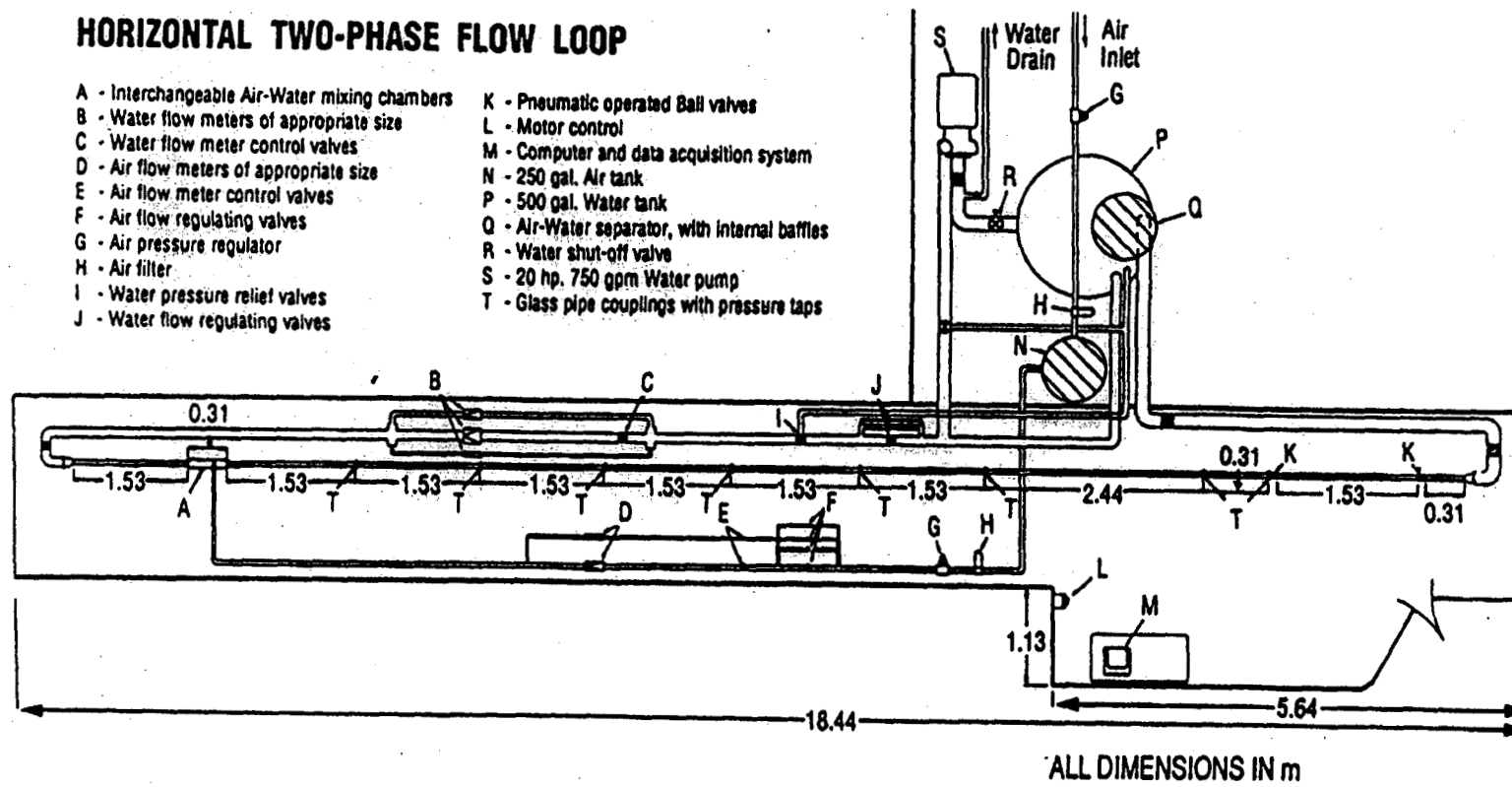


Figure 1. Schematic of Experimental Flow Loop

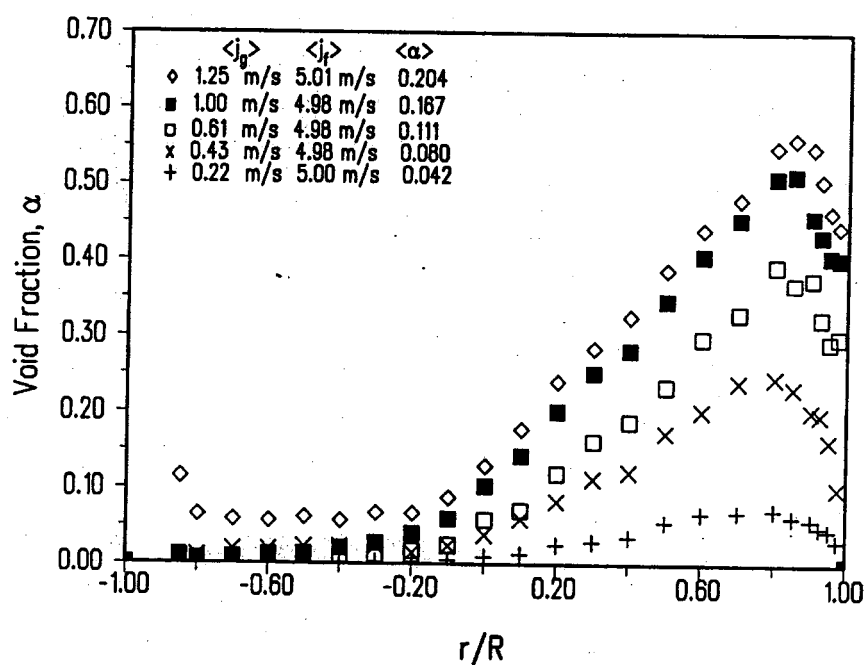


Figure 2. Effect of Gas Flow on Local Void Fraction Distribution

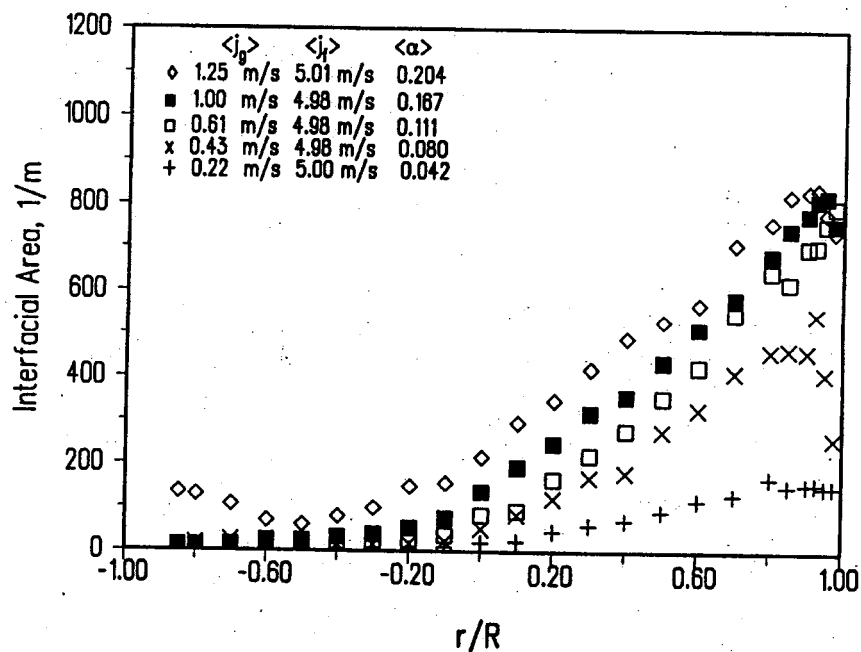


Figure 3. Effect of Gas Flow on Local Interfacial Area Concentration Profile



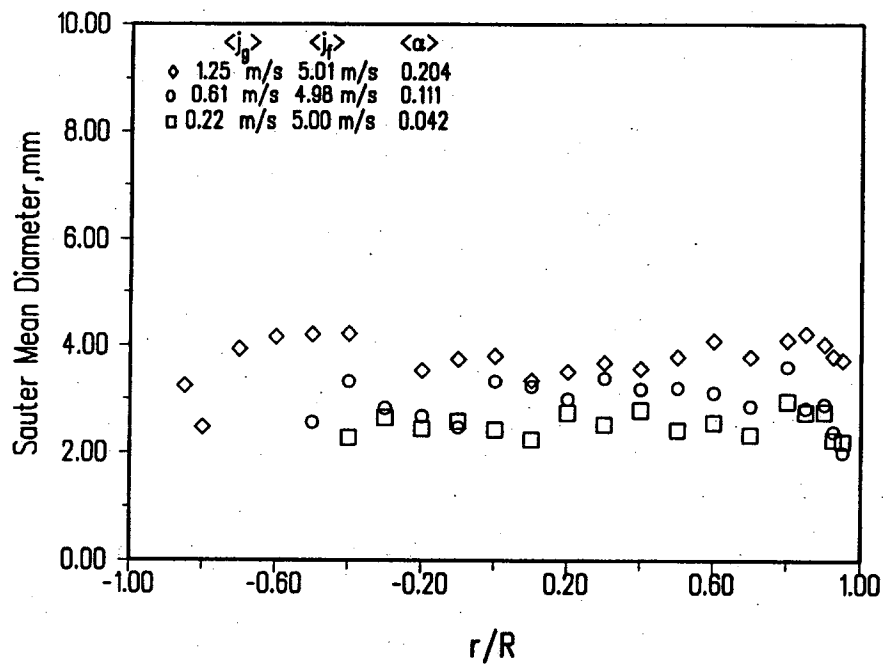


Figure 4. Effect of Gas Flow on Local Sauter Mean Bubble Diameter Distribution

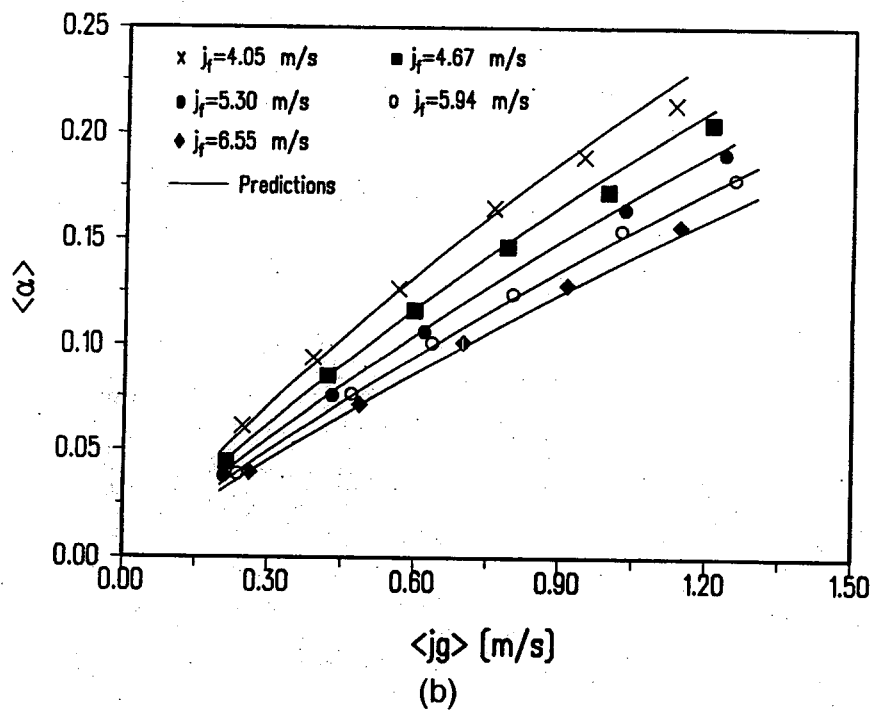
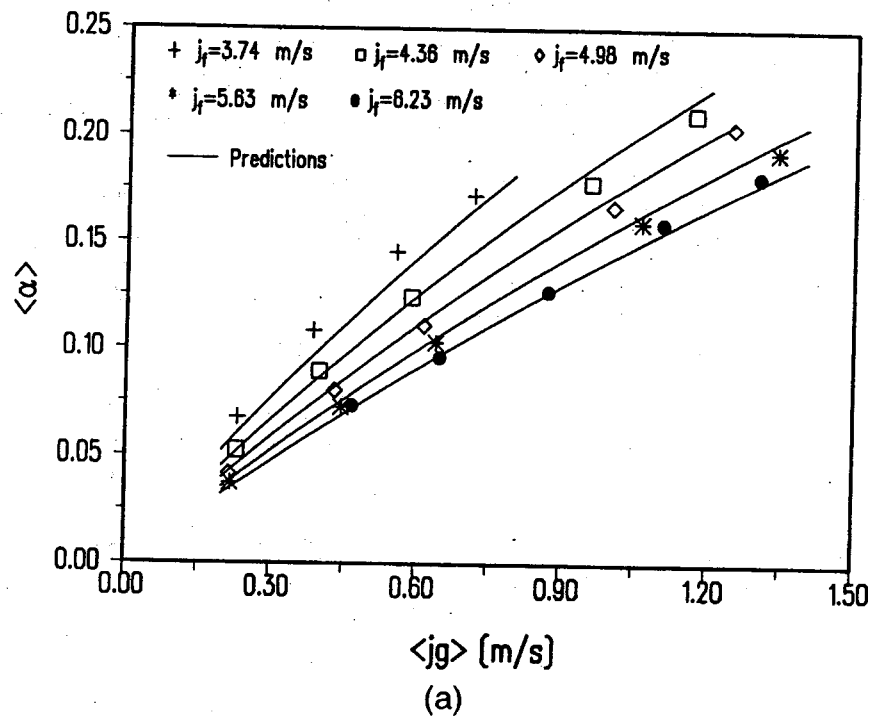


Figure 5. Variation of Average Void Fraction with Superficial Gas Velocity

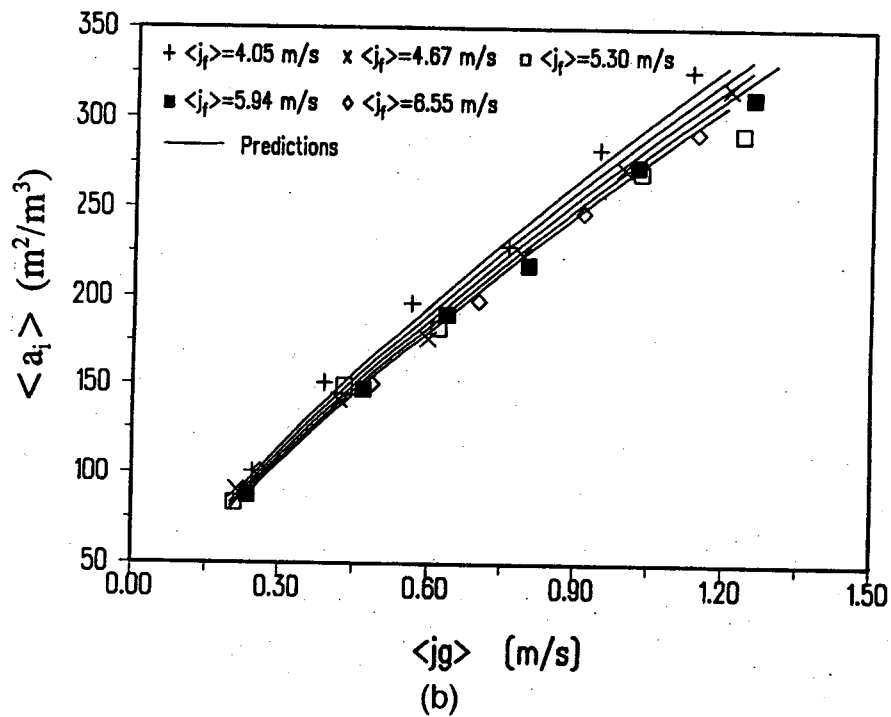
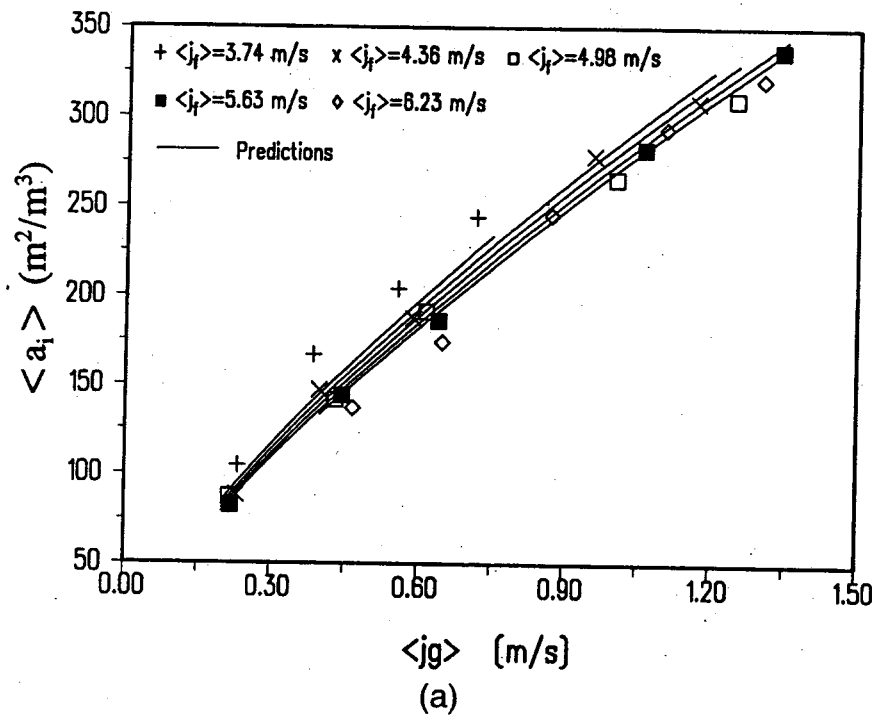


Figure 6. Variation of Average Interfacial Area Concentration with Superficial Gas Velocity

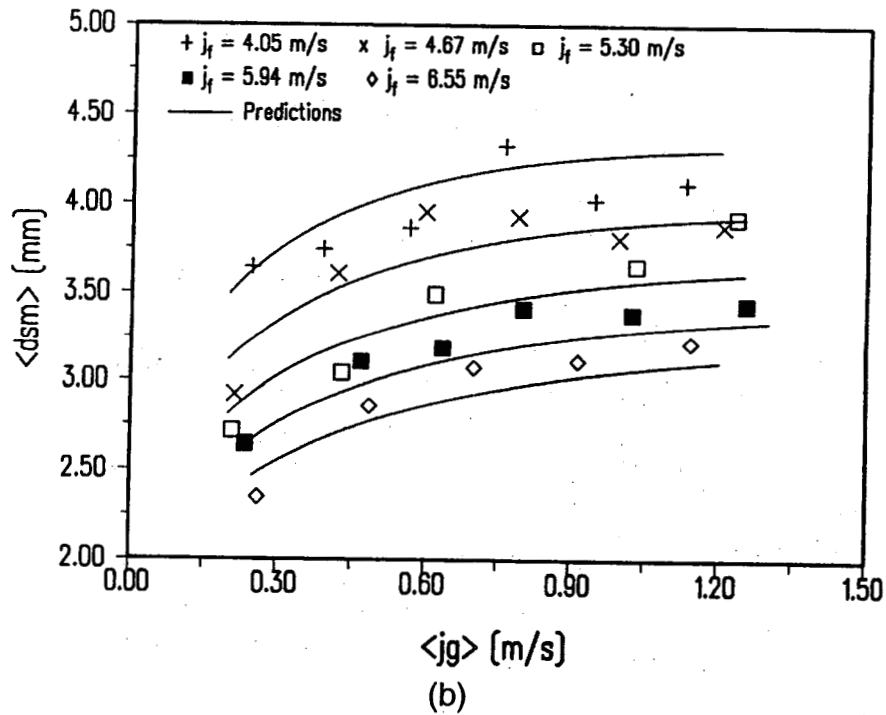
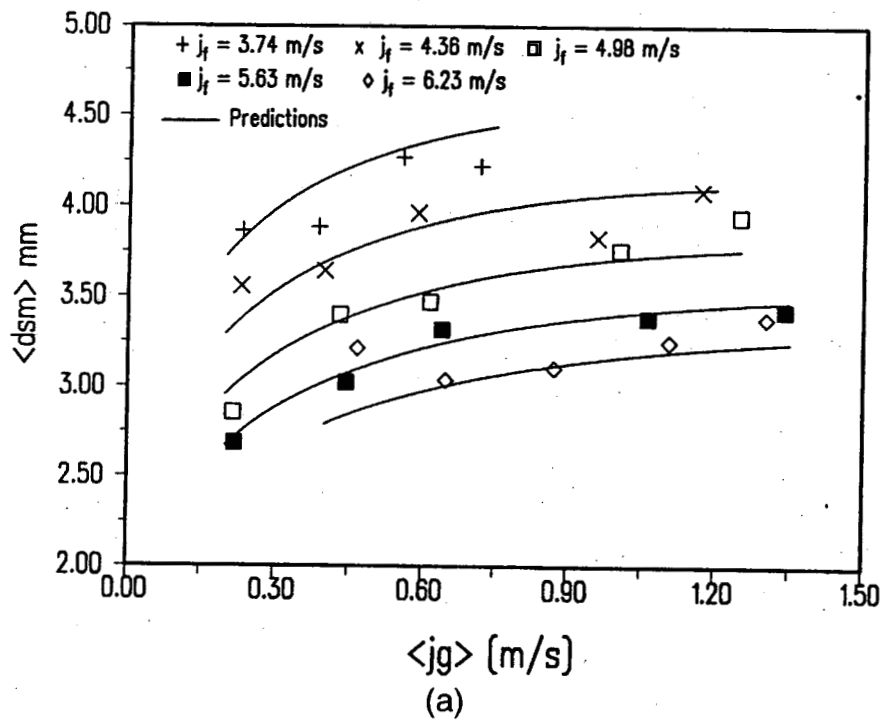


Figure 7 Variation of Average Sauter Mean Diameter of Bubbles with Superficial Gas Velocity

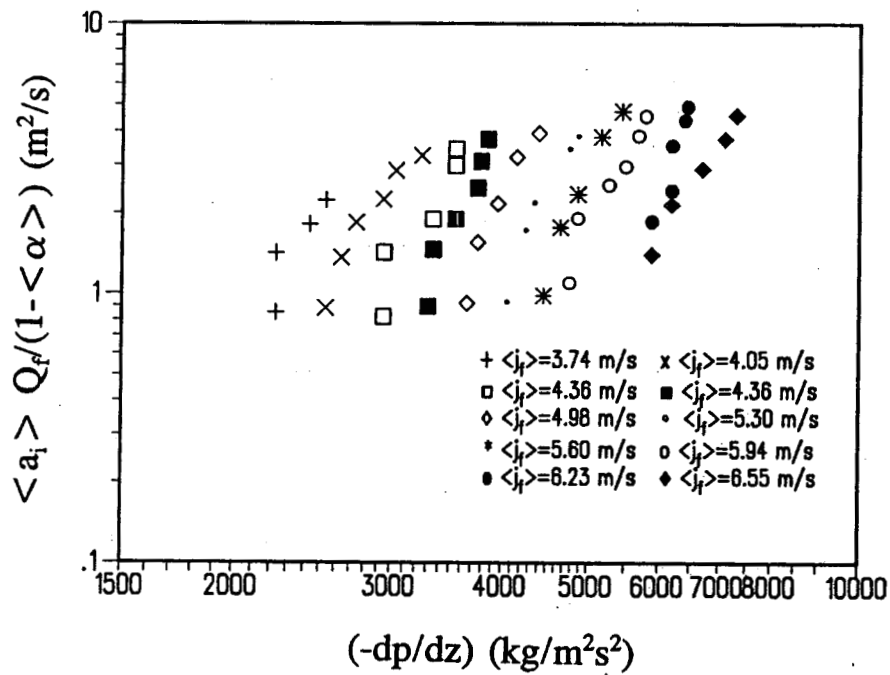


Figure 8. Comparison of Interfacial Area Concentration Data with Energy Dissipation Parameter of Kasturi and Stepanek (1974)

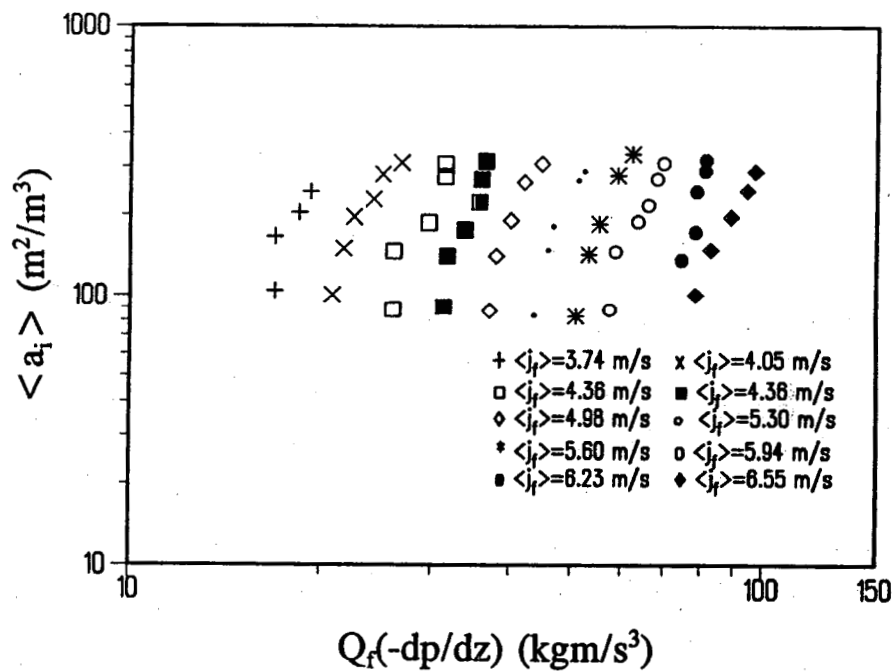


Figure 9. Comparison of Interfacial Area Concentration Data with Energy Dissipation Parameter of Banerjee et al. (1970)

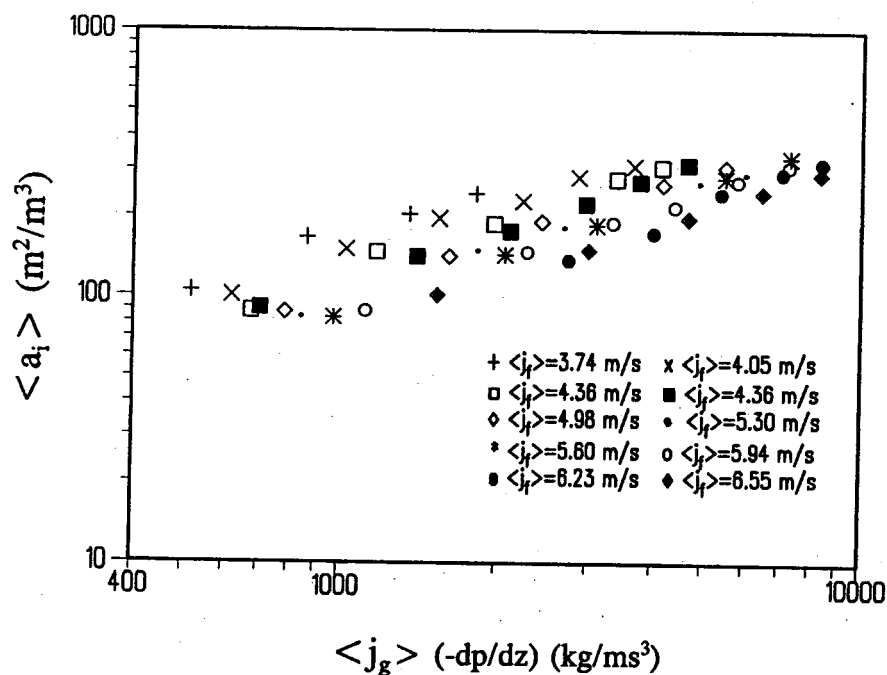


Figure 10. Comparison of Interfacial Area Concentration Data with Energy Dissipation Parameter of Trombouze et al. (1984)

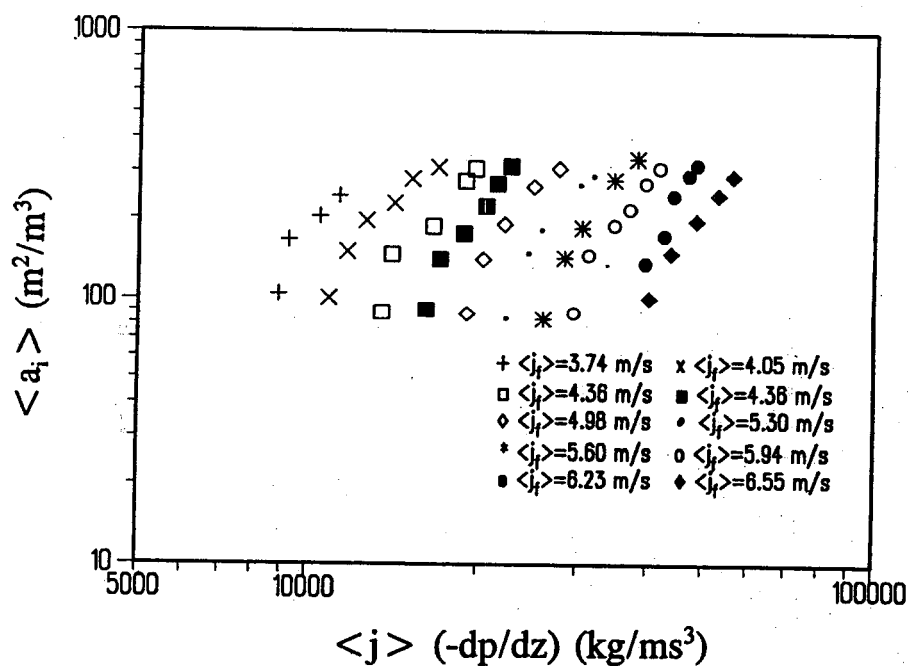


Figure 11. Comparison of Interfacial Area Concentration Data with Energy Dissipation Parameter of Jepsen et al. (1970)

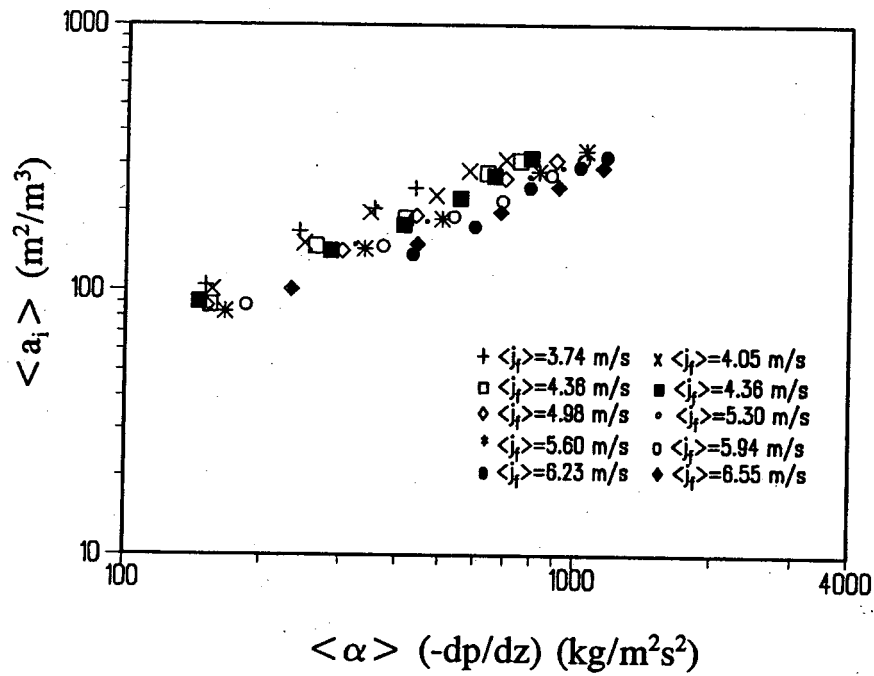


Figure 12. Comparison of Interfacial Area Concentration Data with Energy Dissipation Parameter of Tomida et al. (1978)

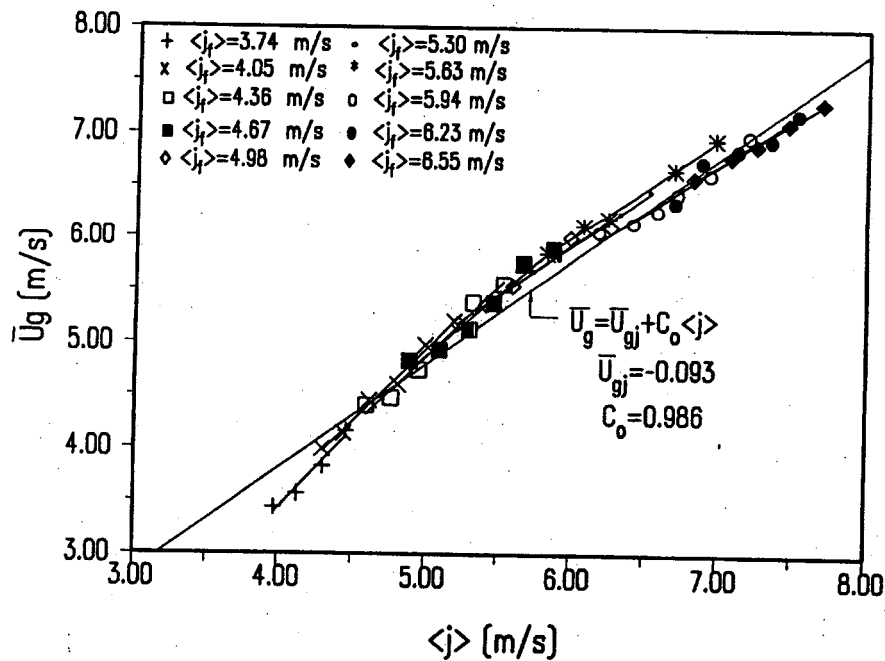


Figure 13. Drift-Flux Presentation of Present Data

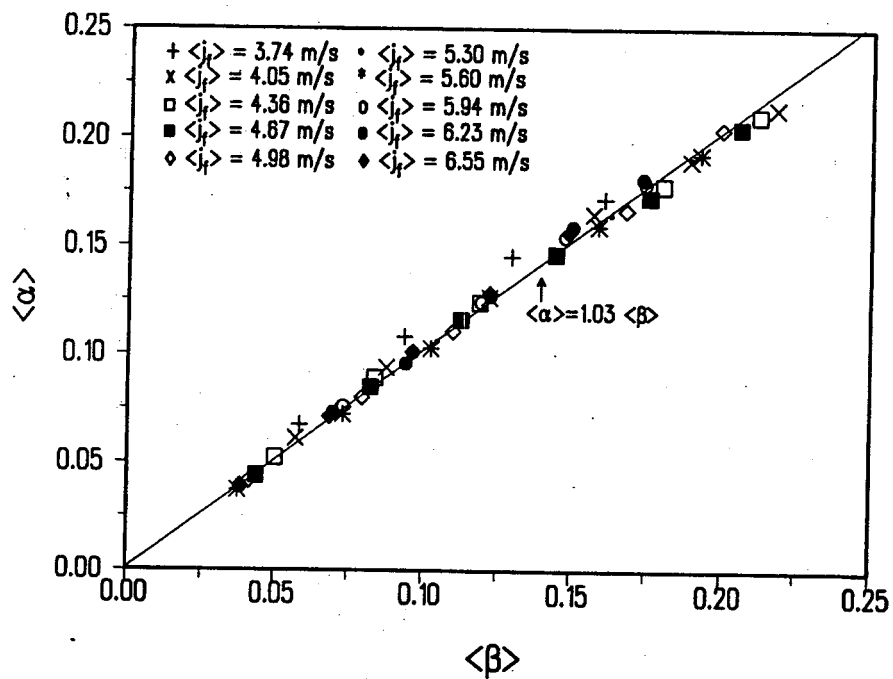


Figure 15. Comparison Between Predicted and Measured Average Void Fractions

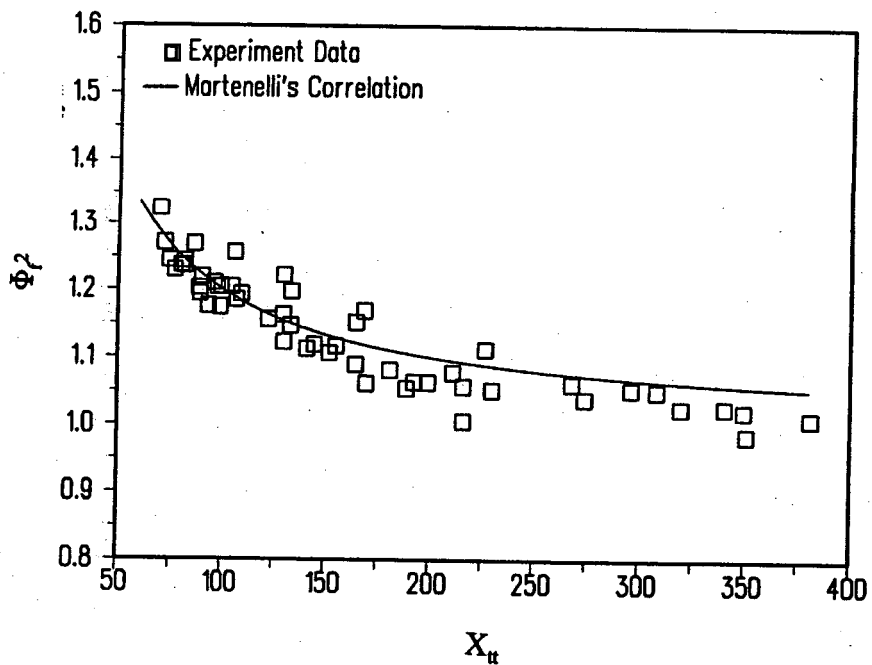


Figure 16. Comparison Between Predicted Pressure Drop Multiplier by Martinelli-Nelson Correlation and Those Measured Values



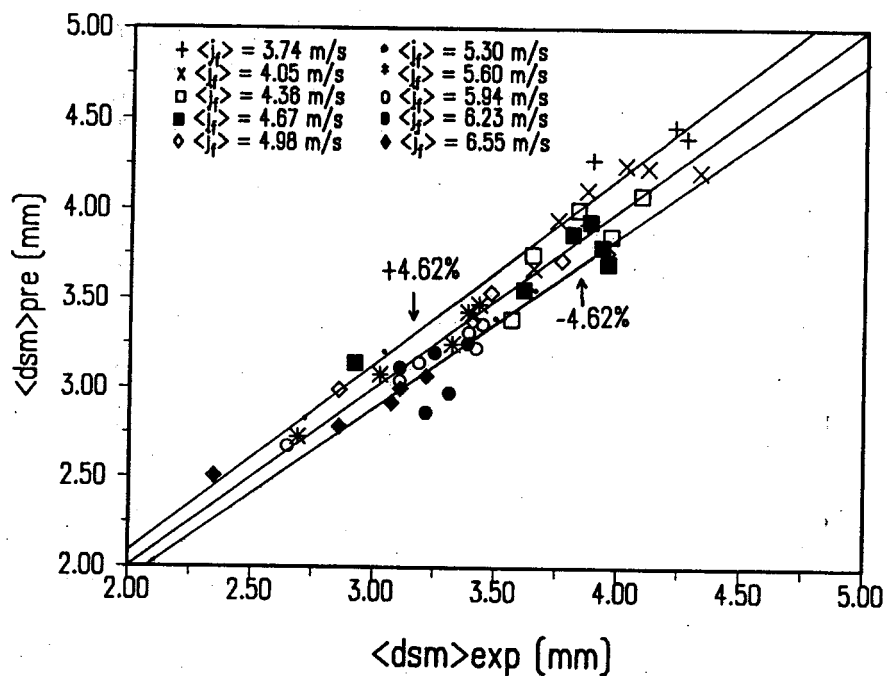


Figure 17. Comparison Between Predicted and Measured Average Sauter Mean Diameters

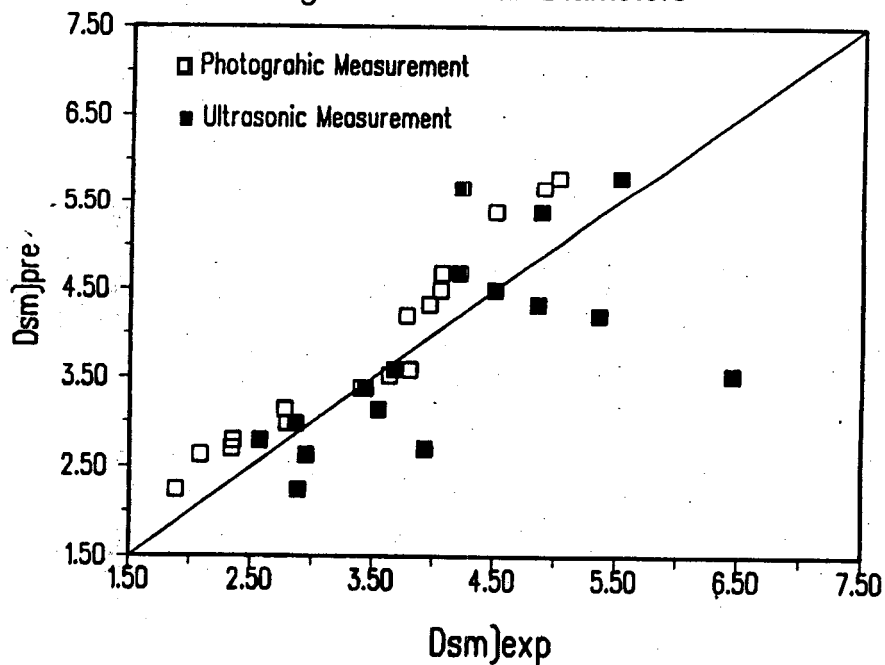


Figure 18. Comparison Between Predicted and Delhay and Brickard's Vertical Flow Data of Photographic and Ultrasound Measurements

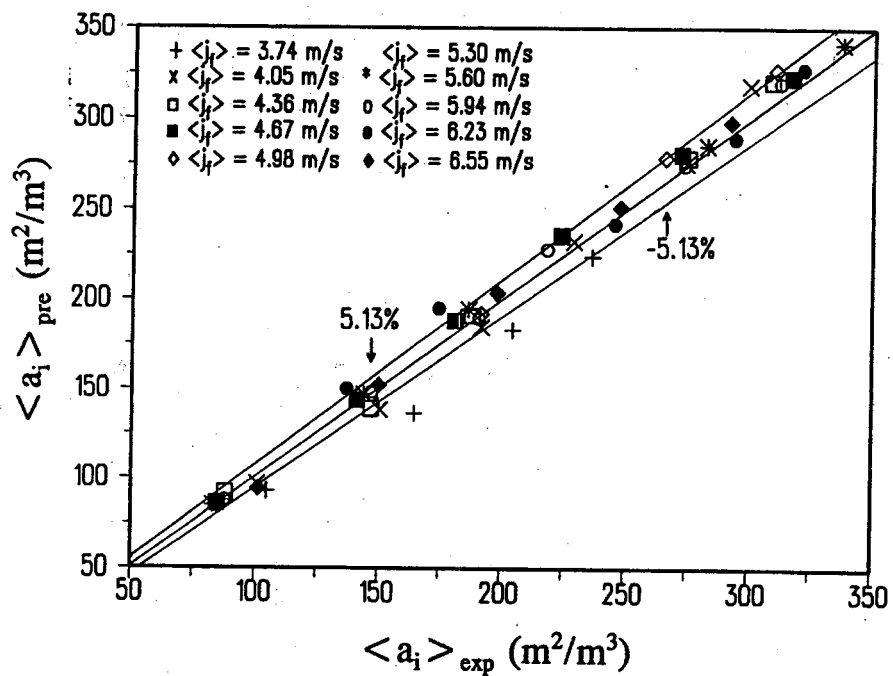


Figure 19. Comparison Between Predicted and Measured Average Interfacial Area Correlations

## 19. SUMMARY AND CONCLUSIONS

Advances in the Study of two-phase flow increasingly require detailed internal flow structure information upon which theoretical models can be formulated. The void fraction and interfacial area are two fundamental parameters characterizing the internal flow structure of two-phase flows. However, little information was available on these parameters, and it is mostly limited to vertical flow configuration. Particularly, there was virtually no database for the local interfacial area concentration in spite of its necessity in multidimensional two-fluid model analysis.

In view of the above, a research program, which has been sponsored by the DOE/BES, has been underway at the University of Wisconsin-Milwaukee. The overall objectives of the research program were to develop instrumentation methods, an extensive database and analysis leading to predictive models for describing the internal flow structure and behaviors of two-phase flow in horizontal configurations. Experimental efforts were directed at developing instrumentation technique for measurements of the local interfacial area concentration and void fraction in the bubbly flow, plug/slug flow, stratified smooth and stratified wavy and annular flow patterns encountered for two-phase flows in horizontal configurations. On the other hand, the analytical efforts were focused on predictive mechanistic models describing the interfacial structure in bubbly and droplet, stratified and annular flows as well as predicting the bubble dynamics in boiling channels.

The literature review of available interfacial area and void fraction measurements methods of Chapter 2 revealed that the available methods are effective for certain idealized cases. Only an average interfacial area could be measured by the chemical absorption method. The photographic and light attenuation methods cannot be used with opaque walls and are limited to transparent bubbly flows with relatively low void fraction. The ultrasonic method is not restricted to such conditions, and this expands the measurement of interfacial area concentration beyond the available range of fluids in non-opaque systems. However, the ultrasonic attenuation method is still limited to low void fraction bubbly flows. In view of the intention of the present investigation to measure local interfacial variables in a horizontal bubbly flows with local void fractions

possibly ranging from zero to 65 %, it was concluded that probe methods must be used. An evaluation of potential probe methods resulted in the selection of the electrical resistivity probe methods because of the relatively simple instrumentation and positive results in conducting liquids reported in the literature.

In Chapter 3, the interfacial area transport equation is derived from the statistical model of the fluid particle transport equations. The basic mechanisms affecting the source and sink terms in the interfacial transport equation are discussed in detail. It is pointed out in Chapter 3 that the use of the multi-sensor probes is essential to generating the experimental data required to develop the closure relations for the source and sink terms in the interfacial area transport equation.

As it is described in Chapter 4, an experimental air-water two-phase flow loop was designed and constructed from pyrex glass tubings. The flow loop was fully instrumented with the pressure transducers and flow metering devices. The double-sensor and four-sensor conductivity probes, hot-film anemometry probe, two-sensor parallel-wire conductivity probe and the eight-point circumferential two-sensor parallel-wire probe methods and their respective signal processing schemes were developed for the interfacial flow structure measurements for the horizontal two-phase flow configurations.

As described in Chapters 5 and 6, we have developed the double-sensor conductivity probe method and its signal processing system for bubbly flow measurements. This probe simultaneously gives following parameters over a wide-range of flow conditions:

- local void fractions and its distributions,
- local interfacial area concentration and distributions,
- local Sauter mean diameter,
- interfacial velocity and
- bubble passing frequency.

As in Chapter 8, the four-sensor conductivity probe design has been developed to measure the interfacial characteristics of large elongated plug/slug bubbles in a horizontal slug flow configuration. The simultaneous use of the double-sensor and four-sensor conductivity probes yields information for the following interfacial characteristics:

- Local void fraction due to small and large bubbles,

- local interfacial area concentration due to small and large bubbles,
- small and large bubbles interfacial velocity, and
- small and large bubble passing frequencies.

It has been demonstrated that the hot-film anemometry method could be used in bubbly flow (Chapter 7) and plug/slug flow (Chapters 9 and 10):

- to identify liquid and gas phases-phase identification,
- to measure the local time-averaged void fraction,
- to construct the local time-averaged liquid velocity and its distribution, and
- to measure the local liquid phase turbulent velocity fluctuations and turbulent intensity

The combination of the hot-film anemometry and multi-sensor conductivity probe methods yields information on the local gas and liquid velocities and, hence, the local relative velocity. It is to be noted that the test sections for the multi-sensor and hot-film probes were designed such that the test section could be rotated to obtain a three-dimensional distribution of the void fraction and interfacial area concentration at a given pipe section. Such a design was necessary since the non-symmetric distribution of the internal flow structure due to gravitational effects occur in the horizontal flow configurations

For stratified, i.e., stratified-smooth, stratified-wavy and stratified-atomizing, flow patterns in the horizontal section, we have developed two-sensor parallel-wire conductivity probe method. This probe design together with its signal processing scheme and experimental results are described in Chapter 11. The data acquisition system has been developed to directly measure the following interfacial characteristics of typical stratified flow patterns:

- the average liquid height and void fraction,
- the average wave height of interfacial waves,
- the wavelength of interfacial waves,
- the frequency of interfacial waves, and
- the speed of propagation of these waves.

The interfacial wave characteristic measurements, in turn, enable us to calculate the interfacial area concentration in the stratified flow patterns.

As illustrated in Chapter 12, an eight-sensor parallel-wire conductivity probe method was developed to measure the interfacial characteristics of a horizontal annular flow-pattern. A total of eight sensors spaced at  $45^\circ$  intervals around the circumference of the test section were enabled us to obtain information on the circumferential liquid film and interfacial wave characteristics. Such design was necessary due to the axisymmetric nature of horizontal two-phase flow systems. The local entrained droplet flow was also measured by the newly developed pitot-tube sampling test section. By tracing the probe in a given cross section of the annular flow core it was possible to measure the local droplet flux at a given probe location. A hydrodynamic model was developed for predicting the circumferential liquid film thickness distribution for a fully-developed annular flow in a horizontal tube. It was demonstrated that both wave and circumferential shear effects could be significant liquid film distribution mechanisms depending on what Reynolds number ranges and/or fluid properties were considered. For the details of this hydrodynamic model, please see the Ph.D Thesis of Jackman as referenced in Chapter 1. Chapter 13 through 18 dealt with the theoretical and mechanistic modeling efforts for describing the interfacial structure of several horizontal two-phase flow patterns. These efforts can be summarized as follows:

Chapter 13 investigated interfacial instabilities of stratified flows. The formulation of the problem proceeded with the solution of the Orr-Sommerfeld equation. The parametric study in terms of viscosity ratio, density ratio, fluid layer ratio, Reynolds number and Froude number and the angle of inclination revealed detailed characteristics of stratified flows,

Chapter 14 described derivations of overall scaling criteria obtained from the parameters needed to preserve the values of dimensionless groups in the normalized continuity, momentum and energy equations. Based on the overall scaling methodology, two-phase flow-pattern transitions were simulated in detail between high-pressure prototype and conceptual models. Although each flow-pattern transition imposes different scaling requirements, it was demonstrated that they all can be represented in a unified form.

Chapter 15 presented an analysis of the spherically symmetric phase change (moving boundary) problem to describe the bubble growth and/or collapse in a boiling channel. Neither the formulation based on the energy integral method nor the results were subject to the so-called "thin thermal boundary layer" approximation used heretofore to solve this problem. Comparison of representative set of experimental bubble collapse data in a near-zero gravity environment with a negligible translational velocity of bubbles and of convective boiling bubble growth experimental data indicated the general validity of the theoretical analysis.

Chapter 16 addressed the droplet disintegration mechanisms and offered a predictive droplet size and size distribution model for an annular flow-pattern. Two Weber number criteria, one based on the classical Kolmogorov theory and the other on Levich's theory, were discussed. It was concluded that when  $\rho_d \leq \rho_c$ , the entrainment of fluid particles by turbulence may be complete, and that the Weber number criterion based on Kolmogorov's theory mechanistically describes the fragmentation of drops and bubbles in a turbulent liquid flow. However, in the case of droplets in a gas stream with  $\rho_d \gg \rho_c$ , the entrainment of droplets by turbulent eddies cannot be complete, and relative motions play a major role instead of eddies in the mechanism of droplet disintegration. The predicted mean sizes were found to agree reasonably well with measured sizes. This indicates that the principal mechanisms involved in a break-up process in a turbulent continuous flow field were properly accounted for in the development of the theoretical model.

Based on the combination of Kelvin-Helmholtz and Rayleigh-Taylor stability theories, a simple mechanistic model was developed to describe the breakup of drops and bubbles in Chapter 17. Breakup was predicted to occur if the growth of disturbances on the leading front was rapid enough relative to the rate at which interfacial disturbances was propagated around the interface. In collaboration with a large number of experimental data for liquid-gas, liquid-liquid and gas-liquid systems, a general methodology was developed to predict the maximum stable fluid particle size in a stagnant fluid. The results are extended to predict the maximum droplet size in a high velocity gas field. Important dimensionless parameters affecting the breakup process were properly identified. They are Weber number, continuous phase viscosity number,

density and viscosity ratio groups. For each case importance of these dimensionless groups was assessed.

Chapter 18 modeled the average void fraction, bubble size and, hence, offered a predictive method for the interfacial area concentration. The void fraction model was based on the Kutateladze's approach in presenting the void-flowing volume concentration relation. The resulting void fraction predictive method was compared with experimental data, and a good agreement appeared to justify the proposed model. Each of the possible external stresses was evaluated, and it was concluded that the maximum bubble size in a high-speed horizontal bubbly flow was mainly controlled by the action of stresses resulting from pressure fluctuations generated by the turbulent liquid fluctuations across a bubble diameter. A detailed model of maximum bubble size and the Sauter mean diameter was developed based on the balance between surface stresses and the dynamic pressure induced by the turbulent fluctuations in the continuous liquid phase. Finally, based on the void fraction and bubble size modeling a predictive method developed for the interfacial area concentration. The good agreement with experimental results indicates that the principal mechanisms involved in a bubble breakup were properly accounted for in the development of a theoretical model.